ATTENTION: The Singapore Copyright Act applies to the use of this document. Nanyang Technological University Library

Diffuse Indoor Optical Wireless Local Area Networks

Wong Wing Kee Damon



School of Electrical and Electronic Engineering

A thesis submitted to the Nanyang Technological University
in fulfilment of the requirement for the degree of
Doctor of Philosophy

2008

ATTENTION: The Singapore Copyright Act applies to the use of this document. Nanyang Technological University Library

Acknowledgements

First and foremost, praise and thanks be to the Lord, who makes all things possible and whose Presence I have constantly relied upon during the course of my studies.

It has not been an easy journey and I was fortunate enough to have received much support and assistance from many people, and would like to express my gratitude and appreciation to the following in particular:

- Dr George Chen, my supervisor, for his patient mentorship during my research, and whose astute guidance on both academic and non-academic matters has been much appreciated. Through the long discussions over lunch and in his office, I have gained much invaluable advice and insight which have helped tremendously.

- Mr Yong Kim Lam, Ms Yvonne Yee Yang Boey, and Ms Seet Lye Ping, the lab technicians, for being ever helpful in helping me with the equipment and resources I needed during my research.

- The friends and colleagues in the Photonics Research Centre, whose companionship and camaraderie have made the journey a thoroughly enjoyable process, and with whom discussions have often yielded greater understanding.

- The Agency for Science, Technology and Research (A*STAR) for their gracious sponsorship of my studies, and especially to the staff of the A*STAR Graduate Academy for their help with administrative matters.

I would also like to thank my family and especially my wife, Cindy, for their unwavering support, encouragement and prayers, and my daughter Clare who has been a constant source of joy and inspiration.

ATTENTION: The Singapore Copyright Act applies to the use of this document. Nanyang Technological University Library

Table of Contents

		Page
	Acknowledgements	i
	Table of Contents	ii
	Summary	vii
	List of Figures	ix
	List of Tables	xv
1	Introduction	1
	1.1 Motivations	1
	1.2 Objectives	6
	1.3 Major contributions of the thesis	8
	1.4 Organization of the thesis	12
2	Introduction to Optical Wireless	14
	2.1 Introduction to the Chapter	15
	2.2 Increase in demand for bandwidth	15
	2.3 Towards wireless communications	18
	2.4 Radio frequency wireless networks	19
	2.4.1 IEEE 802.11	19
	2.4.2 Bluetooth	20
	2.4.3 Ultra Wide Band (UWB)	21
	2.5 Limitations of radio frequency networks	21
	2.5.1 Interference and regulation	22
	2.5.2 Security risks	23
	2.6 Optical wireless communications	25
	2.7 Comparison between optical wireless and radio	28
	2.8 Developments in indoor optical wireless communications	31

ATTENTION: The Singapore Copyright Act applies to the use of this document. Nanyang Technological University Library

3	Optical wireless channel link performance optimization through the study and optimized design of the receiver and transmitter properties		37
	3.1	Introduction to the Chapter	37
	3.2	Recent literature on optical design aspects of optical wireless communications	39
	3.3	Determination of receiver field of view	40
		3.3.1 Impulse response model	41
		3.3.2 Simulation parameters	44
		3.3.3 System design parameters	46
		3.3.4 Conventional grid-based diffusing spot designs	47
		3.3.4.1 Impulse responses	47
		3.3.4.2 Survey of results	53
		3.3.5 Conclusions	59
	3.4	Optimization of diffusing spot pattern distribution	59
		3.4.1 Introduction	59
		3.4.2 Simulated annealing technique	60
		3.4.3 Optimization of spot patterns at a field of view of 30°	72
		3.4.4 Analysis when spot pattern is not centred on ceiling	79
		3.4.5 Comparison with other works	81
		3.4.6 Conclusion	82
	3.5	System performance	83
		3.5.1 Introduction	83
		3.5.2 Communication model	83
		3.5.3 Noise	84
		3.5.4 Bit error rate analysis	86
		3.5.5 System parameters	88
		3.5.6 Simulation results	89
		3.5.7 Improving BER performance through diversity combining techniques	91
		3.5.8 A brief introduction to equalization	95

ATTENTION: The Singapore Copyright Act applies to the use of this document. Nanyang Technological University Library

		3.5.9 Conclusions	96
	3.6	Conclusions to the Chapter	97
4	Zero order minimization and suppression in computer generated holograms		98
	4.1	Introduction to the Chapter	98
	4.2	Recent work on Zero order reduction	102
	4.3	Brief introduction to computer generated holograms	104
		4.3.1 Zero order in computer generated holograms	105
	4.4	Re-utilization of zero order intensity through polarization manipulation	109
	4.5	Zero order suppression by phase compensation	113
		4.5.1 Simulation model	113
		4.5.2 Introduction of a phase compensating element	115
	4.6	Use of phase checkerboard for redistribution of zeroth order energy	118
		4.6.1 The phase checkerboard function	119
		4.6.2 Use of the PCF with a hologram	122
		4.6.3 The combined CGH-PCF optical element	125
	4.7	Simulation of fabrication errors and discussion	132
	4.8	Experimental measurements	137
		4.8.1 Characterization by varying the gray levels	140
		4.8.2 Experiments using the combined SCGH-PCF optical element	145
	4.9	Comparison with other methods	151
	4.10	Conclusion	152
5	Design and Implementation of a Visible Light Optical Wireless Transmission System employing White Light Emitting Diodes		154
	5.1	Introduction to the Chapter	154
	5.2	Motivations driving the use of WLEDs in optical wireless	155
	5.3	Recent Developments in WLED Optical Wireless	158

ATTENTION: The Singapore Copyright Act applies to the use of this document. Nanyang Technological University Library

	5.4	Optical Illumination Design Process	160
		5.4.1 Modelling of the source	160
		5.4.2 Experimental measurements and curve fitting	164
	5.5	Optimization Process	167
		5.5.1 Results from the optimized design	169
	5.6	Experimental measurements and discussion	170
	5.7	Circuit design	173
	5.8	Transmission measurements and discussion	175
	5.9	Comparison with other work	178
	5.10	Conclusion	180
6	Optical design for broadband optical wireless in an aircraft passenger cabin application		182
	6.1	Introduction to the Chapter	182
	6.2	Motivations	183
	6.3	Related work by other researchers	185
	6.4	Wavelength selection	186
		6.4.1 Eye safety considerations	186
		6.4.2 Ambient noise spectral characteristics	189
		6.4.3 White Light Emitting diodes	194
	6.5	Cabin optical network design	195
		6.5.1 Modeling a typical aircraft cabin environment.	196
		6.5.2 Optimization methodology	198
		6.5.3 Optical design for aisle mobile network coverage	200
		6.5.4 Optical design for the stationary network coverage	208
		6.5.5 Optimization for stationary and mobile users	211
		6.5.6 Other possible approaches for source configuration	219

ATTENTION: The Singapore Copyright Act applies to the use of this document. Nanyang Technological University Library

	6.6	System bit error rate performance	219
		6.6.1 Bit Error Rate performance with no multipath effects	220
		6.6.2 System performance modelling considering multipath effects	223
		6.6.3 BER performance considering multipath effects	230
		6.6.4 Discussion on the applicability of the design concepts to other aircraft cabins	
	6.7	Comparison with other work	233
	6.6	Conclusion	235
7	Conclusion and recommendations for future work		237
	7.1	Conclusion	237
	7.2	Recommendations for future work	241
	List of Author's publications		244
	Bibliography		245

ATTENTION: The Singapore Copyright Act applies to the use of this document. Nanyang Technological University Library

Summary

Optical wireless is a form of wireless technology that employs the use of optical waves instead of radio frequency waves as the physical medium for the wireless network. Although radio frequency technology is extremely popular, the achievable bandwidth is limited by regulation which comes about as a result of the interference of various systems occupying the same radio frequency bandwidth. Furthermore, radio frequency systems are inherently susceptible to interception and unauthorized violation due to the penetrative nature of the RF waves. In contrast, optical wireless provides an extremely rich potential in terms of bandwidth, from the hundreds of megahertz to gigahertz and above due to the unregulated optical domain. Furthermore, the confined nature of the optical channel to the physical constraints of the environment would ensure that there is no unnecessary leakage of the optical medium to unauthorized users. .

The scope of this thesis explores several aspects of optical wireless. A method of the design of the spot pattern for indoor optical wireless was developed, which takes into account the requirements of signal uniformity and multipath dispersion at the receiver. In the approach that was developed, the optimum field of view of the receiver was first obtained by studying various conventional spot patterns. The system performance is then specified using a merit function with mixed weights of signal uniformity and multipath dispersion. This ensures a more uniform distribution of signal intensity with no dark spots in the receiving floor. The results show that such a method employed resulted in a 93% improvement in the uniformity of the signal level over conventional grid patterns. The effect of a limited extent of the spot pattern was also explored.

A method to suppress the zero order in the diffracted intensity distribution by using a checkerboard phase plate is also presented. The phase plate results in the zero order intensity being redistributed away from the central location. When used in conjunction with a pre-shifted hologram design to account for the shift of the desired hologram pattern, a far-field reconstruction of the intended pattern can be obtained without any influence of the zero order, effectively rendering the pattern free of the zero order. Furthermore, the effect of various fabrication limits on the checkerboard was also explored and the proposed method is shown to be effective. In particular,

ATTENTION: The Singapore Copyright Act applies to the use of this document. Nanyang Technological University Library

when the same phase error was introduced into the hologram and the combined hologram-checkerboard, an improvement of a 20dB reduction in the central zero order was observed. The method was also experimentally shown. Use of the presented method would allow a higher source power which would maximize the strength of the transmitted signal as the launch power would be limited by the intensity of the diffracted pattern rather than the intensity of the zero order.

A white light emitting diode system that allows both illumination and transmission of data is also presented. Due to their electro-optic nature, white light emitting diodes can also be modulated, and this allows for their use as communication devices and illumination. An optical design process is shown in which the arrangement of light emitting diodes are optimized to obtain a uniform light distribution, When used in a typical office environment, it is shown that the lamps are capable of providing adequate illumination as well as transmission of audio signals.

In the final section, an application is presented for the use of an optical wireless system in the cabin of a commercial airliner. There has been great interest recently in the design of a wireless in flight entertainment for passengers. However due to the sensitivity of the avionics, the use of radio frequency technologies has been extremely limited. Optical wireless can be used to fulfill this particular niche, due to the non-interfering nature of the optical medium with avionics. A model of a typical passenger cabin is developed and the effect of the placement of sources within this environment is studied. Using the results of the study, the arrangement of sources is obtained, and the overall characteristics of the communications scenario are presented. Considerations such as the selection of wavelengths due to eye safety considerations and the potential impact of ambient noise will also be presented.

ATTENTION: The Singapore Copyright Act applies to the use of this document. Nanyang Technological University Library

List of Figures

Figure Number	Description	Page
2.1	Various optical wireless configurations.	27
2.2	Conceptual illustration of multispot diffusing scheme employed by Kavehrad et al [9, 67, 68] and Al-Ghamdi et al [71-74].	36
3.1	Methodologies in the design of an optical wireless system: (a) Conventional design flow and (b) Design flow based on channel requirements.	38
3.2	Impulse response model.	42
3.3	Multiple-bounce impulse response flow.	43
3.4	Illustration of room model used in simulations.	45
3.5	Spot patterns used in the simulation: (a) Lambertian, (b) 2x2, (c) 4x4, (d) 6x6, (e) 8x8 and (f) 10x10, (g) Single point (PT) and (h) Uniform illumination (UNI).	48
3.6	Impulse responses at the detector: (a) Position 'A', FOV 10°; (b) Position 'B', FOV 10°; (c) Position 'A', FOV 90° and (d) Position 'B', FOV 90°.	52
3.7	Results of the (a) average received power, (b) standard deviation of the received power, (c) average delay spread and (d) standard deviation of the delay spread when the spot patterns and field of view are varied.	56
3.8	Visualization of the diffusing spots on the ceiling grid and the pixel representation for a simplified 10x10 grid. (a) represents the grid on the ceiling together the pixel representation when no spots are present (b) represents the scenario when there are 16 spots present as represented by the red dots, and the corresponding pixel representation, represented by the white pixels. The bold box represents the physical size of the ceiling.	63
3.9	Focus of the optimization effort to obtain an optimal placement of diffuse spots on the ceiling (shown by the dashed box).	67
3.10	Flowchart showing program flow of the spot distribution pattern optimization algorithm.	68

ATTENTION: The Singapore Copyright Act applies to the use of this document. Nanyang Technological University Library

3.11	Comparison of results using iterative minimization and simulated annealing.	68
3.12	Comparison of results using simulated annealing and conventional grid designs.	69
3.13	Simulated annealing optimized spot patterns and signal power distribution.	72
3.14	Performance metrics of the obtained results for (a) received power and (b) RMS delay spread.	74
3.15	Obtained spot patterns using SA algorithm: (a) W1=0.1, 4.5m; (b) W1=0.13, 4.5m; (c) W1=0.15, 4.5m, (d) W1=1.00, 4.5m; (e) W1=0.1, 6m; (f) W1=0.13, 6m; (g) W1=0.15, 6m and (h) W1=1.00, 6m.	75
3.16	Relative values of the obtained metrics for the (a) received power and (b) RMS delay spread.	77
3.17	Spot patterns and signal power distribution maps for (a) W1 = 1.00, 4.5m extent and (b) W1 = 0.85, 6m	78
3.18	(a) Extent of pattern when offset 1.5m from centre and (b) corresponding power distribution; (c) extent of pattern when offset 3m from centre and (d) corresponding power distribution.	80
3.19	Block diagram of communications model.	84
3.20	(a) BER performance for a 6m extent hologram and (b) cumulative function for BER performance for 4.5m and 6m holograms.	90
3.21	BER performance for bit rates of 54Mbit/s and 155Mbit/s with and without using a MRC combination scheme of order 3 and 5.	93
3.22	A linear transversal equalizer using an adaptive algorithm for tap weight adjustment. The linear equalizer can be modified into a DFE by introducing the decision feedback from the decision device back into the adaptive algorithm.	95
4.1	Illustration of two beamsplitters (a) uses conventional bulk optics requiring 3 cube beamsplitters to generate four output beams; (b) uses a single holographic optical element to produce seven beams.	100
4.2	(a) Specified 8x8 intensity distribution pattern and (b) corresponding binary phase hologram that produces (a).	106

ATTENTION: The Singapore Copyright Act applies to the use of this document. Nanyang Technological University Library

4.3	Normalized intensity plots for holograms with phase levels (a) [0, 0.8π], (b) [0, 0.9π] and (c) [0, π].	108
4.4	Simulated zero order ratio against the average spot intensity for phase levels from 0.8π to π.	109
4.5	Experimental setup for re-use of zero order energy. (a) shows the first pass of the linearly polarized laser energy through the setup and (b) shows the second pass.	110
4.6	(a) Illustration showing the various elements in the simulation model and (b) Layout of the compensating phase plate.	114
4.7	Plots of the zeroth order intensity with respect to the average spot intensity.	117
4.8	Intensity profile showing the broadened zeroth order and distortions caused by the addition of the rectangular phase aperture. Inset shows the reconstructed distribution.	118
4.9	Geometric sketch of the phase checkerboard function (PCF).	120
4.10	One dimensional intensity plot of the far-field complex amplitude of the phase checkerboard function presented in Figure 4.9.	122
4.11	Implementation of the combined CGH-PCF optical element.	124
4.12	Intensity plot for the CGH with an introduced phase depth error, inset shows the corresponding 2D the intensity distribution.	126
4.13	(a) One dimensional intensity plot for the combined PCF-CGH optical element, and (b) fragmented 2D intensity distribution of the same element.	126
4.14	The far-field distribution functions when (a) a conventional hologram and (b) a shifted hologram are used together with a binary phase checkerboard.	128
4.15	(a) SCGH design and (b) 2D spatial distribution of the resulting intensity plot; (c) one dimensional intensity plot of the SCGH-PCF optical element, showing no fragmentation of the pattern.	130
4.16	(a) 2x2 spot array with zero order using CGH and (b) application of PCF-SCGH technique shifts away zero order with no effect on spot distribution.	131
4.17	Performance of the CGH and SCGH-PCF optical element in the presence of phase level and alignment errors.	134

ATTENTION: The Singapore Copyright Act applies to the use of this document. Nanyang Technological University Library

4.18	The intensity plots when the SCGH has binary phase levels of [0, 0.9π] and the PCF has binary phase levels of (a) [0,0.9π] and (b) [0, 0.8π].	134
4.19	Effect of fill-factor imbalance on the zero order for a CGH and SCGH-PCF.	136
4.20	Structure of a reflective liquid crystal SLM.	137
4.21	Gray level to phase shift specification from the data sheet of the SLM.	138
4.22	Experimental setup to reconstruct the diffracted pattern using a phase-only reflective SLM.	138
4.23	Normalized zero order and diffracted intensities as the gray level of a phase-only SLM is varied.	142
4.24	Far-field reconstruction pattern when the binary gray levels are (a) [0, 55] = [0, π]; and (b) [0, 35] = [0, 0.4 π].	144
4.25	Intensity pattern for (a) Set 0, (b) Set 1 and (c) Set 3 corresponding to [0, π], [0, 0.6π], and [0, 0.4π] binary phase levels in the SCGH respectively.	148
4.26	Diffracted intensity for the SCGH-PCF and the SCGH as the phase level is varied.	149
4.27	Zero order intensity levels for the SCGH-PCF and the CGH. The minimum zero order has also been included as a reference.	150
4.28	Measured shifted zero order intensity as the phase level of the SCGH is varied.	151
5.1	Measured optical spectrum of a typical white light emitting diode.	157
5.2	Definition of terms for the irradiance at an arbitrary location on the receiving plane.	161
5.3	Definition of terms used in the two-dimensional modelling of the irradiance due to an arbitrarily tilted source.	163
5.4	Measurement setup for the characterization of the LED irradiance profile.	164
5.5	Plot of the fitted irradiance profile of the WLED.	166
5.6	Plot of the irradiance obtained from the optimization process.	170

ATTENTION: The Singapore Copyright Act applies to the use of this document. Nanyang Technological University Library

5.7	Measured irradiance profile of the demonstrator system.	171
5.8	Comparison of the irradiance profiles for the optimized system and a system with the WLEDs pointing vertically towards the receiving surface.	172
5.9	Photograph of the lamp consisting of 120 WLEDs.	173
5.10	Setup of WLED communications system.	174
5.11	Setup of demonstration room.	176
5.12	Signal waveform after being transmitted from the WLED lamps and picked up on the photodetector. Input signal is a 1kHz, 20mV sine wave.	176
6.1	Maximum Permissible Exposure (MPE) limits for the wavelength range from 700nm to 1600nm.	187
6.2	Class 1 Allowable Emission Limits (AEL) for 850nm and 1550nm.	189
6.3	Normalized spectral characteristics of (a) sunlight, (b) incandescent light, (c) fluorescent light and (d) white light emitting diode.	191
6.4	Layout of the aircraft cabin geometry based on a Boeing 777 commercial airliner. (a) Top view, (b) front view, (c) side view and (d) perspective view.	197
6.5	Rendered images obtained from the geometry shown in Figure 6.4.	197
6.6	Optimization process flowchart.	199
6.7	Position of the single source: (a) front view and (b) top view.	201
6.8	Ray trace plot for a single source.	201
6.9	Intensity distribution along column M due to a single source.	202
6.10	Ray trace plots for multiple sources.	204
6.11	Intensity distribution due to nine sources.	204
6.12	Optimized intensity distribution due to eleven sources.	205
6.13	Intensity distribution from MATLAB optimization and ASAP ray tracing.	206

ATTENTION: The Singapore Copyright Act applies to the use of this document. Nanyang Technological University Library

6.14	Uncoded transmission capacity along the aisle.	207
6.15	Intensity distribution for seat IDs from 5A to 5E using only the aisle.	208
6.16	Location of the side and dorsal sources.	209
6.17	Received intensity as the tilt angle of the side sources is varied. Also shown is the contribution from the dorsal sources.	210
6.18	Intensity distribution using the optimized parameters in Table 6.3.	214
6.19	Intensity distributions using the optimized parameters obtained from MATLAB and simulated via ray tracing. (a) shows the intensity distribution for the seats 5A to 5E and (b) shows the intensity distribution along the aisle M.	216
6.20	Transmission capacities estimated using multipath dispersion for (a) rows 5A to 5E and (b) along the aisle M.	217
6.21	(a) Received power and (b) estimated transmission capacity across the cabin locations in the ray tracing simulations.	218
6.22	BER for direct sunlight, indirect sunlight and fluorescent lighting conditions.	223
6.23	Illustration showing pre-cursor and post-cursor ISI.	225
6.24	Bit error rate performance in the presence of multipath and ambient noise.	230

ATTENTION: The Singapore Copyright Act applies to the use of this document. Nanyang Technological University Library

List of Tables

Table number	Description	Page
2.1	The rising number of internet users	15
2.2	Approximate bandwidth requirements for various applications	16
2.3	Bandwidth requirements for video transmission	17
2.4	RF exposure limits	30
2.5	Comparison between OW and RF properties	30
3.1	Simulation parameters	45
3.2	Metrics from impulse response simulations	52
3.3	Performance of various patterns at 30° field of view	58
3.4	Comparison of obtained results with other works	82
3.5	Receiver model parameters	89
4.1	Measured and normalized zero order intensities as the gray level in a CGH is varied	141
4.2	Gray level to phase modulation mapping for the SLM	143
4.3	Values used in the SCGH-PCF for input into the SLM	145
5.1	Measurement results for the irradiance of a single WLED	165
5.2	Angles obtained from the optical design optimization	169
5.3	Comparison of the ratio of the minimum and maximum intensity from the obtained results and in comparison with the results from related work	179
6.1	Relevant equations used to calculate the MPE for $T > T_2$	187
6.2	Background illumination measurements	193
6.3	Optimized source separation with respect to the origin at Row 5	205

ATTENTION: The Singapore Copyright Act applies to the use of this document. Nanyang Technological University Library

6.4 Optimized parameters θ, α, β and γ 213

6.5 Receiver model parameters 221

6.6 Transmission bitrate for selected bit error rates 231

ATTENTION: The Singapore Copyright Act applies to the use of this document. Nanyang Technological University Library

1

Introduction

1.1 Motivations

In recent years there has been tremendous growth in the adoption of wireless devices over conventional wired devices for local area networks. The shift towards wireless technologies has been primarily motivated by the mobility of the users, the flexibility of network configuration, as well as the relatively lower cost and ease of setting up new wireless networks over traditional wired networks.

ATTENTION: The Singapore Copyright Act applies to the use of this document. Nanyang Technological University Library

However, with the widespread proliferation of radio frequency wireless networks there has been an increased concern towards interference between these networks, due to the electromagnetic properties of radio frequency waves. This has resulted in regulation of the radio frequency spectrum by government bodies where bandwidth is leased out to operators. For example, in the United States, the Federal Communications Commission controls the use of spectrum. Most commercial wireless local area networks based on radio frequency technologies operate in the license-free 2.4GHz Industrial, Scientific and Medical spectrum, which is limited to 83MHz of the radio frequency spectrum bandwidth[1]. This places an effective constraint on the employable bandwidth which limits the data capacity of devices in this region. Furthermore co-existing networks within the same bandwidth need to employ frequency management techniques to reduce interference effects, limiting frequency re-use.

In addition, the property of radio frequency waves penetrating through and propagating beyond the physical confines of the operating environment have also led to concerns over security, besides requiring proper management of frequency between neighbouring networks. The nature of radio frequency waves allows them to be intercepted by anyone equipped with a suitable antenna, and due to the penetrative nature of radio waves, information sent over wireless within a private wireless network can be detected by unauthorized users located outside the premises of the operating environment, such as an office space. Although information is usually protected by some form of security encoding, such measures can be overcome, resulting in the potential leakage of sensitive confidential information such as financial data. A better option would be to prevent the access of the information carrier altogether.

ATTENTION: The Singapore Copyright Act applies to the use of this document. Nanyang Technological University Library

Optical wireless [2-5] is a technology that can potentially be used as the transmission medium for wireless networks. Unlike radio frequency networks, indoor optical wireless networks make use of optical carriers to transmit information, and are unable to penetrate beyond the physical boundaries of the operating environment. This ensures a high level of security for the wireless network, as only users who are physically within the operating environment can have access to the network, unlike in radio frequency networks. The confinement of the network to its physical boundaries also aids in network management and encourages frequency re-use. As optical wireless networks located in adjacent units in a building would not interfere with each other, the same frequency or wavelength can be used for both networks.

In addition, the bandwidth of optical wireless is not regulated by any governing body, and this implies a potentially unlimited bandwidth that is only constrained by device limitations. In the current age where the demands for bandwidth are ever-increasing due to newer applications such as telepresencing and high definition video, the promise of a virtually unlimited bandwidth offered by optical wireless is particularly attractive. Combined with the advantage of the optical wireless network being limited to the physical boundaries of the network, this led to great interest to research in optical wireless network technology.

A challenge in the use of optical wireless networks is the inherent line-of-sight nature of the optical carrier. To overcome this, an approach that has been employed has been to make use of a diffuse transmitter [6-8], such that the optical carrier is diffusely transmitted over a large area. By making use of the reflections of the carriers off surfaces in the environment, the line-of-sight requirement between the transmitter and the receiver in an optical wireless network can be surmounted.

ATTENTION: The Singapore Copyright Act applies to the use of this document. Nanyang Technological University Library

The use of computer generated holograms as spot diffusers is particularly attractive [9, 10], as it allows the creation of multiple diffused spots. In contrast with a conventional diffuser such a ground glass diffuser, a multiple spot diffuser requires less power. The pattern of the diffused spots has been mainly based on an arbitrarily chosen pattern, usually a regular grid or layout. The field of view of the receiver is in general then chosen to accommodate the diffused spot pattern, and the system performance follows these two design decisions. However, to the best of our knowledge, there has been little emphasis on designing the pattern of the diffused spots and the receiver field of view to obtain the desired system performance parameters. By optimizing the receiver field of view, and then optimizing the diffused spot pattern, the system can be designed in such as way as to achieve certain performance requirements.

Computer generated holograms have been widely used as spot diffusers due to the flexibility in their design where the distribution of spot pattern is limited by the computational complexity of the design process. In comparison with bulk optics such as prisms used conventionally to split beams, computer generated holograms are more robust, lightweight and of a sufficiently small form factor for integration into portable devices. However, the performance of computer generated holograms, particularly the zero order, is sensitive to the phase of the surface relief profile[11]. Due to the complexity of the computer generated hologram, which can be of an almost pseudorandom nature, accurate fabrication of these holograms is challenging, leading to errors in the surface relief profile which brings about a strong zero order. When these holograms are used in optical wireless, the strong zero order presents an eye safety hazard as well as causing a distortion in the desired intensity distribution of the optimized spot pattern. Although the zero order can be reduced through improved

ATTENTION: The Singapore Copyright Act applies to the use of this document. Nanyang Technological University Library

fabrications methods, the complexity of fabrication may not be practical. A potential solution would be to introduce techniques which are able to reduce the zero order despite these fabrication limitations. This alleviates the dependence on the zero order from the quality of fabrication and can be applicable to in the presence of fabrication errors of varying type and magnitude.

In recent years, there has been an increased interest in the use of white light emitting diodes, also known as solid state lighting, for illumination purposes [12-15]. The shift away from conventional incandescent and fluorescent sources has been primarily motivated by the increased quantum efficiency of white light emitting diodes, as well as their increased robustness over conventional sources. With the optoelectronic nature of such devices, which are similar to diodes used in fiber optic communications, white light emitting diodes also have the potential as communications transmitter. In this way, they can be used to fulfill the dual objectives of both illumination as solid state lighting, and transmission of data. Furthermore, in an environment that is illuminated with such a system, there is minimal ambient noise as the intensity of the artificial lighting from the solid state lighting is, itself, the strength of the transmitted data signals.

The wide bandwidth and the non-interfering nature of the optical carrier make optical wireless appealing in environments where radio frequency interference is of major concern. One such area is in passenger aircraft, where the potential for interference with crucial avionics has limited the employment of wireless networks in such vessels, which can reduce significantly the length of cabling required. Wireless networks in such applications are mainly used to transmit in-flight entertainment applications to the users. By exploiting the large bandwidth of optical wireless and

ATTENTION: The Singapore Copyright Act applies to the use of this document. Nanyang Technological University Library

making use of the non-interference with avionics, optical wireless can be used in passenger aircraft to facilitate an onboard wireless network.

In summary, the performance of the optical wireless system is highly dependent on the configuration of the diffusing sources. Obtaining an optimum configuration is important to control the multipath dispersion, which limits the data rate, as well as to obtain a uniform coverage so as to avoid dark spots with no signal, and to ease the dynamic range requirements of the photoreceiver. However, the presence of a strong zero order can affect the distribution at the receiving plane, causing a bias towards the central region thus motivating the efforts towards reduction of the zero order. When considering the sources to be used in optical wireless, recent developments in white light emitting diodes make their utilization potentially viable for illumination as well as communications by exploiting their optoelectronic nature, encouraging the design and prototype development of such a system. Finally, the high data rate and non-interference of the optical wireless system makes the technology particularly desirable in interference-sensitive environments, and motivates its application in a passenger aircraft application where it is essential that critical avionics must avoid influence by other radio frequency devices.

1.2 Objectives

With the virtually unlimited bandwidth and increased network security through confinement of the network to the operating environment, optical wireless has potential for use as an alternative to radio frequency networks. The objectives of this thesis are to further explore the design and application of optical wireless, and can be broadly classified as the following:

ATTENTION: The Singapore Copyright Act applies to the use of this document. Nanyang Technological University Library

1) Study and optimization of receiver and transmitter design for a spot diffusing optical wireless configuration

   a. To study the optimum field of view for a receiver in a conventional spot diffusing environment

   b. To define a methodology of design for the diffused spot pattern distribution, based on communications requirements

   c. To make use of a global optimization technique to obtain the optimal distribution of the diffused spots

   d. To analyze the communications performance and the effect of diversity sub-systems on the system performance

2) Reduction of zero order in computer generated holograms in particular for use in indoor diffused optical wireless

   a) To reduce the zero order by recycling the zero order energy back into the hologram

   b) To reduce the zero order by making use of an additional phase-only optical element

      (i) for phase compensation

      (ii) for redistribution into the higher orders

   c) To simulate and demonstrate the effectiveness of the proposed optical element in the presence of zero order errors through fabrication errors

ATTENTION: The Singapore Copyright Act applies to the use of this document. Nanyang Technological University Library

3) Design and implementation of a visible light optical wireless transmission system employing white light emitting diodes

   a) To model on the irradiance profile for a light emitting diode based on measurements

   b) To optimize the intensity distribution of a lamp consisting of white light emitting diodes such that the detected irradiance is uniform

   c) To implement a system for the delivery and detection of audio signals transmitted via the illumination provided by the white light emitting diodes in a typical operating environment

4) Design and study of an optical wireless system for use in an onboard passenger aircraft environment

   a) To select an appropriate wavelength based on eye safety and ambient noise considerations

   b) To model and perform ray tracing simulations of a realistic cabin environment

   c) To optimize and design the placement and position of the diffused light sources within the aircraft passenger cabin

   d) To study the comparative effects of multipath and ambient noise on the system performance

1.3 Major contributions of the thesis

- For the design and optimization of the system parameters for indoor diffused optical wireless networks, the distribution of signal intensity in the room environment and the multipath delay spread were identified as performance

ATTENTION: The Singapore Copyright Act applies to the use of this document. Nanyang Technological University Library

metrics for the network. Using these parameters, it was found that a receiver field of view of 30° resulted in the best performance when various conventional grid patterns were used as the spot distribution pattern.

- Utilizing this field of view for the receiver, a simulated annealing technique was used to obtain the spot distribution optimized for the chosen performance metrics. By varying the relative weights of the performance metrics, an optimized distribution could be obtained to meet various performance requirements. It was shown that the optimized spot distribution had a better distribution of intensity over conventional grid patterns for the situations where the pattern is centred on the ceiling as well as offset from the centre. Furthermore by making use of equalization and diversity techniques, the performance of the optical wireless system could be further improved for transmission at 155 Mbit/s.

- The zero order presents a considerable limitation in the use of holograms, particularly in optical wireless where the strong zero order distorts the distribution of the diffused signal intensity, and presents an eye safety hazard. By making use of the polarized nature of a coherent light source and an experimental setup, it was shown that the zero order could be re-cycled back into the hologram, although some of the energy was still wasted.

- A phase-only binary optical element in a periodic arrangement, known as a phase checkerboard, was shown to be effective in redistributing the zero order intensity away from the central zero order location, resulting in no zero order

ATTENTION: The Singapore Copyright Act applies to the use of this document. Nanyang Technological University Library

at that central location. By performing an adjustment in the design of the initial spot pattern to take into account the shift produced by the phase checkerboard, it was shown that the desired spot distribution could be obtained with no distortion in the intensity distribution and no visible zero order; the zero order being shifted and redistributed to the tiling points of the phase checkerboard element. Various fabrication errors were simulated, ranging from phase depth errors up to 20% in the hologram and fill factor imbalances up to 60%-40%, and it was shown that the technique was still effective. Experimental results using a spatial light modulator also showed the applicability of the technique.

- A visible light optical wireless transmission system making use of white light emitting diodes was designed and implemented. To overcome the directionality of the white light emitting diodes, optimization was required to determine the angular positioning required to obtain a uniform distribution. In conjunction with values obtained from measurements, the irradiance profile of a white light emitting diode was modeled, and used in the optimization design of a white light emitting diode lamp consisting of 125 diodes to obtain a uniform intensity distribution within a defined region. Optimal values for the angular arrangement of the diodes were obtained and four such lamps were assembled. These were used to illuminate a typical office environment and it was found that there was increased uniformity in the signal intensity as compared to conventional fluorescent lamps. Using a driving circuit to modulate the lamps, it was shown that the developed system was capable of transmission of audio signals.

ATTENTION: The Singapore Copyright Act applies to the use of this document. Nanyang Technological University Library

- The properties of optical wireless networks make the application of such networks in the cabin of a passenger aircraft appealing. A study was made on the dependence of eye safety and ambient noise on the optical wavelength and it was found that 1550nm offers significant advantages. Specifically, the higher permissible emission power and the reduced influence of background lighting conditions compared to other wavelengths is advantageous to the use of optical wireless. A realistic cabin model was simulated using a computer aided design program, and the distribution of sources placed within the environment was modeled via ray-tracing. Making use of the ray-tracing data, various optimization routines were run to obtain an optimal arrangement and positioning of sources to allow for a uniform distribution of received intensity. The resulting ray trace data was then used in communications model analysis to determine the transmission capacity of the system. A modification was made in the calculation of multipath to reduce the number of convolutions required. It was found that the effect of multipath is more significant that ambient noise, particularly at higher bit rates. However, even in the presence of multipath with no equalization, high transmission rates are still possible. For a system where influenced by fluorescent ambient light with no equalization in the presence of multipath, a transmission capacity of 233 Mbit/s is achievable. When equalization is used, the transmission capacity increased to 440 Mbit/s, and this large capacity can potentially be used for the transmission of in-flight entertainment to passengers in the aircraft cabin.

ATTENTION: The Singapore Copyright Act applies to the use of this document. Nanyang Technological University Library

1.4 Organization of the thesis

The contents of this thesis are organized into seven chapters, and the materials are in each Chapter are outlined in the following:

- Chapter 1 contains the motivations behind the work undertaken in this thesis, the objectives, the major contributions resulting from the work done, and the organization of the thesis.

- Chapter 2 consists of a general introduction to the optical wireless, including a look at the global growth of wireless systems, a comparison between radio frequency and optical wireless systems, and development of indoor optical wireless communications.

- Chapter 3 presents the work done in optimizing the system considerations for an indoor spot-diffused optical wireless network, and includes the work done on optimization of the receiver field of view and the spot diffused distribution.

- Chapter 4 comprises of the approaches undertaken to reduce the zero order in computer generated holograms due to fabrication, and consists of the experimental setup to recycle the zero order intensity and the use of additional phase-only optical element to reduce the zero order. The chapter also includes a simulation of the various types of fabrication errors on the zero order, and experimental work done to show the effectiveness of the proposed method.

ATTENTION: The Singapore Copyright Act applies to the use of this document. Nanyang Technological University Library

- Chapter 5 presents the optical design, modeling and development of a visible light optical wireless system capable of illumination and data transmission, including the modeling of sources, the optimization of the spot pattern and a prototype system for the transmission of audio.

- Chapter 6 comprises of the work done in designing an optical wireless system for the aircraft cabin, including the selection of an appropriate wavelength, the modeling and ray tracing simulations in the environment, the optimization process, and a comparative study of the effect of multipath and background ambient light on the system performance.

- Chapter 7 presents the conclusions to the results in the thesis, and recommendations on future work.

ATTENTION: The Singapore Copyright Act applies to the use of this document. Nanyang Technological University Library

2

Introduction to Optical Wireless Communications

2.1 Introduction to the Chapter

Optical wireless has increasingly become popular as an alternative or as a complement to radio frequency wireless due to the potentially unlimited bandwidth and physical network security that optical wireless offers. In this Chapter an introduction is made to the development of optical wireless communications. Firstly, to place the motivations behind this development in context, the increasing demand for broadband wireless bandwidth is briefly discussed, followed by a comparison between radio frequency wireless and optical wireless. Thereafter, the development of optical wireless will be discussed in further detail. Based on the developments to date,

ATTENTION: The Singapore Copyright Act applies to the use of this document. Nanyang Technological University Library

some research areas have been identified and this will be briefly discussed. Further motivations for the work done in this Thesis will be elaborated upon in the specific related Chapters.

2.2 Increase in demand for bandwidth

In recent years, there has been an explosive growth in the demand for bandwidth, primarily driven by the increase in the penetration of broadband internet usage and the corresponding increase in new bandwidth intensive applications. According to a report by the Global Market Information Database [16], the number of internet users in China alone was 236 million, more than that of the United States (183 million) and Germany (43 million) combined. Furthermore, these numbers are expected to grow even further with China's internet users expected to experience a 166% increase from 2004 to 2009, and India slated to become a major increase in the number of internet users Selected highlights of this report are presented in Table 2.1.

Table 2.1 The rising number of internet users [16]

Country	Number of internet users (millions)	% increase from 2004-2009
China	237	166.4
United States	183	7.9
India	93	575.5
Japan	71	8.9
Germany	43	6.5

ATTENTION: The Singapore Copyright Act applies to the use of this document. Nanyang Technological University Library

At the same time, there has been a simultaneous increase in the demand for bandwidth by consumers due to new technologies and services which are becoming increasingly bandwidth-intensive, such as video, gaming, and business multimedia. In global telecommunications company Tellab's press release of their 2006 annual report [17], the increasing demand for bandwidth was illustrated in the comparison of download times. One minute of video takes four times the bandwidth of music and high definition television (HDTV) needs five times more bandwidth than current TV requirements. This agrees well with the large expected increase in internet video, estimated at 20 per cent every five months[18], which is expected to be the main driver for internet bandwidth. Table 2.2 [19] shows the bandwidth requirements that are needed for various transmission requirements:

Table 2.2 Approximate bandwidth requirements for various applications

Transmission	Analog equivalent	Digital equivalent (uncompressed)	Digital equivalent (compressed)
Standard US analog television (NTSC)	6 MHz	270 Mbit/s	2-10 Mbit/s
HDTV (US format)	~ 100 MHz	1.5 Gbit/s	19.3 Mbit/s
Voice telephone	3 kHz	64 kbit/s	~ 10 kbit/s
One standard TV video frame	-	9 Mbits	-
One HDTV video frame (1/60s)	-	25 Mbits	-
1000 spoken words (5 min on phone)	-	20 Mbits	-
1000-word text file	-	60 kbits	-

ATTENTION: The Singapore Copyright Act applies to the use of this document. Nanyang Technological University Library

Furthermore, new business multi-media applications are also quickly gaining popularity, such as telepresencing. Telepresence can be thought of as an evolution to conventional video conferencing, and involves providing a user with multi-sensory inputs such that they are able to re-create a 'live' meeting experience [20]. High-definition video and audio are key components of telepresence systems, further driving the demands on bandwidth. Table 2.3 [21] shows the bandwidth requirements for various resolutions and the exponential increase in bandwidth required in a 4-user video conference at that same resolution, allowing simultaneous transmission.

Table 2.3 Bandwidth Requirements for Video Transmission

Compression	**Resolution**	**Bandwidth for 1 channel, half duplex**	**Bandwidth for Video Conference, 4 users**
MPEG-1	352 x 288	1.15 Mbit/s	13.8 Mbit/s
MPEG-2	720 x 576	4 Mbit/s	48 Mbit/s
MPEG-3 (HDTV)	1920 x 1080	20 Mbit/s	240 Mbit/s
MPEG-4	176 x 144	0.064 Mbit/s	0.768 Mbit/s

ATTENTION: The Singapore Copyright Act applies to the use of this document. Nanyang Technological University Library

2.3 Towards wireless communications

The dual increase in the number of users and the increased bandwidth needs of applications is fueling the demand for even greater capacity delivery to the network cells in the home and office. According to a report in 2006 [22], broadband accounts for 64% of internet connections in the home in the United Kingdom, growing by 56% between December 2004 and December 2005, and there has been increased interest in even faster broadband connections. In Singapore the household broadband penetration reached at similar percentage in early 2007 [23].

From the household and office cells to the individual users the conventional practice has been via wired links. However, with the increasing mindset of users towards mobility, there has been shift towards wireless links rather than wired links. Wireless links have become popular due to their ease-of-use and installation, particularly with the proliferation of mobile computing devices such as laptops, personal digital assistants (PDAs) and mobile gaming consoles with in-built wireless devices.

The drive to have mobile broadband access has led to a huge boom in the Wireless Local Area Network (WLAN) market. According to a press release from industry research firm IDC in June 2003[24], the global WLAN market was expected to increase at a compound growth rate of 13% from 2002 to 2007, with an expected US$1.1 billion in revenues by 2007. In the Asia Pacific region, an IDC press release in March 2004 [25] reported that the WLAN equipment market in the region, excluding Japan, grew 67% year-on-year in 2003, surpassing US$250 million. Some recent figures from IDC [26] indicate that the worldwide market for enterprise WLAN equipment grew by 40% in 2006 to nearly $1.6 billion, with the market expected to

ATTENTION: The Singapore Copyright Act applies to the use of this document. Nanyang Technological University Library

grow a further 30% in 2007. In the Asia Pacific region excluding Japan, in 2006, the WLAN equipment market was worth almost US$500 million, 35% higher than 2005.

2.4 Radio Frequency Wireless Networks

Currently most if not all wireless networks employ the use of radio frequencies as the medium for the transmission of data to users, motivated by the ease of connection via wireless and the high costs of infrastructure wiring for wired links. Wireless networks can be categorized into four classes, namely satellite networks, wireless wide area networks (WWAN), wireless local area networks (WLAN) and wireless personal area networks (WPAN). WWANs and satellite networks, though important categories in the scheme of things, cover extremely large distances nationally and internationally, which is beyond the scope of this thesis and thus will not be mentioned further. In this section a brief introduction to common WLAN and WPAN standards will be presented.

2.4.1 IEEE 802.11

The IEEE 802.11 family of standards [1, 27] are widely adopted standards for WLAN devices today. In particular, IEEE 802.11b is the most popular standard with the widest market penetration, and was approved for use in 1999. 802.11b makes use of the license-free Industrial, Scientific and Medical (ISM) 2.4GHz spectrum, with a maximum capacity of 11 Mbit/s, using a direct spread spectrum sequencing (DSSS) technique. Another newer standard which is finding rapid adoption is the IEEE 802.11g standard which also operates in the 2.4GHz ISM region but by using orthogonal frequency

ATTENTION: The Singapore Copyright Act applies to the use of this document. Nanyang Technological University Library

division multiplexing (OFDM) is able to achieve a capacity of 54 Mbps. The range of operation is up to 100m, however, this results in a reduction in the actual transmission rate possible in the system

IEEE 802.11a is an alternative standard which was also approved in 1999. Unlike IEEE 802.11b/g, 802.11a operates in the 5 GHz U-NII (Unlicensed National Information Infrastructure) spectrum, and is capable of transmitting at 54 Mbps due to the use of OFDM which is similar to IEEE 802.11g. However, it is not compatible with IEEE 802.11b due to the difference in frequency band. Due to the wide early adoption of IEEE 802.11b and the backward compatibility offered by IEEE 802.11g, the adoption of IEEE 802.11a has been much slower.

802.11n [28] is a next generation WLAN standard that presents an evolution of technologies from the currently deployed 802.11a, 802.11b and 802.11g. The major advancement is the employment of multiple in multiple out (MIMO) methods to enable transmit diversity in the communications system, allowing a throughput of four times more than that of previous 802.11 standards. The standard is currently still in the draft phase and is yet to be finalized.

2.4.2 Bluetooth

Bluetooth [29] is defined as a WPAN specification for short range communication between devices, and operates in the unlicensed 2.4 GHz ISM region. Bluetooth-enabled devices are capable of transmission at about 1

ATTENTION: The Singapore Copyright Act applies to the use of this document. Nanyang Technological University Library

Mbps, at a distance of a few metres, and is meant primarily as a cable-replacement standard for communication between devices. The specification has also gained wide acceptance and adoption in most portable devices today.

2.4.3 Ultra Wide Band (UWB)

UWB, also commonly known as impulse radio [30, 31] is a technology that operates on an extremely wide-bandwidth by transmitting very narrow and low power pulses, principally for short range communication over a few meters. This potentially allows a large capacity in the hundreds of megabits. In the past, development of UWB was hindered by fears of interference with other currently existing wireless systems due to the wideband nature of UWB. However, this has been somewhat alleviated by the US Federal Communications Commission (FCC) Report and Order of 2002 [32, 33] which approved the use of UWB subject to certain emission controls.

2.5 Limitations of radio frequency networks

Although RF WLANs are extremely popular, there are some limitations to the use of the networks, specifically interference between devices occupying the same frequency spectrum, which has led to regulation and licensing of the RF spectrum, and the potential security concerns due to the propagation of RF carriers.

ATTENTION: The Singapore Copyright Act applies to the use of this document. Nanyang Technological University Library

2.5.1 Interference and regulation

One of the major concerns in the use of any form of wireless network is the amount of bandwidth that is available to that particular network and is largely determined by spectrum allocation by government bodies. Spectrum allocation is necessary so as to avoid or minimize interference between RF signals, which can hamper the detection of these signals. Spectrum assignment can be made on a licensed or unlicensed basis [34].

In licensed spectrum assignment the operator or manufacturer is exclusively assigned a particular segment of the spectrum by buying or leasing that segment. This is commonly found in cellular telephony where the service providers have exclusive use of that spectrum. However, this can be extremely expensive as well as inconvenient. For example, one of the earliest commercial WLAN products was Motorola's Altair [35] in the 1980s, which licensed the use of the 18-19 GHz spectrum. The company actually set up offices to facilitate user negotiation with the FCC in different areas. On changing the location of the WLAN, the user had to contact the company, which then had to liase with the FCC over operation. As can be expected, this was extremely inconvenient.

Another form of spectrum allocation which has become exceedingly popular and arose as an answer to licensed spectrum is the release of certain sections of the spectrum as unlicensed spectrum, with the most widely known being the 2.4 GHz ISM spectrum which is widely used by some of the specifications mentioned earlier. Unlicensed spectrum allows different

ATTENTION: The Singapore Copyright Act applies to the use of this document. Nanyang Technological University Library

services and operators to make use of the spectral band without licensing. However, as a result of the 'free' nature of the spectrum, wireless receivers would have to contend with potentially numerous sources of interference. For example, a WLAN receiver could face interference from cordless phones, microwave ovens and Bluetooth devices all operating in the same region, which can degrade the performance of the channel.

The net effect of interference and regulation is that it limits the bandwidth that each system can make use of, thus forcing 'artificial' limits on the physical capacity of the system. At this juncture it would be appropriate to briefly discuss the implications of UWB, which seems to purposely flout the rules by employing an extremely large bandwidth that overlaps with other existing systems. The FCC ruling imposed a strict spectral 'mask' that limits the emission power for UWB devices across the allowable bandwidth. This effectively limits the range of operation. Also, the net effect of multiple UWB devices operating in the same proximity could potentially still cause some interference. Finally, in mission control sensitive environments where instrumentation sensitivity is extreme crucial such as aircraft communications, control and instrumentation, use of UWB is still under close scrutiny[36].

2.5.2 Security Risks

Another recent concern that is drawing much attention due to the growing popularity of wireless networks is the potential security vulnerability of a wireless network. Unlike wired connections, a wireless network transmits data all over the broadcast medium, including through the physical boundaries of the operating environment, such as the office walls. A recent report by

ATTENTION: The Singapore Copyright Act applies to the use of this document. Nanyang Technological University Library

Information Security Magazine [37] found that 'dozens of unsecured wireless LANs' while driving between Leesburg and Dulles International Airport in the US, with a similar report by the BBC [38] discovering 'a dozen' wireless networks along a one kilometer stretch in London. Wireless network security risks can be classified into three major categories [30]:

1. Accidental attack

   This occurs when a user accidentally logs onto a wireless network unknowingly, and is usually non-malicious in nature although it does represent a compromise in network security.

2. Passive attack

   Also known as 'sniffing', this is an extremely common form of attack where the intruder attempts to steal information being transmitted, and can be easily implemented using open-source tools[39]. Due to the nature of this form of attack it can be extremely difficult to detect.

3. Active attack

   These are malicious attacks which are aimed at modifying the data being transmitted over the network and are often conducted after information has been obtained through 'sniffing'. Masquerade attacks, also known as 'spoofing' as defined by the US Senate on Cyberspace

ATTENTION: The Singapore Copyright Act applies to the use of this document. Nanyang Technological University Library

Security [40] involve the attacker making use of 'sniffed' information to access the network as an authorized user, and then performing illegal acts such as obtaining or tampering with classified information. Active attacks can also consist of denial of service attacks [41] where an attacker overloads a network with requests rendering the network unable to function in a proper manner.

Although much of the vulnerability of wireless networks comes from the victims ignorance and reluctance to enable the in-built security features, for example WEP in IEEE 802.11, research [42-44] has shown that these features are not waterproof and may still be compromised by determined individuals with the right tools.

2.6 Optical Wireless Communications

Optical wireless is an alternative to radio as a means of providing the channel for the wireless link. In optical wireless, data is transmitted by modulating a light source such as a laser or a light emitting diode, which then transmits the information in freespace. The modulated light waves carrying the information are detected and demodulated through the use of a photodetection circuit. Optical wireless communications (OWC) can be categorized into whether they are based on line of sight (LOS), and whether or not they are in a directed configuration[45]. LOS means that there is an unobstructed LOS that exists between the transmitter and the receiver, while in non-LOS communications this unobstructed path does not exist. In non-LOS channel configurations, the system makes use of reflecting surfaces, primarily the walls and the ceilings, to allow the signal to reach the receiver. This creates a

ATTENTION: The Singapore Copyright Act applies to the use of this document. Nanyang Technological University Library

measure of redundancy so that even if the LOS between the main reflecting surfaces, such as a spot on the ceiling, is obstructed, the receiver is still able to detect the signals via the secondary reflecting surfaces such as the office walls. The term "directed" is usually used to refer to transmitter and receivers with a narrow field of view. The various configurations are shown below in Figure 2.1.

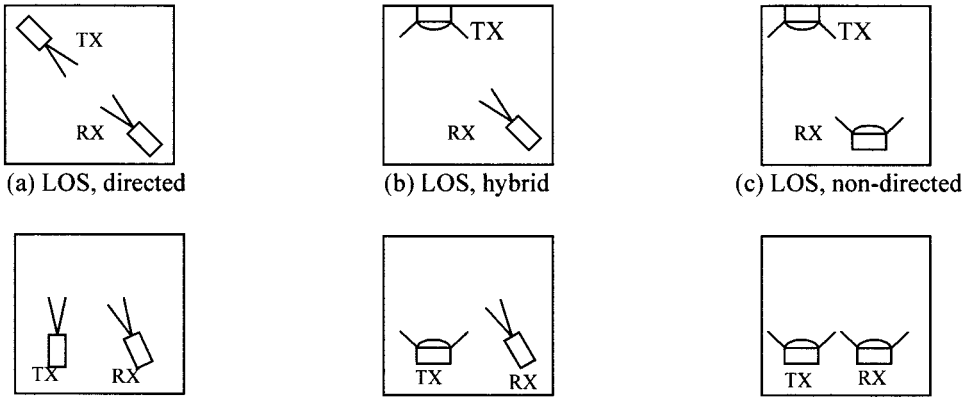


Figure 2.1 Various optical wireless configurations (TX = transmitter, RX= receiver).

The most common configuration is Figure 2.1(a), which is the use of directed receivers and transmitters. LOS-based OWC involves directing and adjusting the transmitter and the receiver such that they are pointed at each other. Such directed links are already in use today and run the gamut from extremely short ranges in chip-scale optical interconnects [46-48] to 'last mile' links connecting the high bandwidth backbone fiber architecture to metropolitan urban networks [49, 50]. Jeong et al [51] recently demonstrated a 8 x 10-Gb/s WDM signal transmission over a distance of 3.4km using a single optical receiver. A common type of directed link is the infrared link found in portable devices making use of the Infrared Data Association (IrDA) standard [52]. One of the latest standards proposed by the IrDA is the Very Fast Ir

ATTENTION: The Singapore Copyright Act applies to the use of this document. Nanyang Technological University Library

(VFIr) standard [53] , which is capable of providing up to 16Mb/s and 10 Mb/s or higher throughput, which allows Ethernet access (10 Mb/s) and MPEG2 motion picture transfer (11.08 Mb/s). While the use of directed, LOS configurations usually means that less power needs to be transmitted, the narrow field of view nature of the configuration means that shadowing of the receiver would result in a link loss between the transmitter and the receiver, as there is only a single transmission path. Furthermore, a high degree of stability must exist between the transmitter and the receiver to ensure that the link is maintained. The vulnerability of the configuration to shadowing and the tight stability requirements would imply that the configuration is less suitable for mobile wireless networking in an indoor environment.

To counter the effect of shadowing, the common approach is to make use of diffuse reflecting surfaces such as the walls or ceilings to act as reflectors so that redundancy is added to the channel configuration. The two most common diffuse configurations are shown in Figure 2.1(c) and Figure 2.1(e). Essentially, both systems make use of wide field of view for both receiver and transmitter, the main difference being the nature of the reflecting surfaces and the LOS. In Figure2.1(c), a direct LOS exists between the transmitter and the receiver, and the diffusing surfaces (walls) act as secondary sources to maintain the link if the LOS is blocked. In Figure 2.1(e), the diffusing surfaces (ceiling and walls) are the means by which the receiver is able to obtain the signal. Diffuse optical wireless systems thus make use of multiple paths from the transmitter to the receiver such that the receiver is no longer dependent on the transmitter-receiver LOS.

ATTENTION: The Singapore Copyright Act applies to the use of this document. Nanyang Technological University Library

2.7 Comparison between optical wireless and radio

In comparison to radio, optical wireless has the advantage of a virtually unlimited bandwidth. Optical wireless signals are unable to penetrate the physical boundaries of the operating environment, such as walls, and as a result there is no interference between two optical wireless networks which can be used in offices located next to each other. In radio, interference is highly likely and some form of network planning would be necessary to ensure that there is minimal effect on both networks. A consequence of the optical wireless network having no interference with neighbouring networks is that no regulation or legislation seems likely, and there exists a large bandwidth available in the optical domain. For example, considering the wavelength range from 780nm to 1550nm, the available bandwidth is more than 150 THz. The abundance of bandwidth and the lack of regulation would imply that the capacity of the system would only be limited by the physical constraints of the devices as well as the characteristics of the transmitted signal.

Furthermore, unlike radio, optical wireless is generally immune to the effect of multipath fading. Multipath fading is common in radio, and can potentially cause deep fades resulting in channel outage. Multipath fading can be reduced by having employing multiple antennas to average out the fades. As the antenna for a radio system is typically on the order for the wavelength ($\sim 10^{-1}$ to 10^{-2}m for 2.4GHz) the number of employable antennas is limited in radio. In optical wireless however the size of the photodetector at from $1mm^2$ to $1cm^2$ is approximately 100 to 10,000 wavelengths, and acts as a sort of averaging, spatial diversity effect to avoid fading. However, as both radio and optical wireless are both freely propagating in freespace, both are susceptible to multipath dispersion effects on the system performance.

ATTENTION: The Singapore Copyright Act applies to the use of this document. Nanyang Technological University Library

Another difference between radio and optical wireless is the range afforded by the systems. Due to the penetrative nature of radio, network coverage can extend from a few metres to hundreds of metres. On the other hand, optical wireless is unable to penetrate the physical boundaries of the operating environment and is limited to indoor usage. However this property can be advantageous as well. By being constrained to the operating environment, optical wireless networks in neighbouring environments would not interfere and this would allow wavelength reuse as mentioned earlier. Furthermore, the non-penetrative nature of the optical wireless networks reduces the vulnerability of the network to outside attack by unauthorized users as they would be unable to access the network unless they were physically within the operating environment. This is especially critical where sensitive information such as financial or defense-related data is transmitted over a wireless network, and access control is important.

Optical wireless can have a higher health risk as compared to a RF channel, especially with regards to the eye safety tolerance levels. Generally the amount of light that the eye is able to tolerate without permanent damage would determine the level of optical wireless power that can be transmitted safely. The safe permissible energy level, also known as the maximum permissible energy (MPE) varies with the wavelength being used, and this would be discussed in further detail in a later chapter of this thesis. For radio frequency radiation, the main health risk is due to the induction of RF fields and currents inside the body [54]. The Specific Absorption Rate (SAR) in a body is determined by parameters such as frequency and intensity, and varies throughout the body. The largest SAR is found at all frequencies to be in the neck. In general, however, the typical emitted power of wireless networks is less than the SAR exposure limits. Table 2.4 gives the RF exposure limits

ATTENTION: The Singapore Copyright Act applies to the use of this document. Nanyang Technological University Library

Table 2.4 RF exposure limits. (from [54])

Frequency Range (MHz)	**Power Density (W/m^2)**
>400-2000	$\frac{f}{200}$
2000 – 300000	10

A summary of the discussion of the differences between optical wireless and radio is presented in Table 2.5. Generally optical wireless can be seen to offer some distinct advantages in the bandwidth and in the increased security of the channel. The greater potential health risks can be somewhat mitigated through the proper choice of the appropriate wavelength and limiting the power to safe levels.

Table 2.5 Comparison between OW and RF Properties

Property	**Infrared**	**Radio**
Multipath Fading	No	Yes
Multipath Dispersion	Yes	Yes
Range	Low	High
Penetration	Low	High
Health Risks	High (eyes)	Low
Bandwidth	Unregulated	Regulated

ATTENTION: The Singapore Copyright Act applies to the use of this document. Nanyang Technological University Library

2.8 Developments in indoor optical wireless communications

The configuration shown in Figure 2.1(e) was first proposed in a milestone paper by Bapst and Gfeller in 1978 [6], which was the first to suggest the use of IR in a wireless Local Area Networking (LAN) application. An array of 10 LEDs with an average optical output of 100mW was used as a 'spotlight' to diffuse the signal power into the reflecting surfaces of the room. Up to 8 of the spotlights could be used together to adjust for different room shapes and sizes. Using a wavelength of 950nm, the paper reported achieving a bit rate of 125kb/s up to a distance of 10-20m, depending on the room lighting conditions.

Subsequently, Barry et al [55] obtained a method to calculate the impulse response of an optical wireless system by subdividing each surface in an indoor environment into multiple absorbers and reflectors. By calculating the power received and subsequently re-transmitted by each reflector, the complete impulse response of the indoor environment can be determined by propagating the transmitted energy from the source, to each reflector a number of times depending on the number of bounces required, to the receiver. Using this model and the impulse response obtained as a result, channel characteristics could then be simulated and analyzed. The optical wireless channel is different from radio, in that the impulse response is highly dependent on the indoor environment and differs for each different room configuration. This was mentioned in Barry's work and also shown experimentally[7, 56]. As a general expression for impulse response is difficult to obtain for all configurations, Barry's expression has thus been extremely useful in calculating the impulse response for specific situations.

Marsh and Kahn [8, 57, 58] improved upon Gfeller's earlier work by using, 8 x 806nm laser diodes were passing through a 3mm thick Plexiglas diffuser to produce

ATTENTION: The Singapore Copyright Act applies to the use of this document. Nanyang Technological University Library

a Lambertian radiation pattern with an averaged emitted power of 475mW. The modulation scheme was based on On-Off Keying (OOK), and equalization was done using a 4 tap Decision Feedback Equalizer (DFE). The receiver was made up of a $1cm^2$ PIN photodiode with a 2cm-radius glass hemisphere providing an omni-directional optical gain. Using this system, the authors were able to achieve a transmission rate of 50Mbit/s over a distance of 2.9m in the presence of bright sunlight. Further studies conducted on the non-directed optical wireless configuration showed that a 100Mbit/s transmission rate would also be possible [59, 60].

Diffuse, non-directed configurations have the penalty of inefficient power transmission due to the wide field of view of the transmitter. Due to the nature of high optical path loss, spreading the emitted power over a large angle becomes very inefficient as much of the power is lost due to path loss, and less total power reaches the reflecting surfaces. The large field of view at the receiver also results in high multipath effect due to the large number of paths that reach the receiver, which leads to Inter Symbol Interference (ISI). Moreover, the large receiver field of view also means that significant ambient light could be detected by the receiver which increases the noise level. The net effect of these disadvantages is high transmission power requirement and lower data rates.

Yun and Kavehrad [61] propose a novel means to avoid these issues by using a combination of spot diffusers and fly-eye receivers. Spot diffusing is also known as a quasi-diffuse link. Instead of spreading the light over a Lambertian or hemispherical emission profile, the emitted power is projected onto a small area of the diffusing surface such as the ceiling using collimated or slightly diverted beams. Multiple LOS paths are achieved by having more than one diffusing spot in the configuration. At the same time, the receivers are designed to collect the signals from

ATTENTION: The Singapore Copyright Act applies to the use of this document. Nanyang Technological University Library

each LOS diffusing spot by focusing the power from each spot onto a separate photodetector, which reduces multipath effects since each detector only receives signals from a single LOS, while still maintaining the multipath redundancy that a diffuse configuration provides. The fly-eye detector technique can be also thought of as a form of imaging diversity, where instead of a single detector used to receive the transmitted signals, an array of detectors are used. In the experiment, a 780nm laser was used to project a diffusing spot on a wall, with the distance between the diffusing spot and the receiver being about 3m. With an emitted power of only 2dBm, the bit rate was found to be 704kb/s. The use of imaging diversity and spot diffusing was continued in [62, 63], where it was shown that use of imaging receivers would reduce the required transmission power by 13dB for LOS links, and by more than 20dB in non-LOS links.

Jungnickel et al [64, 65] was able to achieve a 155Mb/s transmission at a distance of nearly 2m using a ceiling mounted imaging diversity receiver and using both VCSEL directed transmitters (0.3mW) and Lambertian beam diffuse transmitters (400mW) mounted at table level. This was achieved using an Imaging Infrared Receiver (IIRR). The IIRR consists of a lens and a camera, which is used together to map the position of users on the photodiode array. When a user is detected, the appropriate photodiodes on the array are used for either selection or combining. Furthermore, the IIRR only needed 2ms to track the transmitter and re-establish the link when there was a change in the receiver position.

Angular diversity [66] is another form of diversity that can be used to combat multipath dispersion. Similar to imaging diversity, multiple detectors are used. However, the angle and the field of view of each detector are controlled such that noise from ambient lighting sources is reduced. Using angular diversity with a

ATTENTION: The Singapore Copyright Act applies to the use of this document. Nanyang Technological University Library

maximal ratio combining scheme, a 100 Mbit/s transmission capacity was found to be feasible. To demonstrate, a prototype system making use of angle diversity was set up which was able to be able to transmit up to 70 MBit/s at bit error rate of 10^{-9} at an operating range of 4 m.

Instead of using multiple sources to produce the desired diffused transmission energy pattern, another approach was suggested by Eardley et al [11] utilizing computer generated holograms. A computer generated hologram, optimized using simulated annealing techniques [67] was used to produce a uniform distribution of the optical power distribution. The main contribution was the use of a hologram rather than a lens in obtaining a uniform distribution of power on the room floor using a transmitter located at the ceiling, in a configuration similar to Figure 2.1(b). In a typical office environment, the floor area is rectangular rather than circular. The use of a typical ground glass or lens to diffuse the optical power would result in a round pattern. By using a hologram instead, a uniform rectangular or indeed any other far field diffraction pattern could be formed with relative ease. Also, by generating a uniform output radiation pattern, the eye safety risks due to high laser power emission could be lowered significantly, since the amount of light that could enter the eye is significantly lower. In the prototype testing, the resulting hologram pattern achieved a uniform intensity of ±15%. The light outside the cell has an intensity of -16dB as compared to within the cell. However, due to likely fabrication errors, the central zero order spot was found to be 1-3% of the laser power.

Using a hologram as a spot diffuser was further explored upon by Kavehrad et al [9, 68, 69]. Instead of projecting using the hologram as a uniform illuminator, the hologram was used to produce a multiple-spot diffusing configuration, where the spots were projected onto the ceiling as shown in Fig. 2.2. Using the multiple spot

ATTENTION: The Singapore Copyright Act applies to the use of this document. Nanyang Technological University Library

method, it was found that there was a 2dB improvement in the uniformity compared to using Lambertian patterns. Compared with earlier work where each spot was produced by a separate source, this also reduces the number of sources required as the hologram can be used to generate an arbitrary array of sources, reducing the complexity of the transmitter and enabling a more compact design for portable devices. In [9], the multi-spot diffusing scheme was in tandem with a receiver with angular diversity of 7, consisting of 7 detectors each with a different field of view, where the signal picked up at each detector can be termed as one 'branch'. Following detection of the transmitted signal at each branch, the branches were then combined in the well-known Maximal Ratio Combination scheme, where the signals at each branch are weighted by SNR at that branch, after which the signals from all the branches are summed. This has the effect of enhancing the contribution from branches with good signals ("high SNR"), and downplaying the contribution from branches with poor signal quality, producing an overall better SNR post-summation. When such a scheme was compared to a diffuse transmitter and receiver scheme, it was found that a 10dB improvement in the SNR was detected. These methods, when combined with the proper coding to improve the signal performance, were found to be able to facilitate the a link supporting hundreds of megabits with an acceptable bit error rate [70, 71]. Recent work by Al-Ghamdi and Elmirghani [72-75] have also made use of a similar scheme. Figure 2.2 illustrates the multispot diffusing concept.

ATTENTION: The Singapore Copyright Act applies to the use of this document. Nanyang Technological University Library

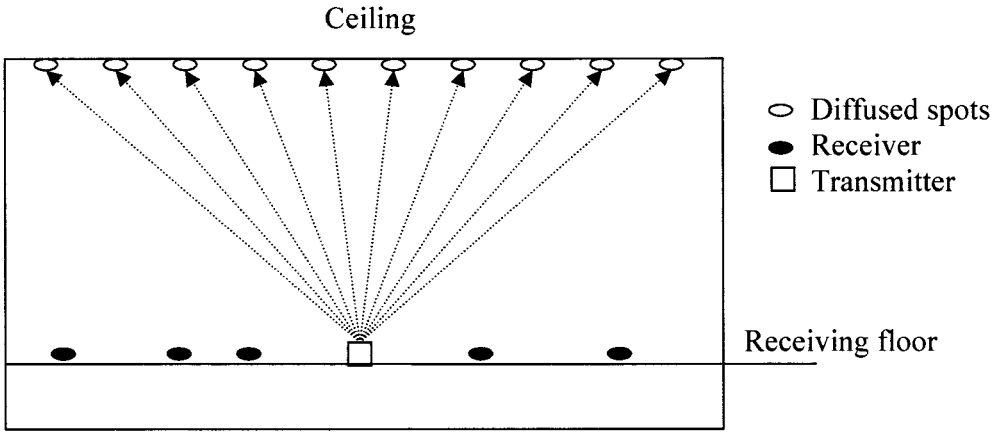


Figure 2.2 Conceptual illustration of multispot diffusing scheme employed by Kavehrad et al [9, 68, 69] and Al-Ghamdi et al [71-74].

More recently, there has been an increase in the interest towards using multiple-in-multiple-out (MIMO) techniques for optical wireless communications. MIMO [76] is a multiplexing technique that makes use of time and spatial diversity at the transmitter to improve the quality of the transmitted signal, allowing higher transmission rates or improved robustness. Previously some work was done in using the MIMO concept as an algorithm in determining the multiple path response [77]. Simon and Vilrotner [78] showed that the Alamouti space time block code which can be considered to be a basic form of MIMO can be easily modified for an optical channel. Garfield et al [79] demonstrated that using MIMO extended the range of the optical wireless network, and Takase and Ohtsuki numerically showed that a MIMO link was able to improve the capacity of a system by 50% to about 210 Mbit/s [80].

ATTENTION: The Singapore Copyright Act applies to the use of this document. Nanyang Technological University Library

3

Optical wireless channel link performance optimization through the study and optimized design of the receiver and transmitter properties

3.1 Introduction to the Chapter

In previous works making use of multiple spot diffusing techniques, the spot pattern is either fixed as a grid of spots [10] or is chosen from various geometrically simple designs such as diamond or line-strips [73]. The receiver field of view is then selected based on limiting the field of view, generally such that only a single spot lies within the field of view, but subject to further modifications. The important optical characteristics of the channel are thus defined in this way.

ATTENTION: The Singapore Copyright Act applies to the use of this document. Nanyang Technological University Library

In this Chapter, we introduce a new method of designing the optical characteristics for an optical wireless system. Instead of selecting the pattern first, we first identify important criteria in the performance of an optical wireless system, namely the uniformity of the power intensity distribution and the multiple path delay spread. Using these two characteristics a study of various conventional spot patterns would be used to determine the optimum receiver field of view that gives the best overall characteristics for various types of patterns. Once this has been determined, the receiver field of view is fixed, and carried over into the next part of the section. A simulated annealing algorithm is then used to determine the spot intensity pattern that would further enhance the channel performance. The communications aspects of the channel would then be determined. In this way, the optical wireless channel can thus be designed to fulfill channel requirements. Figure 3.1 compares the methodologies of the conventional approaches and the approach that will be followed in the rest of this chapter.

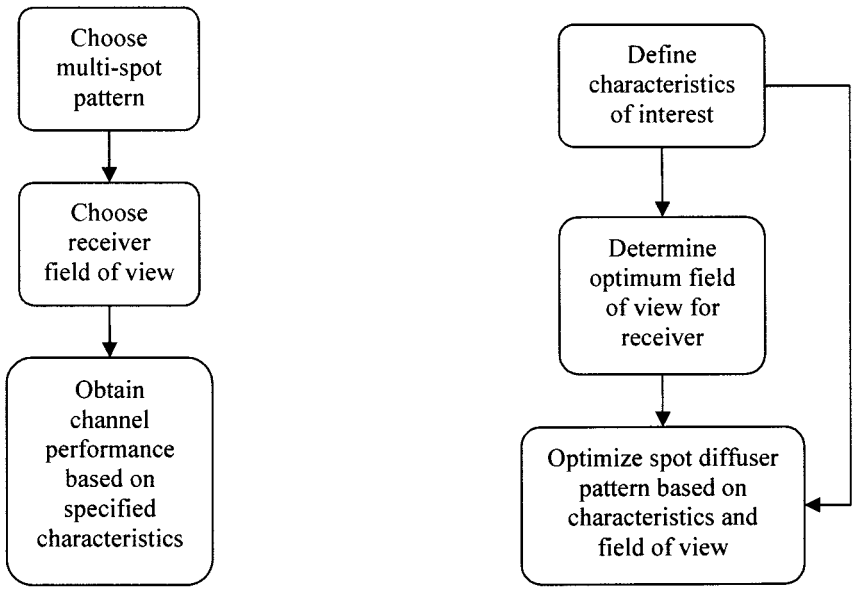


Figure 3.1 Methodologies in the design of an optical wireless system

(a) Conventional design flow and (b) Design flow based on channel requirements.

ATTENTION: The Singapore Copyright Act applies to the use of this document. Nanyang Technological University Library

3.2 Recent literature on optical design aspects of optical wireless communications

Although the design of the optical characteristics of the elements in an optical wireless system are important in determining its performance, there have been far fewer recent research efforts in this area compared to other work in the coding and modulation aspects of optical wireless [80-82]. Some of the earliest optical wireless systems by Gfeller and Bapst [6] made use of a purely diffuse transmitter combined with a wide angle lens for the receiver. While this was easy to design, a large fluctuation can be observed across the receiving floor, particularly at the corners when such a configuration is used. Yun and Kavehrad [61] proposed the use of s spot-diffusing multiple line-of-sight configuration to improve the robustness of the system, and Pakravan et al [83] suggested that holographic multi-lobe diffusers could be used to implement such a system. In [66], Carruthers and Kahn demonstrated a refinement of the diffusing spot configuration by using narrow beam laser diode-based transmitters together with narrow FOV receivers to reduce multipath noise. More recently, in [9, 84], Jivkova and Kavehrad have reported on the use of computer generated holograms as spot array generators to generate the array of diffusing spots, which has enables the projection of a large number of spots as well as a large flexibility of design over individually directed sources, and Al-Ghamdi and Elmirghani have contributed further by suggesting that a line strip spot diffuser is promising for optical wireless[72, 74].

Yet, there seems to have been a lack of a more thorough approach in the design of how the optical sources in a multispot diffusing configuration can be optimally placed, as well as the optimal field of view of a receiver, with most work making use of arbitrary configurations or selecting out of a small number of

ATTENTION: The Singapore Copyright Act applies to the use of this document. Nanyang Technological University Library

configurations. For example, Carruthers and Kahn[66] only compared the performance of a transmitter with 8 lobes against a diffuse transmitter, and a receivers with FOVs of 20° and 60°. In [9, 84], Jivkova and Kavehrad analyzed a series of 2x2, 3x3, 10x10 multispot transmitter, and Lambertian emitter. Later in [10, 85], they surmised that the receiver FOV should accommodate the 10x10 multispot pattern such that there is only one spot in each receiver FOV. Al-Ghamdi and Elmirghani surveyed uniform, diamond, line strip spot diffusers against a conventional diffuse transmitter in [72, 74], with arbitrarily set wide or narrow angle receiver FOV. In 2000, Yang and Lu [86] reported on the optimization of sources by using the ratio of the intensity at the corner against the intensity at the center as a cost function. Up to 16 sources were optimized. Although the ratio used has merit in determining the intensity difference at the corner and centre, it ignores dips and valleys in the detected intensity between the corner and centre. Also, no optimization of receiver FOV was reported. Most recently, in [87], Sivabalan and John analyzed the effect of the positions of up to 3 diffusing spots on the received power and bandwidth on an arbitrarily determined wide FOV receiver.

3.3 Determination of receiver field of view

The receiver field of view (FOV) determines the angle beyond which no signals are accepted by the detector. While a large FOV is able to accept more signals over a larger extent, resulting in greater received power and less vulnerability to line of sight (LOS) blocks, the tradeoff is a stronger multipath dispersion effect which limits the system bandwidth. The opposite is true for receivers with a small FOV.

ATTENTION: The Singapore Copyright Act applies to the use of this document. Nanyang Technological University Library

Objective

The objective of this section is to study the effect of various transmitter spot pattern configurations on the system performance and as a result, to determine an optimum FOV that offers the best performance across various transmitters spot patterns.

Methodology

A simulation will be used to model the room environment using the impulse equation between a source and a receiver. To determine the system performance, two metrics are defined, the standard deviation of the spread of the signal power distribution, and the average delay spread. Using these metrics, the receiver FOV that gives the desired performance across various transmitter patterns will be determined.

3.3.1 Impulse response model

The impulse response between a single source and a single receiver can be determined using the following equation from Barry [45], which is itself based on the irradiance of a receiving area from a diffuse source based on radiometric principles[88]

$$h(t;S,R)=\frac{n+1}{2\pi}\cos^{n}(\phi)\cdot d\Omega\cdot rect\left(\frac{\theta}{FOV}\right)\cdot\delta(t-\frac{r}{c}) \tag{3.1}$$

where n is the Lambertian mode number of the source, ϕ is the angle between the source normal $\vec{n}_s$ and the line connecting the source to the receiver, $d\Omega$ is the solid angle subtended by the receiver at the source, and is defined as

$$d\Omega=\frac{\cos\theta\bullet A_R}{r^2} \tag{3.2}$$

ATTENTION: The Singapore Copyright Act applies to the use of this document. Nanyang Technological University Library

where θ is the angle between the receiver normal $\vec{n}_R$ and the line connecting the receiver and the source, *FOV* is the half-angle of the receiver FOV, r is the distance between the source and the receiver, and c is the speed of light in a vacuum. *FOV* limits the number of paths reaching the receiver by ignoring paths whose angle at the receiver is more than *FOV*. The properties defined in Equations (3.1) and (3.2) are illustrated in Figure 3.2 below.

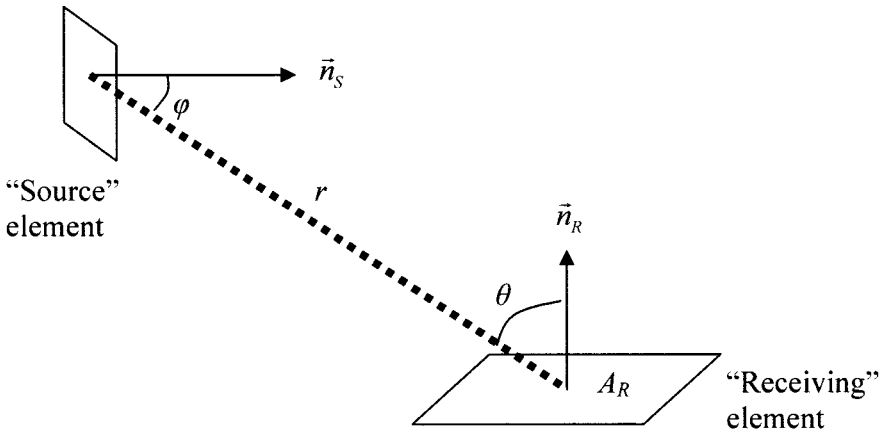


Figure 3.2 Impulse response model.

The effective result of (3.1) is that the impulse response is simply a scaled and delayed delta Dirac function. By multiplexing the application of (3.1), the impulse response between a source and a receiver off any number of reflecting surfaces can be obtained. Figure 3.3 illustrates an example of an impulse response measure with two elements and three bounces, resulting from a single spot that is 'bounced' off the ceiling from a transmitter located at the receiving plane.

ATTENTION: The Singapore Copyright Act applies to the use of this document. Nanyang Technological University Library

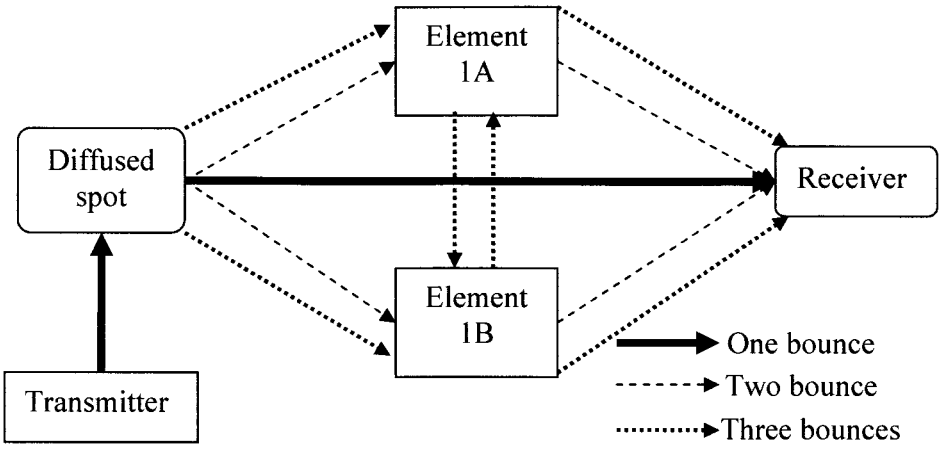


Figure 3.3 Multiple-bounce impulse response flow.

From the conditions in Figure 3.3, there are three possible paths that can be taken by the signal from the diffused spot to reach the receiver which can be determined by making use of Equation (3.1). For the single bounce response, the impulse response from the Transmitter to the diffused spot on the ceiling is first determined. Then, the impulse response from the diffused spot to the receiver is determined. By multiplying the two results and taking into account losses due to reflection at the bounce, the impulse response from the Transmitter to the Receiver can thus be obtained. In a similar way, for the two bounce response, the impulse response from the Transmitter to the diffusing spot is first calculated. Then, the impulse responses from the diffusing spot to Element 1A, and from Element 1A to the receiver are then calculated, taking into account taking into account losses at each bounce. By combining the three impulse response, the total impulse response for the path from the Transmitter, to the diffusing spot, to Element 1A, and finally to the Receiver can thus be determined. Similarly, the impulse response from the path from the Transmitter to the diffusing spot to Element 1B and to the Receiver can be found. In determining the three-bounce impulse response, the path is traced from the

ATTENTION: The Singapore Copyright Act applies to the use of this document. Nanyang Technological University Library

Transmitter to the diffusing spot, to Element 1A, to Element 1B, and to the Receiver using Equation (3.1) at each juncture. The trace is repeated for three bounce response from the Transmitter, to the diffusing spot, to Element 1B, to Element 1A and to the receiver. By summing the various impulse responses determined, the complete impulse response for the system from the source to the receiver can thus be found.

3.3.2 Simulation parameters

A typical room size of 6m x 6m x 3m was used in the model, with a ceiling and wall reflectivity of 0.7. A Lambertian mode number of 1 was used for the diffusing surfaces. No objects were simulated to be in the room. To collect the transmitted impulse response, a $1cm^2$ active area photodetector directed vertically at the ceiling, placed 1m above the receiving floor to emulate a typical table height, is used. The transmitter was placed at the center of the room and directed vertically at the ceiling, with a total power of 1W directed into the diffusing spot patterns at the ceiling. Figure 3.4 illustrates the geometry described. The simulation is carried out in a 'dark' environment without any illumination from light sources or from windows. The simulation parameters are summarized in Table 3.1

ATTENTION: The Singapore Copyright Act applies to the use of this document. Nanyang Technological University Library

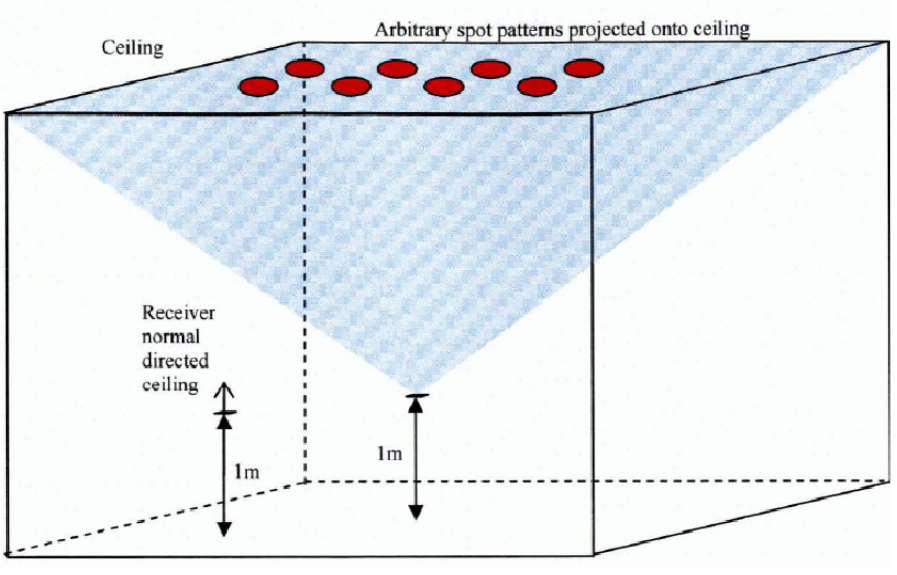


Figure 3.4 Illustration of room model used in simulations.

Table 3.1 Simulation Parameters

Parameter	**Description**
Room size	6m x 6m x 3m
Receiving plane	1m above floor
Lambertian mode number	1
Size of photodetector	$1cm^2$
Wall reflectivity	0.7
Total power incident on ceiling	1W

ATTENTION: The Singapore Copyright Act applies to the use of this document. Nanyang Technological University Library

3.3.3 System design parameters

An important metric to determine the performance of a wireless mobile network is the root mean square (RMS) delay spread, τ_{RMS} [89]

$$\tau_{RMS} = \sqrt{\overline{\tau^2} - (\overline{\tau})^2} \tag{3.3}$$

where τ is the delay associated with the signal, relative to the first arriving signal, $P(\tau)$ is the associated power of the signal, $\overline{\tau}$ is the mean delay spread as defined below

$$\overline{\tau} = \frac{\sum P(\tau) \cdot \tau}{\sum P(\tau)} \tag{3.4}$$

and $\overline{\tau^2}$ is the second moment of the delay spread

$$\overline{\tau^2} = \frac{\sum P(\tau_k) \tau_k^{\,2}}{\sum P(\tau_k)} \tag{3.5}$$

A higher RMS delay spread limits the data rate that can be transmitted, and a typical conservative estimate of the data rate can be found by calculating the inverse of $10\sigma_\tau$. It should be noted that this data rate does not take into account equalization and other forms of signal conditioning which could be used to increase the data rate. To analyze the uniformity of the signal power distribution, the standard deviation of the received power across all detector positions in the room is calculated, using the following expression:

$$\sigma_P = \sqrt{\frac{\sum (X - \mu_P)^2}{N}} \tag{3.6}$$

where X is the received power at each of the sampled points in the receiving plane, μ_P is the average received power and N is the number of sampled points.

ATTENTION: The Singapore Copyright Act applies to the use of this document. Nanyang Technological University Library

3.3.4 Conventional grid-based diffusing spot designs

Diffusing spots are typically arranged in square grid-type designs which are easy to implement. In this section, various numbers of diffusing spots arranged in such grids will be used in the model, together with various receiver FOV values, to determine the combination of spot pattern and more importantly the receiver FOV that will give the best results for the metrics defined earlier. The optimum FOV obtained will be used in the optimization of the spot pattern in Section 3.3. In practical implementation, losses can be expected at the transmitter such as absorption and back reflection at the hologram mask. However, for the scope of this section, it is assumed that there is no loss in power from the transmitter to the ceiling.

3.3.4.1 Impulse Responses

To analyze the effect of spot patterns and receiver FOV on the system response, the model was run with 8 different spot patterns and 5 different FOVs for the receiver. A Lambertian diffuse pattern was used for the transmitter, as well as 5 other grid-based designs as shown in Figure 3.5: 2x2, with a 2.85m separation between the spots; 4x4, with a 1.35m separation; 6x6, with a 0.90m separation; 8x8, with a 0.60m separation distance and 10x10, with a 0.45m separation distance. Each pattern had a total of 1W which was equally distributed into all the spots in the design, and is centred on the room ceiling. Patterns consisting of a single spot (PT) as well as the case of uniformly illumination (uniform) were also used. Values of 10°, 20°, 30°, 45° and 90° were used for the receiver FOVs.

ATTENTION: The Singapore Copyright Act applies to the use of this document. Nanyang Technological University Library

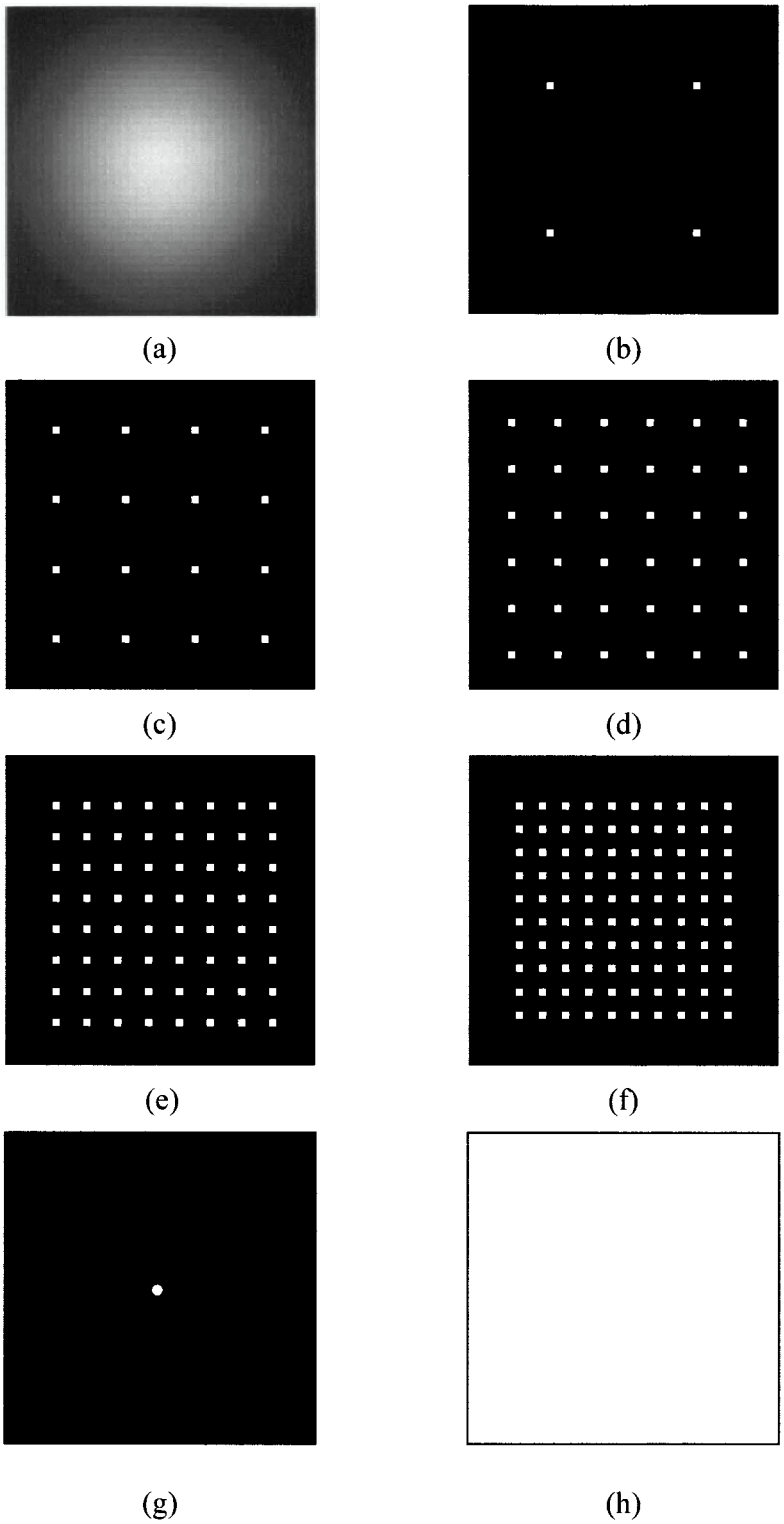


Figure 3.5 Spot patterns used in the simulation:

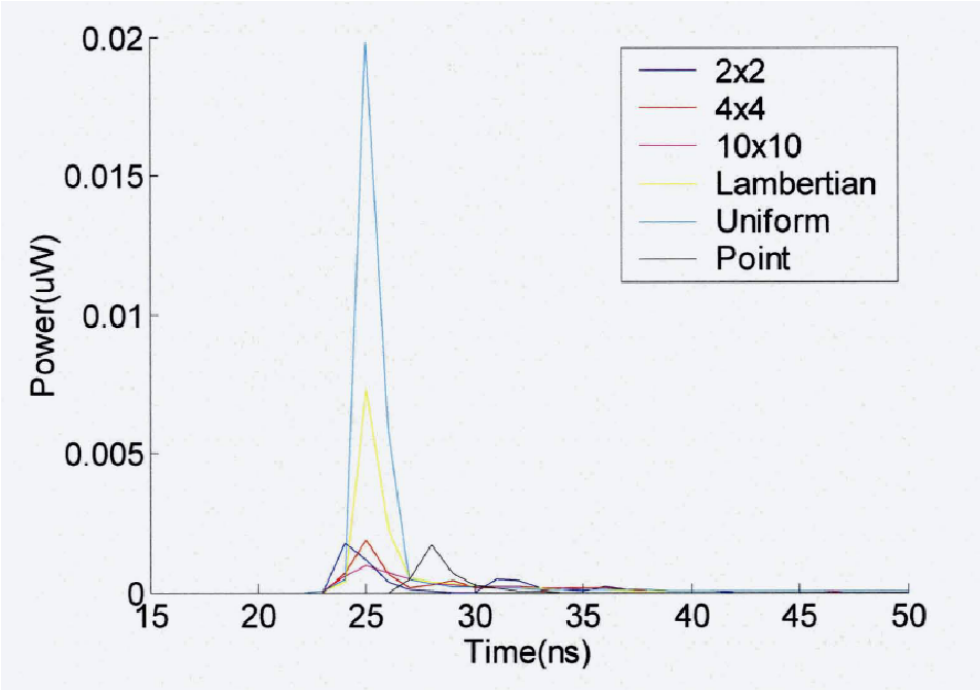
(a) Lambertian, (b) 2x2, (c) 4x4, (d) 6x6, (e) 8x8 and (f) 10x10, (g) Single point (PT) and (h) Uniform illumination (UNI).

ATTENTION: The Singapore Copyright Act applies to the use of this document. Nanyang Technological University Library

The impulse response plots for some of the spot patterns and FOVs are shown in Figure 3.6. The detector is placed at two positions within the room representing the ideal scenario where the receiver is placed in the centre of the receiving floor and in non-ideal scenario where the receiver is located towards the corner. The received power and delay spread results are tabulated in Table 3.2. At position 'A', the detector is placed near the room corner with coordinates (0.75, 0.75, 1.0) and at position 'B, the detector is placed the exact room center (3.0, 3.0, 1.0). In Figure 3.6(a), the received power is very low. This can be attributed to the 10° FOV of the receiver and the placement at the corner, resulting in only 2nd order bounces from the walls to be received by the detector and thus the generally lower receiver power. The Lambertian pattern results in more signal power being received as the wider coverage of the pattern allows some of the 1st order signals from the ceiling to be reflected onto the detector. The highest power detected was when the ceiling was uniformly illuminated using Figure 3.5(h), giving a substantially higher power as compared to the other patterns. This is due to the uniform illumination of the ceiling which increases the number of sources within the FOV. The tradeoff is that the impulse response is longer compared as to when other patterns are used. At the same time however, the uniformly illuminated area ensures that some 1st order bounces are received. Due to the higher intensity of these signals as compared to 2nd order bounces, the delay spread, which is also dependent on the relative intensity of the received signals as can be seen from Equations (3.3) to (3.5), the delay spread is smaller as compared to the other patterns. When the 10° FOV detector is placed at the room center, or position 'B;, the limited FOV only allows 1st order signals from the ceiling to be received. As the 2x2 and 4x4 patterns do not have spots that are within the receiver FOV, no signal is received resulting in a lost connection at the center when these two patterns are

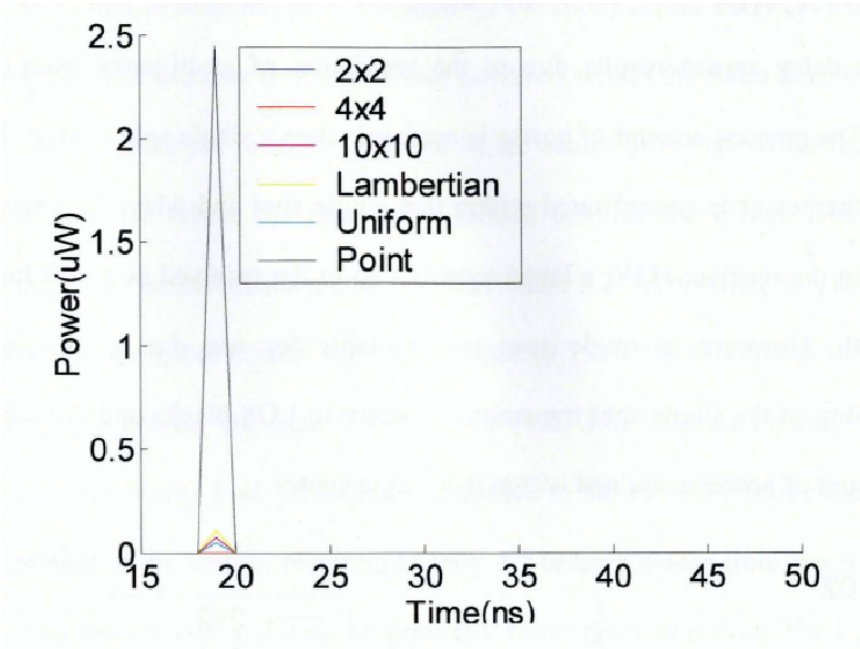
ATTENTION: The Singapore Copyright Act applies to the use of this document. Nanyang Technological University Library

used. When a single spot lies within the FOV, such as in the 10x10 design, a negligible delay spread results due to the restriction of multi-paths entering the detector. The greatest amount of power is received when a single spot is used. This is since all the power is concentrated within that single spot and when the single spot falls within the receiver FOV, a large contribution to the received power is from the direct path. However, a single spot is unsuitable for use due to the inherent susceptibility of the single spot transmitting pattern to LOS blocks and the relatively large amount of power contained within that single spot.

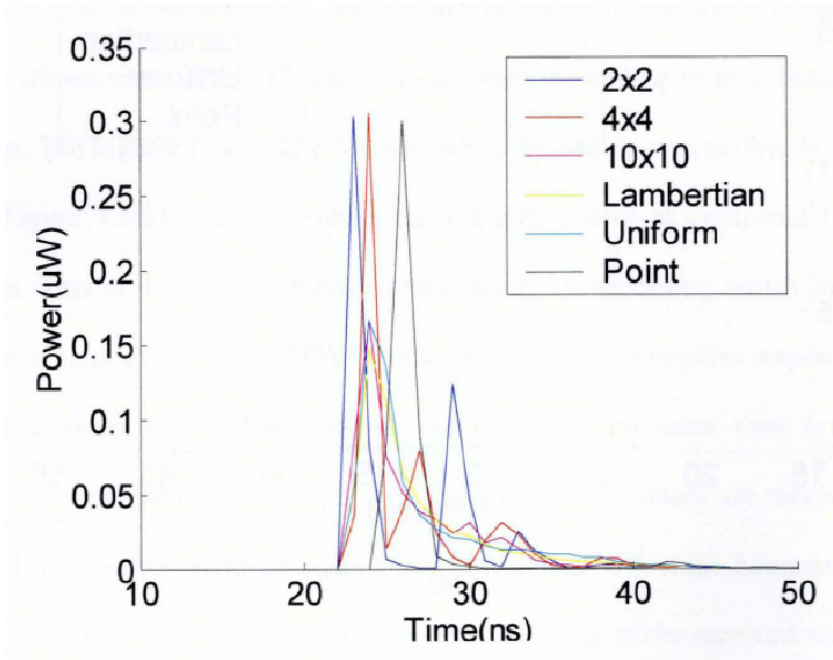


(a)

ATTENTION: The Singapore Copyright Act applies to the use of this document. Nanyang Technological University Library



(b)



(c)

ATTENTION: The Singapore Copyright Act applies to the use of this document. Nanyang Technological University Library

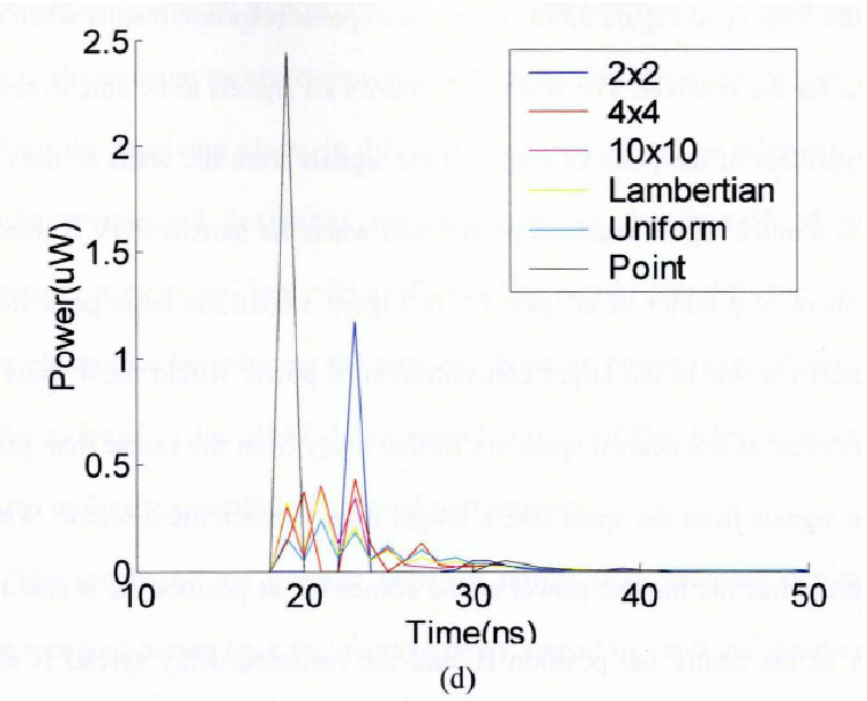


Figure 3.6 Impulse responses at the detector: (a) Position 'A', FOV 10°; (b) Position 'B', FOV 10°; (c) Position 'A', FOV 90° and (d) Position 'B', FOV 90°.

Table 3.2 Metrics from impulse response simulations

		Power (μW)		Delay Spread (ns)	
FOV	Pattern	Pos 'A'	Pos 'B'	Pos 'A'	Pos 'B'
10°	2x2	0.005	0.000	3.99	NA
10°	4x4	0.005	0.000	3.79	NA
10°	10x10	0.004	0.073	3.57	0.00
10°	Lambertian	0.012	0.107	2.56	0.00
10°	Uniform	0.028	0.048	1.93	0.00
10°	Single	0.003	2.442	0.99	0.00
90°	2x2	0.635	1.355	4.46	3.56
90°	4x4	0.621	1.411	4.30	4.34
90°	10x10	0.590	1.605	4.15	4.06
90°	Lambertian	0.594	1.537	4.29	4.39
90°	Uniform	0.632	1.28	4.61	4.64
90°	Point	0.501	2.59	2.82	3.25

ATTENTION: The Singapore Copyright Act applies to the use of this document. Nanyang Technological University Library

Figure 3.6(c) and Figure 3.6(d) show the impulse response results when a wide FOV is used for the receiver. The wide FOV allows all signals to be able to reach the detector, regardless of the point of origin of the signals from the walls or the ceiling. This leads to a much higher received power than when the narrow FOV is used, with an improvement of a factor of at least 10. In Figure 3.6(d), the large peak from the 2x2 spot pattern is due to the larger concentration of power within the 4 spots of the pattern. However, as the nearest spots are further away from the centre than the other designs, the signals from the spots take a longer time to reach the detector. While the uniform pattern has the highest power at the corner i.e. at position A, it also has the least power in the centre i.e. position B, and the resulting delay spread is also the highest of the different spot patterns used. This is due to the uniform distribution of the spots with equal power in each, resulting in many signals with similar amplitudes reaching the receiver. This is undesirable, as, to minimize the effect of delay spread, ideally there should only be a single strong signal, with the subsequent paths being as weak as possible and this can be seen from Figures 3.6(c) and 3.6(d), where the uniform pattern has the longest impulse response of the various patterns considered.

3.2.4.2 Survey of results

To further analyze the results, another metric, the standard deviation of the received power at various parts of the room, σ_P, is taken into consideration. 400 locations were considered, uniformly distributed at the receiving plane with a separation of 0.3m between each location. From the earlier results, particularly at the narrower FOVs, certain positions may be unable to receive any signals if no sources, either 1st order from the ceiling or 2nd order from the walls, fall within the receiver FOV. This is particularly prevalent at the corners, which tend to suffer a sharp drop-

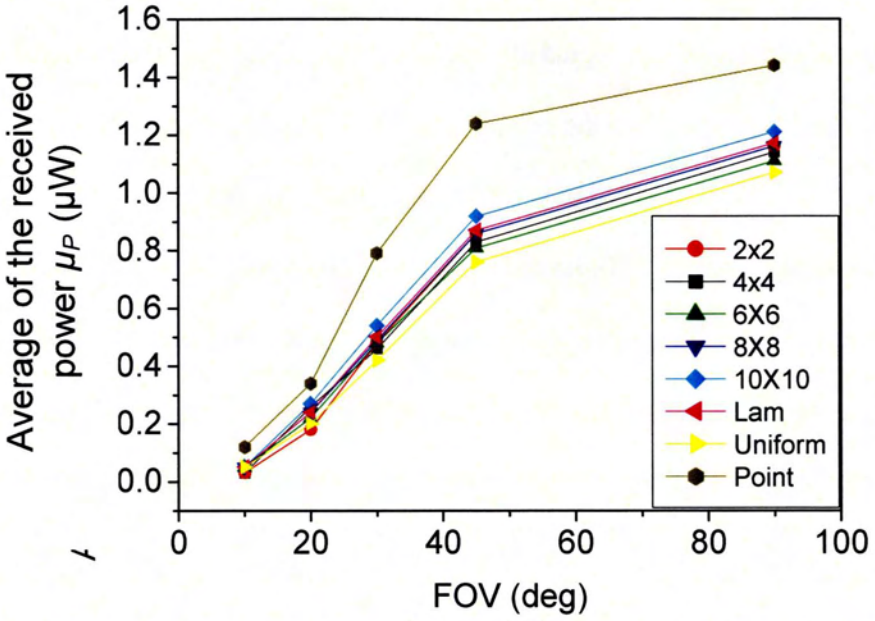
ATTENTION: The Singapore Copyright Act applies to the use of this document. Nanyang Technological University Library

off in power as compared to positions near the room centre. A low standard deviation relative to the average received power would imply that the signal power distribution throughout the receiving plane, in this case the floor, would be more uniform than a high relative standard deviation, and would reduce the drop-off at the corners. Furthermore, a more uniform signal distribution would simplify the design of the receiver electronics by reducing the required dynamic power range of the electronics. Also, the average of the RMS delay spread across all the detector positions, μ_τ, is calculated to for the overall delay spread performance.

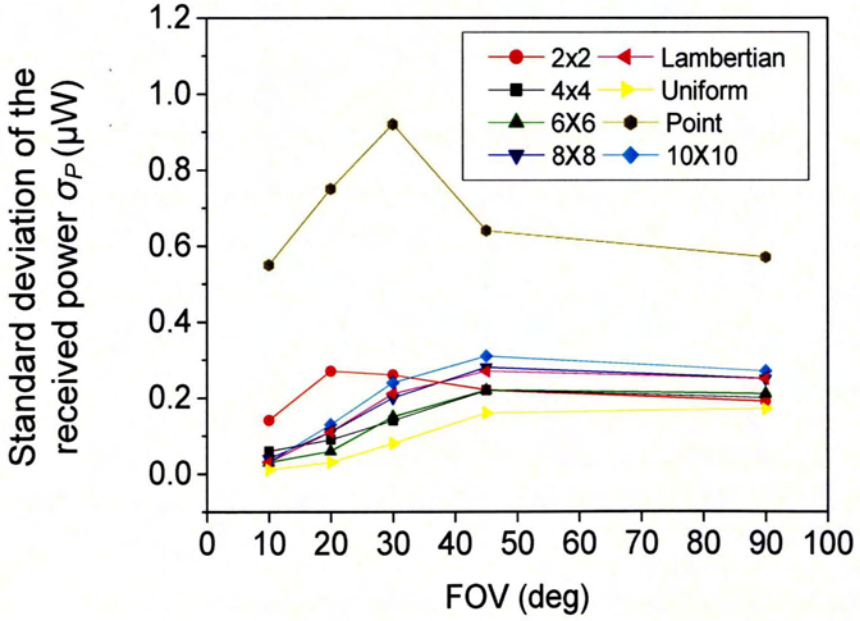
The graphs of the average received power (μ_P), standard deviation of the average received power (σ_P), the average delay spread (μ_t) and the standard deviation of the RMS delay spread across all the locations (σ_t) are shown in Figures 3.7(a), (b), (c) and (d). The receiver FOV has a large impact on the system performance. As the FOV is reduced, the number of multipaths reaching the detector is reduced, which reduces the delay spread, limiting multipath dispersion effects and increasing the possible data rates. However, the tradeoff is that with a reduction in FOV, few paths reaching the detector means that the average received signal power is also reduced accordingly. The smaller gradient in Figure 3.7(a) between the 45° and 90° FOV can be attributed to the type of signals that are prevented from reaching the receiver. At 90°, as earlier mentioned, all signals reaching the detector are accepted. When the FOV is reduced to 45° however, the weaker 2nd order signals from the walls are rejected more than the stronger 1st order signals from the ceiling. For example, when the receiver is placed at the room centre, a 45° FOV describes a circle of radius 3m at the ceiling. Effectively this means only 1st order signals from the ceiling is accepted. When the FOV is increased to 90° at the same position, the additional power at the

ATTENTION: The Singapore Copyright Act applies to the use of this document. Nanyang Technological University Library

receiver is due to the acceptance of 2nd order signals from reflections off the room walls.

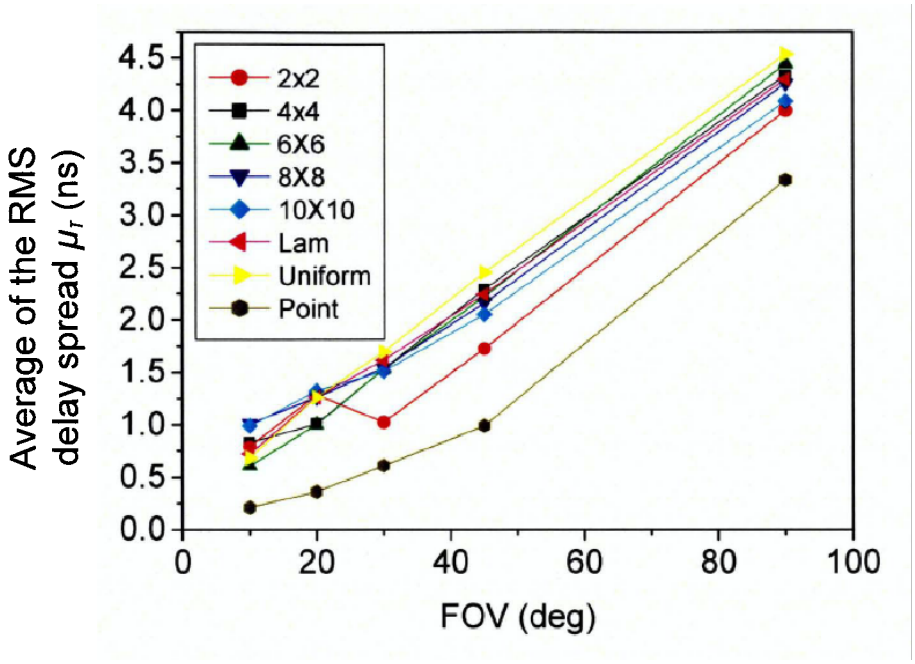


(a)

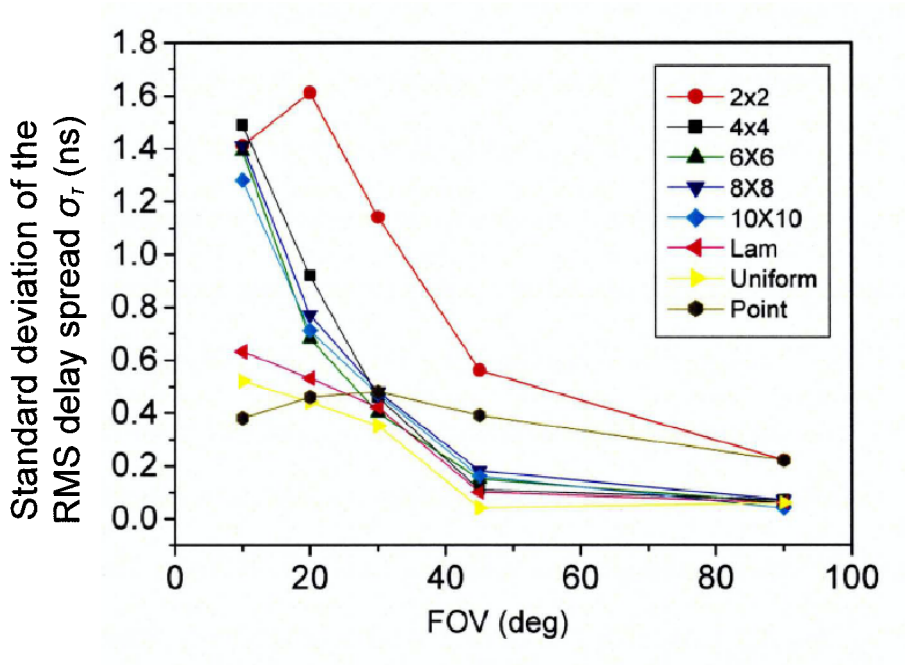


(b)

ATTENTION: The Singapore Copyright Act applies to the use of this document. Nanyang Technological University Library



(c)



(d)

Figure 3.7 Plotted results of the (a) average received power, (b) standard deviation of the received power, (c) average delay spread and (d) standard deviation of the delay spread when the spot patterns and field of view are varied.

ATTENTION: The Singapore Copyright Act applies to the use of this document. Nanyang Technological University Library

From Figure 3.7(a) and 3.7(c), except for the 2x2 spot pattern, the variation of the spot patterns do not have a large effect on the average performance of the system with a variation of within 10% when different patterns are used. However, the choice of patterns affects σ_P, with a variation of more than 50% of the standard deviation values, particularly at narrower FOVs. At an FOV value of 10°, σ_P is as much as μ_P, indicating a large variation in the received power throughout the room. This implies that some locations are not receiving any signals. Although an extremely low delay spread of less than 1ns is possible at this FOV, alignment is needed for the spot distribution with the room size to ensure that the receiver is able to receive signals, which may be difficult to ensure practically. The single point and 2x2 spot patterns are clearly unsuitable for use at narrow FOVs as σ_P is larger than μ_P.

From Figure 3.7(b), it can be observed that use of a wide FOV of 45° and 90°, allows a low σ_P relative to μ_P to be achieved. However, the tradeoff is a higher μ_t due to a larger number of multipaths being allowed to reach the detector. A maximum RMS delay spread of 1.85ns is used as a cutoff value. Using a conservative estimate of $1/(10 \times \sigma_\tau)$, this delay spread value gives a maximum data rate of approximately 54 Mbit/s, which is equivalent to the transmission bit rate specified in currently the most popular wireless standard, IEEE 802.11b, which is used as a benchmark. Use of equalizers and other communication techniques such as diversity can be used to increase the data rate further but this value will be used as a performance benchmark within the scope of this paper. From the graphs shown in Figure 3.7(c), the maximum FOV within this benchmark is seen to be 30°.

Although a FOV of 20° gives a better delay spread performance according to Figure 3.7(c), the larger relative σ_τ from Figure 3.6(d) implies a larger variation in the delay spread performance. Furthermore, at 30°, the larger FOV doubles the μ_P as

ATTENTION: The Singapore Copyright Act applies to the use of this document. Nanyang Technological University Library

observed from Figure 3.6(a), with the tradeoff being a 20% increase in μ_t. A larger FOV would also simplify the design of the spot pattern. Using a 20° FOV, for a detector placed at the corner to be able to see a spot, the spot must be less than 2.5m away from the corner. If a 30° FOV detector is used, the spot need only be less than 6.5m away from the corner, reducing the likelihood of a dropped link if the transmitter is offset from the centre. Based on the arguments given above it can be concluded that a receiver FOV of 30° would give a good balance of delay spread and signal power distribution performance.

Table 3.3 Performance of various patterns at 30° field of view

Pattern	Average Power μ_P (μW)	Standard deviation of Power σ_P (μW)	Average Delay Spread μ_τ (ns)	Standard deviation of Delay Spread σ_τ (ns)
2x2	0.48	0.26	1.02	1.14
4x4	0.46	0.14	1.53	0.46
6x6	0.48	0.15	1.53	0.40
8x8	0.49	0.20	1.54	0.48
10x10	0.54	0.21	1.51	0.47
Lambertian	0.50	0.24	1.61	0.42
Uniform	0.42	0.08	1.69	0.35
Point	0.79	0.92	0.61	0.48

ATTENTION: The Singapore Copyright Act applies to the use of this document. Nanyang Technological University Library

The performance of the various spot patterns at a 30° FOV is summarized in Table 3.3. The high standard deviation of the single point and 2x2 spot patterns for received power and delay spread indicate a large variation in the system performance, making the pattern clearly unsuitable for use at this FOV value. Due to the large illumination area when the Lambertian and uniform spot patterns are used, they result in the highest average delay spread values. The uniform illumination pattern has the lowest σ_P, but at the expense of higher μ_t and the lowest μ_P. The 4x4 and 6x6 spot patterns result in σ_P being the lowest, with the 4x4 pattern performing marginally better in terms of consistency when the ratio of the σ_P over the μ_P is determined.

3.3.5 Conclusions

In this section, a simulation was used to model the impulse response of an indoor room environment. Using this model, various spot patterns were used and their impact on the system performance over various receiver FOVs was analyzed using the metrics for standard deviation of the received signal power uniformity and the average delay spread. Using the metrics as a guideline, a receiver FOV of 30° was found to meet the desired performance criteria.

3.4 Optimization of diffusing spot pattern distribution

3.4.1 Introduction

In this section, the optimum field of view as determined in the previous section will be utilized. It was previously shown that a 30° field of view provides the optimum performance that meets the desired design parameters. Using this optimum field of view, a global optimization technique will be used to optimize the spot patterns to further improve the system performance throughout the receiving plane.

ATTENTION: The Singapore Copyright Act applies to the use of this document. Nanyang Technological University Library

Objective

Given the optimum field of view determined earlier, a transmitter spot pattern will be obtained that improves the system performance as determined by the standard deviation of the received signal power distribution and the delay spread at any point in the room.

Methodology

Using the room model from the earlier section, a global optimization technique is used to obtain the transmitter spot pattern that gives the optimum results. Initially the spot pattern will be optimized for one parameter, namely σ_P to form a baseline in the performance. After that, a merit function will be introduced to allow optimization of the spot pattern for more than one parameter i.e. σ_P and μ_P

3.4.2 Simulated annealing technique

Using the optimum FOV as determined in Section 3.2, the spot pattern was next optimized using a simulated annealing (SA) technique for this optimum FOV of 30°. The simulated annealing technique was proposed by Kirkpatrick et al [90] as a means of finding a global minimum in an optimization process. It is analogous to the annealing process of a molten metal, in which a material finds the lowest possible energy state during the cooling process. The chief advantage of using the SA technique is that it avoids being trapped in a local minimum by introducing a temperature coefficient that is slowly reduced. The governing equation is

$$P = \exp\left(-\frac{df}{T}\right) \tag{3.7}$$

ATTENTION: The Singapore Copyright Act applies to the use of this document. Nanyang Technological University Library

where P is the probability of accepting an undesired result df, and T is the current temperature. The technique uses a random search process. If a desired result is obtained, the technique accepts the change as the best obtained result. If an undesired result is obtained, that undesired result is accepted with a probability of P. This avoids the algorithm from working on the assumption that the first minimum is the global minimum, as can be the case when a simple iterative minimization (IM) process is utilized, which simply only accepts desirable results with no probability of accepting undesired results.

The performance of the simulated annealing method is largely affected by the cooling schedule, which determines the performance of the method in avoiding local minima and reaching a truly global minimum. The parameters of the cooling schedule are primarily specified by the initial starting temperature, ending condition and the cooling rate. The initial starting temperature T_0 is problem specific, but it should produce in an average increase in the acceptance probability χ_0 of about 0.8 [91]. To obtain T_0, the method suggested by Kickpatrick[82] was adopted, in which an initial search was conducted to determine the average cost function increase $\overline{\Delta f}$. Using this value of $\overline{\Delta f}$, the initial temperature T_0 can be determined from $T_0 = -\overline{\Delta f}/ln(\chi_0)$. The ending condition can be specified in terms of a fixed ending temperature or when no further improvements in the cost function can be observed. The latter was adopted in the following work. Finally, the cooling rate is an important determinant of the performance of the annealing algorithm. If the cooling rate is too fast, the algorithm may not be able to locate the global minimum, while too a slow cooling rate would be computationally inefficient. Exponential cooling schemes [91], where the cooling rate is a fixed proportion $T_{n+1} = \beta T_n$ and linear cooling schedules [92], where the cooling rate is a fixed decrement i.e. $T_{n+1} = T_n - \Delta T$, and were both initially explored, and it

ATTENTION: The Singapore Copyright Act applies to the use of this document. Nanyang Technological University Library

was found that the exponential cooling scheme was preferable in the optimization. To determine the value of β, we varied β from 0.8 to 0.95, and found that a value of 0.93 consistently provided a good balance between computational time and performance.

In this section we employ the use of computer-generated holograms (CGH) as a spot array generator. Computer generated holograms are a type of hologram which can be designed without the need to have the actual object imaged. The hologram is formed through use of mathematical models, in this case the far-field Fraunhoffer diffraction regime. The SA approach has been used in previous studies in the design of a hologram with spot-weighted intensities [67], as well as able to optimize the hologram mask to convert a point source into an extended source, with the lowest cost function as compared to the error reduction and input output methods [93], and in general the SA algorithm can be used to produce an arbitrary spot distribution function when used in a Gerchberg-Saxton bidirectional algorithm [94].

The SA algorithm is employed to determine the optimum distribution of spots on the room ceiling to achieve a desired performance metric. In the implementation of the optimization technique, the room model, multiple bounce impulse response model and the SA algorithm were developed in a MATLAB operating environment and were coded specifically for the purpose of this work. If the location of each spot was allowed to freely vary, the computational load would be extremely high as the spots could be located anywhere on the ceiling, coupled with the possibility that the location of hundreds of such spots may need to be optimized. Furthermore, this could be difficult to implement in a CGH-based spot array generator in which the possible spot locations have a fixed regular spacing. To constrain the spot locations and to facilitate a more efficient optimization of the spot distribution, the room ceiling is discretized into a 40x40 sized grid, allowing a total of 1600 possible spot locations.

ATTENTION: The Singapore Copyright Act applies to the use of this document. Nanyang Technological University Library

The grid can be easily mapped to the target function of a CGH. For illustrative and visualization purposes, in the following text, pixels are used as patches within the grid to identify the location of the diffused spots. Figure 3.8 shows a simplified example to illustrate the preceding description.

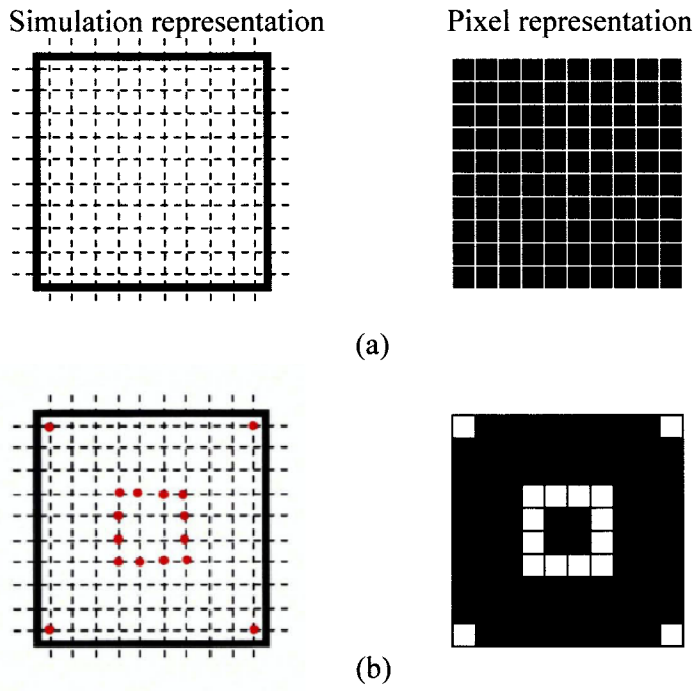


Figure 3.8 Visualization of the diffusing spots on the ceiling grid and the pixel representation for a simplified 10x10 grid. (a) represents the grid on the ceiling together the pixel representation when no spots are present (b) represents the scenario when there are 16 spots present as represented by the red dots, and the corresponding pixel representation, represented by the white pixels. The bold box represents the physical size of the ceiling.

Once the optimized spot distribution pattern in the far-field has been determined, the actual hologram that would produce such a pattern can be easily determined using iterative techniques such as the Gerchberg-Saxton algorithm

ATTENTION: The Singapore Copyright Act applies to the use of this document. Nanyang Technological University Library

mentioned earlier or by other techniques such as using simulated annealing or genetic algorithms [95]. For the purpose of the simulation, it is taken that a binary phase-only computer generated hologram is used to generate the spot pattern. A typical design process involves first specifying the intensity distribution of the reconstructed pattern. Next, a random binary phase hologram is generated. To determine the far-field intensity of this generated hologram, a Fourier Transform is performed, and the results are compared against the desired spot distribution. Changes are made to the hologram, and the process is repeated using one of the various optimization routines mentioned earlier until the desired pattern is obtained, or the optimization routine comes to an end due to pre-specified exit parameters being reached. As previously mentioned, the optimization of the phase profile for the CGH has been well-researched. However, we are more concerned with the optimization of the projected spot pattern on the ceiling as shown in Figure 3.9 rather than obtaining the corresponding hologram and this would be the focus of this section and the main contribution of this Chapter. Once the pattern has been obtained, the pattern can be used as the target design to generate the corresponding CGH.

ATTENTION: The Singapore Copyright Act applies to the use of this document. Nanyang Technological University Library

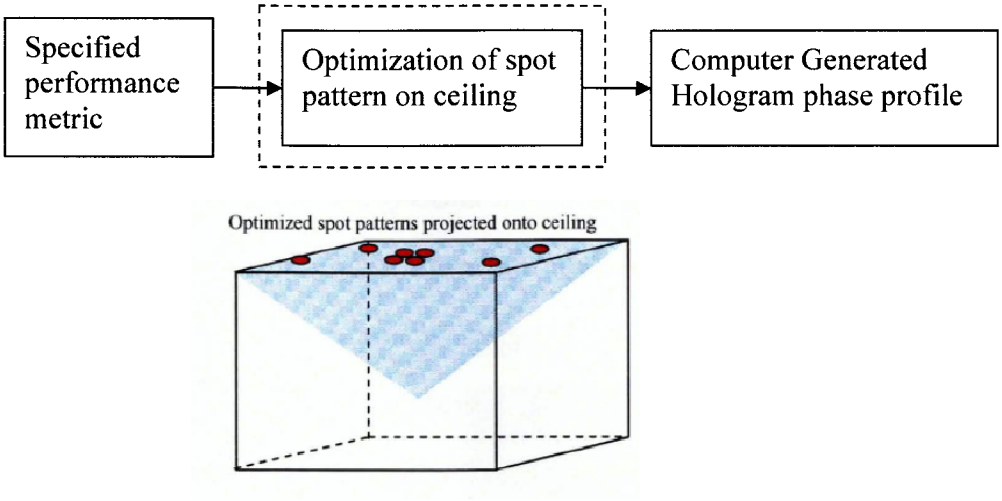


Figure 3.9 Focus of the optimization effort to obtain an optimal placement of diffuse spots on the ceiling (shown by the dashed box).

The algorithm begins with a randomly generated array of spots. A dark pixel represents no illumination by the transmitter, while a light pixel represents a diffusing spot. At each iteration, four random pixels which are symmetric about the origin are inverted. The need for symmetry is due to the symmetry of the ±1 orders in the far-field diffraction pattern of a binary-phase hologram, and simplifies the design of the hologram. If the pixels were previously dark, they are made light, and if light, are made dark. The relevant metric such as the standard deviation of the received power is then calculated, and compared with the previous result to give *df*, where an undesired result may or may not be accepted depending on *P*. The iterations are repeated till the end of one cycle, whereby the annealing temperature is reduced, and the cycle of iterations begins anew for the new temperature. The process is run till no improvement can be observed. A simplified flowchart of the approach used in shown in Figure 3.10.

ATTENTION: The Singapore Copyright Act applies to the use of this document. Nanyang Technological University Library

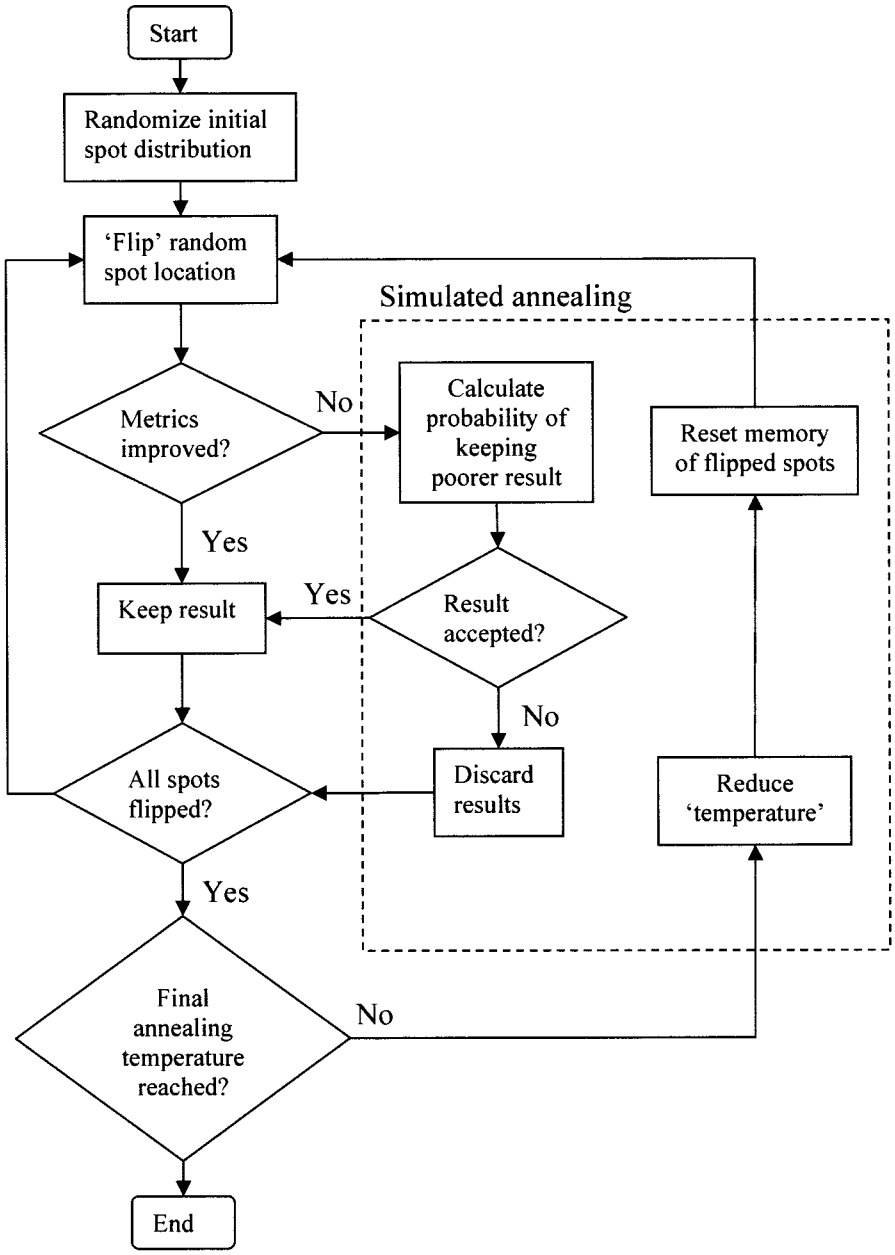


Figure 3.10 Flowchart showing program flow of the spot distribution pattern optimization algorithm.

ATTENTION: The Singapore Copyright Act applies to the use of this document. Nanyang Technological University Library

To determine the performance of the SA algorithm, a comparison is made between two runs, one using a simple IM algorithm, the other using the SA algorithm. Both were specifically developed and coded within the MATLAB programming environment. The IM algorithm is a basic error minimization algorithm which does not include the probability of acceptance in simulated annealing. As a 'blind' algorithm, the method only accepts changes in the spot pattern that would result in an improvement of the cost function, unlike simulated annealing which can accept undesirable results early on in the hope of obtaining a global minimum. The IM method stops when no further improvements in the cost function can be observed. Both methods used the same cost function which is to minimize σ_P and the plots of the results for the IM and the SA methods are shown in Figure 3.11, which plots the number of cycles required against the normalized σ_p. On the plot for the IM approach, the minimum value is obtained after about 2300 cycles. The graph also reflects the hard optimization nature of the algorithm, which only moves downwards. From the plot of the graph obtained using the SA technique, there is a higher probability of accepting undesired results in the early cycles when the temperature is high. As the number of cycles increase, the temperature drops and the probability of accepting undesired results drops. The obtained standard deviation using the SA algorithm is an improvement of 19% over the IM approach after about 7000 iterations. However, the tradeoff is that the SA algorithm requires approximately twice the computing time than the simpler IM method.

ATTENTION: The Singapore Copyright Act applies to the use of this document. Nanyang Technological University Library

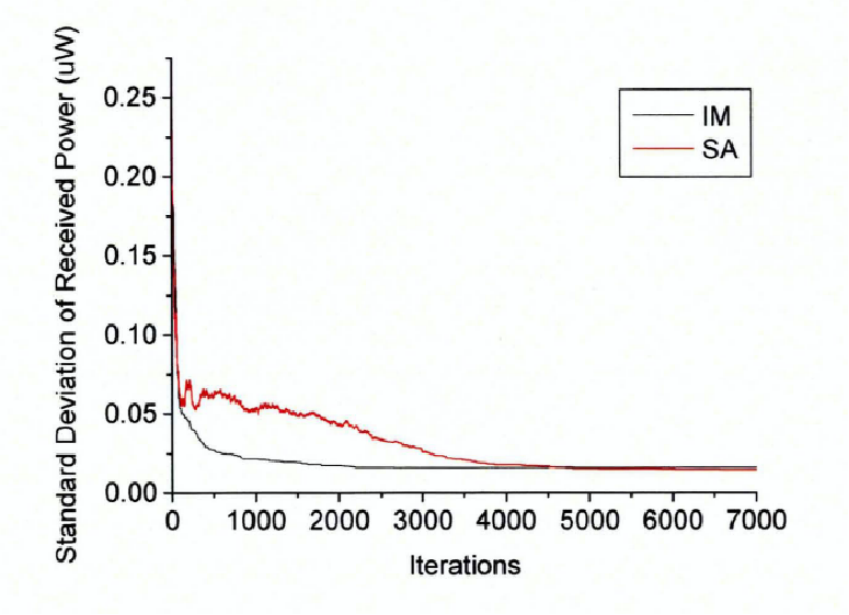
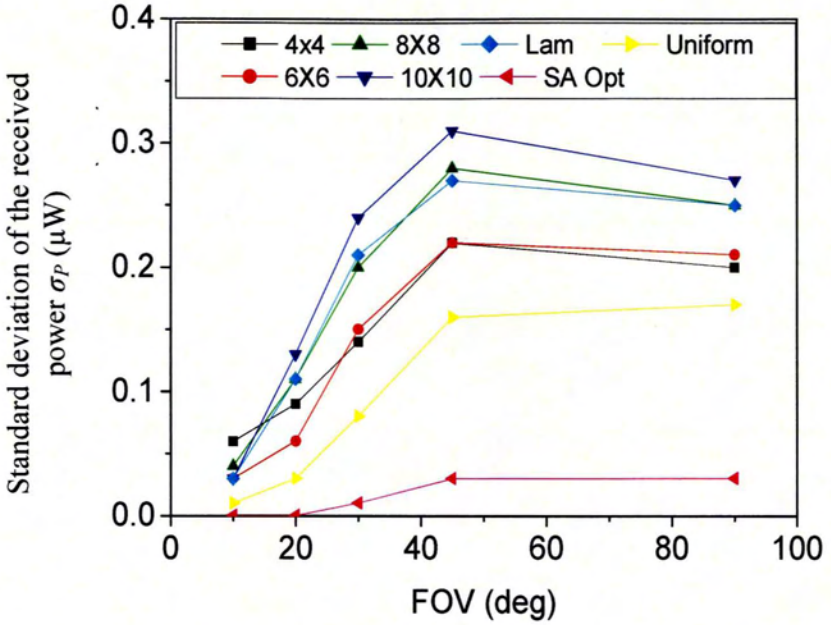


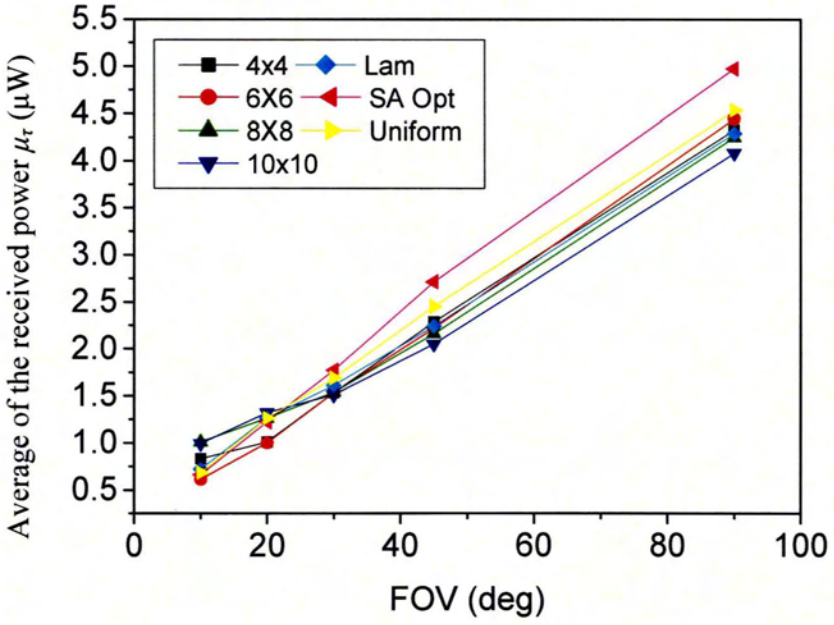
Figure 3.11 Comparison of results using iterative minimization (IM) and simulated annealing (SA).

To determine the minimum standard σ_P that can be achieved using the SA method, five runs were conducted using the various FOV values that were described in the earlier sections to obtain the specific pattern that gives the minimum σ_P for each value of the receiver FOV. A comparison is made between the graphs of the conventional grid designs and the optimized results in Figure 3.12, and the accompanying spot patterns are shown in Figure 3.13. Using the SA technique, a reduction of the σ_P by a factor of 7 can be achieved. It can be generally observed that this is achieved by having a higher spot density at the edges and corners rather than at the centre. However, the tradeoff is a slightly higher μ_t than the conventional designs which is more apparent at the larger FOVs for 45° and 90°. At 30° FOV, the SA obtained pattern is still able to achieve a delay spread of 1.77ns, less than the benchmark of 1.85ns, still achieving a 93% reduction in the σ_P below that of the conventional grid designs, and 87.5% reduction over the uniform illumination pattern.

ATTENTION: The Singapore Copyright Act applies to the use of this document. Nanyang Technological University Library



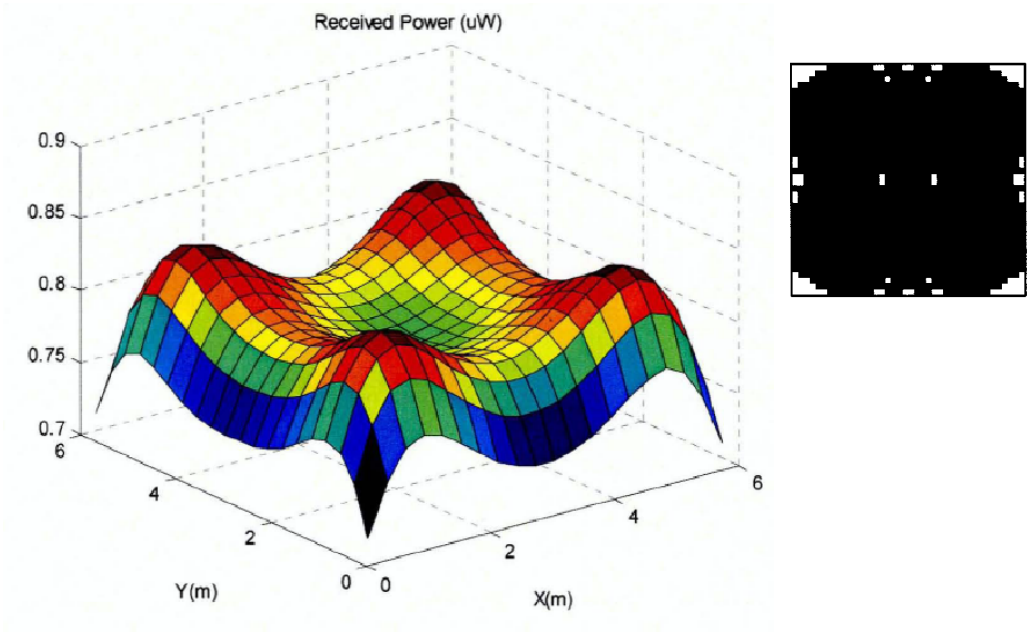
(a)



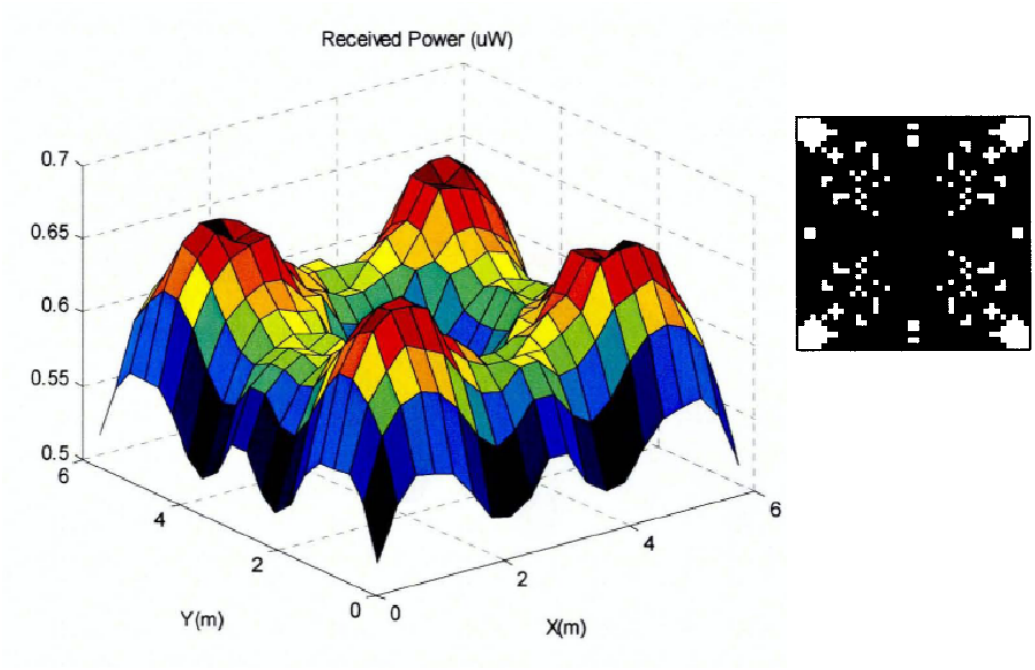
(b)

Figure 3.12 Comparison of results using simulated annealing and conventional grid designs for (a) Standard deviation of received power and (b) average RMS delay spread performance.

ATTENTION: The Singapore Copyright Act applies to the use of this document. Nanyang Technological University Library

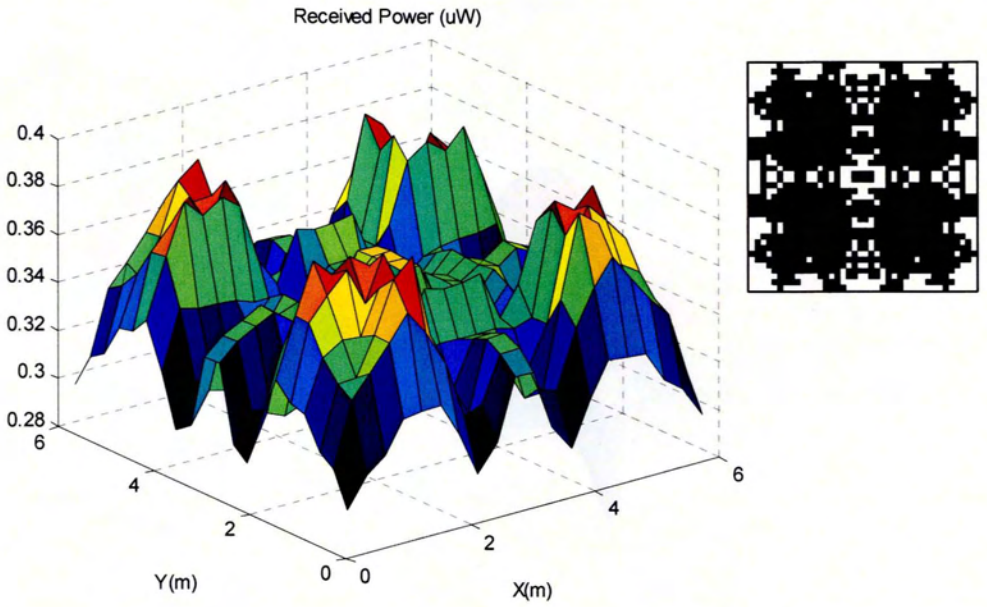


(a)

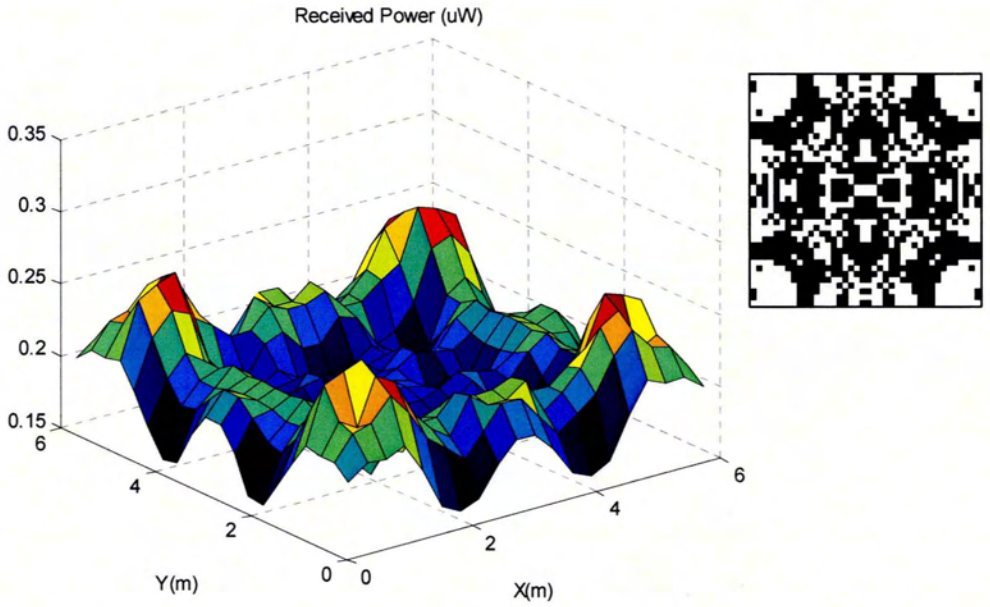


(b)

ATTENTION: The Singapore Copyright Act applies to the use of this document. Nanyang Technological University Library

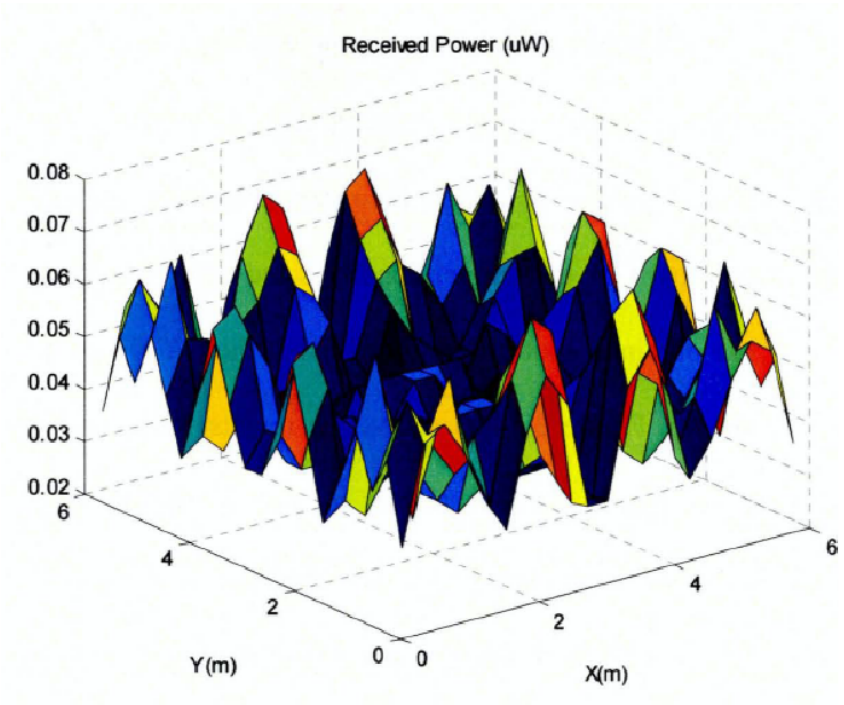


(c)



(d)

ATTENTION: The Singapore Copyright Act applies to the use of this document. Nanyang Technological University Library



(e)

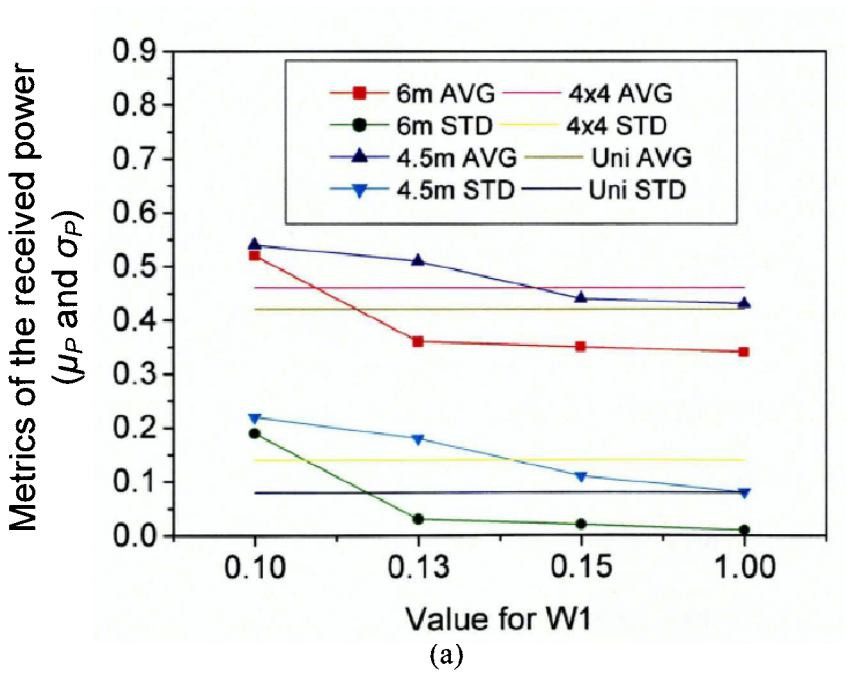
Figure 3.13 SA Optimized spot patterns and signal power distribution for FOV of (a) 90°, (b) 45°, (c) 30°, (d) 20° and (e) 10°.

3.4.3 Optimization of spot patterns at a field of view of 30°

In the previous subsection, when the SA algorithm was set to run to minimize the σ_P only, the corresponding μ_t was found to still be below the benchmark of 1.85ns. To determine the tradeoff between σ_P and μ_t at the 30° receiver FOV, another round of optimization was performed. Instead of optimizing for only one parameter, a merit function was assigned to the SA algorithm to take into account the optimization of μ_t (W2) as well as σ_P (W1). With a normalized total weight of 1.0, various combinations of weights for the two parameters can be run to obtain the spot patterns. The optimization was also performed for two sizes of the overall extent of the spot pattern. For the first size, the spot pattern was allowed to cover the entire ceiling surface and for the second spot size, the extent of the pattern was limited to only a 4.5m x 4.5m

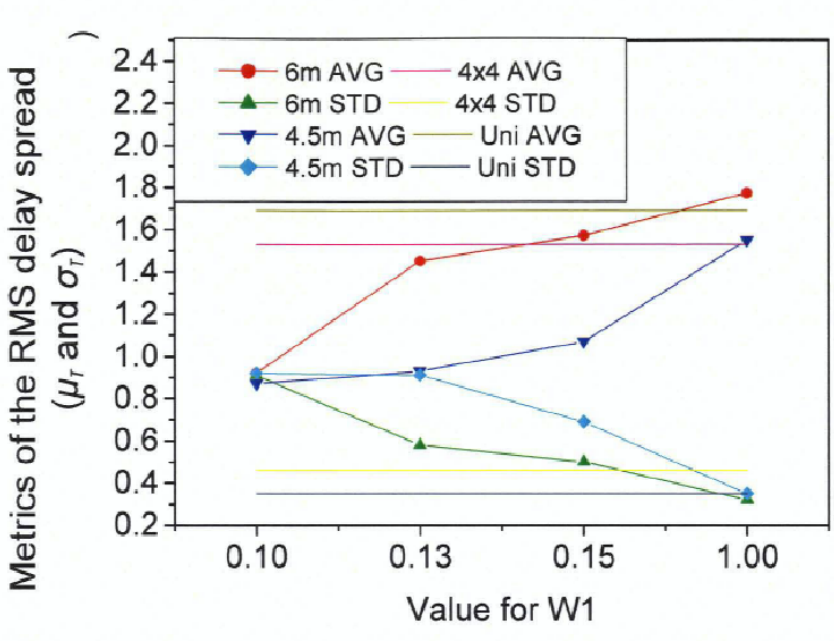
ATTENTION: The Singapore Copyright Act applies to the use of this document. Nanyang Technological University Library

extent, which is 56.25% of the total ceiling surface area. The 6m extent simulates an ideal condition in which the hologram pattern matches the size of the ceiling, while the 4.5m extent spot pattern is used to simulate a hologram projection and ceiling size mismatch, as well as the extent of the conventionally sized grid holograms shown earlier. In Figure 3.15, the obtained spot distributions using the SA algorithm for the various conditions are shown. Figure 3.14(a) shows the results for μ_P and σ_P on the same graph, and likewise, Figure 3.14(b) shows μ_τ and σ_t. In the graphs, the normalized weight for μ_t is the complement of the described power standard deviation weight i.e. W1 + W2 = 1. Results from the 4x4 and uniform spot patterns have also been included in the graphs to serve as a basis of comparison. These were chosen as comparison as the 4x4 pattern has the lowest variation of the grid patterns surveyed, while the uniform pattern as the lowest variation of all the patterns in Table 3.3.



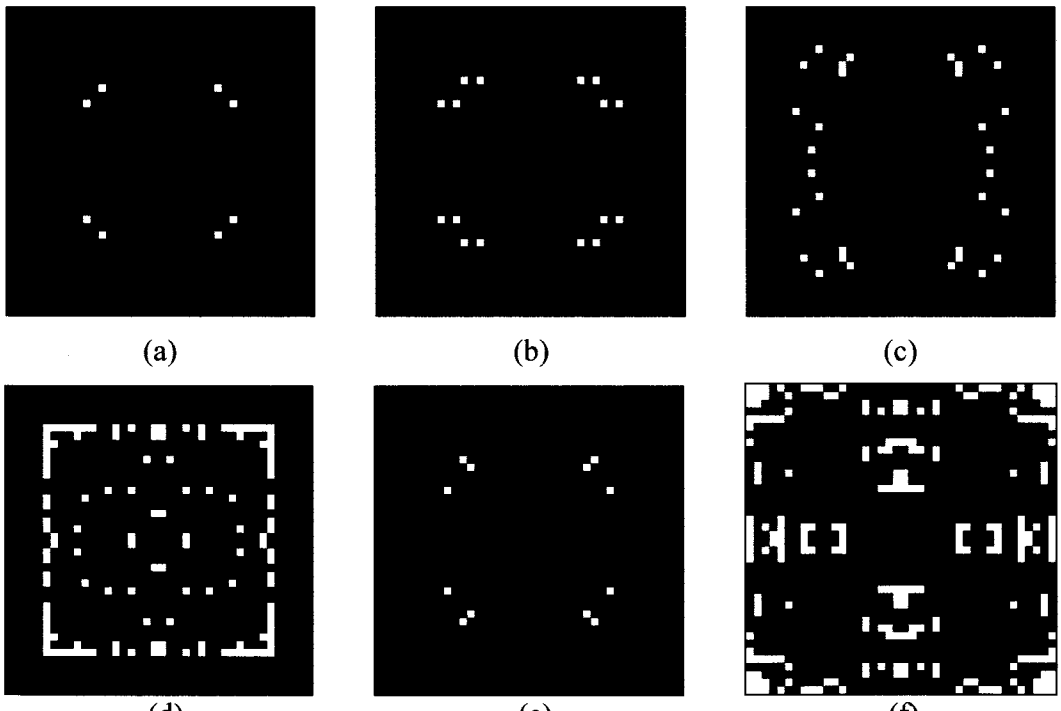
(a)

ATTENTION: The Singapore Copyright Act applies to the use of this document. Nanyang Technological University Library



(b)

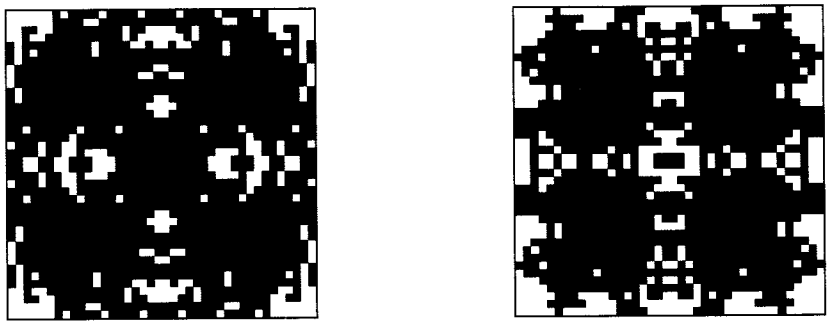
Figure 3.14 Performance metrics of the obtained results for (a) received power and (b) RMS delay spread.



(a) (b) (c)

(d) (e) (f)

ATTENTION: The Singapore Copyright Act applies to the use of this document. Nanyang Technological University Library



(g) (h)

Figure 3.15 Obtained spot patterns using SA algorithm:

(a) W1=0.1, 4.5m; (b) W1=0.13, 4.5m; (c) W1=0.15, 4.5m,

(d) W1=1.00, 4.5m; (e) W1=0.1, 6m; (f) W1=0.13, 6m; (g) W1=0.15,

6m and (h) W1=1.00, 6m.

As W1 which is the weight for σ_P is increased, μ_P and σ_P drop while μ_t increases. This is because a larger weight is placed on the SA algorithm in optimizing σ_P over the μ_t, resulting in a tradeoff. By optimizing for a more uniform power distribution via emphasis on W1, the RMS delay spread is adversely affected since a greater number of multipath signals reach the detector and this is evident from the graphs. The drop in σ_t with the increase in W1 also shows that a more consistent delay spread performance is achieved, although this comes at the cost of increased average delay spread as mentioned earlier. When the system is optimized for a higher value of W2, a delay spread of less than 1ns is obtained. However, the high σ_t relative to the low average RMS delay spread implies a large variation in the actual delay spread values, which may be undesirable. It is also observed from the graphs that the extent of the size of the spot pattern affects the obtained results. When the spot pattern is limited to an area of 4.5m x 4.5m, there is a drop in the metrics for the received power by a factor of at least 2.5 as compared to the larger spot pattern. Although the smaller pattern is also

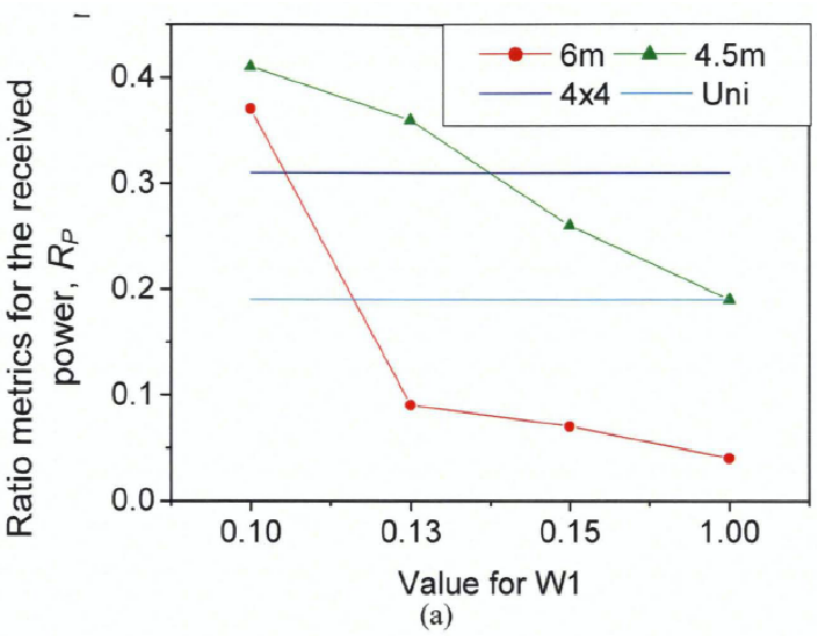
ATTENTION: The Singapore Copyright Act applies to the use of this document. Nanyang Technological University Library

able to achieve a better delay spread performance, the relatively higher σ_t also indicates a larger variation in the delay spread performance.

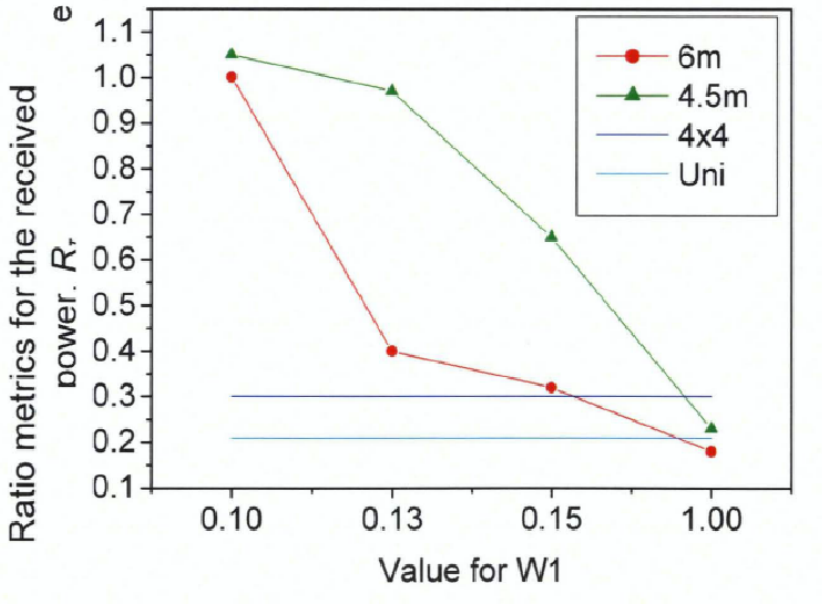
The performance of the various spot patterns obtained via the SA technique should be analyzed both in terms of the absolute metric values as well as the relative ratios of the standard deviation over the average. Although a low standard deviation of either the delay spread or received power is certainly desirable, a low average of that metric compared to the standard deviation implies an inconsistent system performance and therefore the ratio should also be considered in evaluating the performance of the spot patterns. R_P is defined as σ_P over μ_P, and R_t is defined as σ_t over μ_t, and the graphs are shown in Figure 3.16. For the 4.5m x 4.5m sized spot pattern the spot pattern obtained that optimized only σ_P gives the best performance of the other results in terms of the ratio i.e. the consistency of the performance of the system. When compared to the 4x4 spot pattern, it is interesting to note that the absolute results are 6.5% more and 1.3% more for the μ_P and μ_t respectively, use of the SA algorithm has reduced the R_P and R_t by a factor 39% and 23% respectively. Furthermore, in comparison with the results from the uniform signal power distribution, it is observed that the performance is similar with respect to both absolute and relative values. However, while the uniform pattern required illumination of the entire ceiling, the 4.5m x 4.5m pattern only required illumination of 56.25% of the room ceiling. For the 6m x 6m sized pattern, a value of 0.15 for W1 reduces R_P by more than 78% as compared to the 4x4 pattern, while still maintaining a comparable absolute and relative RMS delay spread performance. The higher uniformity of the signal power results is due to the larger extent of the spot distribution, and it can be observed that the optimized spot patterns have a high concentration of spots at the corner to compensate for the lower corner power. The

ATTENTION: The Singapore Copyright Act applies to the use of this document. Nanyang Technological University Library

resulting intensity distribution for the 4.5m extent pattern with W1=1, and the 6m pattern with W1 = 0.85 are shown in Figure 3.17. In comparing the optimized pattern for the 6m extent with the uniform illumination pattern, it is observed when W1 = 1, R_P and R_t are less than that of uniform illumination pattern by 79% and 14% respectively, with the tradeoff being a 4.7% increase in the average delay spread.



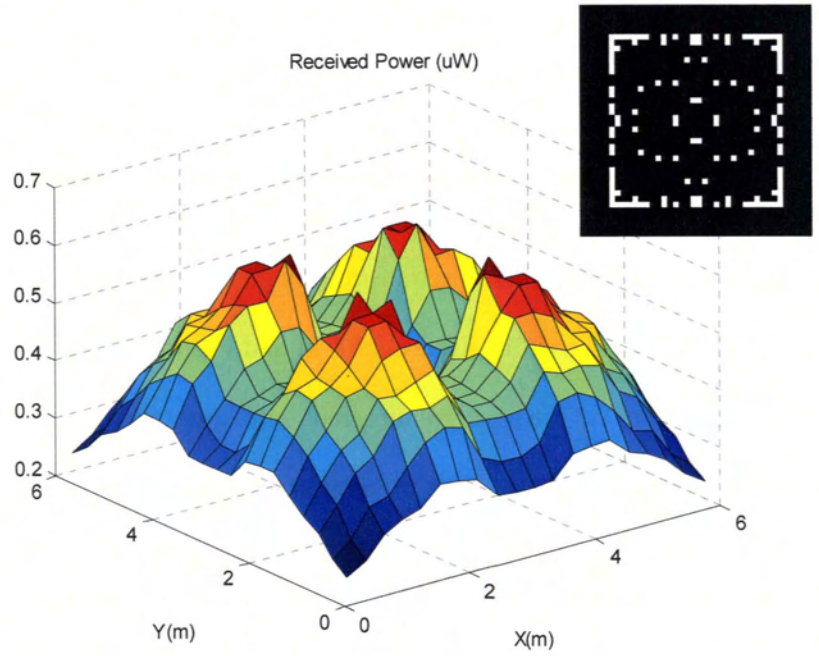
(a)



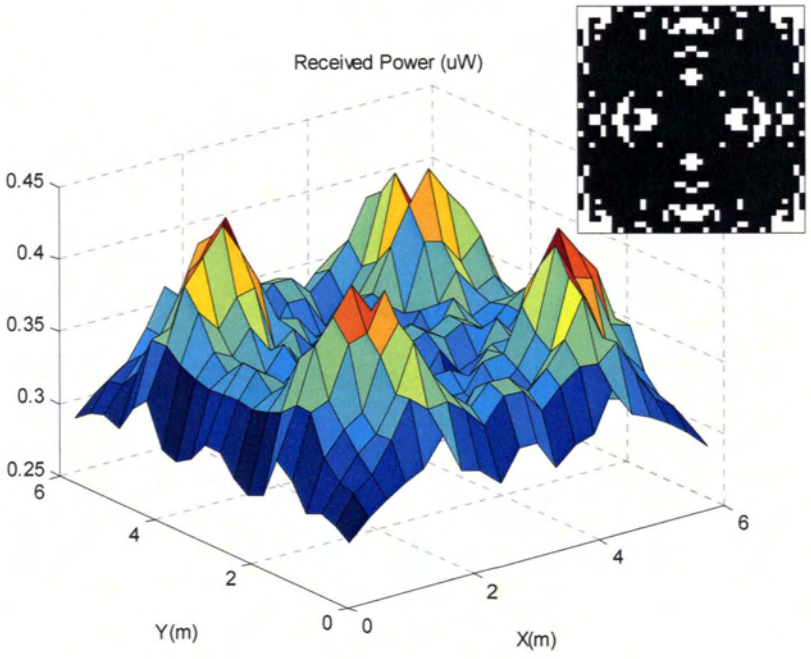
(b)

Figure 3.16 Relative values of the obtained metrics for (a) received power and (b) RMS delay spread.

ATTENTION: The Singapore Copyright Act applies to the use of this document. Nanyang Technological University Library



(a)



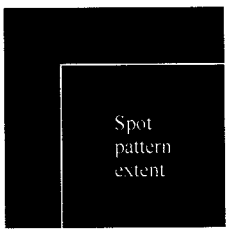
(b)

Figure 3.17 Spot patterns and signal power distribution maps for (a) W1 = 1.00, 4.5m extent and (b) W1 = 0.15, 6m.

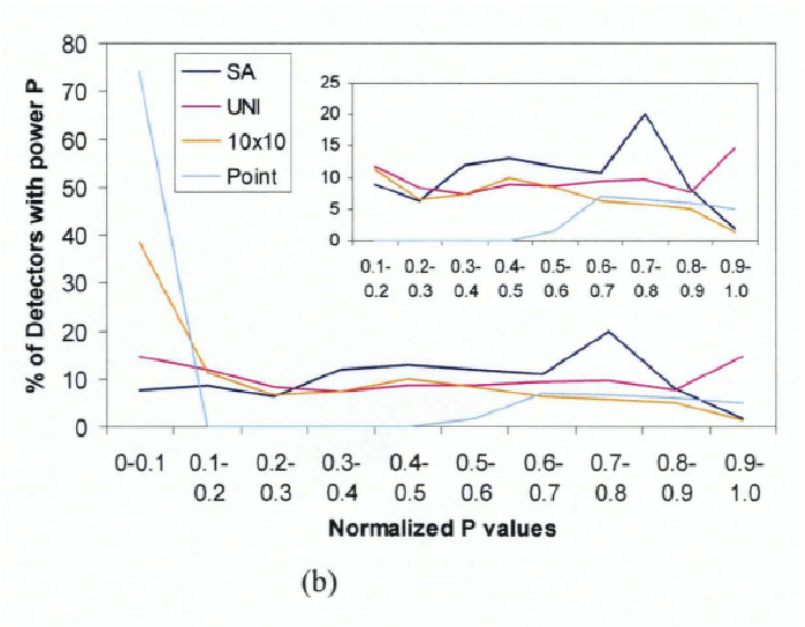
ATTENTION: The Singapore Copyright Act applies to the use of this document. Nanyang Technological University Library

3.4.4 Analysis when spot pattern is not centered on the ceiling

In the prior analysis, it was always assumed that the spot patterns are located at the centre of the ceiling. However, this may not always be the case, as the transmitter could be located in any location in a mobile transceiver. To analyse the performance of the transmitting patterns when not centred at the room ceiling, two scenarios are considered, in which the transmitting patterns are diagonally offset 1.5m and 3m respectively, as shown in Figure 3.18(a) and Figure 3.18(c). To simplify the analysis, the segments of the pattern directed onto the surrounding walls are not considered. The SA pattern for W1=1, the uniform pattern, a 10x10 grid and a single spot were shifted, and the results are shown in Figure 3.18(b) and Figure 3.18(d).

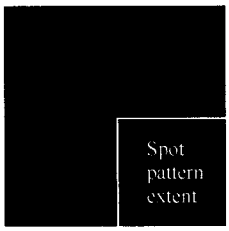


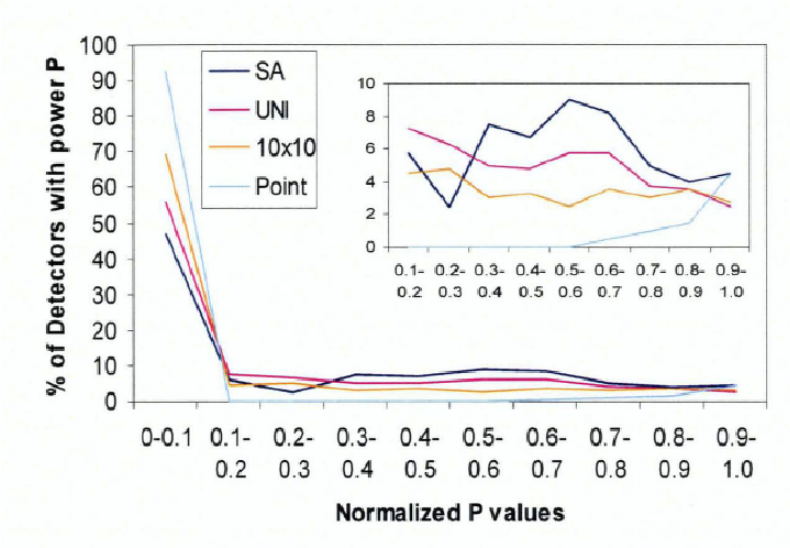
(a)



(b)

ATTENTION: The Singapore Copyright Act applies to the use of this document. Nanyang Technological University Library





(c) (d)

Figure 3.18(a) Extent of pattern when offset 1.5m from centre and (b) corresponding power distribution; (c) extent of pattern when offset 3m from centre and (d) corresponding power distribution.

Figure 3.18(b) and Figure 3.18(d) show the percentage of detector locations that received a normalized power within the range on the horizontal axis. The single Point pattern results in a poor distribution of power, with more than 70% of the locations for both scenarios receiving only 0.1 of the normalized power P. The SA-obtained pattern resulted in the best spatial distribution of the various patterns studied. In both situations, SA had the lowest percentage of points with normalized power less than 0.1. At normalized powers beyond 0.3, SA has a higher percentage than the various other patterns for most of the ranges. For the 1.5m offset, the SA pattern resulted in a 11.75% improvement in the number of locations which received a higher normalized power beyond 0.3. For the 3m offset, the improvement was even better with 14% of the locations having a normalized power of 0.3 or more. The better spatial distribution of the power is due to the higher spot density at the corners of the SA pattern as can be seen in Figure 3.15(c). When the pattern is offset to the corner,

ATTENTION: The Singapore Copyright Act applies to the use of this document. Nanyang Technological University Library

this translates into a higher concentration of spots in the centre which results in a better spatial distribution.

3.4.5 Comparison with other works

A summary of the relevant results from recent works by other researchers is presented in Table 3.4, together with the results obtained from the work in the Chapter. Together with the multipath dispersion, the ratio of the maximum power to the minimum power in decibels as reported in the referenced research is also included. Although this metric was not specifically used in the merit function of the optimization process, it provides a simple and convenient means of comparison against other works.

As can be observed from the Table, the optimized results for the 6m extent pattern with W1=1 is better than the results from Jivkova and Kavehrad [9] and Al-Ghamdi and Elmirghani [74], achieving a lower max-min ratio and multipath delay when compared to the both of these results. Furthermore, although the achieved delay spread is higher than that obtained by Yang and Lu [86], the tradeoff is that their max-min ratio was more than 9dB higher than that of the optimized results. Hence, although the delay spread results were not the least, a good balance between the uniformity of signal distribution and delay spread has been achieved by the optimized spot pattern.

ATTENTION: The Singapore Copyright Act applies to the use of this document. Nanyang Technological University Library

Table 3.4 Comparison of obtained results with other works

Research	Recommended configuration	Max to Min Power ratio (dB)	Maximum Delay Spread (ns)
Jivkova and Kavehrad [9]	10x10 grid	3dB	2.5ns
Al-Ghamdi and Elmirghani [74]	LSMS	4.3dB	2.25ns
Yang and Lu [86]	16 sources	11dB	0.6ns
Work presented in Thesis	SA Optimized (W1=0.15, 6m)	1.76dB	1.85ns

3.4.6 Conclusion

To optimize the transmitter spot pattern, a simulated annealing technique was utilized. Although the simulated annealing technique takes up to twice that of the time required as compared to the simple iterative minimization technique, the obtained performance can be up to 20% better. Using the field of view of 30° determined from the previous section, the transmitter spot pattern was optimized, first for the standard deviation of the received power only, and later using a merit function to also take the delay spread performance into consideration. Comparing against the performance of a conventional 4x4 spot pattern whose performance is close to that of other patterns at the 30° field of view, it was found that the optimization produced results that gave an improvement close to 80% for the 6m extent spot pattern.

ATTENTION: The Singapore Copyright Act applies to the use of this document. Nanyang Technological University Library

3.5 System Performance

3.5.1 Introduction

In the previous two sections, optimum design parameters for the transmitter and the receiver were obtained. The basis of the optimization was based on optical performance characteristics such as uniformity of the signal power distribution and the delay spread. The parameters could be further analyzed by incorporation into an optical communications model to obtain metrics such as the bit error rate and the signal to noise ratio. In wireless communications, it is common to use diversity techniques to try to improve the system performance. By understanding the limitation of the system when only one receiver is used, diversity techniques can be proposed to further improve the system performance.

Methodology

The system communications performance will first be obtained using a communications model to find the signal to noise and bit error rate performance. Using a single receiver as a baseline for the analysis, diversity techniques will be later introduced to improve the system to meet performance specifications.

3.5.2 Communication model

The communications model used is an Intensity Modulated Direct Detection (IM/DD) setup. The transmitter, which is a laser source, is directly modulated by the information that is to be transmitted. A binary modulation scheme is considered, where the transmitted signal is either in the OFF or ON mode, representing two possible intensity levels. The signals are transmitted and propagated through the

ATTENTION: The Singapore Copyright Act applies to the use of this document. Nanyang Technological University Library

system, and the resulting response can be found by convolving the impulse response of the system with the message signal.

At the receiver, the signal is detected and converted into current by multiplying the signal with the quantum efficiency of the detector. At the same time, noise is introduced into the system and can comprise of ambient noise, shot noise and thermal noise. The received signal is passed into a decision making block which makes a decision on what the received signal is perceived to be. A block diagram of the communications model can be seen in Figure 3.19.

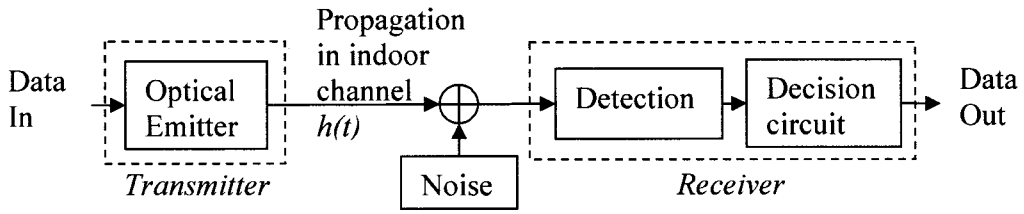


Figure 3.19 Block diagram of communications model.

3.5.3 Noise

At the receiver, the transmitted signal is detected. At the same time, noise is introduced into the receiver blocks which can consist of shot noise and Johnson, also known as thermal noise [96, 97]. These serve to deteriorate the signal quality by reducing the signal to noise ratio and resulting in a poorer received signal. Shot noise and thermal noise are the two major contributors of noise for photoreceivers used in communications systems, and the following discussion is limited to these two contributions.

ATTENTION: The Singapore Copyright Act applies to the use of this document. Nanyang Technological University Library

Shot Noise

Shot noise, also known as quantum noise, is due to the random nature of the electric current, and leads to current fluctuations in the detected signal, even in the presence of a constant, stable source. The noise can be considered to be 'white', i.e. constant spectral density. As such, the noise can be quantified with Gaussian statistics and a commonly used measure of noise is the noise variance σ^2_s, which is defined as follows[98] :

$$\sigma_s^{\,2} = 2qI_R B \tag{3.9}$$

where q represents the charge of an electron, B is the noise bandwidth of the detector and I_R is the photocurrent. I_R itself can be decomposed into the sum of three components

$$I_R = I_S + I_{BG} + I_D \tag{3.10}$$

where I_S is the received signal current, I_{BG} is the current due to ambient noise, and I_D is the dark current. In most cases the dark current is trivial compared to the contribution due to the signal current and the ambient noise current, and thus this would be taken as negligible for the rest of the analysis.

Johnson Noise

Johnson noise, also known as thermal noise, arises due to the random motion of electrons in a conductor, causing a current fluctuation, and affected by the electrical components particularly resistors, in a photodetection circuit. Johnson noise is 'white' up to about 1 THz, and can be modeled as a stationery Gaussian process with noise variance σ_T^2 given by [98]

$$\sigma_T^2 = \frac{4k_B T}{R_L} B \tag{3.11}$$

ATTENTION: The Singapore Copyright Act applies to the use of this document. Nanyang Technological University Library

where k_B is the Boltzmann constant, T is the operating temperature in Kelvins, B is the receiver noise bandwidth, and R_L is the load resistor. However, the impact of the increase in the R_L is a drop in the bandwidth of the receiver due to an increase in the RC time constant. A popular compromise is to use trans-impedance preamplifiers which, while having a large input resistance to reduce the thermal noise, is able to provide a higher bandwidth than using low-impedance loads[99].

3.5.4 Bit error rate analysis

For a digital receiver, the performance is determined by the bit error rate (BER), which gives the probability of the decision circuit in the receiver identifying the wrong bit. The errors come about as a result of the various noise forms introduced in Section 3.4.3, resulting in a wrong decision made by the decision circuit. For a binary OOK transmission, each bit has the same probability of being transmitted. Thus, there is a 50% or a 0.5 probability that each bit would be transmitted. The error probability P_B for the communication model can be therefore determined by the conditional error probability of detecting a '1' bit when a '0' bit is transmitted, *P(1/0)* and the probability of detecting a '0' bit when a '1' bit is transmitted, *P(0/1)* :

$$P_B = P(0) \bullet P(1/0) + P(1) \bullet P(0/1) \tag{3.12}$$

or

$$P_B = 0.5\left[P(1/0) + P(0/1)\right] \tag{3.13}$$

ATTENTION: The Singapore Copyright Act applies to the use of this document. Nanyang Technological University Library

due to the unbiased data equal probability that a '1' or a '0' bit would be transmitted. The conditional error probability can be determined by first considering noise as an independent Gaussian random variable [99, 100] with zero mean and variance σ^2, as defined earlier, and with probability density function

$$p(n) = \frac{1}{\sigma\sqrt{2\pi}} \exp\left[-\frac{1}{2}\left(\frac{n^2}{\sigma^2}\right)\right] \tag{3.14}$$

First consider the case when a '1' is detected but a '0' is transmitted. The statistic into the decision circuit, I, is a Gaussian random variable with mean I_0 and variance σ_0^2, defined as the sum of the thermal and quantum noise for the '0' state

$$\sigma_0^{\,2} = \sigma_{t,0}^{\,2} + \sigma_{s,0}^{\,2} \tag{3.15}$$

Defining the decision threshold as γ_0, where a '1' is decided if $I > \gamma_0$, and '0' if $I < \gamma_0$, the error of probability of wrong detection can thus be found by integrating Equation (3.14) from γ_0 to infinity, and in a similar manner for when '0' is detected when '1' is transmitted

$$P(1/0) = \frac{1}{\sigma_0\sqrt{2\pi}} \int_{\gamma_0}^{\infty} \exp\left[-\frac{1}{2}\frac{(I-I_0)^2}{\sigma_0^{\,2}}\right] dI \tag{3.16}$$

$$P(0/1) = \frac{1}{\sigma_1\sqrt{2\pi}} \int_{-\infty}^{\gamma_0} \exp\left[-\frac{1}{2}\frac{(I-I_1)^2}{\sigma_1^{\,2}}\right] dI \tag{3.17}$$

ATTENTION: The Singapore Copyright Act applies to the use of this document. Nanyang Technological University Library

Defining Q as $Q(x) = \frac{1}{\sqrt{2\pi}} \int_x^\infty \exp\left[-\frac{y^2}{2}\right] dy$, Equations (3.16) and (3.17) can be re-expressed as

$$P(1/0) = Q\left(\frac{\gamma_0 - I_0}{\sigma_0}\right) \tag{3.18}$$

$$P(0/1) = Q\left(\frac{I_1 - \gamma_0}{\sigma_1}\right) \tag{3.19}$$

Using the optimum decision threshold rule [97] gives the threshold photocurrent below

$$\gamma_0 = \frac{\sigma_0 I_1 + \sigma_1 I_0}{\sigma_0 + \sigma_1} \tag{3.20}$$

Using Equation (3.18), (3.19) and (3.29), it can be shown that P(1/0) = P(0/1). Thus, the BER is reduced to

$$P_B = Q\left(\frac{I_1 - I_0}{\sigma_1 + \sigma_0}\right) \tag{3.21}$$

3.5.5 System Parameters

Using the power distribution results from Figure 3.14(b), the BER performance of the system was simulated. To avoid the need for equalization due to multipath, the transmission bitrate was chosen to be 54 MBit/s, which is the value corresponding to $1/(10 \times \sigma_\tau)$, as shown in Section 3.2.4.2. Receiver bandwidth for the system digital signal was set to 0.75 of the bitrate to minimize noise [101]. However, the tradeoff is that only 93.6% of the signal power would be captured as a result. The

ATTENTION: The Singapore Copyright Act applies to the use of this document. Nanyang Technological University Library

load resistance was taken to be 200Ω. The simulation values used, including universal constants, are presented in Table 3.5. The responsivity and load resistance was set at 0.9 A/W and 200 Ohm based on typical values. To determine the signal current, the received power at the detector was multiplied by the detector responsivity. The total emitted source power remains at 1W.

Table 3.5 Receiver Model Parameters

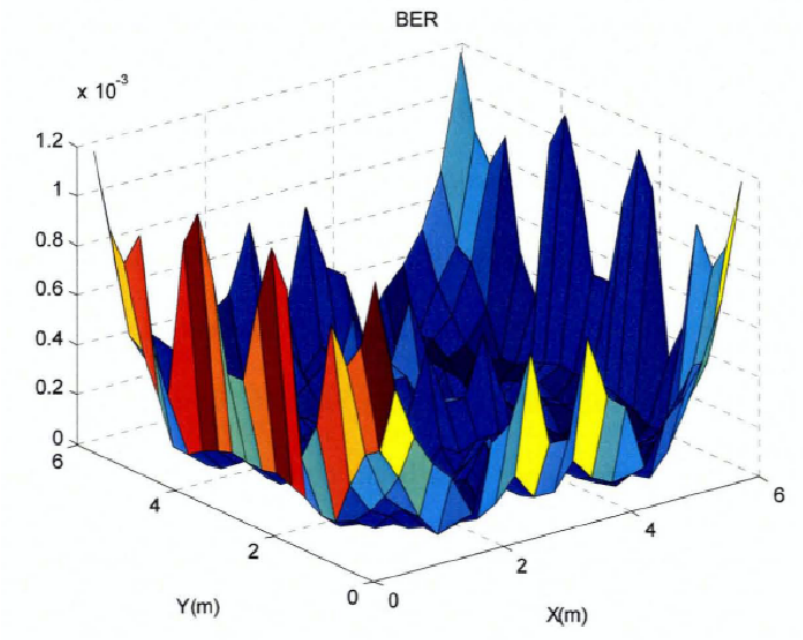
Parameter	**Value**
Responsivity, R	0.9 A/W
Bitrate, R_b	54Mbit/s
Bandwidth, B	$0.75*R_b$ Hz
Boltzmann's Constant, k_B	1.38×10^{-23} J/K
Electron Charge, q	1.6×10^{-19} C
Temperature, T	293K
Load Resistance, R_L	200Ω

3.5.6 Simulation results

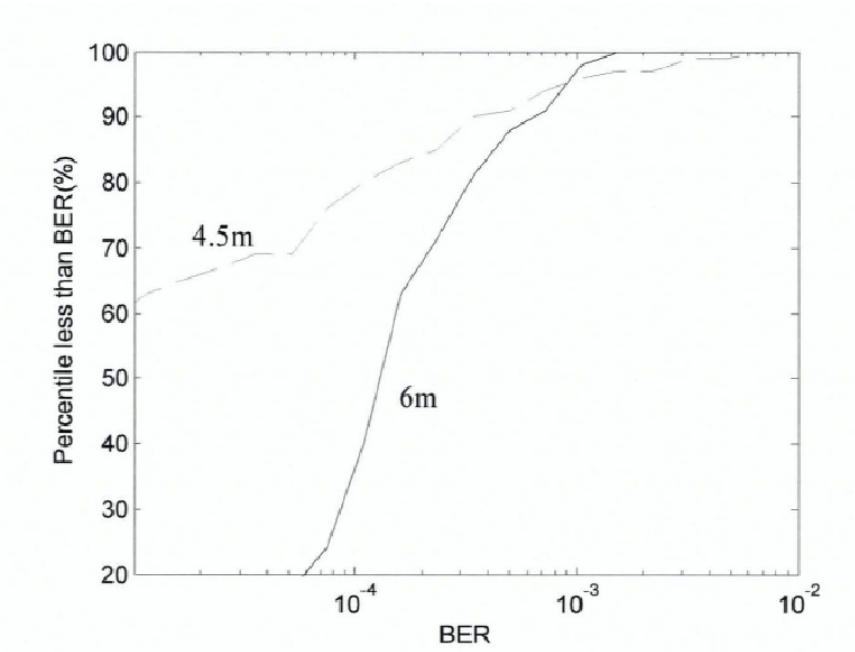
The parameters in Table 3.4 were used in the model to obtain the BER of the indoor optical channel, as defined from Equations (3.11), (3.19) and (3.21). The modulation type used is a Non Return to Zero On Off Keying method such that the transmitter is ON when a '1' is transmitted, and OFF when a '0' is transmitted. At the detector, the received power P_{state} is converted to photocurrent by multiplying with the detector responsivity, which is taken as $R = 0.9$.

ATTENTION: The Singapore Copyright Act applies to the use of this document. Nanyang Technological University Library

In Figure 3.20 (a), the BER is plotted as a function of the receiving plane. The higher BER values are found near the walls and the corners, corresponding to the lower power at these positions as can be seen from Figure 3.15. In general the central areas can be observed to have a relatively uniform BER performance.



(a)



(b)

Figure 3.20 (a) BER performance for a 6m extent hologram and (b) cumulative function for BER performance for 4.5m and 6m holograms.

ATTENTION: The Singapore Copyright Act applies to the use of this document. Nanyang Technological University Library

From Figure 3.20(b), the cumulative distribution of the locations corresponding to the BER values are shown for about the 6m case where W1= 0.85, and the 4.5m scenario where W1 = 1. The plot shows that the case where the 6m hologram is used has a better control over the BER, with 80% having a BER of not more than 2.5 x 10^{-4}, and 100% having a BER of 10^{-3} or less. When the 4.5m extent hologram is used, there is a greater spread as evidenced from the plot which has a larger BER performance range. From another perspective, it can also be inferred that the 6m spot pattern produces more predictable results than the 4.5m spot pattern, due to the wider spread of the diffuse spots achieved. However, it can be observed that 95% of the locations are still able to obtain a BER of 10^{-3} or less. It should also be noted that the BER performance has been obtained based on baseband OOK modulation, entirely without any form of error coding or higher order modulation. One of the major sources of the signal degradation is the thermal noise contribution. This can be reduced by optimizing the transimpedance amplifier together with the photodetector. Elmirghani et al [102] showed that the thermal noise for a 70MHz bandwidth PIN-BJT circuit could be reduced to 2.7pA/$\sqrt{}$Hz. Using such an optimized circuit could reduce the thermal noise by about 20dB, resulting in large improvement in the BER.

3.5.7 Improving BER performance through diversity combining techniques

A commonly used approach to improve the performance of a communications system is to make use of diversity combining techniques through the use of more than one receiver [103]. Each detector receives a separate copy of the transmitted signal, whereupon it is processed in various schemes. The simplest scheme is known as a Pure Selection (PS) scheme, where the copies from the different receiver branches are

ATTENTION: The Singapore Copyright Act applies to the use of this document. Nanyang Technological University Library

compared against another and the receiver with the best SNR is used. Although simple to implement, needing only a comparator, the scheme only makes use of one copy and discards the others.

A better but more complicated combining scheme is known as Maximal Ratio Combining (MRC). In this scheme, the signal from each *i*-th branch is weighted with a value w_i equal to the received signal to noise ratio at that branch. This maximizes the SNR of branches with a good signal, while minimizing the impact of branches with poor SNR. The SNR using such a scheme can be found to be given by [63]

$$SNR_{MRC} = \sum_{i}^{J} w_i \frac{(I_1 - I_0)_i^2}{(\sigma_0 + \sigma_1)_i^2} \tag{3.22}$$

where J is the total number of diversity branches, also known as the diversity order, and $(I_1 - I_0)_i^2$ and $(\sigma_0 + \sigma_1)_i^2$ are the signal and noise values at the *i*-th branch. Equation (3.22) can be seen as the sum of the SNR received at the different branches.

$$SNR_{MRC} = \sum_{i}^{J} SNR_i \tag{3.23}$$

If the SNR at each branch is taken as an average output SNR, a good approximation to the SNR as a result of the MRC can be found by

$$SNR_{MRC} = J \times SNR_{mean} \tag{3.24}$$

Using a diversity order of 3, the improvement in the bit error rate resulting from the improvement in the SNR is shown in Figure 3.19. Use of a diversity order of three

ATTENTION: The Singapore Copyright Act applies to the use of this document. Nanyang Technological University Library

leads to an improvement in the BER, resulting in a maximum BER value of 10^{-7} for a 54Mbit/s transmission. Another simulation was run using the same parameters but at a transmission bit rate of 155Mbit/s. This is somewhat higher than the value for no multipath dispersion effect. However, the effect is moderate due to the low RMS delay spread and equalizers can be used to reduce the effect of multipath dispersion. When no diversity is used, the BER performance of the signal has a maximum of 0.0391 with an average of about 0.0155. However, use of a MRC diversity combination scheme improves the channel performance by a large margin and results in a BER plot that is similar to 54Mbit/s with no diversity. The maximum BER is about 10^{-3}, with an average of about 10^{-4}. Use of more diversity branches would further improve the SNR. For example, from Figure 3.21, when a diversity order of five is used the BER can be seen to improve. However, this would be at the expense of increased complexity in the receiving circuit, in particular in co-phasing and aligning the received signals.

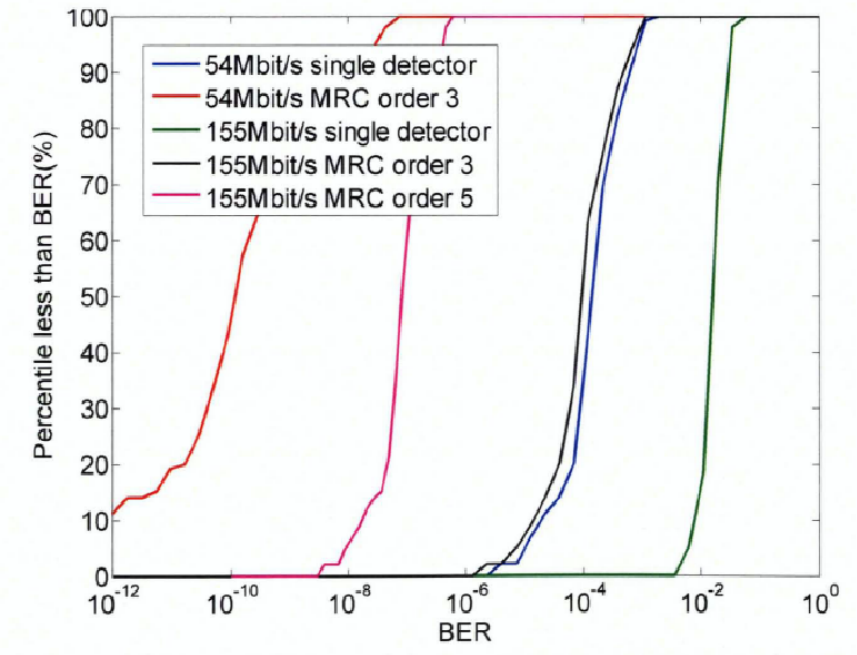


Figure 3.21 BER performance for bit rates of 54Mbit/s and 155Mbit/s with and without using a MRC combination scheme of order 3 and 5.

ATTENTION: The Singapore Copyright Act applies to the use of this document. Nanyang Technological University Library

3.5.8 A brief introduction to equalization

Equalizers are often used in receivers to combat multipath dispersion. Although the work presented in the Chapter avoided multipath dispersion by setting the delay spread as a control parameter and setting a conservative transmission bitrate such that no multipath dispersion effects would be experienced, in implementation wireless receivers employ some form of equalization[8, 104]. Although equalizers are not within the scope of the Thesis and will not be modeled, for the sake of completeness, a brief overview of equalization is described in the following

In essence, the objective of an equalizer is to remove channel effects from the received signal[34, 103, 105], primarily multipath dispersion which leads to intersymbol interference. Equalizers act as inverse filters, such that the product of the multipath channel and the equalizer produces a desired transfer function, for example a completely flat transfer function. In this manner, the effects of multipath can be removed. Practically, a realizable filter should have a rational transfer function that can be implemented. In digital communications, linear traversal filters, also known as Finite Impulse Response filters, are used as linear equalizers due to their stability. Such filters usually consist of a number of delay lines, known as taps, each with a weighting value w. The received signal is sampled at the sampling frequency, usually the symbol period T, to produce the discrete samples [y_k, y_{k-T}, $y_{k-2T...}$]. The length of the FIR filter and the number of taps is usually determined by the expected multipath response and the degree of ISI suppression required [106]. For a short symbol with severe ISI, the number of taps required can be quite large. As the channel response may not be stationary, particularly for mobile devices, the filter weights are often adaptive[107, 108]. Typically during the transmission of a message, a known training message precedes the actual data to be sent. The equalizer compares the transmitted

ATTENTION: The Singapore Copyright Act applies to the use of this document. Nanyang Technological University Library

training message with the pre-stored training message to determine the multipath channel response, and determines the updated weights using an adaptive algorithm. Zero forcing (ZF) and Minimum Mean Square Error (MMSE) are two common adaptive algorithms. ZF true to its name, forces a completely flat transfer function with no multipath and is optimum for ISI suppression. However, as channels tend to add noise, which tends to be amplified by the ZF equalizer, lowering the SNR and reducing signal quality. In contrast, MMSE minimizes the mean square error between the transmitted signal and the equalizer of the output, and generally performs better in the presence of some noise. Using either algorithm, the effect of the weights is to alter the transfer function of the equalizer in order to filter out the ISI effects. The summed output is then passed to a decision device to determine the detected symbol.

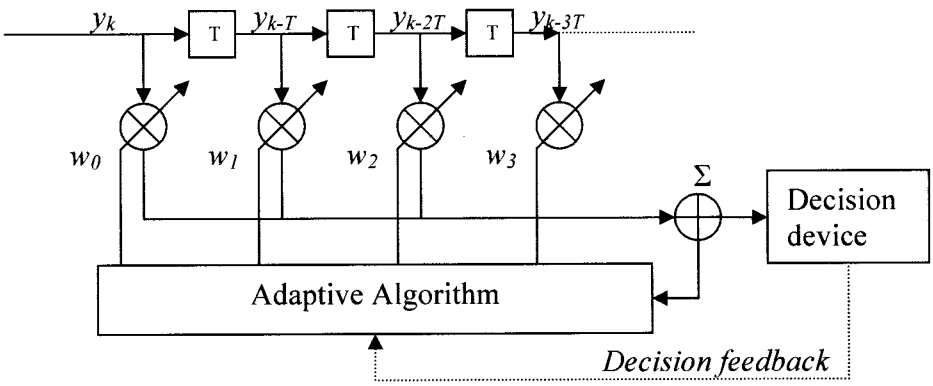


Figure 3.22 A linear transversal equalizer using an adaptive algorithm for tap weight adjustment. The linear equalizer can be modified into a DFE by introducing the decision feedback from the decision device back into the adaptive algorithm.

Another common type of equalizer used is the decision feedback equalizer [34, 103, 105], which consists of the linear equalizer together with an additional feedback mechanism. The decision feedback equalizer takes the determined symbol

ATTENTION: The Singapore Copyright Act applies to the use of this document. Nanyang Technological University Library

and incorporates it into the adaptive mechanism, utilizing feedback as 'prior knowledge' to remove ISI effects from message bits which have already been detected. Although widely used in cases of severe ISI, a major concern is error propagation, since a falsely detected prior bit would adversely affect the accuracy of the detection of the next bit. Figure 3.22 shows the schematic of a typical linear equalizer that can be converted into a DFE.

While equalizers are effective in minimizing ISI, the tradeoff is an increase in system complexity. For example, the transmission of the training message would reduce throughput. Further, when multiple taps are used, there is an increase in the system complexity. Research has shown that the equalizer is the most expensive component of a data demodulator, consuming over 80% of the total computational cost during the demodulation of a given signal[109].

3.5.9 Conclusions

In this section, a brief study was made on the communications performance characteristics using the designed parameters from the earlier section. A receiver communications model was used to obtain the BER and SNR performance of the system. It was found that without using any coding or diversity techniques, a BER of 10^{-3} is achievable. However, if a higher SNR is required, diversity is one technique that can be considered. MRC is a form of diversity combining that offers good improvement in the signal quality at the cost of increased complexity in the receiver circuit. At a transmission capacity of 155Mbit/s an average BER of 10^{-4} could be achievable using a MRC order of 3.

ATTENTION: The Singapore Copyright Act applies to the use of this document. Nanyang Technological University Library

3.6 Conclusions to the Chapter

In this Chapter, a study of the optimum receiver field of view for an indoor wireless optical system was studied for various diffusing spot patterns, and it was found that a field of view of 30° offered an optimal balance between power distribution uniformity and the RMS delay spread. Using this value of the field of view, a simulated annealing approach was carried out to optimize the pattern of the diffusing spots and it was shown that using such an approach results in better uniformity and delay spread characteristics over conventional grid-based spot patterns when the spot pattern was centered on the ceiling as well as offset. A model of the communications block was then used to characterize the performance of the optical wireless system using the BER, and it was shown that the combination of optimized receiver field of view and diffusing spot pattern allowed a 54Mbit/s transmission rate at a BER of 10^{-3} with no coding required. Furthermore, by using a diversity combination technique such as MRC at an order of three, the signal transmission could be improved to 155Mbit/s while still maintaining a BER of about 10^{-4}.

ATTENTION: The Singapore Copyright Act applies to the use of this document. Nanyang Technological University Library

4

Zero order minimization and suppression in computer generated holograms

4.1 Introduction to the Chapter

In the previous section a computer generated hologram was suggested to be used as a spot diffuser to distribute the transmitted signal from an optical wireless transmitter to the receiving floor, and it was shown that optimization techniques were applicable in the design of the transmitter and receiver to meet channel requirements. The flexibility and ease of design of the hologram make it an appropriate choice for implementation in an optical wireless transmitter.

ATTENTION: The Singapore Copyright Act applies to the use of this document. Nanyang Technological University Library

Computer generated holograms (CGH) [110, 111] can be defined as a class of diffractive optics which are formed by making use of known physical relationships between the object field and the far-field. As such, unlike conventional holography the actual physical object is not required. By specifying the complex amplitude of the desired far-field reconstruction, the CGH can be determined by back-propagating the far-field complex amplitude. The flexibility of the intensity distribution of the CGH has found it being used in many applications where a beam splitter is required. In particular, a major advantage of CGHs over bulk beam splitters employing prism optics is the lightweight and small form factor. Furthermore, the number of beams split from a bulk beam splitter is often dependent on the number of beam splitting elements such as cube-beam splitters, making splitting a single beam into multiple beams impractical. In contrast, the number of beams that can be split from a holographic beam splitter is limited by computational and fabrication limitations, but a 1-to-100 beam splitter is not drastically difficult to implement. An illustration of a comparison between bulk optics and a hologram in a beam splitter application is shown below in Figure 4.1. While microlens arrays or prism arrays are also possible for the generation of multiple beams, there are some inherent limitations. Microlens arrays are well-suited for producing a regular array of spots. However, it lacks the flexibility of a CGH when a more complicated irregular spot pattern is desired. As well, a prism array would face a similar issue, and can be exacerbated by the fragility of the elements. In contrast, a CGH offers flexibility of spot pattern and robustness over these methods.

ATTENTION: The Singapore Copyright Act applies to the use of this document. Nanyang Technological University Library

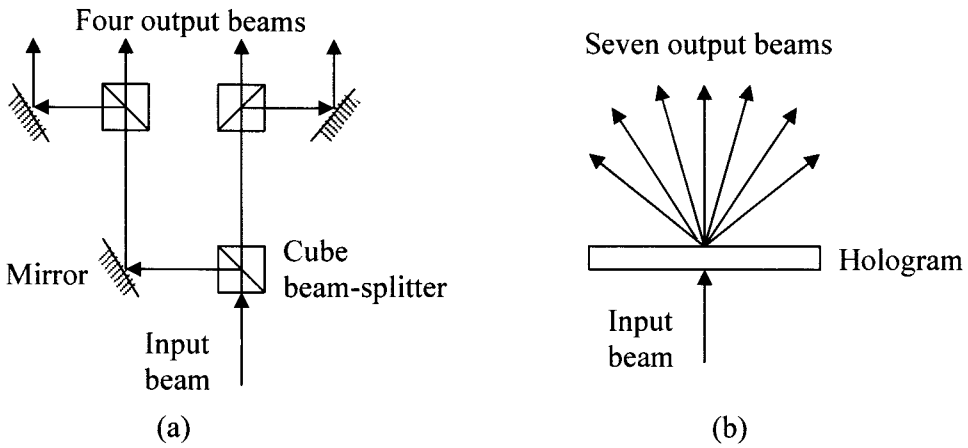


Figure 4.1 Illustration of two beamsplitters: (a) uses conventional bulk optics requiring 3 cube beamsplitters to generate four output beams; (b) uses a single holographic optical element to produce seven beams.

A limitation to the use of holograms is the intensity in the zero order that arises from phase imperfections in the hologram. The zeroth order intensity represents a waste of useful energy which goes into the zeroth order rather than the diffracted spot pattern. This affects indoor optical wireless performance where a strong zeroth order decreases the effectiveness of the hologram by reducing the intensity in the diffracted spots, distorting the desired intensity distribution pattern. Eye safety concerns may arise due to a strong zeroth order. In applications where holograms are also used as fan-outs for optical interconnects it is usually undesirable to have a strong zeroth order as it affects the distribution of signal energy for multiplexed "one-to-many" layouts.

The zero order can come about due to errors in the hologram design such a fill-factor which does not result in a 50-50 ratio between the 0 and π levels in a binary hologram design[112], resulting in an excess phase which leads to zero order. In Fourier optics, the excess phase can be seen as being energy when the spatial frequency is zero, i.e. a sort of 'DC' unmodulated energy due to insufficient

ATTENTION: The Singapore Copyright Act applies to the use of this document. Nanyang Technological University Library

modulation of the plane wave. Careful hologram design to ensure a balanced 50-50 fill factor could remove the zero order. However, it has been found that even in the case of an ideally designed binary hologram with no zero order present, fabrication errors can still lead to phase errors in the uneven etch depths or uneven etch areas [11], resulting in the zero order. Due to the aperiodic and pseudorandom structure of holograms, the separation between the surface relief structures can vary from the minimum feature size (mfs) to several multiples of the mfs. It is widely known in fabrication that such structures can be difficult to produce accurately, with errors possible in the photolithography step causing over or underdevelopment of the photoresist, or during the etching step where under or over-etching is possible. Although the fabrication process can be optimized to reduce the fabrication errors, the pseudorandom structure of holograms in the widely varying feature sizes can make it a challenge to do so.

In this Chapter, several methods are studied to reduce the zero order produced in a hologram. The first method makes use of the polarized nature of light to re-use some of the zeroth order energy to enhance the diffracted order. In the second approach, a method was attempted to reduce the zero order through phase compensation by addition of a second phase plate. The third approach involves utilizing a high spatial frequency phase function to redistribute the zero order energy away from the central zeroth order location. It will be shown that the last method is the most promising and is resilient to several types of common fabrication errors.

ATTENTION: The Singapore Copyright Act applies to the use of this document. Nanyang Technological University Library

4.2 Recent work on Zero order reduction

In recent years, while there has been considerable interest in eliminating the zero order in digital holograms [113-116], there have been less efforts towards suppression of the zero order in computer generated holograms (CGH). Some of the earliest methods of zero order suppression in CGH were the use of physical blocks, in which an obstruction is simply placed in the centre of the reconstructed pattern to physically block the zero order, such as in[117]. This 'hard block' method requires that some prior knowledge of the size of the zero order to be known in order to design a block to avoid affecting the area surrounding the zero order. Furthermore, a high degree of precision is required as well. Later, Jutamulia and Gregory [118] proposed the use of a special photoluminescent material known as electron trapping (ET) as a soft stop. In this method, uniform 488nm blue light is first used to expose the ET material placed at the back focal plane of a lens, resulting in excitation of the electrons in the zero order spot followed by emission of photons. These electrons now have less energy then the other electrons in the ET film. Next, infrared light at 1064nm containing desired pattern was passed through the lens and focused onto the ET film. As the electrons in the zero order contain less energy than the other electrons in the film, there is reduced emission from the zero order, and the emissions from the ET film has a reduced zero order component. However, such a method would require accurate alignment and the use of two lasers, as well as an efficiency depending on the photoluminescence efficiency of the ET film.

The previous methods can be categorized as ‘passive’ methods due to the correction of the zero order after it has been emitted. Other ‘active’ methods have been proposed to eliminate the zero order during the design of the hologram itself during the generation of the hologram phase pattern. One of the earliest ways [119]

ATTENTION: The Singapore Copyright Act applies to the use of this document. Nanyang Technological University Library

involves designing the spot array such that it is designed in an off-axis manner, resulting in a spot array that is away from the centre of the reconstruction plane. In this way, the 'off-axis' hologram is physically away from the influence of the zero order. Then, in [112], O'Shea suggested that the zero order in a Dammann grating could be eliminated through setting a design condition that the difference in area between the π-phase regions and the zero-phase regions be equal, as it was found that the intensity of the zero order was related to the difference between these two areas. Later, Morrison [120] proposed a method to simplify the design of spot array generators by making use of symmetries within the grating pattern, and through the combination of a translational shift of a section of the grating unit cell with a phase offset of π, an even-numbered spot array could be generated with no zero order. In 2005, Liu et el [121] recommended the use of a non-bias architecture for an optical spectral processor for real signals by using an amplitude spatial light modulator (SLM) in tandem with a phase SLM retain the phase and amplitude information of the real input signal to minimize its dc bias, such that the produced spectrograms have a reduced dc bias and increasing the discrimination sensitivity. Finally, in more recent work, Palima and Daria[122] have suggested a way of suppressing the zero order due to fill factor mismatch in the pixels of phase-only SLMs, by specifying the exact complex field in the reconstruction plane. A corrective beam is included in the design to coincide with the zero order beam due to the SLM fill factor mismatch, destructive interfering with and correcting for the zero order.

Although such 'active' methods are attractive, there are some limitations to their use. In particular, many of the methods, such as [112] [120] [121] [122], are highly dependent on the quality of the produced phase profile. As has been shown in [11], although the design was devoid of any zero order, the reconstructed pattern was

ATTENTION: The Singapore Copyright Act applies to the use of this document. Nanyang Technological University Library

found to possess a rather strong zero order, which was attributed to fabrication limitations due to the high degree of variance of the effective spacing between pixels in a complicated surface relief structure. Particularly when the pixel sizes are small, fabrication limitations can limit the effectiveness of such methods. Also, while [121] and [122] have been demonstrated in SLMs and are well-suited to such devices, SLMs can be considered to be controlled environments where the exact characteristics such as the fill factor is known. However, such specific characteristics can be difficult to identify for fabricated components due to fabrication variations. [121] also requires control of the amplitude and phase which is a challenge to fabricate. Finally, although off-axis hologram patterns such as [119] can be produced which are away from the zero order, it is well-known that this limits the functional area and also causes a reduction in the diffraction efficiency due to the shape of the diffraction envelope away from the centre.

4.3 Brief introduction to computer generated holograms

In this section computer generated holograms will be briefly introduced. From scalar diffraction theory, the Fraunhoffer approximation of the far-field complex amplitude U_2 from a diffracting plane U_1 is given by [123]:

$$U_2(x,y) = \frac{e^{jkz} e^{j\frac{k}{2z}(x^2+y^2)}}{j\lambda z} \int_{-\infty}^{\infty}\int U_1(\xi,\eta)\exp[-j\frac{2\pi}{\lambda z}(x\xi+y\eta)]d\xi d\eta \qquad (4.1)$$

where (x, y) and (ξ, η) represent rectangular coordinates in U_2 and U_1 respectively, z represents the distance between U_1 and U_2, λ is the wavelength of the propagating wave and k is the propagation vector. By making use of Equation (4.1) and defining the desired far-field complex amplitude, the corresponding hologram in the diffracting

ATTENTION: The Singapore Copyright Act applies to the use of this document. Nanyang Technological University Library

plane can be determined by use of an iterative optimization routine, such as simulated annealing and genetic algorithm, and can be specified as amplitude or phase holograms. During the optimization process, quantization and pixelation of the complex amplitude in the diffracting plane is performed according to the hologram requirements. Phase holograms are preferable over amplitude holograms due to the better diffraction efficiencies, and can be further categorized as continuous surface relief holograms, or discretized phase level holograms with 2^m levels, where m represents the number of etch processes required.

Binary phase holograms are phase-type holograms which only contain two phase heights. The advantage of binary phase holograms over higher order holograms is that only one etching fabrication step is required. However, binary phase holograms have some limitation in the design of the diffracted spot pattern due to the reflection symmetry in the ±1 orders. In certain applications where symmetry is expected, such as in optical interconnects and optical wireless, the symmetry requirement is not an issue, and in fact serves to simplify the design process by only requiring half of the diffracted spot pattern to be specified. To maximize the energy into the ±1 orders and to eliminate the zero order, the binary phase levels should be set as [0, π], with a 50-50 balanced fill-factor in the ratio of the 0 and π phase areas.

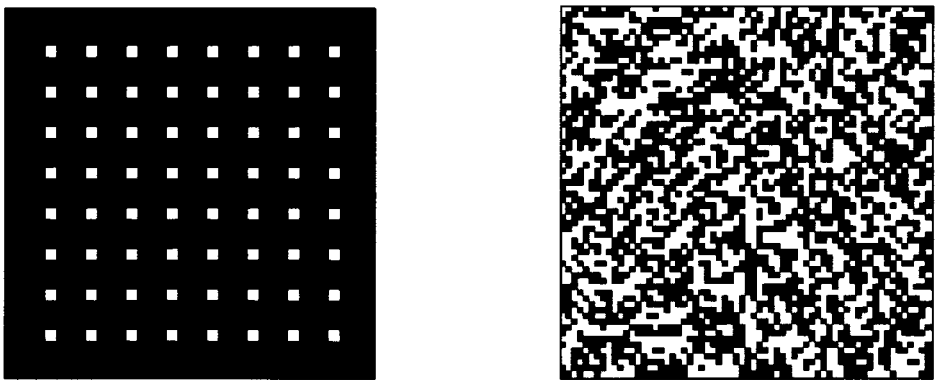
4.3.1 Zero order in computer generated holograms

In an ideal hologram with [0, π] phase levels and a 50% fill factor, there would thus be no zero order. However, due to fabrication limitations, these requirements may be a challenge to meet, especially in the case of a computer generated hologram. Due to the aperiodic and pseudorandom structure of holograms, the separation between the surface relief structures can vary from the minimum feature size (mfs) to several multiples of the mfs. It is widely known in fabrication that such structures can

ATTENTION: The Singapore Copyright Act applies to the use of this document. Nanyang Technological University Library

be difficult to produce accurately, with errors possible in the photolithography step causing over or underdevelopment of the photoresist, or during the etching step where under or over-etching is possible. Although the fabrication process can be optimized to reduce the fabrication errors, the pseudorandom structure of holograms can make it a challenge to do so. These errors contribute to the zero order through an imbalance of the fill factor and by inaccurate reproduction of the required etch depths.

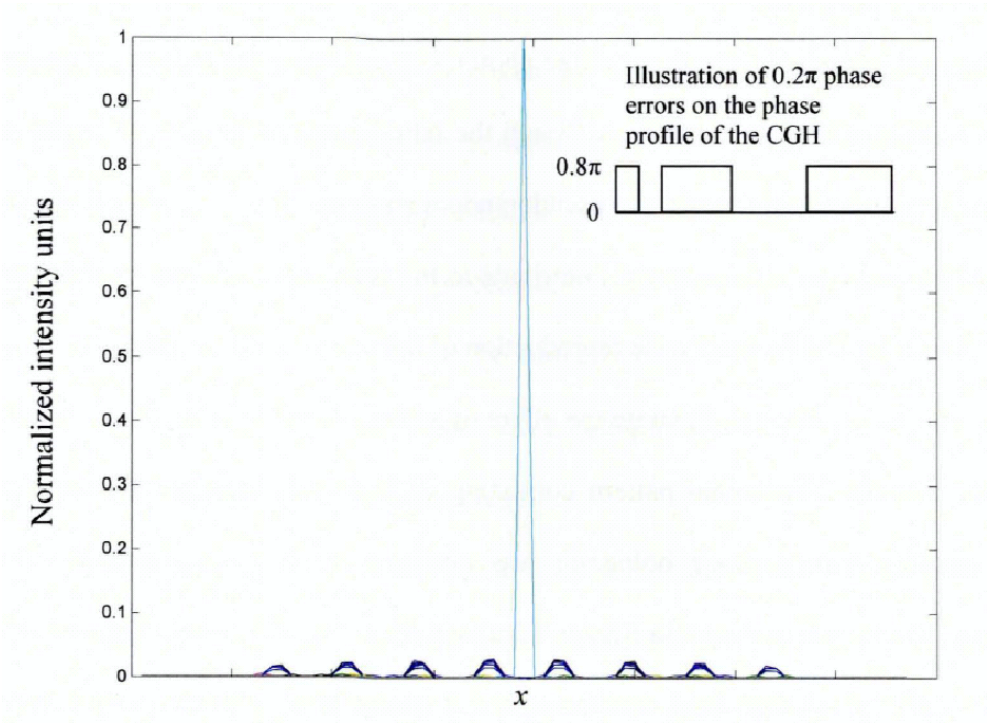
A study is done to illustrate the effect of an etch depth error on the zero order. A spot intensity distribution pattern consisting of 8x8 spots was specified and the corresponding binary phase hologram was obtained using a simulated annealing process. The former is shown in Figure 4.2(a) and the latter is shown in Figure 4.2(b), where 'dark' pixels are used to represent a 0 phase level and the 'white' pixels represent the π phase levels. Simulations were run where the phase depths were varied from 0.8π to π, and the resulting spot intensity patterns were produced. Figure 4.3 shows the two-dimensional spot intensity distribution for the holograms with phase levels $[0, 0.8\pi]$, $[0, 0.9\pi]$ and $[0, \pi]$, representing a 20%, 10% and 0% phase errors respectively, with the intensity normalized to the peak intensity. The zero order metric of interest is defined as the amount of intensity in the zero order relative to the average spot intensity, and is plotted in Figure 4.4 as the phase levels are varied.



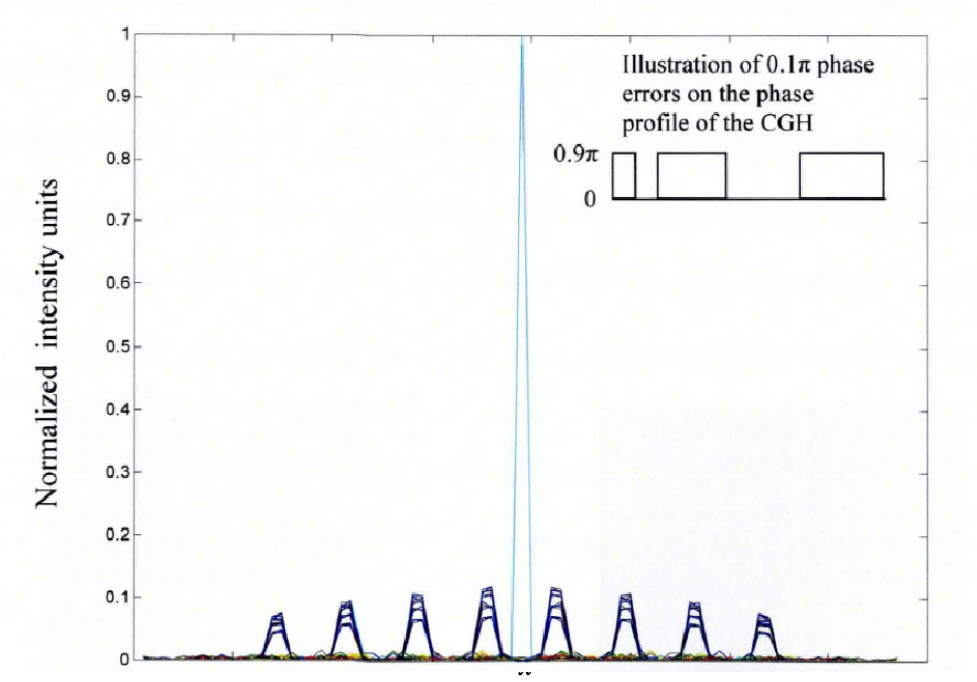
(a) (b)

Figure 4.2 (a) Specified 8x8 intensity distribution pattern and (b) corresponding binary phase hologram that produces (a).

ATTENTION: The Singapore Copyright Act applies to the use of this document. Nanyang Technological University Library

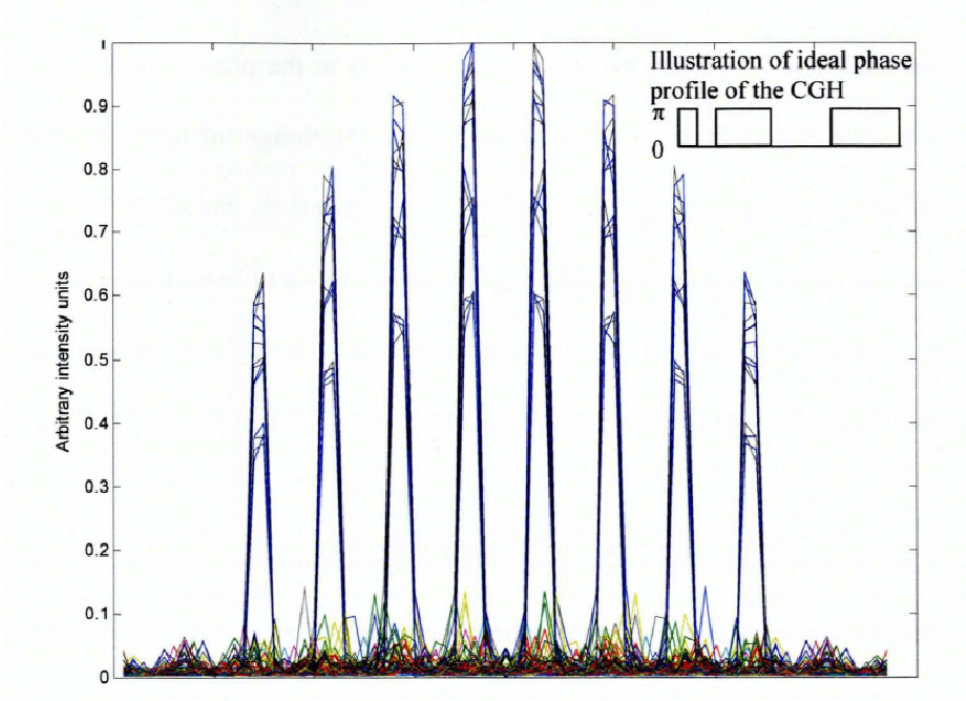


(a)



(b)

ATTENTION: The Singapore Copyright Act applies to the use of this document. Nanyang Technological University Library



(c)

Figure 4.3 Normalized intensity plots for holograms with phase levels (a) [0, 0.8π], (b) [0, 0.9π] and (c) [0, π]. Inset illustrates the phase error introduced into the CGH phase profile.

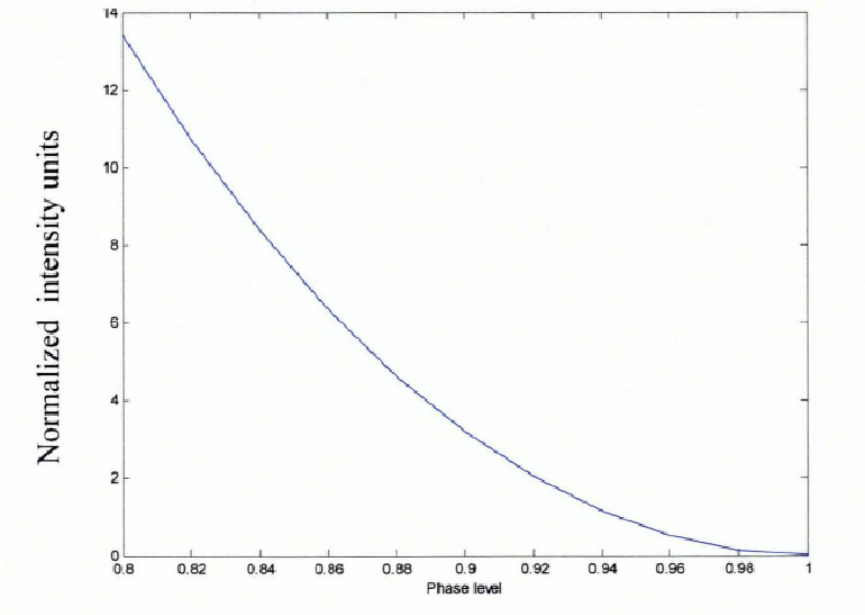


Figure 4.4 Simulated zero order ratio against the average spot intensity for phase levels from 0.8π to π.

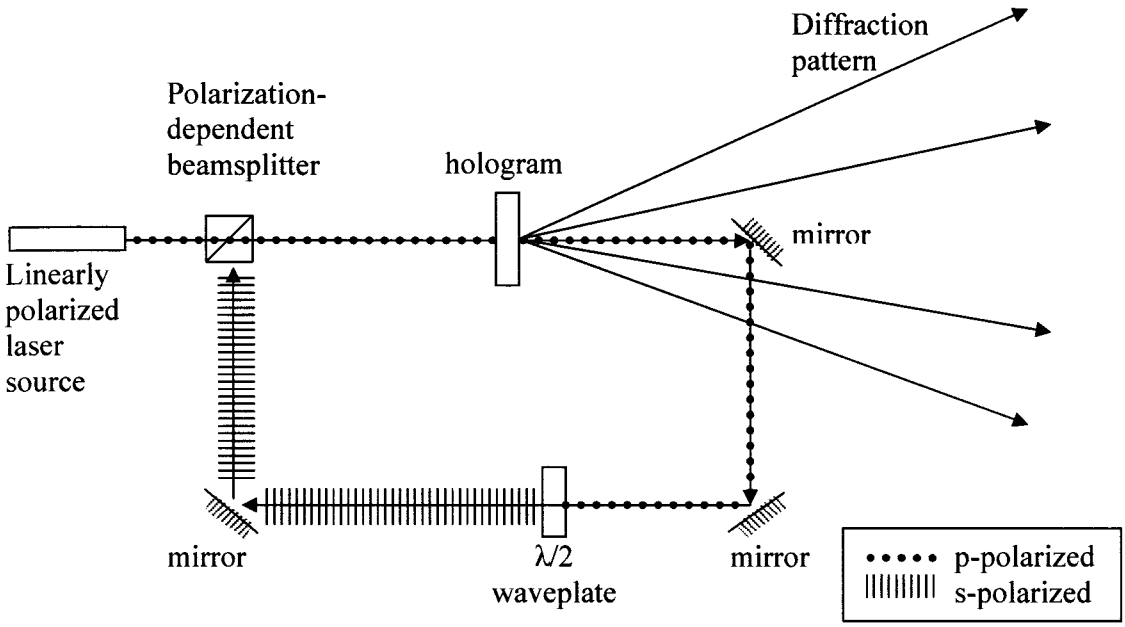
ATTENTION: The Singapore Copyright Act applies to the use of this document. Nanyang Technological University Library

From Figure 4.4, it can be observed that errors in the phase would lead to an exponential-like rise in the zero order intensity. A phase height of 0.95π leads to the same amount of energy in the zeroth order as compared to the average spot, and decreasing the phase height to 0.8π causing the zero order ratio to increase to about 13 times the average spot intensity. This clearly shows how sensitive the zero order is to phase errors and indicates the need to minimize the zero order intensity.

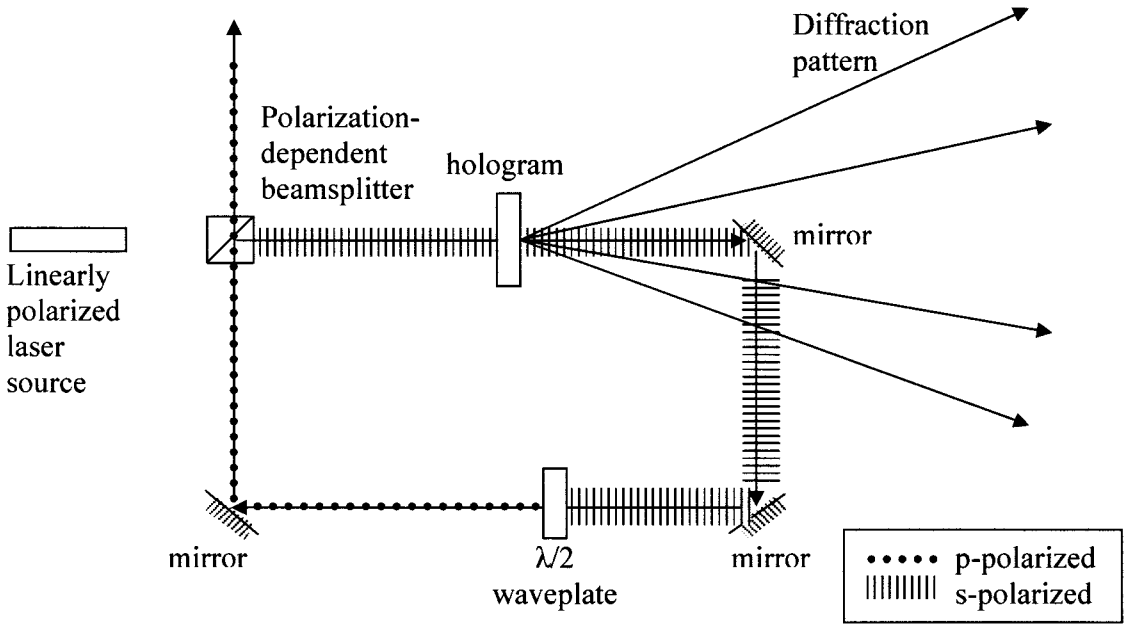
4.4 Re-utilization of zero order intensity through polarization manipulation

From the previous section, it can be observed that the zero order in holograms is extremely sensitive to phase level errors. Furthermore, the nature of the surface relief structures of a hologram would make optimization of the fabrication, while certainly a viable option, extremely challenging. Hence approaches that would be able to reduce the zero order while avoiding further the need for precise control of the surface relief structures would be extremely attractive. A technique is proposed in this section where some of the zero order energy is re-used to strengthen the diffraction orders by making use of commercially and commonly available bulk optical elements, and the setup is shown in Figure 4.5 on the following page.

ATTENTION: The Singapore Copyright Act applies to the use of this document. Nanyang Technological University Library



(a)



(b)

Figure 4.5 Experimental setup for re-use of zero order energy. (a) shows the first pass of the linearly polarized laser energy through the setup and (b) shows the second pass.

ATTENTION: The Singapore Copyright Act applies to the use of this document. Nanyang Technological University Library

The setup in Figure 4.5 makes use of the polarization properties of coherent light from a laser source by manipulating the polarization angle as the wavefront passes through the optical setup. The main components in the setup are a polarizing cube beam splitter and a λ/2 waveplate. The polarizing cube beamsplitter reacts differently depending on the polarization direction of the incident beam. In the setup, a polarizing cube beamsplitter was used which transmits reflects *s*-polarized light and transmits *p*-polarized light. The linearly laser source is rotated in such a manner that *p*-polarized light is incident onto the beamsplitter, which transmits the energy in its entirety with a high efficiency. As the *p*-polarized wavefront passes through the hologram, part of the energy is diffracted into the diffraction orders. However, due to fabrication errors on the hologram, some of the incident energy is undiffracted and exits the hologram as zero order intensity, where it undergoes reflections in the setup to re-direct the wavefront back into the beamsplitter. A λ/2 waveplate is placed in the direction of the wavefront and is rotated in such a way that the incident *p*-polarized beam undergoes a 90° rotation and emerges as *s*-polarized wavefront.

The second pass through the optical system is described in Figure 4.5(b). The *s*-polarized wavefront is reflected by the polarization dependent beamsplitter back into hologram, where it is again diffracted into the diffraction order. In this way some of the zeroth order energy has been re-utilized. However, due to the phase errors present in the hologram, some of the *s*-polarized is transmitted as zero order energy, where it re-traces the path, passing through the λ/2 waveplate where it is rotated back into *p*-polarized energy. Due to the polarization direction, however, the *p*-polarized wavefront is not reflected at the polarizing beamsplitter and the beam is transmitted out of the setup, as shown in Figure 4.5(b).

ATTENTION: The Singapore Copyright Act applies to the use of this document. Nanyang Technological University Library

A fabricated hologram on quartz with phase errors was placed into the setup shown in Figure 4.5, and a 7mW He-Ne linearly polarized laser was used as the source. Without use of the polarizing beam splitter, about 3mW was measured by a photodetector placed into the path of the zeroth order. When the polarizing cube beamsplitter was replaced and the components rotated as described earlier, the zero order intensity was approximately reduced by 50%.

The proposed technique can be used as implemented as a means of re-utilizing zero order intensity and reducing wastage of the source energy. However, some positioning is required to ensure that the diffracted image does not suffer from a displaced image due to the second pass of the wavefront through the optical system. Also, despite reducing the zero order, some wastage is still experienced on the second pass. Another potential limitation would be its application in optical wireless communications where the second pass may cause some form of intersymbol interference. The path length through each pass of the optical system is approximately 0.5m, which translates to a 1.67ns interval between each pass in freespace. For signals with a relatively long symbol duration in microsecond, the second pass does not present a significant problem. However, for gigahertz signals with short symbol durations of 1ns or less, the addition of a second path could cause intersymbol interference. The interference could possibly be mitigated by reducing the path length and utilizing the repeated symbol as error correction by retransmission, if pre-empted and expected. In illumination or visual applications, such intersymbol interference would not be considered a critical limitation.

ATTENTION: The Singapore Copyright Act applies to the use of this document. Nanyang Technological University Library

4.5 Zero order suppression by phase compensation

From the earlier sections, the zero order was seen to have been caused by fabrications errors which lead to phase errors. The phase errors result in an excess of phase which imbalances the fill factor of the hologram, causing some of the incident energy to be undiffracted and transmitted as zero order. In this section a method is proposed to reduce the zero order by compensating for the excess phase, by means of the inclusion of an additional phase function such that the complex amplitude after the combined element has no zero order.

4.5.1 Simulation model

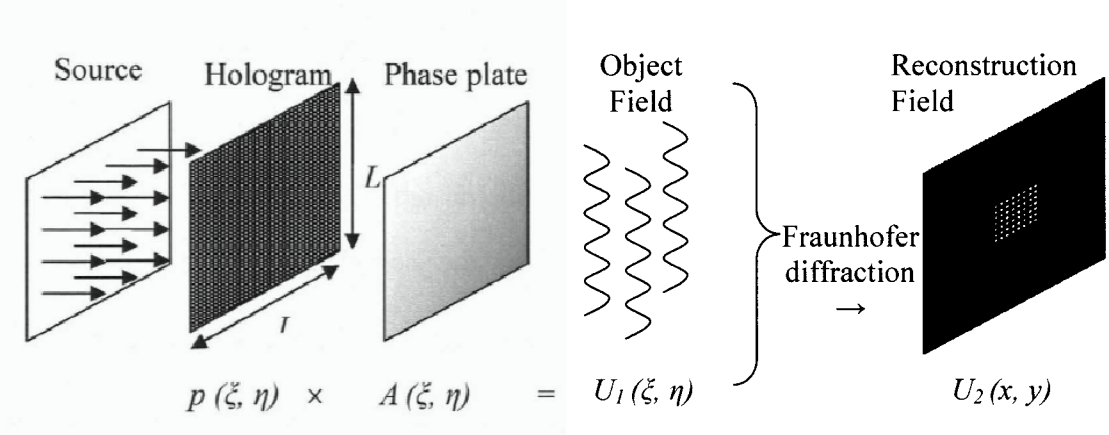
In Section 4.2, Equation (4.1) was presented as the governing equation which propagates the complex amplitude from the hologram to the far-field diffraction regime.

$$U_2(x,y) = \frac{e^{jkz} e^{j\frac{k}{2z}(x^2+y^2)}}{j\lambda z} \int_{-\infty}^{\infty}\int U_1(\xi,\eta)\exp[-j\frac{2\pi}{\lambda z}(x\xi + y\eta)]d\xi d\eta \qquad (4.1)$$

In actual effect, ignoring the additional quadratic phase element in front of the double integral, Equation (4.1) can be treated as the Fourier Transform of $U_1(\xi,\eta)$. To model the effect of an additional phase function after the hologram, a simulation model is implemented as shown in Figure 4.6(a). The hologram field is represented as $p(\xi, \eta)$ which contains the phase information of the hologram. An additional phase plate with a transmittance function $A(\xi, \eta)$ is used to modify the complex wavefront after $p(\xi, \eta)$. Using a plane wave with uniform amplitude to be the incident wave, the wavefront after the object plane $U_1(\xi, \eta)$ is thus the product of the complex amplitude function

ATTENTION: The Singapore Copyright Act applies to the use of this document. Nanyang Technological University Library

of the hologram mask field and the phase plate i.e.$U_1(\xi, \eta) = p(\xi, \eta) A(\xi, \eta)$. Taking the reconstruction field $U_2(x, y)$ to be in the far-field Fraunhofer diffraction region, and applying Equation (4.1), U_2 can be determined by multiplication of the Fourier Transform of the object field with a phase factor i.e. $U_2(x, y) = \theta(x, y) F[U_0(\xi, \eta)]$. The corresponding intensity distribution in the far-field is given by $I_2 = |U_2(x, y)|^2$.



(a)



Phase function for the compensating phase plate

$$\phi(\xi,\eta) = \begin{cases} 0 & \text{for } \xi,\eta > w \\ \pi & \text{for } \xi,\eta \le w \end{cases}$$

(b)

Figure 4.6 (a) Illustration showing the various elements in the simulation model (b) Layout of the compensating phase plate.

ATTENTION: The Singapore Copyright Act applies to the use of this document. Nanyang Technological University Library

4.5.2 Introduction of a phase compensating element

To attempt to compensate for the excess phase caused by fabrication errors and to reduce the corresponding zero error, an additional phase function is proposed to be introduced into the system. For simplicity and ease of fabrication, the phase function mask is chosen to be a binary mask with a square aperture of width w, with a phase function given below. An illustration of the geometry of the element is shown in Figure 4.6(b).

$$\phi(\xi,\eta)=\begin{cases}0 & \text{for } \xi,\eta > w \\ \pi & \text{for } \xi,\eta \le w\end{cases} \tag{4.2}$$

The phase mask is converted into the complex amplitude transmission function $A(\xi,\eta)=\exp[j\pi\phi(\xi,\eta)]$. To determine the performance of the phase mask, a 10% error is introduced into the hologram mask $p(\xi, \eta)$, and the zero order intensity ratio I_0 against the average spot intensity I_s is calculated as w is varied from 0 to the size of the hologram. The obtained results are plotted in Figure 4.7 against w normalized against the size of the hologram. From the results, as the width of the aperture w is varied, there is a drop in the geometric zeroth order intensity leading to a near zero minimum when w is at 0.7 which can be seen in the Figure 4.7. At this value of w, the phase mask acts as an ideal diffracting element with equal amounts of additional π and 0 phase, a balanced phase element which is able to compensate for the excess phase from the hologram and thus effectively suppresses the zeroth order at the geometrical location.

It was also observed in the simulation results that the addition of the phase plate caused a broadening of the zeroth order, together with a distortion of

ATTENTION: The Singapore Copyright Act applies to the use of this document. Nanyang Technological University Library

reconstructed image as shown in Figure 4.8. Without the phase plate, the zeroth order occupied a single pixel in the reconstruction field (the "geometric" location). When the phase plate was incorporated into the simulation setup, there was a broadening in the size of the zeroth order spot, occupying more pixels. This can be attributed to the phase function of the square phase plate, which also undergoes diffraction and results in production of its own diffraction pattern at the centre, despite the missing zeroth order, with the size of the produced diffraction pattern dependent on w. Also, the distribution of the zeroth order intensity within the broadened zeroth order spot size became non-uniform. Although the geometric zeroth order was effectively suppressed, the broadened zeroth order led to secondary peaks in the zeroth order spot such that the peak intensity in the broadened zero order does not coincide with the geometrical location. To quantify these secondary effects, the ratios of the total zeroth order power I_{oT} and the peak zeroth order power I_{oP} and the average diffracted spot intensity I_s are also plotted in Figure 4.7.

From Figure 4.7, it can be observed that for values of w less than 0.55, the peak zero order and the geometric zero order share the same plot. This is as there is little noticeable broadening in the zero order. Between $w = 0.55$ and $w = 0.82$, the two plots diverge with I_o dropping to zero while I_{oP} shows a slight increase. The plots imply that as the w is increased, indicating a change in the fill factor, the geometric zero order drops and reaches a minimum where $w = 0.7$, which represents a 50% fill factor for the square phase plate. However, if the broadened zero order is observed in its entirety, it can be seen that the peak intensity within the zero order does not actually drop to zero but occurs beside the geometric zero order. Although the geometrical zeroth order was suppressed, the energy within the geometrical zeroth order was re-distributed into the broadened zeroth order spot. Of even greater note is

ATTENTION: The Singapore Copyright Act applies to the use of this document. Nanyang Technological University Library

the ratio of I_{oT} against I_s which represents the total zero order intensity as a ratio against the average spot intensity, and shows an increase as w is varied as shown in Figure 4.7. This is due to the distortion of the diffracted spots. In calculating the average spot intensity I_s, the geometric locations of the original diffracted spots were used. With the addition of the phase plate, the resultant distortion of the diffracted spots leads to a lower amount of diffracted energy in the defined spot locations, and hence to a corresponding increase in the I_{oT}/I_s ratio. Although the introduction of the rectangular phase plate is effective in eliminating the geometric zeroth order, the broadening of the zeroth order leading to an increase in the overall zero order intensity and the distortion of the diffracted spot elements are challenges in the proper application of this technique.

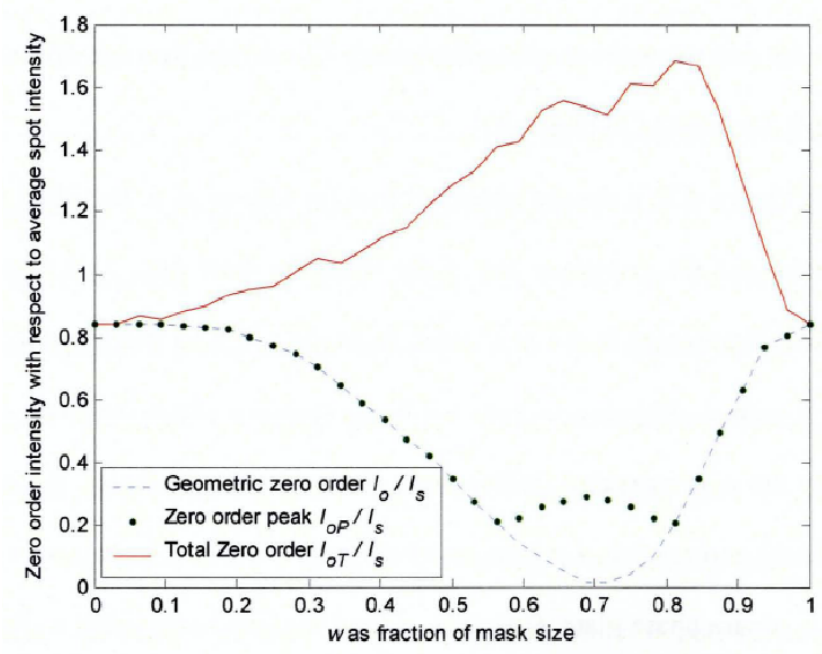


Figure 4.7 Plots of the zeroth order intensity with respect to the average spot intensity.

ATTENTION: The Singapore Copyright Act applies to the use of this document. Nanyang Technological University Library

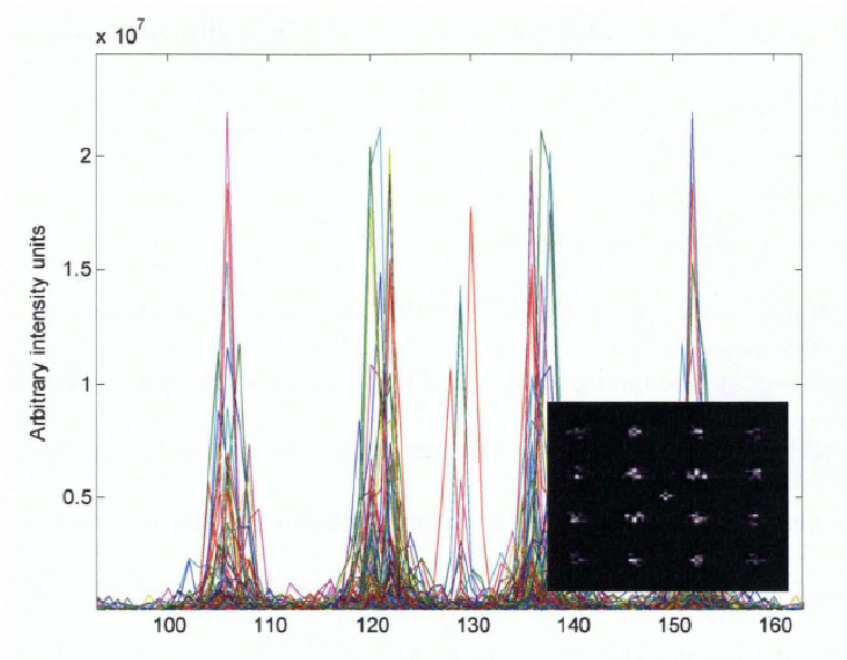


Figure 4.8 Intensity profile showing the broadened zeroth order and distortions caused by the addition of the rectangular phase aperture. Inset shows the reconstructed distribution.

4.6 Use of phase checkerboard for redistribution of zeroth order energy

In this section, we introduce the use of another type of phase function known as the phase checkerboard function for re-distributing the zero order energy away from the central location. The previous section showed that use of an additional phase plate can be effective in suppressing the zero order in the far-field spot-distribution pattern of a hologram. However, in doing so, consideration must also be made for the phase function of the additional phase plate as it was observed that the phase plate also contributes to the resulting intensity distribution, causing distortion if not properly accounted for as was observed in Figure 4.7. In this section we show that by using a phase checkerboard function, the zero order intensity can be effectively re-

ATTENTION: The Singapore Copyright Act applies to the use of this document. Nanyang Technological University Library

distributed to the higher order locations, resulting in a diffracted pattern that is virtually free of zero order effects.

4.6.1 The phase checkerboard function

A binary phase checkerboard function (PCF) is a two-dimensional pattern which consists of an alternating sequence of [0, π] phase levels, and can be considered to be one of the elementary forms of a Dammann grating. A similar function was used in [124] to generate a fan-out for the purpose of coupling optical signals into fibers. In our proposed approach the phase checkerboard function will be used to redistribute the energy in the zeroth order away into the higher orders.

First, the PCF can be expressed as in Equation (4.3), where 2Γ is the period between each copy of the unit cell $c(\xi,\eta)$, which contains the basic checkerboard phase information.

$$k(\xi,\eta) = c(\xi,\eta) \otimes \mathrm{comb}\left(\frac{\xi}{2\Gamma},\frac{\eta}{2\Gamma}\right) \tag{4.3}$$

The unit cell $c(\xi, \eta)$ is defined as in the following in Equation (4.4), where the size of each pixel in the PCF is taken to be Γ. A geometric sketch of the phase checkerboard function which has been mathematically expressed in Equations (4.3) and (4.4) is illustrated in Figure 4.9.

$$\begin{aligned} c(\xi,\eta) = {} & \mathrm{rect}\left(\frac{\xi}{\Gamma},\frac{\eta}{\Gamma}\right) \otimes \delta\left(\xi-\frac{\Gamma}{2},\eta+\frac{\Gamma}{2}\right) \bullet \exp(j\pi) \\ & + \mathrm{rect}\left(\frac{\xi}{\Gamma},\frac{\eta}{\Gamma}\right) \otimes \delta\left(\xi+\frac{\Gamma}{2},\eta+\frac{\Gamma}{2}\right) \\ & + \mathrm{rect}\left(\frac{\xi}{\Gamma},\frac{\eta}{\Gamma}\right) \otimes \delta\left(\xi-\frac{\Gamma}{2},\eta-\frac{\Gamma}{2}\right) \\ & + \mathrm{rect}\left(\frac{\xi}{\Gamma},\frac{\eta}{\Gamma}\right) \otimes \delta\left(\xi+\frac{\Gamma}{2},\eta-\frac{\Gamma}{2}\right) \bullet \exp(j\pi) \end{aligned} \tag{4.4}$$

ATTENTION: The Singapore Copyright Act applies to the use of this document. Nanyang Technological University Library

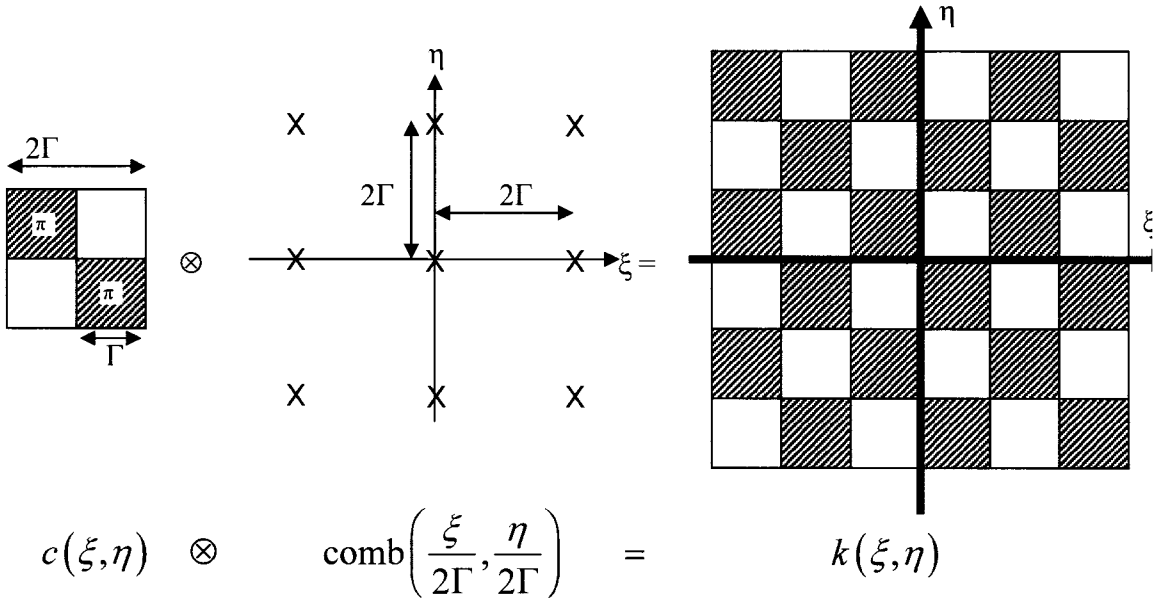


Figure 4.9 Geometric sketch of the phase checkerboard function (PCF).

Applying the Fourier Transform on Equation (4.4) and ignoring scalar constants,

$$C(x,y) = \mathrm{F}\left[c(\xi,\eta)\right]$$

$$\begin{aligned}
&= \left\{|\Gamma|^2 \,\mathrm{sinc}(x\Gamma, y\Gamma) \bullet \exp\left[-j\pi(\Gamma x - \Gamma y)\right]\right\} \otimes \left[-\delta(x,y)\right] \\
&\quad + \left\{|\Gamma|^2 \,\mathrm{sinc}(x\Gamma, y\Gamma) \bullet \exp\left[-j\pi(-\Gamma x - \Gamma y)\right]\right\} \otimes \left[\delta(x,y)\right] \\
&\quad + \left\{|\Gamma|^2 \,\mathrm{sinc}(x\Gamma, y\Gamma) \bullet \exp\left[-j\pi(\Gamma x + \Gamma y)\right]\right\} \otimes \left[\delta(x,y)\right] \\
&\quad + \left\{|\Gamma|^2 \,\mathrm{sinc}(x\Gamma, y\Gamma) \bullet \exp\left[-j\pi(-\Gamma x + \Gamma y)\right]\right\} \otimes \left[-\delta(x,y)\right]
\end{aligned}$$

$$\begin{aligned}
&= |\Gamma|^2 \,\mathrm{sinc}(x\Gamma, y\Gamma) \bullet \left\{-\exp\left[-j\pi(\Gamma x - \Gamma y)\right]\right. \\
&\qquad + \exp\left[j\pi(\Gamma x + \Gamma y)\right] \\
&\qquad + \exp\left[-j\pi(\Gamma x + \Gamma y)\right] \\
&\qquad \left. - \exp\left[-j\pi(-\Gamma x + \Gamma y)\right]\right\}
\end{aligned}$$

ATTENTION: The Singapore Copyright Act applies to the use of this document. Nanyang Technological University Library

Since

$$\begin{aligned} \mathrm{F}\left[\exp(j\pi)\right] &= \mathrm{F}\left[\cos(\pi)+j\sin(\pi)\right] \\ &= \mathrm{F}\left[-1+j0\right] \\ &= -\delta(x,y) \end{aligned}$$

Using Euler's Principle $\exp(j\theta)=\cos\theta+j\sin\theta$ and letting $E=\pi\Gamma\left(x-y\right)$ and $G=\pi\Gamma\left(x+y\right)$, the exponential in *C(x,y)* thus becomes

$$\begin{aligned} &-(\cos E-j\sin E)+(\cos G+j\sin G)+(\cos G-j\sin G)-(\cos E+j\sin E) \\ &=2\cos G-2\cos E \\ &=2\cos\pi\left(\Gamma x+\Gamma y\right)-2\cos\pi\left(\Gamma x-\Gamma y\right) \\ &=-4\sin\left(\pi\Gamma x\right)\sin\left(\pi\Gamma y\right) \end{aligned}$$

Ignoring scaling constants, *C(x,y)* is expressed in Equation (4.5) where $x = n/2\Gamma$ and $y = m/2\Gamma$, and $n, m = [0, \pm1, \pm2, \pm3\ldots]$.

$$C\left(x,y\right)=\sin\Gamma x\sin\Gamma y\bullet\mathrm{sinc}\left(x\Gamma,y\Gamma\right) \tag{4.5}$$

For the comb replicating function in 2Γ in Equation (4.3), the FT is simply another comb function with points separating by $\frac{1}{2\Gamma}$

$$\mathrm{F}\left[\mathrm{comb}\left(\frac{\xi}{2\Gamma},\frac{\eta}{2\Gamma}\right)\right]=\mathrm{comb}\left(x2\Gamma,y2\Gamma\right) \tag{4.6}$$

The full expression for the binary phase checkerboard in the far-field is thus

$$\begin{aligned} K\left(x,y\right)&=\sin\left(\pi\Gamma x\right)\sin\left(\pi\Gamma y\right)\bullet\mathrm{sinc}\left(x\Gamma,y\Gamma\right)\bullet\mathrm{comb}\left(x2\Gamma,y2\Gamma\right) \\ K\left(x=\frac{n}{2\Gamma},y=\frac{m}{2\Gamma}\right)&=\sin\left(\frac{\pi n}{2}\right)\sin\left(\frac{\pi y}{2}\right)\bullet\mathrm{sinc}\left(\frac{n}{2},\frac{m}{2}\right)\bullet\mathrm{comb}\left(n,m\right) \end{aligned} \tag{4.7}$$

ATTENTION: The Singapore Copyright Act applies to the use of this document. Nanyang Technological University Library

where $n, m = [0, \pm1, \pm2, \pm3\ldots]$. From the expression, it can be observed that only odd values of $[n,m]$ result in non-zero values of $K(x, y)$. In particular, the zero order and even orders have been suppressed and the corresponding distance between the remaining non-zero orders is $1/\Gamma$. An intensity plot of the PCF is shown in Figure 4.10.

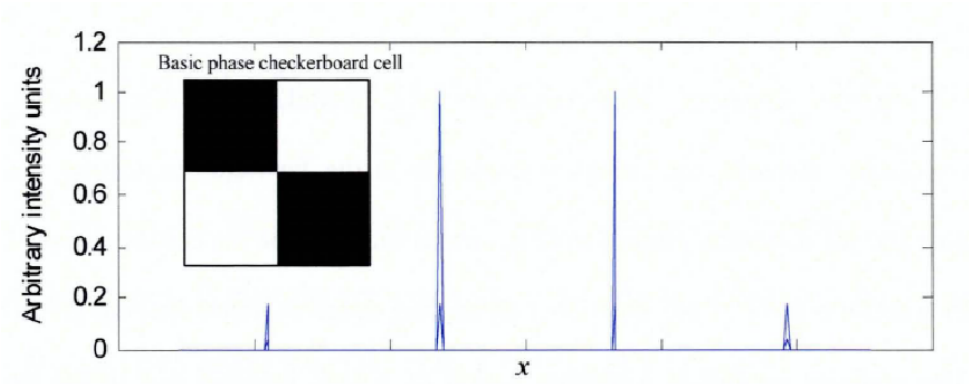


Figure 4.10 One dimensional intensity plot of the far-field complex amplitude of the phase checkerboard function presented in Figure 4.9.

4.6.2 Use of the PCF with a hologram

As detailed earlier, the diffracting field $U_1(\xi, \eta)$ can be considered to be a binary phase CGH $H(\xi, \eta)$ consisting of an array of pixels with 0 or π phase modulation which was optimized during the simulated annealing design process. To facilitate the discussion on how a PCF can be used to re-distribute the zero order, the hologram is re-expressed in an alternate form in the following discussion. It should be noted that there is no change in the produced distribution pattern when the following expressions are used.

$H(\xi, \eta)$ can also be realized as the product of a comb sampling function with a phase function $p(\xi, \eta)$ which contains the hologram phase information at the sampled locations. Each sampled point in $H(\xi, \eta)$ can be considered to be a square pixel with

ATTENTION: The Singapore Copyright Act applies to the use of this document. Nanyang Technological University Library

size Δ representing the size of the pixel at that location, and $H(\xi, \eta)$ can thus be mathematically re-expressed as the convolution of the sampled hologram information with a rectangular function representing the pixel dimensions.

$$H(\xi,\eta)=\left[\text{comb}\left(\frac{\xi}{\Delta},\frac{\eta}{\Delta}\right).p(\xi,\eta)\right]\otimes\left[\text{rect}\left(\frac{\xi}{\Delta},\frac{\eta}{\Delta}\right)\right] \tag{4.8}$$

Using the Fraunhoffer approximation in the far-field diffraction regime and the convolution theorem, the complex amplitude in the far-field, neglecting scalar constants and the quadratic phase function, can be shown to be the convolution of the Fourier transform (FT) of $p(\xi, \eta)$ with a replicating comb function spacing given by $1/\Delta$. The complex amplitude is further scaled by a sinc function due to the pixel geometry.

$$U_2(x,y)=\left[\text{comb}(x\Delta,y\Delta)\otimes P(x,y)\right]\cdot\left[\text{sinc}(x\Delta,y\Delta)\right] \tag{4.9}$$

To combine the PCF with the CGH, the PCF can first be fabricated on a separate substrate from the CGH. In contrast with the pseudorandom nature of complex CGH surface relief structures, the periodicity and regularity of the PCF function is intuitively easier to fabricate, allowing greater control of the fabrication structures and minimizing fabrication errors in the surface relief structure of the PCF. The PCF after fabrication is then used with the CGH by placing the fabricated structures of both substrates to be in contact with each other, which are then held, as shown in Figure 4.11.

ATTENTION: The Singapore Copyright Act applies to the use of this document. Nanyang Technological University Library

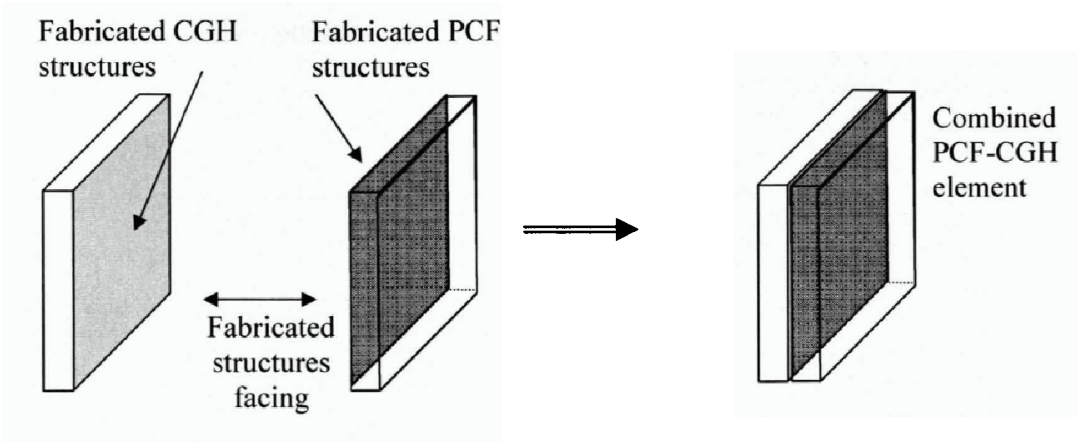


Figure 4.11 Implementation of the combined CGH-PCF optical element.

By placing the fabricated surface relief structures in contact, the resultant complex amplitude after the combined CGH-PCF phase element can thus be seen as the product of the phase functions of the CGH and PCF functions:

$$\begin{aligned} U_3(\xi,\eta) &= H(\xi,\eta)\bullet k(\xi,\eta) \\ &= \left\{\left[\text{comb}\left(\frac{\xi}{\Delta},\frac{\eta}{\Delta}\right).p(\xi,\eta)\right]\otimes\left[\text{rect}\left(\frac{\xi}{\Delta},\frac{\eta}{\Delta}\right)\right]\right\}\bullet k(\xi,\eta) \end{aligned} \tag{4.10}$$

Applying the far-field Fraunhoffer approximation for Equation (4.10) results in the complex amplitude as presented in Equation (4.11).

$$\begin{aligned} U_4(x,y) &= \left\{\left[\text{comb}(x\Delta,y\Delta)\otimes P(x,y)\right]\cdot\left[\text{sinc}(x\Delta,y\Delta)\right]\right\}\otimes K(x,y) \\ \therefore U_4(x,y) &= \left\{\left[\text{comb}(x\Delta,y\Delta)\otimes P(x,y)\right]\cdot\left[\text{sinc}(x\Delta,y\Delta)\right]\right\} \\ &\quad\otimes\left[\sin(\pi\Gamma x)\sin(\pi\Gamma y)\bullet\text{sinc}(x\Gamma,y\Gamma)\bullet\text{comb}(x2\Gamma,y2\Gamma)\right] \end{aligned} \tag{4.11}$$

The amplitude of U_4 can be determined from Equation (4.11), and can be described as the convolution of the complex amplitudes of the Fourier Transforms of the CGH

ATTENTION: The Singapore Copyright Act applies to the use of this document. Nanyang Technological University Library

with the PCF, with the latter being a replicating function with a distance of $1/\Gamma$ between the non-zero locations.

4.6.3 The combined CGH-PCF optical element

In the earlier section the combined CGH-PCF optical element was proposed. The advantage of this approach is that it allows the geometrical zero order (GZO) located at the centre of the CGH reconstruction pattern to be shifted to the non-zero locations of the PCF together with the convolved diffraction patterns. As described earlier, the GZO is caused by fabrication errors, which in effect bring about a phase error such that the effective fill factor of the CGH is not 50-50 for the binary phase levels $[0, \pi]$. The excess phase from the CGH results in the GZO. To illustrate, a scenario is described where the phase levels of the CGH is $[0, 0.9\pi]$, caused by inadequate etch depth of the surface relief structure. In U_2, the effect of this error is a strong zero order in the GZO location at the centre of the U_2 as can be seen in Figure 4.12. Introducing the same error into U_3 as described above, and setting $\Gamma=\Delta$, such that the minimum features sizes of the CGH and the PCF are the same, it can be observed that the zero order and the spot intensity patterns are shifted away from the GZO as seen in Figure 4.13. The result is similar to radio frequency modulation techniques, where a baseband signal is translated into a passband signal by modulating with a carrier frequency. In this application, the PCF acts as a 'carrier' signal which translates the baseband CGH 'signal' into higher spatial frequencies, which in this case is $1/\Gamma$. Although the zero order in the GZO is not observable, the resulting diffraction pattern is undesirable as the CGH pattern has been distorted due to the fragmentation of the desired pattern.

ATTENTION: The Singapore Copyright Act applies to the use of this document. Nanyang Technological University Library

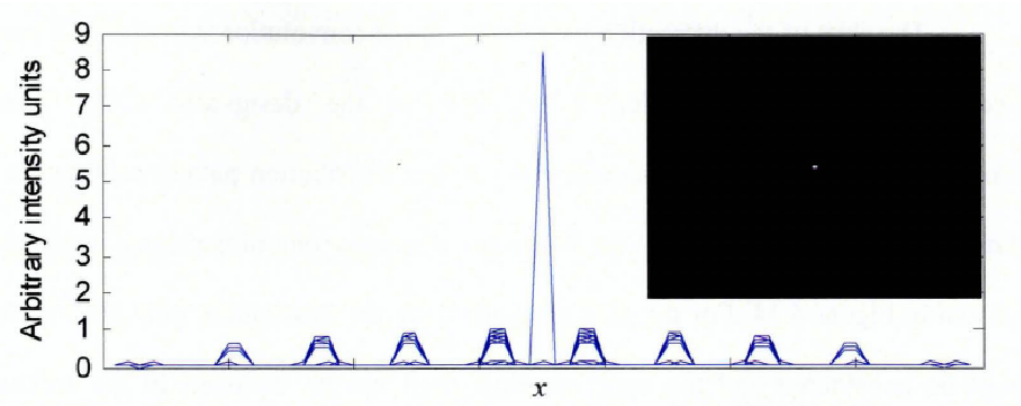
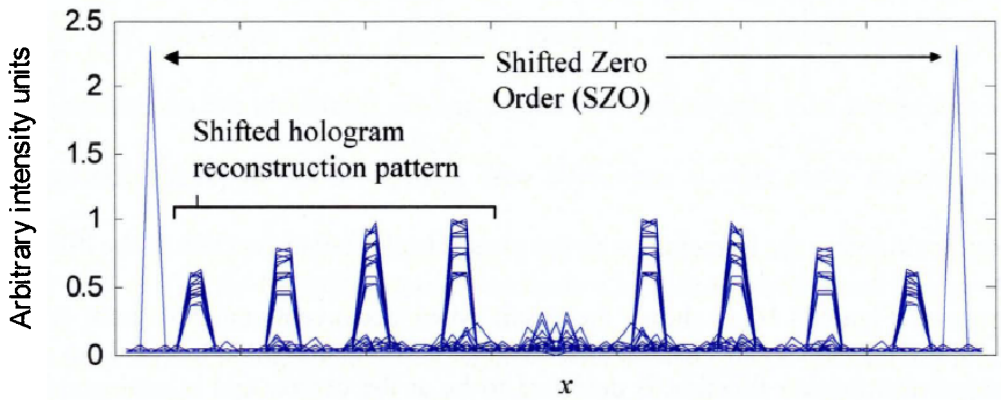
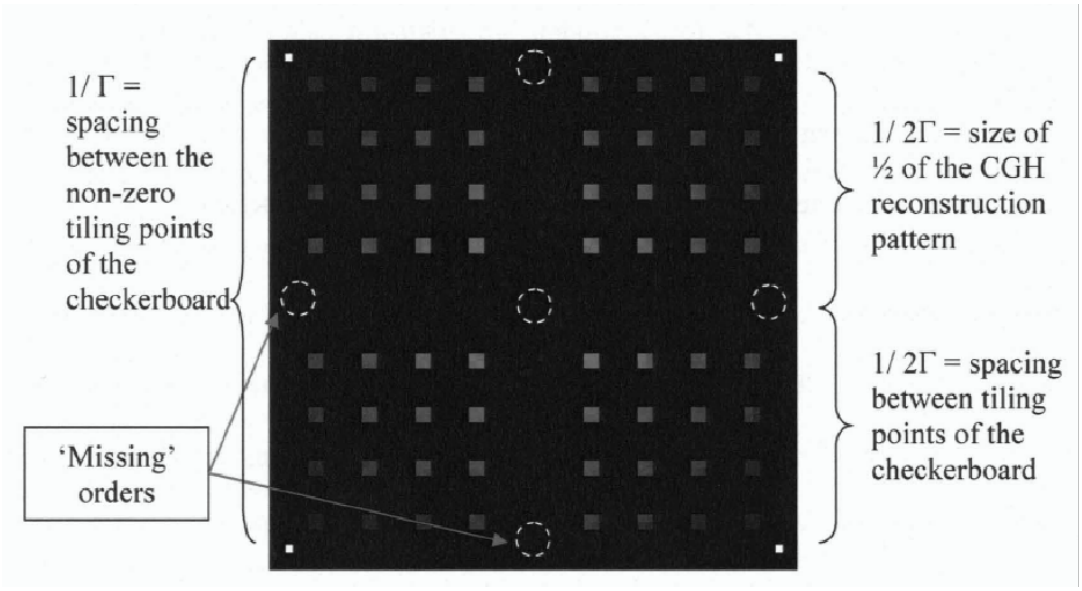


Figure 4.12 Intensity plot for the CGH with an introduced phase depth error, inset shows the corresponding 2D the intensity distribution.



(a)



(b)

Figure 4.13 (a) One dimensional intensity plot for the combined PCF-CGH optical element, and (b) fragmented 2D intensity distribution of the same element.

ATTENTION: The Singapore Copyright Act applies to the use of this document. Nanyang Technological University Library

The shift of the diffraction pattern due to the convolution with the PCF can be accounted for by performing a pre-shift in the designated CGH pattern. Conventionally CGHs are designed with the spot distribution pattern centered in the far-field reconstruction plan. To illustrate, a simple one-dimensional example is shown in Figure 4.14. For the sake of simplifying the illustration, only the ±1 orders will be considered and the sinc^2 envelope will not be included in the following discussion. Practically, the sinc^2 envelope helps to contain the energy within the desired ±1 orders by reducing the intensity in the higher order. *H(x)* represents the far-field reconstruction of an arbitrary function, *K(x)* represents the far-field reconstruction of a checkerboard function, and U_4 represents the corresponding far-field pattern when *H(x)* is convolved with *K(x)*, as in the frequency-domain result from multiplying the hologram with the phase checkerboard function at the diffracting aperture. Figure 4.14(a) shows the result when a conventional hologram with the desired distribution function is designed to be at the centre, and is analogous to the two-dimensional results from Figure 4.13. Figure 4.14(b) shows the outcome when the desired distribution function 'pre-shifted' to the sides rather than at the centre. Through convolving with *K(x)*, the 'pre-shift' is 'corrected' by bringing the shifted, fragmented components back to the centre of the distribution function.

ATTENTION: The Singapore Copyright Act applies to the use of this document. Nanyang Technological University Library

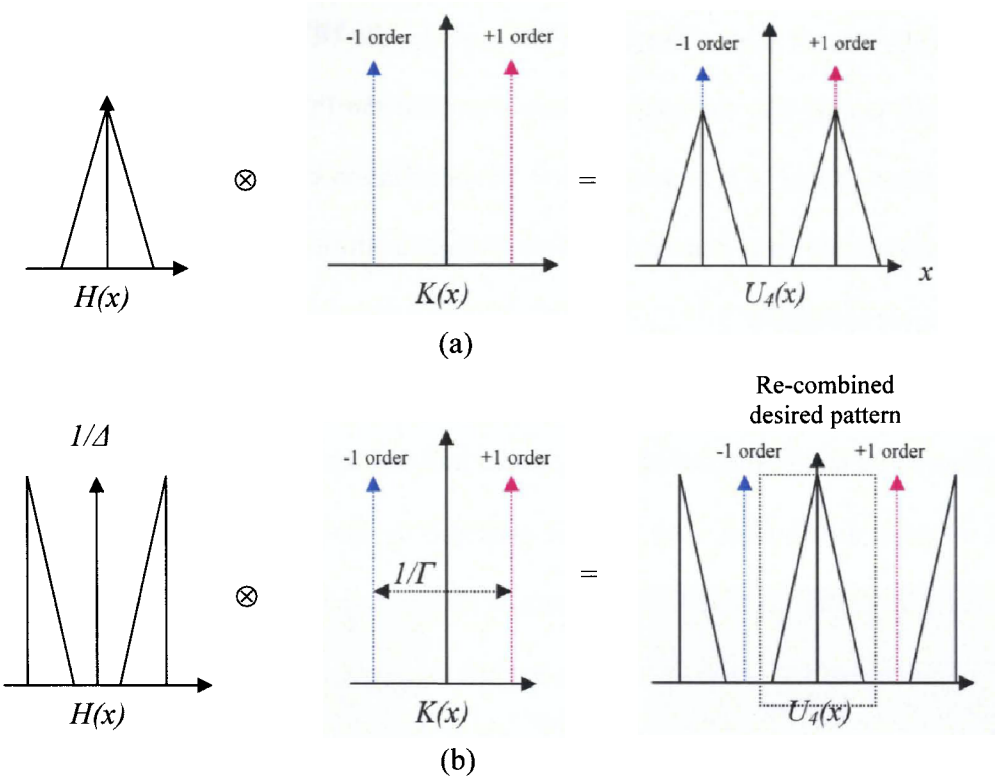


Figure 4.14 The far-field distribution functions when (a) a conventional hologram and (b) a shifted hologram are used together with a binary phase checkerboard.

Figure 4.14(b) also illustrates the importance of selecting the period of the checkerboard basic cell, as denoted by 1/2Γ, which determines the location of the diffraction orders of *K(x)*. Considering only the non-zero locations, the spacing between the non-zero orders becomes 1/Γ as the even orders have been suppressed. The proper choice of Γ can be determined from the analytical expression of the binary phase hologram given in Equation (4.9). As can be observed, due to pixelation, the binary phase hologram is repeated every 1/Δ units in the far-field. By setting 1/Γ to be equal to 1/Δ, each copy of *H(x)* can be reproduced without interference from other copies and that interference can occur if the diffraction orders of *K(x)* are too close i.e. 1/Γ < 1/Δ. Furthermore, by designing the distribution pattern to be at the edges of the *H(x)*, the condition 1/Γ = 1/Δ ensures that the diffracted pattern can be de-fragmented

ATTENTION: The Singapore Copyright Act applies to the use of this document. Nanyang Technological University Library

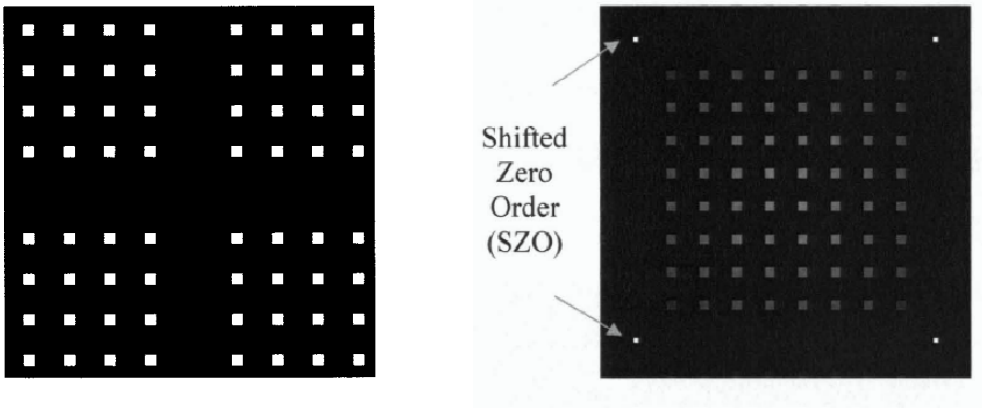
to obtain the desired pattern. In the hologram plane, the $1/\Gamma = 1/\Delta$ condition translates to an equal feature size for both the hologram and the PCF, simplifying fabrication requirements. There is also no increase in computation complexity required, as the same computation grid can be used to design a shifted hologram as well as a conventional hologram.

To make use of the PCF in the two-dimensional sense, the desired spot distribution pattern is fragmented and shifted into the corners during the design of the spot intensity distribution, such that the pattern is designed to be at the corners rather than at the centre, as shown in Figure 4.15(a) compared to Figure 4.2(a). The convolution due to the PCF thus serves to shift the spot distribution pattern back to the intended centred distribution, overcoming the fragmentation described earlier.

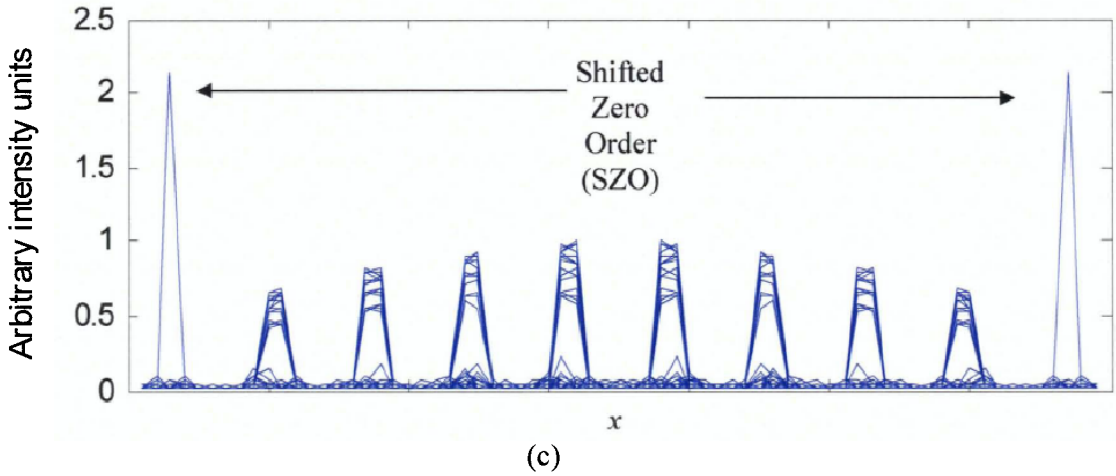
Applying this shifted hologram (SCGH) technique together with the PCF, and setting the phase levels of the SCGH to $[0, 0.9\pi]$, the intensity distributions in Figures 4.15(b) and 4.15(c) are obtained. In comparison with Figure 4.12, the zero order intensity in the GZO has been redistributed into locations of the non-zero locations of the PCF, now termed as the shifted zero orders (SZO). The zero order intensity can be observed to have been decoupled from the fabrication accuracy of the CGH. In comparison with the complex surface relief structure of a CGH, the periodicity and simplicity of the PCF would allow a better control over fabrication parameters and a more accurate reproduction of the PCF. Another useful application of the SZO which may not be immediately obvious is in spot diffusing applications for indoor optical wireless. In these applications, it is desired to improve the spread of the transmitted signal over a larger area such that signal energy is diffused more uniformly throughout the receiving plane, usually the floor. This can be achieved by increasing number of diffusing spots at the edges of the CGH distribution pattern as shown in

ATTENTION: The Singapore Copyright Act applies to the use of this document. Nanyang Technological University Library

Chapter 3. Using the SCGH-PCF method, the energy in SZO can be exploited to complement the increased number of diffusing spots such that the greater corner intensity arises as a combined effect of the increased number of spots as well as the SZO, improving uniformity of signal power distribution as well as the range of the optical wireless system. Although a line grating can yield a similar effect in place of the PCF, the resulting SZO would only be re-distribute in a one-dimensional manner which would not be as useful as the PCF's two dimensional distribution.



(a) (b)

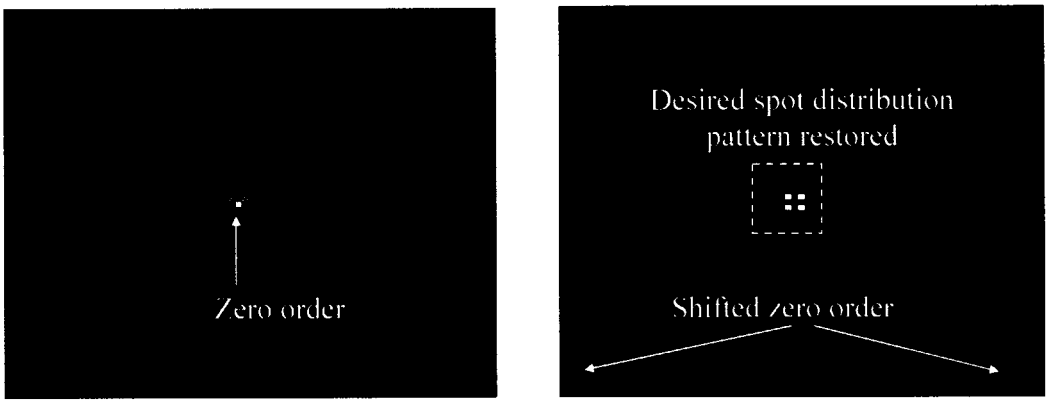


(c)

Figure 4.15 (a) SCGH design and (b) 2D spatial distribution of the resulting intensity plot; (c) one dimensional intensity plot of the SCGH-PCF optical element, showing no fragmentation of the pattern.

ATTENTION: The Singapore Copyright Act applies to the use of this document. Nanyang Technological University Library

Another advantage to the SCGH-PCF technique proposed here is that it does not affect spots which are designed to be located at the centre of the reconstruction field. The convolution introduced by the PCF shifts away the zero order and simultaneously returns the pre-shifted segments of the SCGH back to the intended locations. An illustration is shown in Figure 4.16, where a design specification requires that a 2x2 spot array clustered at the centre. Setting the phase levels at [0, 0.9π], the phase errors result in a GZO as can be observed in Figure 4.16(a). Figure 4.16(b) shows the spot intensity distribution pattern when the SCGH-PCF approach is used to design the 2x2 spot pattern. Phase levels of [0, 0.9π] have also been set for the SCGH. It can be observed that the desired clustered 2x2 spot distribution at the centre is restored while the energy in the zero order has been shifted to the SZO locations.



(a) (b)

Figure 4.16 (a) 2x2 spot array with zero order using CGH and (b) application of PCF-SCGH technique shifts away zero order with no effect on spot distribution.

To determine if there is any change in the diffraction efficiency, an experiment was carried out using the original CGH and the SCGH-PCF by introducing the same error into the phase holograms. The diffraction efficiency is defined as the proportion

ATTENTION: The Singapore Copyright Act applies to the use of this document. Nanyang Technological University Library

of energy into the desired spot pattern. The phase height was varied from 0.8π to π, and it was found that on average the difference between the diffraction efficiency of the CGH and SCGH-PCF was only about 0.4%.

4.7 Simulation of fabrication errors and discussion

In this section the effect of fabrication errors on the performance of the SCGH-PCF optical element will be simulated and discussed. First, the effect of phase depth errors will be determined by varying the phase levels of the SCGH and PCF from 0.8π to 1.0π. As a reference, the GZO due to phase level errors in a conventional CGH was simulated, and this is shown in Figure 4.17 as GZO/I_s which represents intensity in the GZO taken as a ratio over the average spot intensity. It can be observed from Figure 4.17 that there is a large exponential increase in the GZO/I_s ratio at the reduced phase height. Next, the effect of varying the phase levels in the SCGH of the combined SCGH-PCF optical element was simulated, while the phase height of the PCF was held constant at binary values [0, π]. The use of the SCGH-PCF element results in all the energy in the zero order being re-distributed to the higher orders, and this is represented as SZO/I_s in Figure 4.18. The values of SZO/I_s as compared to GZO/I_s is about four times lower due to the redistribution of the GZO intensity into the four SZOs, as was illustrated in Figure 4.15(b). At the same time, there is no zero order in the GZO location. Finally, the effect of phase levels on the PCF was explored by varying the phase levels of the PCF from 0.8π to 1.0π, while maintaining [0, 0.9π] binary phase levels for the SCGH. This results in energy in the SZO and the GZO, with the GZO intensity due to the phase level variation in the PCF. The GZO in this scenario is represented as $(GZO/I_s)_K$ in Figure 4.17. As the phase levels in the PCF are reduced to represent increasing phase depth errors, the $(GZO/I_s)_K$ increases. However,

ATTENTION: The Singapore Copyright Act applies to the use of this document. Nanyang Technological University Library

the amount of energy in the GZO is much less than the scenario where a conventional hologram is used. For example, when the binary phase levels of the CGH are [0, 0.9π], the GZO/I_s ratio is 3.195. When such binary phase levels is used in the SCGH and the PCF, the corresponding $(GZO/I_s)_K$ ratio is 0.0837, a 38.1720 reduction as compared to the previous case for the CGH. A similar trend can be observed throughout the phase values simulated in Figure 4.17. Furthermore, the performance of the SCGH-PCF element can be observed to be tolerant to errors in the PCF. From Figure 4.17, when there is a 2% error in the CGH phase level resulting in [0, 0.98π] phase heights, the GZO/I_s ratio is approximately 0.1 In the combined SCGH-PCF optical element, the phase levels corresponding to such a ratio are [0, 0.8907π] for the PCF, an approximate 11% phase error, suggesting that there is a fivefold tolerance in the phase. Also, this 11% occurs when a 10% error has been introduced into the SCGH, and it is interesting to note that the GZO performance for this scenario is on par with the zero order performance of a tightly controlled fabrication process which allows only a 2% error. Figure 4.18(a) shows the GZO which arises due to [0, 0.9π] binary phase levels in the SCGH, and Figure 4.18(b) shows GZO when [0, 0.8π] are the phase levels in the PCF.

ATTENTION: The Singapore Copyright Act applies to the use of this document. Nanyang Technological University Library

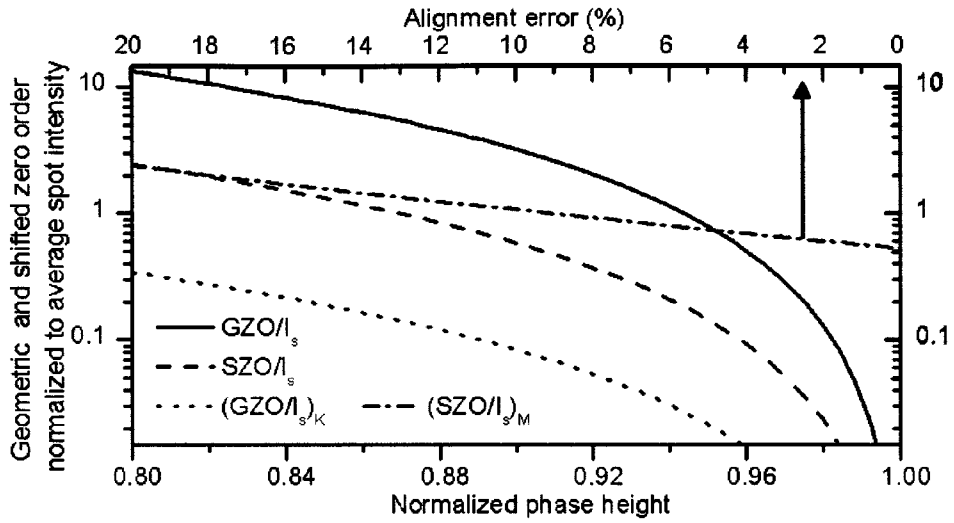


Figure 4.17 Performance of the CGH and SCGH-PCF optical element in the presence of phase level and alignment errors.

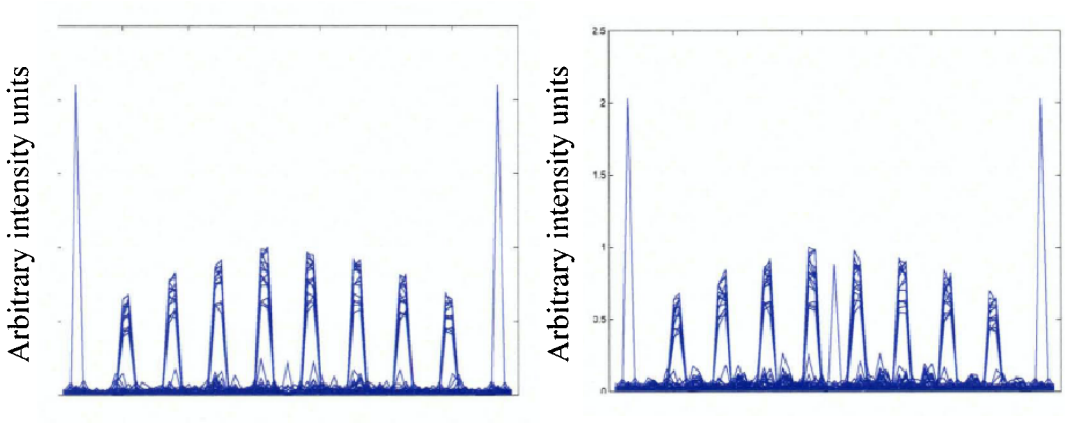


Figure 4.18 The intensity plots when the SCGH has binary phase levels of [0, 0.9π] and the PCF has binary phase levels of (a) [0,0.9π] and (b) [0, 0.8π].

During these simulations, it was also observed that there was minimal change in the relative intensity distribution within the spots, implying that use of the SCGH-PCF has not resulted in distortion of the desired spot distribution. Another potential source of error is misalignment between the SCGH and the PCF. To determine its effect, a variable misalignment error was introduced into a model containing the PCF

ATTENTION: The Singapore Copyright Act applies to the use of this document. Nanyang Technological University Library

and a SCGH with a 0.9 phase height, with 0% misalignment representing aligned overlay of the PCF pixel on the SCGH pixel. No GZO was observed but there was an increase in the SZO/I_s ratio, defined as $(SZO/I_s)_M$ for this scenario. The increase in SZO/I_s is less drastic than the increase due to phase errors and the results are also shown in Figure 4.17. At small errors (<5%) the performance deterioration is not particularly significant, and with nanometer-scale alignment[125] such errors can be minimized. The results suggest that the PCF-SCGH shows a good tolerance for zero order errors due to various fabrication errors.

Another possible type of fabrication error is due to unbalanced fill-factors, i.e. the portion of the hologram that is at a π phase height should be equal to the portion with a 0 phase height. When this condition is satisfied, there is no excess phase and the zero order can be avoided. Barring design problems, an unbalanced fill-factor can also arise during the fabrication process. This is due to the pseudorandom structure of the hologram with a wide range of sizes of hills and valleys in the fabricated structure. As a result, smaller features become over-etched while larger feature tend to be under-etched, causing an unbalanced fill-factor error. In comparison, for surface relief structures which are regular and periodic, as in the PCF, an accurate reproduction of the structures would be easier to accomplish. Simulations were run to determine the effect of the fill-factor error on the zero order and if the PCF was also able to redistribute the zero order. A simulation was run using a conventional CGH with binary phase values [0, π]. The fill factor was varied from 50-50 to 60-40, represented as 50% to 60% in Figure 4.19, with the percentage representing the portion that the π phase occupies over the CGH. The zero order intensity ratio GZO/I_{sF} is used to determine the zero order performance as before, and is plotted in Figure 4.19 as the fill factor is varied. It can be observed from the Figure that there is an almost

ATTENTION: The Singapore Copyright Act applies to the use of this document. Nanyang Technological University Library

exponential increase in the GZO/I_{sF} ratio suggesting that the intensity in the zero order is highly sensitive to the fill-factor. Another simulation was run using the proposed SCGH-PCF optical element. The fill-factor of the SCGH with binary phase levels [0, π] was varied to simulate fabrication errors. The PCF is taken to have been reproduced accurately due to the more periodic nature of its phase structure. Similar to the scenario described earlier for the phase depth controls, use of the PCF with the SCGH results in the intensity of the GZO being redistributed to the sampling points of the PCF, with the zero order efficiency in the shifted zero orders being represented as SZO/I_{sF} in Figure 4.19. Although the SZO/I_{sF} also increases as the fill-factor is made more unbalanced, it can be observed to increase at a slower rate when no PCF is used. In this simulation, the effect of fill-factor on the PCF is not explored. However, it would be logical to expect that a trend would be between the GZO/I_{sF} and SZO/I_{sf} similar to the Figure 4.19 could be expected in such a scenario, due to the reduced efficiency of the PCF in shifting away the zero order.

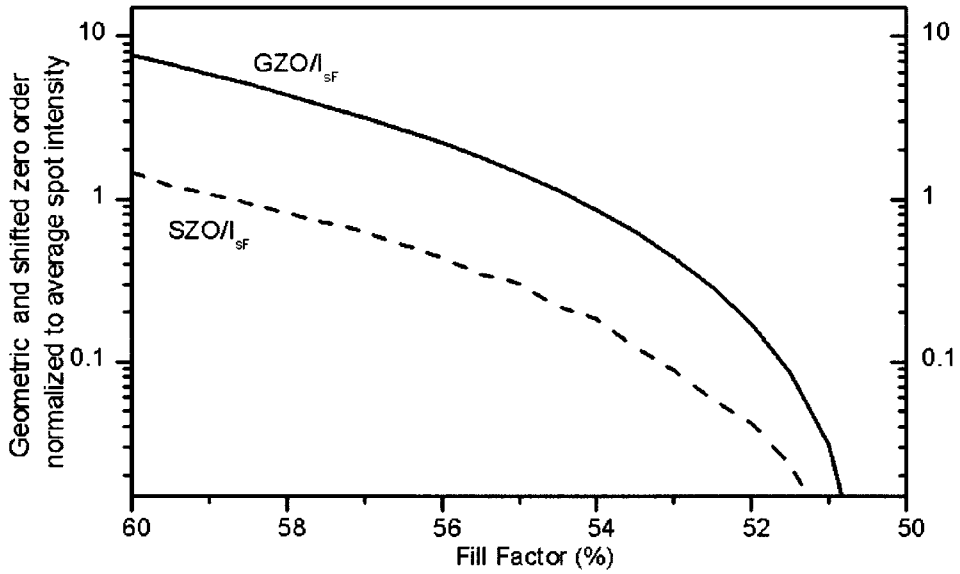


Figure 4.19 Effect of fill-factor imbalance on the zero order for a CGH and SCGH-PCF.

ATTENTION: The Singapore Copyright Act applies to the use of this document. Nanyang Technological University Library

4.8 Experimental measurements

To test the SCGH-PCF approach to reduce the zero order, an experiment was carried out using a phase-only reflective liquid crystal Spatial Light Modulator (SLM) ("512x512 SLM System") from Boulder Non-Linear Systems. The SLM consists of 512x512 pixels, with each pixel having a pitch of 15μm. The side view of the SLM is shown in Figure 4.20

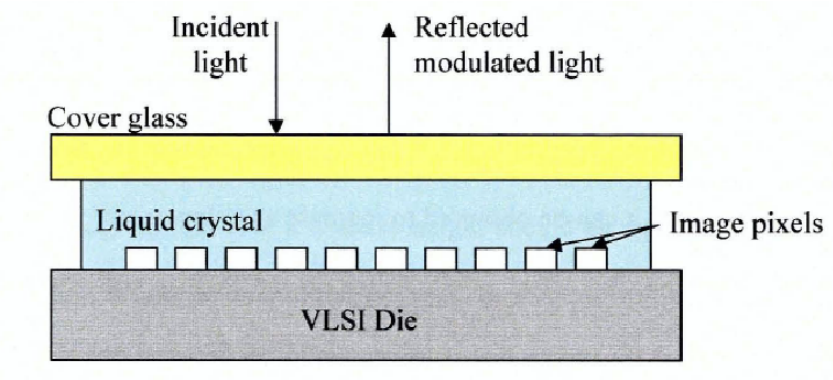


Figure 4.20 Structure of a reflective liquid crystal SLM.

Illustration is not drawn t to scale.

In using the phase-only SLM, the pixelated nature of the backplane of the liquid crystal also produces diffraction, and more importantly a zero order intensity in the reconstructed image even when the phase modulation is set to [0, π]. However, by calibrating the measurements, the minimum achievable zero order can be used as a reference level to indicate the zero order that is irreducible.. From the datasheet of the SLM, the phase modulation corresponding to the gray levels settings is shown in Figure 4.21. These gray levels will be used to characterize the SLM to determine the relative magnitudes of diffracted energy and the zero order as the gray levels are varied. The setup for the SLM for the reconstruction of the hologram pattern is shown in Figure 4.22.

ATTENTION: The Singapore Copyright Act applies to the use of this document. Nanyang Technological University Library

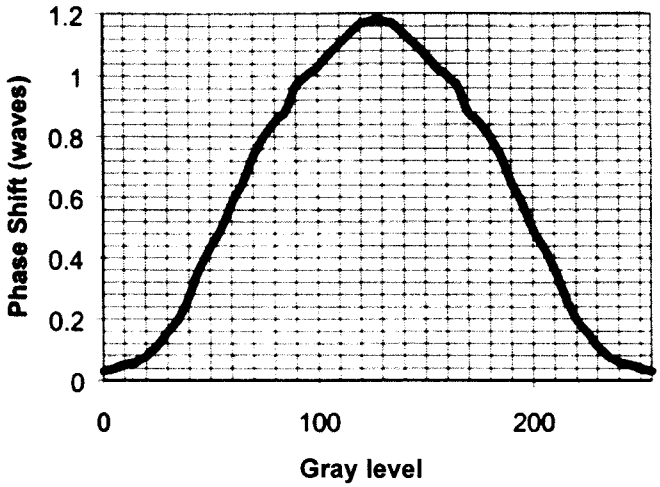


Figure 4.21 Gray level to phase shift specification from the data sheet of the SLM. [126]

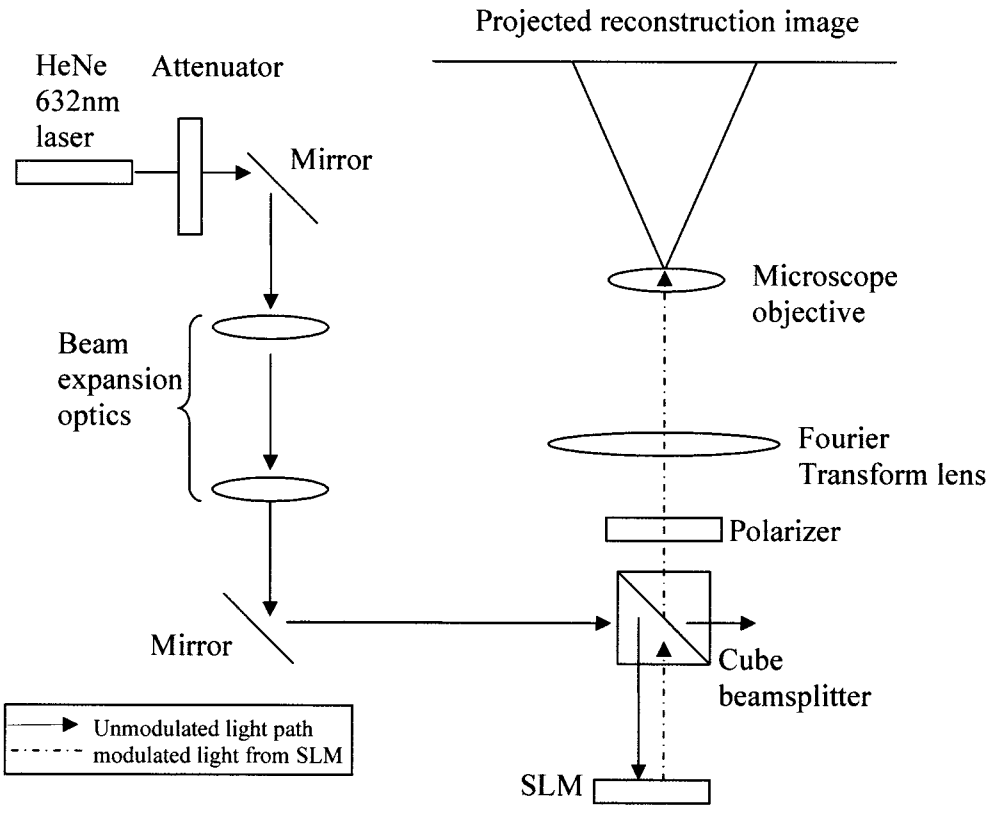


Figure 4.22 Experimental setup to reconstruct the diffracted pattern using a phase-only reflective SLM.

ATTENTION: The Singapore Copyright Act applies to the use of this document. Nanyang Technological University Library

The phase-only SLM consists of an array of nematic liquid crystals (NLC) which acts as a variable birefringent device. In such a device, the NLC molecules are aligned in parallel along the extraordinary axis. When a voltage is applied across a pixel, the increase in the electric field induces an electric dipole in each NLC molecule[123], tilting the molecules in the direction of the electric field, resulting in a reduction of the refractive index along the extraordinary axis. A sufficiently high enough voltage can result in complete alignment of the NLC molecules with the electric field, such that the birefringence of the device is minimum. In contrast, when there is no applied field, the NLC molecules revert to their original parallel spatial orientation, such that birefringence of the pixel is maximum. By aligning the polarization direction of the incident light in parallel with the extraordinary axis of the NLC-SLM, phase-only spatial modulation and control of the incident beam can thus be achieved.

The HeNe laser was oriented in such a way so as to align the linearly polarized beam to the extraordinary axis of the NLC-SLM. An attenuator was placed at the output of the laser to attenuate the beam intensity as it was found that the high sensitivity of the CCD camera used to capture the reconstructed pattern was over-saturated when no attenuator was used. To ensure that the incident laser beam fully engaged the SLM, the beam diameter was expanded using the pair of lenses. The expanded beam is reflected by the non-polarizing 50-50 cube beamsplitter into the active area of the SLM. Depending on the voltage setting of the pixel at the SLM backplane, the reflected light may or may not be modulated. A polarizer placed at the back of the beamsplitter helps to further filter out any depolarized light. The phase-modulated light is then focused onto the focal plane of the microscope objective, and is projected onto a screen where the intensity of the diffracted energy is measured. To

ATTENTION: The Singapore Copyright Act applies to the use of this document. Nanyang Technological University Library

capture the diffracted image, the microscope objective is replaced with a CCD camera which is placed at the back focal plane of the Fourier Transform lens.

4.8.1 Characterization of the SLM by varying the gray levels

In order to the verify gray level to phase level modulation mapping as specified in Figure 4.21, characterization of the SLM was performed using the setup shown in Figure 4.22. A conventional 8x8 spot CGH pattern was used in the SLM to measure the intensity in the zero order and that of the diffracted pattern. As the SLM has 512x512 pixels, to fully use the active area of the SLM, the 64x64 pixel of the hologram was tiled 8x8 times such that the tiled pattern filled the entire active area of the SLM. Using Figure 4.21 as a reference, the gray levels were varied such that the binary phase levels in the image input into the SLM were [0, G], where G refers to the gray level modulation. In the simulation, only one wavelength of phase modulation is required and hence the gray level variation was limited in range from 0 to 95.

Inputting these holograms into the SLM and projecting the reconstructed pattern such that the zero order and diffracted spots were separated enough to be measurable, the zero order and diffracted energy were measured via a power meter. As an added precaution, an aperture was constructed that limits the incident power into the power meter such that only the zero order was measured by the power meter. Due to the limitations of the size of the active area of the power meter, it was not possible to measure the energy of the entire diffracted pattern of the hologram. Instead, a cluster of spots from the diffracted image was measured and the intensity as the gray level is varied in the SLM can be used as indicative of the extent of modulation. The measured results are shown in Table 4.1 below. To improve the readability of the effect on the zero order intensity and diffracted energy as the gray

ATTENTION: The Singapore Copyright Act applies to the use of this document. Nanyang Technological University Library

level is varied, the zero order intensity was normalized against the minimum zero order intensity while the diffracted energy was normalized against the maximum diffracted energy. The normalized values are plotted in Figure 4.23 and are also included in Table 4.1.

Table 4.1 Measured and normalized zero order intensities as the gray level in a CGH is varied

Gray level	Measured Diffracted Intensity (μW)	Measured Zero order Intensity (μW)	Normalized Diffracted	Normalized Zero Order
0	0.19	152.00	0.13	8.26
25	0.42	126.00	0.29	6.85
35	0.69	100.00	0.47	5.43
38	0.81	89.00	0.55	4.84
40	0.92	80.20	0.63	4.36
50	1.46	23.90	1.00	1.30
55	1.43	18.40	0.98	1.00
60	1.08	42.00	0.74	2.28
70	0.25	117.00	0.17	6.36
75	0.21	129.00	0.14	7.01
85	0.41	118.00	0.28	6.41
95	0.47	115.00	0.32	6.25

ATTENTION: The Singapore Copyright Act applies to the use of this document. Nanyang Technological University Library

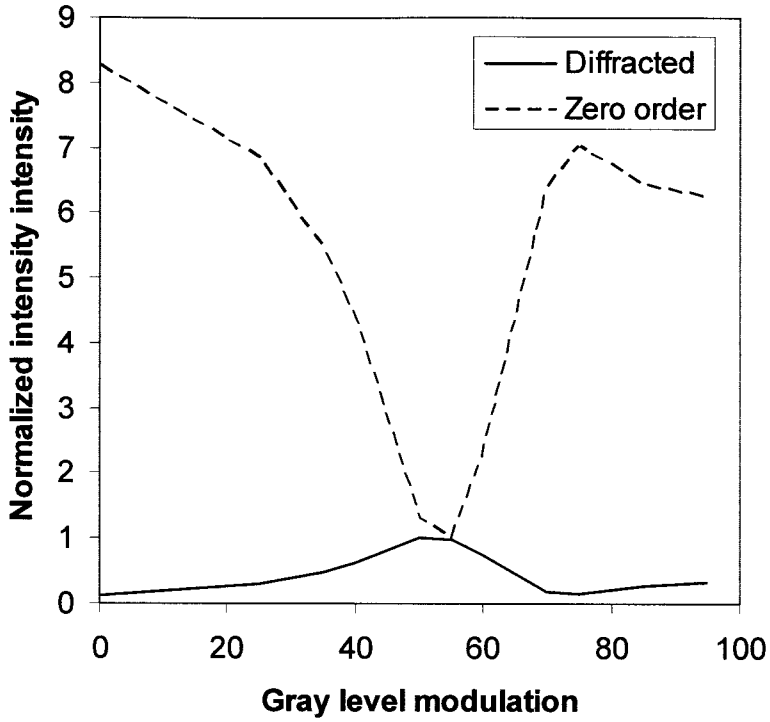


Figure 4.23 Normalized zero order and diffracted intensities as the gray level of a phase-only SLM is varied.

From Figure 4.23, it can be observed that as the gray level is increased from 0 to 55, the normalized diffracted intensity increases while the normalized zero order intensity decreases. This agrees well with the trend from the datasheet in Figure 4.21 which indicates an increase in the phase modulation level from 0 to 0.5λ corresponding to 0 to π radians as the gray level is increased from 0 to 55. As the gray level is further increased from 55 to 95, the phase modulation should further increase from 0.5λ to λ corresponding to π to 2π radians. Ideally the diffracted energy and zero order should return to a similar level when the phase modulation is 0 or 2π radians as it corresponds to effectively no phase difference between the two phase levels. However, it can be observed from Figure 4.23 that the diffracted energy increased beyond the gray level of setting of 75. Due to the unexpected behaviour of the SLM

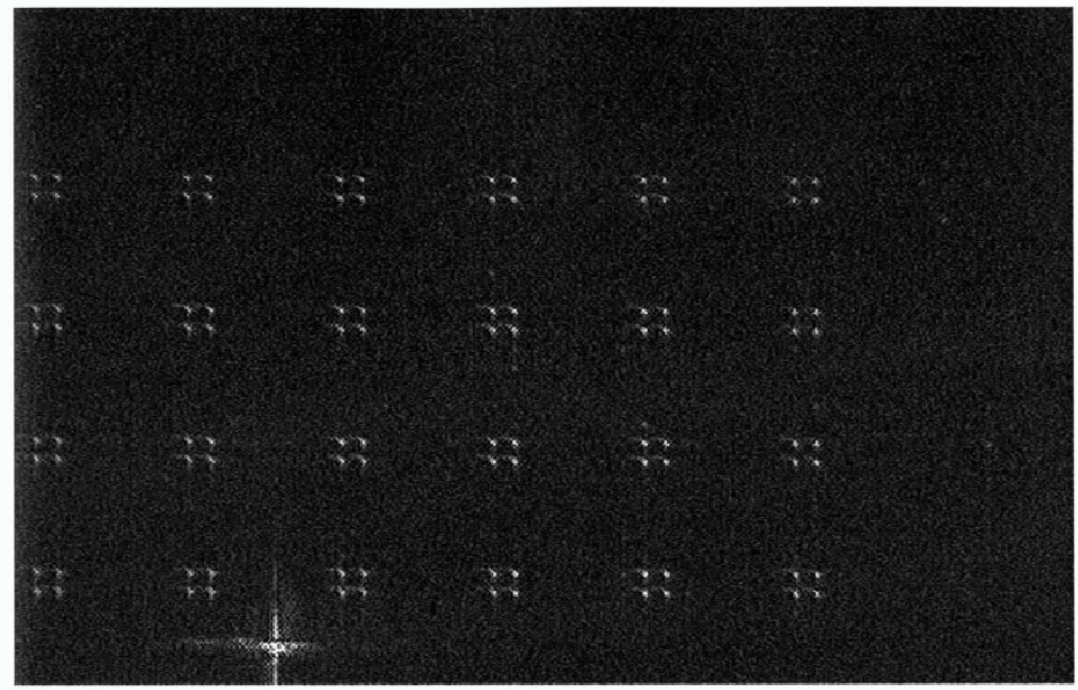
ATTENTION: The Singapore Copyright Act applies to the use of this document. Nanyang Technological University Library

beyond the gray phase level of 75, phase modulation was limited to gray levels of 75 and below, which correspond to phase modulation levels of 0.8λ or 1.6π. Making use of the results from Figure 4.23 and the characterization specification from Figure 4.21, the gray-level to phase modulation was mapped out as shown in Table 4.2. Images of the reconstructed pattern at gray levels of 55 and 35 are also shown in Figures 4.24(a) and 4.24(b) respectively. It can be observed that the diffracted intensity when the gray level is 35 is much lower than when the gray level is 55.

Table 4.2 Gray level to phase modulation mapping for the SLM

Gray	λ	π
0	0	0
25	0.1	0.2
35	0.2	0.4
38	0.25	0.5
40	0.3	0.6
50	0.4	0.8
55	0.5	1
60	0.6	1.2
70	0.7	1.4
75	0.8	1.6

ATTENTION: The Singapore Copyright Act applies to the use of this document. Nanyang Technological University Library



(a)



(b)

Figure 4.24 Far-field reconstruction pattern when the binary gray levels are (a) [0, 55] = [0, π]; and (b) [0, 35] = [0, 0.4 π].

ATTENTION: The Singapore Copyright Act applies to the use of this document. Nanyang Technological University Library

4.8.2 Experiments using the combined SCGH-PCF optical element

Using the obtained results from Section 4.7.1, the phase levels for a SCGH-PCF element were mapped to gray levels. Letting the binary phase levels of a SCGH be [0, θ], when a PCF with [0, π] phase levels is added in a SCGH-PCF configuration, the resulting phase levels in the combined SCGH-PCF element would thus result in four possible phase levels

$$SCGH \in \{0, \rho\} + PCF \in \{0, \pi\} \rightarrow SCGH - PCF \{0, \rho, \pi, \rho + \pi\} \qquad (4.12)$$

Taking into consideration that the maximum phase modulation due to the hardware limitations is 1.6π which corresponds to the maximum phase being $(\rho + \pi)$, the maximum phase level of the SCGH is thus $\rho = 0.6\pi$. To stay within this limitation, three different sets of values corresponding to $\rho = 0.4\pi, 0.5\pi, 0.6\pi$ were used in the experiment, and the gray levels sets are shown below in Table 4.3. Set 0 was included as a reference to determine the performance when there is no error in the SCGH.

Table 4.3 Values used in the SCGH-PCF for input into the SLM

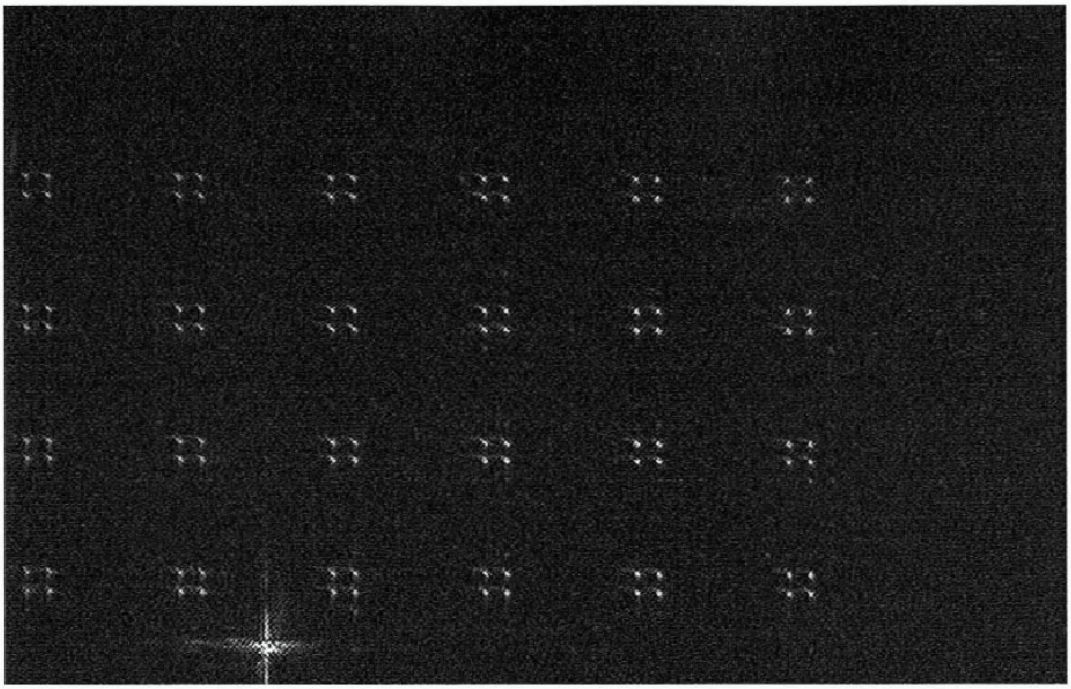
	Set 0		Set 1		Set 2		Set 3	
SCGH-PCF phase heights	Phase levels	Gray levels	Phase levels	Gray levels	Phase levels	Gray levels	Phase levels	Gray levels
0	0	0	0	0	0	0	0	0
ρ	π	55	0.6π	40	0.5π	38	0.4π	35
π	π	55	π	55	π	55	π	55
$\rho + \pi$	1.6π	75	1.6π	75	1.5π	73	1.4	70

ATTENTION: The Singapore Copyright Act applies to the use of this document. Nanyang Technological University Library

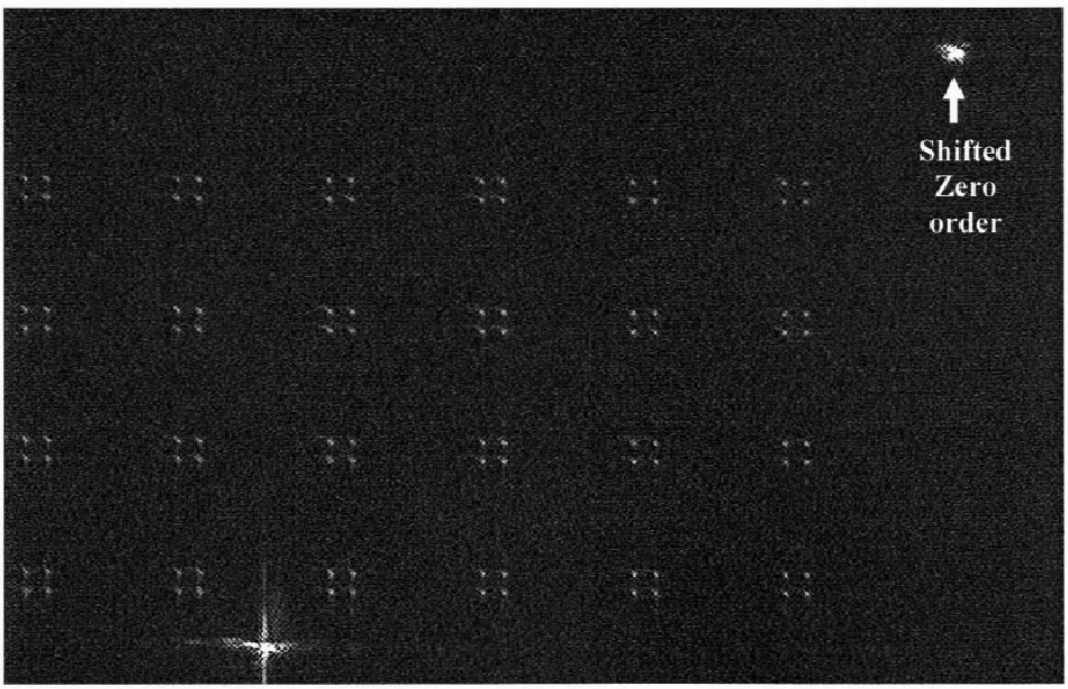
The SCGH-PCF gray levels from Table 4.3 were input into the SLM and the resulting zero order and diffracted energy in the reconstruction pattern were measured in the same way as in Section 4.7.1. Using a CCD camera, images of the reconstructed pattern were also captured. Figure 4.25(a) shows the reconstructed pattern for Set 0, when there is no phase error in the SCGH. The same intensity distribution pattern is observed as in Figure 4.24(a), and this is expected as the combined SCGH-PCF element should return the same intensity distribution as that of a CGH when there is no zero order present.

Figure 4.25(b) shows the intensity pattern when the phase levels are from Set 1. It can be observed that the shifted zero order appears due to the redistribution of the geometrical zero order intensity to the shifted zero order locations. Three other shifted zero orders also can be observed in the other three other corners of the diffracted spot distribution pattern. However, due to the size of the CCD used, only one quadrant could be captured. Figure 4.25(c) shows the intensity pattern for Set 3 where the SCGH levels are at [0, 0.4 π]. It can be observed that the diffraction pattern is stronger than compared to a CGH having the same binary phase levels but with no PCF as in the scenario presented in Figure 4.24(b).

ATTENTION: The Singapore Copyright Act applies to the use of this document. Nanyang Technological University Library

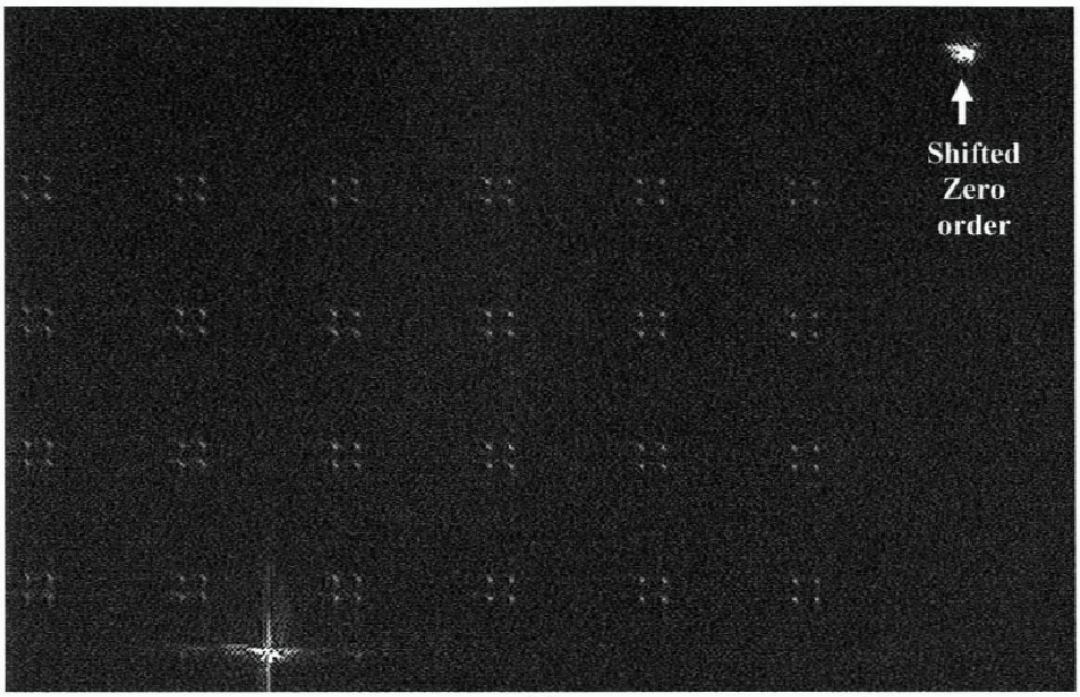


(a)



(b)

ATTENTION: The Singapore Copyright Act applies to the use of this document. Nanyang Technological University Library



(c)

Figure 4.25 Intensity pattern for (a) Set 0, (b) Set 1 and (c) Set 3 corresponding to [0, π], [0, 0.6π], and [0, 0.4π] binary phase levels in the SCGH respectively.

To further quantify the results, measurements were made of the zero order and the diffracted intensity in the same manner as in Section 4.7.1. As mentioned earlier, due to limitations in the hardware setup it was not possible to entirely capture the total diffracted intensity and as such the measured value only presents a fraction of the total diffracted energy. However, the relative changes in the diffracted intensity as the phase level is varied should be indicative of the performance of the hologram. Also, the zero order intensity of the SCGH-PCF with no phase errors using the gray levels from Set 0 was also measured, and it was found that the zero order intensity was comparable to the CGH hologram with no phase errors.

The measured diffracted intensity and zero order results are plotted in Figures 4.26 and 4.27 respectively. To compare against the diffracted and zero order

ATTENTION: The Singapore Copyright Act applies to the use of this document. Nanyang Technological University Library

intensities having the same gray level in the CGH as in the SCGH when no PCF was employed, the results from the CGH measurements performed earlier have also been included. The gray level modulation in the x-axis of Figure 4.26 and 4.27 indicate the binary phase level of the SCGH and CGH, which are taken to have one level at zero phase and one level at the phase modulation indicated on the x-axis. Also, the PCF applied to the SCGH is taken to have [0, π] binary phase levels. As can be observed from Figure 4.26, as the gray level increases towards π the diffracted intensity increases for both the CGH and the SCGH-PCF holograms. When the SCGH-PCF hologram is compared to the CGH hologram, the diffracted intensity can be observed to have increased by approximately 20% throughout the range of phase levels tested. Taking these results on their own, they imply that use of the SCGH-PCF does not adversely affect the distribution of the intensity but rather is advantageous by enhancing the diffracted intensity.

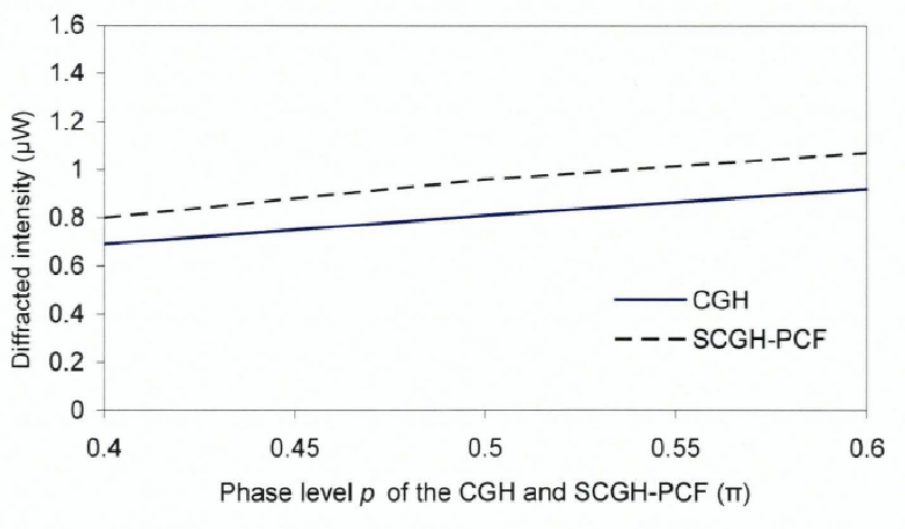


Figure 4.26 Diffracted intensity for the SCGH-PCF and the CGH as the phase level is varied.

ATTENTION: The Singapore Copyright Act applies to the use of this document. Nanyang Technological University Library

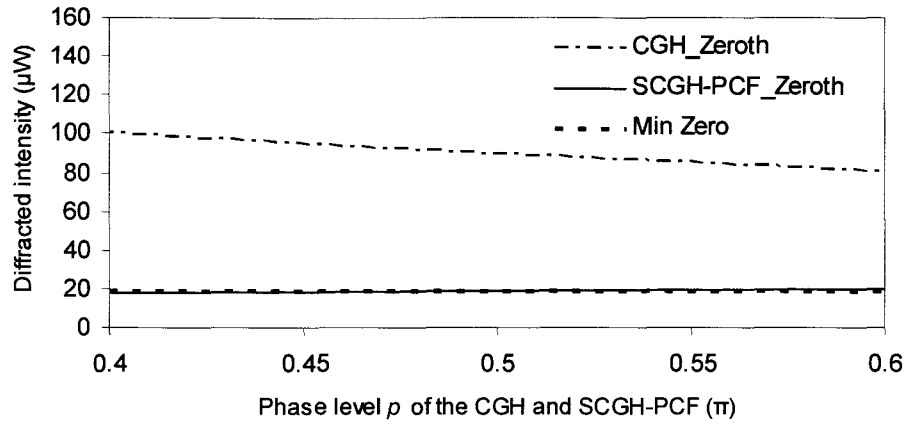


Figure 4.27 Zero order intensity levels for the SCGH-PCF and the CGH. The minimum zero order has also been included as a reference.

Figure 4.27 above shows the zero order intensity as the phase levels in the SCGH-PCF and the CGH is increased. It can be observed that a decrease in the phase level results in an increase in the zero order intensity for the conventional CGH pattern. The interesting result is when the SCGH-PCF pattern is used, as the phase level is decreased, the zero order intensity is almost constant, suggesting the increase in the zero order energy is now transferred to the diffracted patterns and the shifted zero order. The minimum achievable zero order is also included in Figure 4.27 as a comparison and it can be seen that use of the SCGH-PCF has resulted in reducing the zero order to near minimum levels, even though the SCGH itself has non-ideal phase levels. Taking the minimum level to be due to the contribution from the physical characteristics of the SLM itself, it can be concluded that the SCGH-PCF optical element has suppressed the zero order that arises from the phase level errors in the SCGH. Furthermore, from Figure 4.26, it can be observed that some of the zero order energy has been redistributed to the diffracted energy, enhancing the desired spot distribution pattern. The sum of the intensities in the four shifted zero orders is plotted

ATTENTION: The Singapore Copyright Act applies to the use of this document. Nanyang Technological University Library

in Figure 4.28. As the phase level decreases, the shifted zero order increases, which agrees well with the earlier simulation results. The difference between the decrease in the zero order and the increase in the shifted zero order could be attributed to distribution of the zero order intensity to diffracted intensity as well as some of the higher order locations.

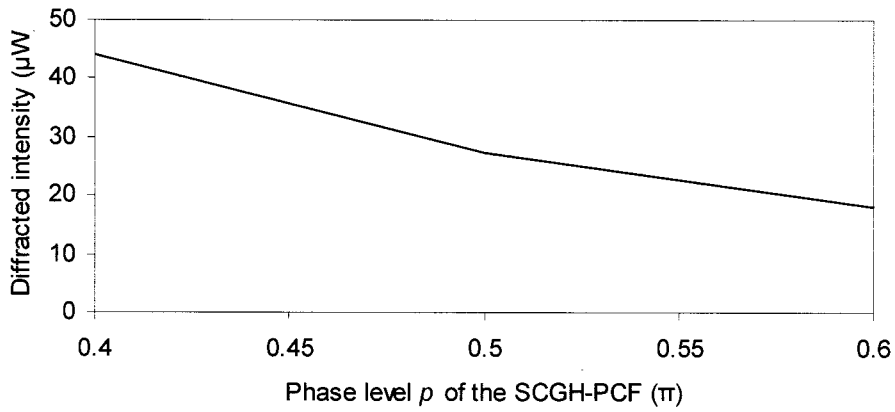


Figure 4.28 Measured shifted zero order intensity as the phase level of the SCGH is varied.

4.9 Comparison with other methods

In comparison with physical blocks of the type in [117] or [118], although some positioning is required to align the SCGH and PCF elements, this can be done by visually aligning the two elements, whereas the methods in [117] or [118] require functional alignment where the actual pattern has to be reconstructed for the blocks to be placed. Further, through the SCGH-PCF method, the desired spot pattern remains at the centre of the reconstruction plane and it is the zero order which is shifted away. This is in contrast with the method in [119], where the pattern is shifted away instead, leading to a reduced diffraction efficiency. As was shown, the SCGH-PCF method

ATTENTION: The Singapore Copyright Act applies to the use of this document. Nanyang Technological University Library

was shown to have a similar diffraction efficiency as when a conventional CGH was used.

While methods like in [112] or [120] are important to eliminate the zero order in during the design of the phase profile, they do not take into account the zero order introduced during fabrication. In the earlier section, in contrast, the SCGH-PCF method has also been shown to be resilient to fabrication errors for both phase errors and fill factor errors, and can be used together with [112] or [120]. Although fair criticism of the method can be that it simply transfer the fabrication errors from the SCGH to the PCF, the results from Section 4.7 have shown good tolerance to fabrication errors on the PCF. Furthermore, as a regular repeating pattern, the PCF is less challenging to fabricate than the varying sized structures of a phase profile of a binary spot array generator.

4.10 Conclusion

Diffractive optics are useful elements in many applications for creating a regular array of spots or an arbitrary diffraction pattern. However, one of the challenges with the use of diffractive optical elements is the zeroth order in the reconstructed image. The zeroth order is sensitive to phase errors in the surface relief structures in binary phase holograms, such as fill-factor errors and etch depth errors.

To suppress the zeroth order three methods were studied in this chapter. The first involved using a setup consisting of bulk optics. By making use of the polarization properties of the source, the zero order could be reduced and reused to enhance the diffracted orders. However, due to the inability to fully re-use the zero order, approximately 25% of the zero order would be wasted.

ATTENTION: The Singapore Copyright Act applies to the use of this document. Nanyang Technological University Library

The second approach involved placing a square phase plate into the path of the complex wavefront after the hologram to compensate for the excess phase causing the zeroth order. Although the geometric zeroth order was effectively suppressed, the addition of the square phase plate led to a distortion of the diffracted spot array as well as broadening the zeroth order, and makes this method impractical.

The third approach was found to be the most useful in obtaining a diffracted pattern free of the zeroth order and without any distortion in the diffracted pattern. By making use of a phase checkerboard phase element, the zero order intensity can be effectively redistributed to the higher order. The fragmentation caused during the redistribution process can be corrected for by pre-shifting the desired spot distribution during the design of the hologram. In such a manner, the fragmentation due to the phase checkerboard element serves to combine the pre-shifted portions back into the desired spot distribution. Various fabrication errors were simulated and it was shown that the proposed technique is applicable in these scenarios to overcome the zero order error. While the performance of the zero order depends on the phase checkerboard, the simplicity of fabrication due to its periodic nature makes it preferable over optimization of the more complex hologram structures. Furthermore, it was also shown that the combined optical element is more resilient to phase errors as compared to a conventional hologram. Experimental measurements using a spatial light modulator have also demonstrated the viability of the application of this technique in redistributing the zero order intensity. The application of the technique to diffractive optics systems in reducing the effect of the zeroth order could improve the performance of optical wireless communications substantially.

ATTENTION: The Singapore Copyright Act applies to the use of this document. Nanyang Technological University Library

5

Design and implementation of a visible light optical wireless transmission system employing white light emitting diodes

5.1 Introduction to the Chapter

Traditionally near-infrared wavelengths from 850nm to 1550nm have been suggested for use in indoor optical wireless due to their maturity in commercial optical fiber optic applications. In recent years there has been an increased interest in the use white light emitting diodes (WLED) as a replacement for indoor illumination. The opto-electronic nature of the WLED can be exploited to modulate the WLED

ATTENTION: The Singapore Copyright Act applies to the use of this document. Nanyang Technological University Library

such as to incorporate a data signal within the illuminated area. This chapter explores the use of WLED in a visible light optical indoor wireless application, and will report on the efforts made in the optical design, electronic design and finally the illumination and communication capabilities of the prototype WLED optical wireless system. In particular, the diffuse nature of the WLED intensity profile is exploited to achieve a uniform illumination through optimization of individual tilt angles in a lamp consisting of 125 WLEDs. A transmission system was set up to verify the optimized parameters and also to demonstrate the use of WLEDs in a wireless communication application.

5.2 Motivations driving the use of WLEDs in optical wireless

Past research efforts have been focused on employing near-infrared telecommunications wavelengths due to the maturity of fiber optic component technology, which facilitates the use of available optical components such as sources and detectors in an optical setup. However, concerns with regards to eye safety at wavelengths below 1200nm limit the transmit power of such devices [127]. Beyond 1200nm, the water in the eyes found in areas such as the vitreous humour, aqueous humour and the lens provides an additional safety factor due to water absorption at these wavelengths, which protect the photosensitive retina from damage. As will be shown in more depth later in Chapter 6, a typical 1550nm source can emit 10dB more power than a 850nm source with both having the same safety classification. In contrast to specialized near infrared communication sources, visible light illumination is ubiquitous in most living and commercial environments. If information could be somehow encoded into visible light, such sources would be both illuminative as well as communicative.

ATTENTION: The Singapore Copyright Act applies to the use of this document. Nanyang Technological University Library

White light emitting diodes (WLEDs) are one possible solution. Recently, advances in the field of WLEDs have raised the prospect of replacing conventional illumination sources with WLEDs. Light emitting diodes (LED) are solid-state optoelectronic devices which produce photos through the recombination of electrons and holes in a pn junction. Unlike conventional incandescent lighting, where light is produced as a by-product of heating a filament, LEDs are extremely efficient and can theoretically produce 'cool' light with little or no heat produced as a by product. One of the major breakthroughs in recent years was the development of a high intensity GaN-based blue LED by S. Nakamura at the Nichia Corporation in 1994 [128] which was at that time reported to have the highest output in the world. By coating the LED structure with a phosphor layer of ytrrium aluminum garnet (YAG) doped with Cerium (Ce), the blue light produced from the LED optically pumps the phosphors, producing yellowish light. Although this implies that a white LED effectively only produces blue and yellowish light, the combined light is interpreted by the retina as being 'white' light. Figure 5.1 shows the optical spectrum of a white light emitting diode. The color temperature of the white light can be varied by modifying the phosphors, such as adding red phosphors to create a 'warmer' white [129]. Alternate methods to produce white light involve making use of the light emitted from an array of colored LEDs [15] such as red, green and blue LEDs. By varying the intensity of the produced light from each LED, it would be possible to produce white light of a desired color temperature. However, the main disadvantage of such an approach is that thorough color mixing from the LED array can be a challenge to implement effectively [14].

ATTENTION: The Singapore Copyright Act applies to the use of this document. Nanyang Technological University Library

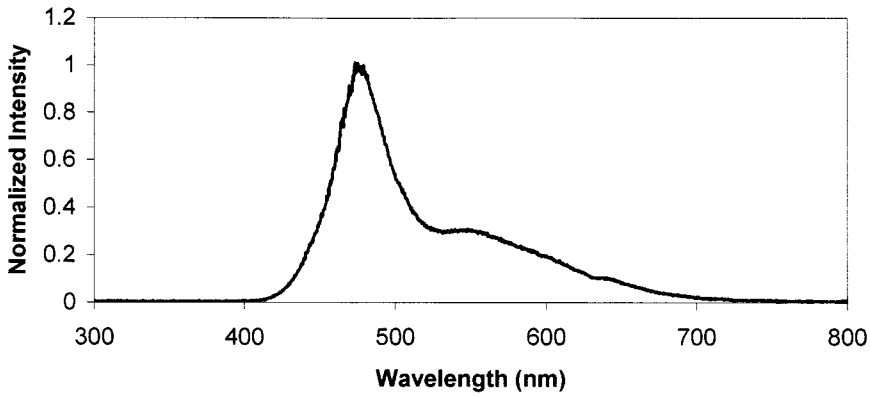


Figure 5.1 Measured optical spectrum of a typical white light emitting diode.

The adoption and trend towards solid-state lighting based on WLEDs has been primarily driven by potential energy savings from their improved efficiency, robustness and lifetime over currently employed illumination devices such as fluorescent and incandescent lighting [13]. Based on a US Department of Energy report in 2001 [12], successful penetration of solid state lighting based on an optimistic scenario where the prices of solid state lighting drop to incandescent lighting levels, 273THw of energy could potentially be saved in each. The huge potential has resulted in research interests to try to reach the large potential market for solid state lighting.

In additional to illumination purposes, the optoelectronic nature of solid state lighting can also be exploited as a means of data transfer. The human eye is generally unable to detect changes in light intensity at frequencies beyond 60Hz. By modulating the illumination produced by solid state lighting at frequencies above 60Hz, the light illumination can be used to transmit data as well as provide illumination simultaneously. When infrared wavelengths are used in conventional optical wireless communications, illumination is usually considered to interfere with the received

ATTENTION: The Singapore Copyright Act applies to the use of this document. Nanyang Technological University Library

signal quality as background noise, since the responsivity of commercial photodiodes extends into the visible range. However, by making use of illumination energy as the signal energy instead, the performance of the optical wireless system can be improves as the illumination in the indoor environment in increased.

5.3 Recent Developments in WLED Optical Wireless

The development of WLEDs for use in optical wireless systems is a recent one and most of the work has been produced by a group of Japanese researchers from Keio University. The first concept of such a system was proposed in 2001 by Tanaka et al [130], where it was stipulated that WLEDs could be used to establish a wireless home link, and a simulation model was presented to prove the theoretical concept. Later, in 2003, Komine and Nakagawa [131] reported on an integrated system combining power-line communications and WLEDs for a fully networked indoor home environment. The simulation model utilized an ideal Lambertian radiation profile for the WLED model and assumed that noise was additive white Gaussian noise. The bit rate was set at 1Mb/s and the results showed that about 99% of the receiving floor in the room had a SNR of more than 22dB. A demonstration system was also presented in the model to prove the concept of the integrated system. It was also reported to be capable of file transmission although no further details on the communications aspects were provided. Then, in a further development to the simulation model, multipath and reflection effects were included in [132], where similar to infrared wireless, it was found that multipath effects had severe effect on the system capacity.

In [133], some efforts were made to study the configurations of the various aspects in the visible light system, including the type of WLED and the modulation

ATTENTION: The Singapore Copyright Act applies to the use of this document. Nanyang Technological University Library

scheme. Of particular interest is the optical design of the WLED lighting system, which was based on the number of LED chips per lamp and the space between each chips. The criteria for the illumination aspect of the design was based on obtaining a minimum illumination of 200 lux and a maximum of 1000 lux, where a lux is a SI unit for illumination. Next, in [134], Komine et al investigated the effects of shadowing on system performance via a simulation model. Akin to that of infrared optical wireless, it was found that shadowing effects were mitigated when more WLED lamps were utilized, and was found to be particularly effective at higher transmission rates such as 800 Mbps. Most recently, Sugiyama et al[135] developed two new modulation schemes for visible light optical wireless, with the choice of scheme chosen depending on actual system requirements.

In 2006, Amirshahi and Kavehrad[136] reported on their findings in the use of visible light optical wireless together with broadband powerline networks. In the widely publicized work, they found through simulations based on multipath considerations only, that the theoretically achievable transmission for the visible light optical wireless link was as high as 1Gbps.

From the optical aspects of the work surveyed, it was observed that most of the optical design in the arrangement of WLEDs for the illumination of the indoor environment was done arbitrarily, resulting in large differences between the corners and the central regions of the simulated environments. Although the work in [133] presented some aspects of optical design with regards to the spacing between the LED chips, the illumination criteria was based more on a minimum level and a generous upper limit was 5 times that of the minimum level. Also, though most of the work reported has claimed that the minimum illumination levels are sufficient for office work, large variations in the illumination levels may be uncomfortable for users as

ATTENTION: The Singapore Copyright Act applies to the use of this document. Nanyang Technological University Library

well as a potential source of link outages particularly at the corners. To correct for this, optimization processes can be used to determine the optimum position of the WLEDs to achieve a more uniform distribution of illumination from the centre to the corners. In the following sections an optical wireless system is proposed incorporating optical design elements to ensure a uniform illumination of the room by making use of an optimization algorithm. The electronic design will also be presented. Finally the experimental system is assembled and measurements will be made to determine the performance of the optical wireless systems.

5.4 Optical Illumination Design Process

5.4.1 Source modelling

Conventionally, illumination design is carried out by making use of photometric methods and expressions rather than radiometric ones. However, due to equipment limitations, the proceeding work carried out employs radiometric quantities. However, if necessary, conversion of radiometric to photometric quantities can also be performed by integrating the received wavelength spectrum with the typical sensitivity of the human eye.

The following model is used to determine the illumination due to a WLED mounted on the ceiling a distance S away from the receiving plane. In a typical office environment, S is approximately 2m, representing the distance from the ceiling to a desktop height level. In this room model, as the LED active area is usually less than 1cm^2 which is about 2-3 orders less than the typical distances simulated, the LED can be approximated as a point source. Thus, the irradiance H on a surface due to a point source is defined as the product of the radiant intensity J of the source and the solid angle Ω subtended by the surface from the source. With reference to Figure 5.2, if the

ATTENTION: The Singapore Copyright Act applies to the use of this document. Nanyang Technological University Library

source is defined to be located in a 'ceiling' plane at a perpendicular distance S away from a 'receiving' plane, and letting θ_T be the tilt angle of the source with respect to the normal of the ceiling plane and θ_R be the angle between the normal of the ceiling plane and a vector connecting any arbitrary point on the receiving surface to the source, H can be written as

$$H(\theta_T;\theta_R,S) = J(\theta_T,\theta_R)\cdot\Omega(\theta_T;\theta_R,S) \tag{5.1}$$

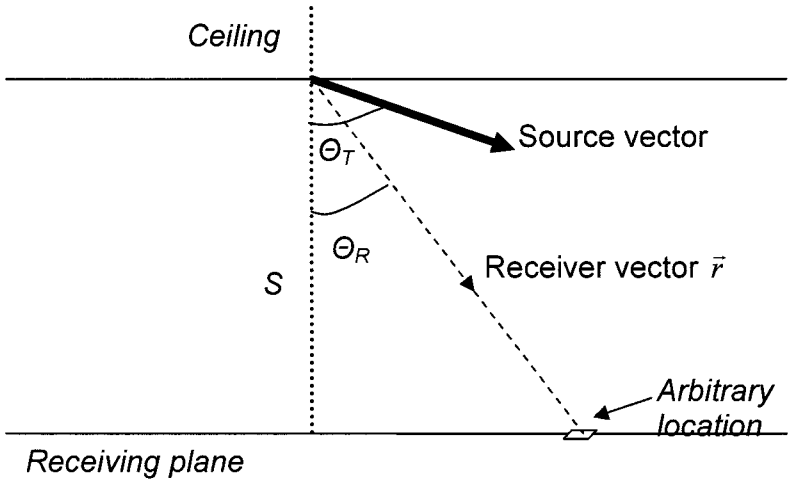


Figure 5.2 Definition of terms for the irradiance at an arbitrary location on the receiving plane.

For a source irradiating a flat surface, the solid angle subtended by the receiving surface is reduced by a factor of $\left(\frac{\cos\theta_R}{S}\right)^2$ and $\cos(\theta_R)$ due to the source-to-surface angle and reduced effective area respectively[88], such that

$$H(\theta_T;\theta_R,S) = J(\theta_T;\theta_R,S)\cdot\left(\frac{\cos\theta_R}{S}\right)^2\cos\theta_R \tag{5.2}$$

ATTENTION: The Singapore Copyright Act applies to the use of this document. Nanyang Technological University Library

A more general two-dimensional expression can be obtained by letting the irradiance be re-expressed as $H\left(\theta_{Tx},\theta_{Ty};X,Y,S\right)$, where θ_{Tx} and θ_{Ty} represent the x and y tilt angles of the source with respect to the x-z and y-z planes respectively, and where (X,Y) represents the location of the receiving area. With reference to Figure 5.3, the following quantities can be determined, where s_x and s_y represent the projection of the source direction vector onto the x and y planes respectively.

$$s_x = S\tan\theta_{Tx}$$

$$s_y = S\tan\theta_{Ty}$$

$$\tan\theta_1 = \frac{\sqrt{X^2+Y^2}}{S}$$

$$\tan\theta_2 = \frac{\sqrt{s_x{}^2+s_y{}^2}}{S}$$

$$L_1 = \sqrt{s_x{}^2+s_y{}^2}$$

$$L_2 = \sqrt{X^2+Y^2+S^2}$$

$$L_3 = \sqrt{S^2+L_1{}^2}$$

$$L_4 = \sqrt{(X-s_x)^2+(Y-s_y)^2}$$

$$\cos\Delta\theta = \frac{L_2{}^2+L_3{}^2-L_4{}^2}{2L_2L_3} \tag{5.3}$$

ATTENTION: The Singapore Copyright Act applies to the use of this document. Nanyang Technological University Library

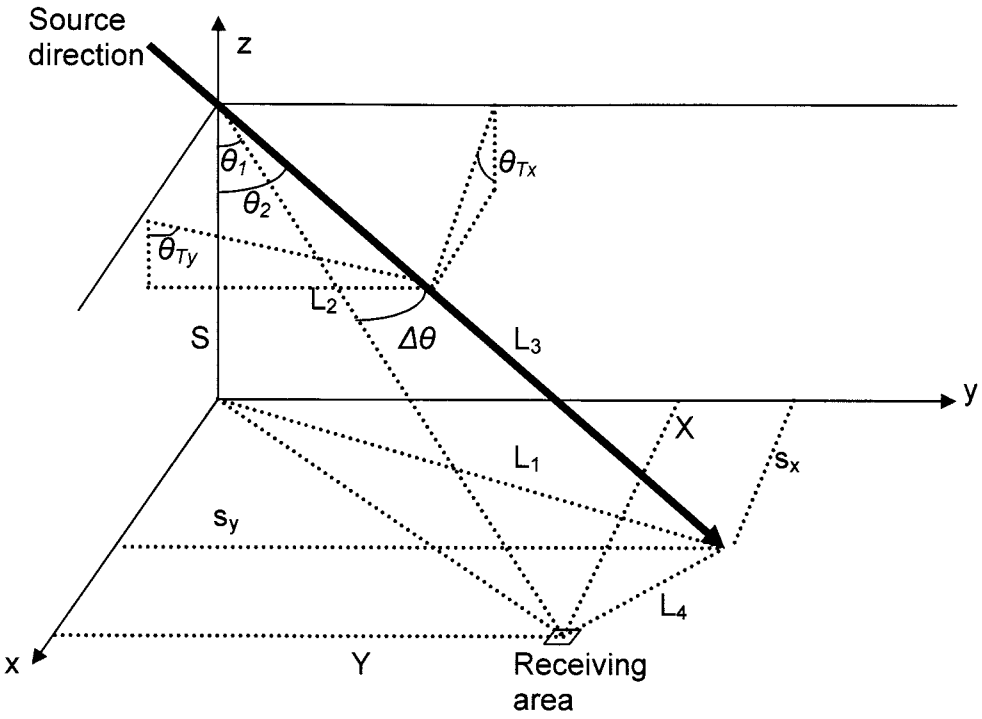


Figure 5.3 Definition of terms used in the two-dimensional modelling of the irradiance due to an arbitrarily tilted source.

Due to the generally rotationally symmetric nature of the radiant intensity J of a source, only the relative angle $\Delta\theta = \theta_T - \theta_R$ between the LED source angle and the direction of the receiving area is required, i.e. $J(\Delta\theta, S)$. Using the preceding equations, the general expression for the irradiance on a flat surface due to a source can be found to be given by the following, where $\Delta\theta$ is obtained by using the expression (5.3) obtained earlier.

$$H(\theta_{Tx}, \theta_{Ty}; X, Y, S) = J(\Delta\theta, S) \cdot \left(\frac{\cos\theta_1}{S}\right)^2 \cos\theta_1 \qquad (5.4)$$

ATTENTION: The Singapore Copyright Act applies to the use of this document. Nanyang Technological University Library

5.4.2 Experimental measurements and curve fitting

In the implementation of the illumination design, commercially available WLEDs (Agilent/Avargo HLMP-CW15-VY0DD) were used due to their high brightness levels. The radiant intensity J of the WLEDs was experimentally determined by first characterizing the irradiance profile H of the WLEDs. This was done by mounting the WLEDs a distance of 2m away from a surface to emulate the model being considered in Figure 5.1, and making measurements of the irradiance distribution along this receiving plane surface. The measurement setup is shown in Figure 5.4 and the measurement results are tabulated in Table 5.1

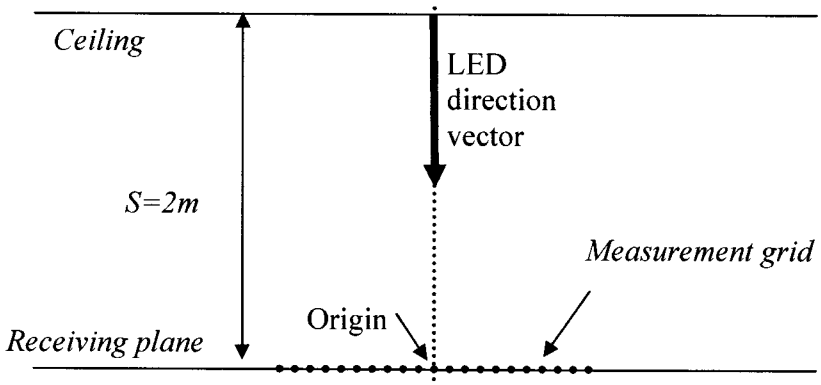


Figure 5.4 Measurement setup for the characterization of the LED irradiance profile.

ATTENTION: The Singapore Copyright Act applies to the use of this document. Nanyang Technological University Library

Table 5.1 Measurement results for the irradiance of a single WLED

Angle (°)	Horizontal irradiance (μw/cm^2)	Normalized irradiance to maximum	Distance from Origin (cm)
0	1.7324	1	0
2.862	1.4477	0.836	10
5.71	1.0222	0.59	20
8.53	0.6652	0.384	30
11.31	0.3704	0.214	40
14.036	0.2206	0.127	50
16.7	0.1315	0.076	60
19.29	0.0873	0.05	70
21.8	0.0697	0.04	80
24.23	0.0582	0.034	90
26.565	0.0506	0.029	100
28.81	0.0478	0.028	110
30.964	0.0411	0.024	120
33.024	0.0364	0.021	130
34.992	0.0324	0.0187	140
36.87	0.0292	0.01686	150

The results from the experiments were fitted using a commercial curve fitting software called TableCurve, and Equation (5.5) was found to represent the best fit for the measurement results.

$$y = \frac{a + cx^2 + ex^4}{1 + bx^2 + dx^4 + fx^6} \tag{5.5}$$

where a=1.007920829, b=0.001774131, c=-0.000393527, d=-1.54455x10^{-6}, e=5.72618x10^{-7}, f=2.13791x10^{-9}, and y and x being the relative irradiance and

ATTENTION: The Singapore Copyright Act applies to the use of this document. Nanyang Technological University Library

displacement respectively. The plot of the irradiance profile is given in Figure 5.5. With reference to Figure 5.3, since the $\theta_1 = \theta_2$, and since the source and receiver direction vectors are parallel, radiant intensity J can then be obtained by dividing the measured irradiance with the solid angle at that point.

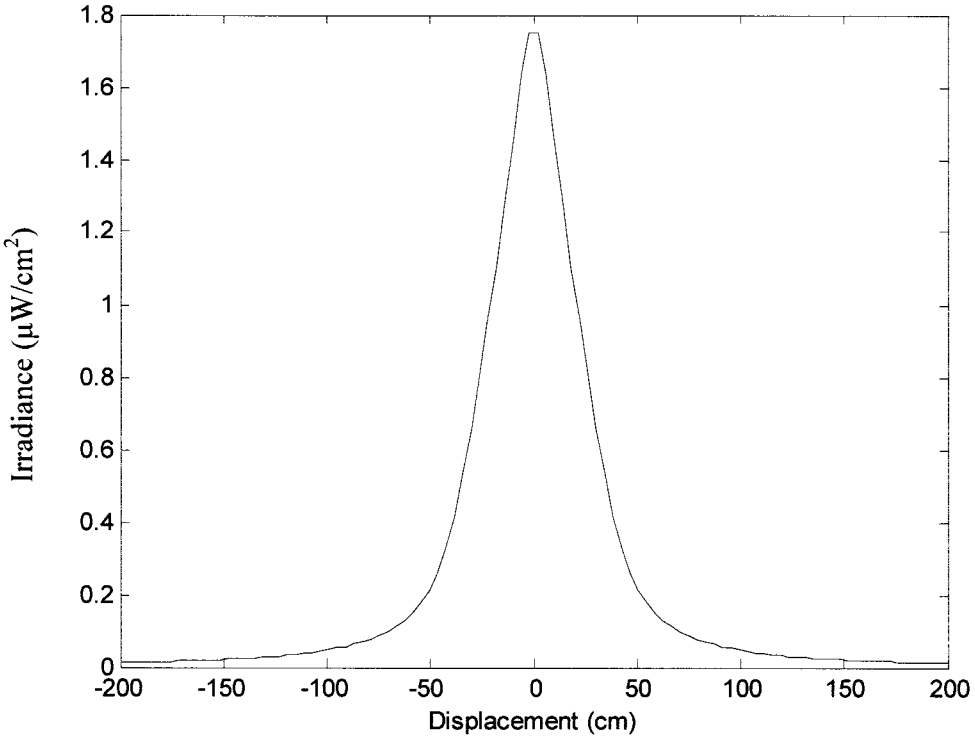


Figure 5.5 Plot of the fitted irradiance profile of the WLED.

To determine the minimum lighting level required for general illumination, measurements using a power meter (Newport 2835-C) were taken in various room environments such as meeting rooms and tutorial rooms around the campus, and it was found that the minimum acceptable irradiance was about 25μW/cm^2. From the characterization of the WLED performed earlier, it was found that the irradiance at the centre of the profile was observed to be about 1.7μW/cm^2. For a WLED, the viewing angle is defined as the cone angle within which the relative intensity is more than 50% of the peak. For the particular WLED modeled (Agilent/Avargo HLMP-

ATTENTION: The Singapore Copyright Act applies to the use of this document. Nanyang Technological University Library

CW15-VY0DD) the 15° viewing angle means that when $\Delta\theta$ is greater than 15°, the radiant intensity drops to 50% of the peak. Due to the sharp dropoff, and in order to increase the coverage of the WLEDs while meeting the minimum irradiance level, multiple WLEDs would have to be incorporated into a single lamp.

5.5 Optimization Process

To obtain an arrangement of WLEDs that would result in a level of illumination on a desktop level located 2 metres below the WLEDs that would meet the required level, an optimization routine was written in MATLAB, using expressions (5.3), (5.4) and (5.5) obtained earlier for the irradiation profile of a source with arbitrary tilt angles and the experimental measurements of the WLEDs. The positions of the WLEDs within a single lamp were fixed, with each WLED having two degrees of angular freedom representing their tilt angles with respect to the normal of the lamp. A $1m^2$ square area with 51x51 points under the lamp was used as the target receiving area for the optimization routine, and the irradiance within each (X, Y) point in the square area would be determined by the sum of the irradiation due to contributions from all the WLEDs, i.e. $H_{XY} = \sum_{N} H\left(\theta_{Tx}, \theta_{Ty}; X, Y, S\right)$, where N represents the number of WLEDs.

To estimate the number of WLEDs required, an estimation was first made based on general illumination requirements. For visual tasks in the office environment, a minimum of 200 lux is recommended by the Illumination Engineers Society [137]. For the WLEDs used, the maximum illuminance provided by one WLED is 7500mcd. Approximating each WLED as a point source, with a separation distance of 2m between the ceiling and receiving plane, the illumination provided per WLED is about 1.875 lux. To meet the recommended illumination level,

ATTENTION: The Singapore Copyright Act applies to the use of this document. Nanyang Technological University Library

approximately a minimum of 107 WLEDs would have to be used. Adding an additional 10% margin, the number of WLEDs per lamp was rounded up to 120. However, during early simulations, it was found that such a large number resulted in long computational times such that optimization could not be performed. Also, it would not be efficient to optimize 120 individual WLEDs per lamp. A compromise was made to optimize only 30 'sources', and later on in the assembly process each source would be represented by four WLEDs.

To quantize the performance of the WLEDs on the irradiance level for different angular tilts, a merit function is required. First, the average irradiance level in the room was determined. A least-squares method was then used to calculate the total difference of the irradiance levels from the mean level across the irradiated area of interest. The expression for the merit function M is given by Equation 5.6 below

$$M = \sum_{T} \left| H_{XY} - \bar{H}_{XY} \right|^2 \tag{5.6}$$

where H_{XY} represents the irradiance at the receiving points as defined earlier, T is the total number of points under consideration, and $\bar{H}_{XY}$ represents the average irradiance level. The optimization routine acts to reduce the value of M by varying the tilt angles of the WLEDs. A minimum irradiance level for the irradiated area is ensured by a program flow control routine that rejects average levels that are below the minimum.

ATTENTION: The Singapore Copyright Act applies to the use of this document. Nanyang Technological University Library

5.5.1 Results from the optimized design

The obtained angles are shown in Table 5.2, where θ_x represents the tilt in the x-axis direction, and θ_y representing the tilt in the y-axis direction. A plot of the obtained results can be seen in Figure 5.6 which shows the irradiance within the target area. The irradiance level of the target area obtained from the simulation is 7.6μW/cm^2, and to achieve the required level of 25μW/cm^2, each of the WLEDs in the program was replaced with four WLEDs, with a total of 120 WLEDs required in order to be able to meet the required level.

Table 5.2 Angles obtained from the optical design optimization

LED	θ_x	θ_y	LED	θ_x	θ_y	LED	θ_x	θ_y
1	-13.9	-11.6	*11*	-8.3	14.6	*21*	16.7	-6.1
2	-13.1	-12.2	*12*	-0.2	9.5	*22*	12.4	0.1
3	-13.3	-3.9	*13*	6.5	-12.4	*23*	14.3	10.6
4	-13.9	10.0	*14*	-0.7	-16.0	*24*	13.1	13.6
5	-12.3	13.1	*15*	0.1	-1.6	*25*	-0.1	-11.0
6	-12.1	12.8	*16*	-4.3	0.3	*26*	16.0	-11.7
7	-5.4	-12.4	*17*	6.4	0.0	*27*	16.4	0.0
8	-12.0	-13.6	*18*	2.7	12.3	*28*	15.3	9.2
9	-14.4	-0.3	*19*	12.6	-13.6	*29*	11.1	14.5
10	-13.8	2.7	*20*	12.8	-12.5	*30*	0.0	15.1

ATTENTION: The Singapore Copyright Act applies to the use of this document. Nanyang Technological University Library

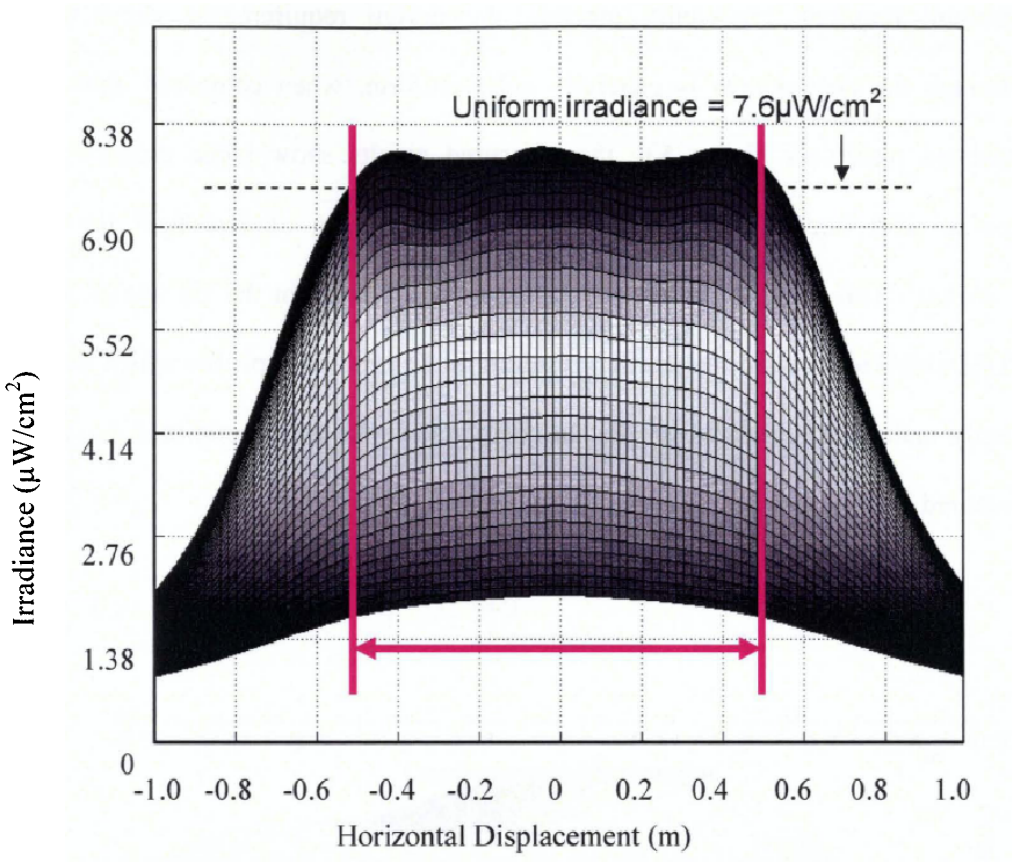


Figure 5.6 Plot of the irradiance obtained from the optimization process.

5.6 Experimental measurements and discussion

Using the optimized angles from Table 5.2, 120 WLEDs were used to assemble the demonstrator system, with 4 WLEDs being used to represent one angle from Table 5.2. Templates representing the various angles were constructed and used as aides during the assembly process so as to ensure that the WLEDs were tilted in a consistent and correct manner. To avoid influence from ambient light, measurements were carried out in a completely dark room environment with the demonstrator system mounted 2m away from the receiving surface. The measurements were made in a 1m by 1m grid, and the irradiance profile is shown in Figure 5.7. From the results, most of the measured locations in the grid have an irradiance that is more than the

ATTENTION: The Singapore Copyright Act applies to the use of this document. Nanyang Technological University Library

minimum required 25μW/cm^2, meeting the design requirements stated earlier. Although the central area is generally quite uniform, when compared against the simulated results in Figure 5.6, the measured results show some dropoff at the corners, with one of the corners having an irradiance of less than the target 25μW/cm^2. This could be attributed to some inaccuracies in the tilt angles for the WLEDs directed toward that corner, resulting in an irradiance profile which does not exactly match the simulated profile. In comparison with an unoptimized design, the measured irradiance was observed to be more uniform.

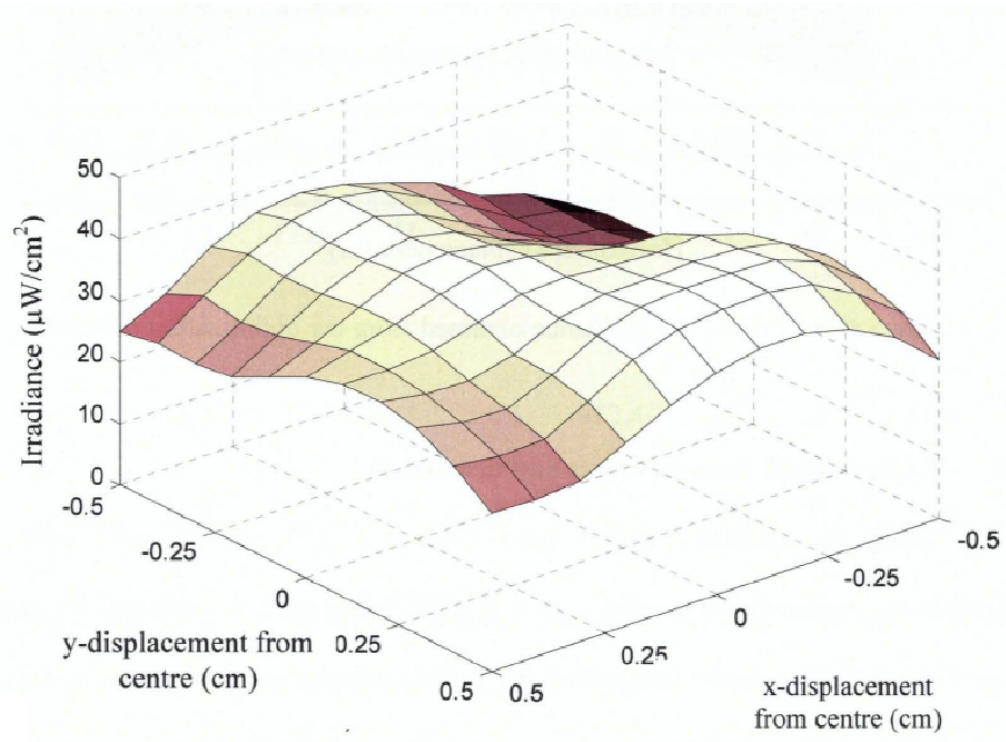


Figure 5.7 Measured irradiance profile of the demonstrator system.

ATTENTION: The Singapore Copyright Act applies to the use of this document. Nanyang Technological University Library

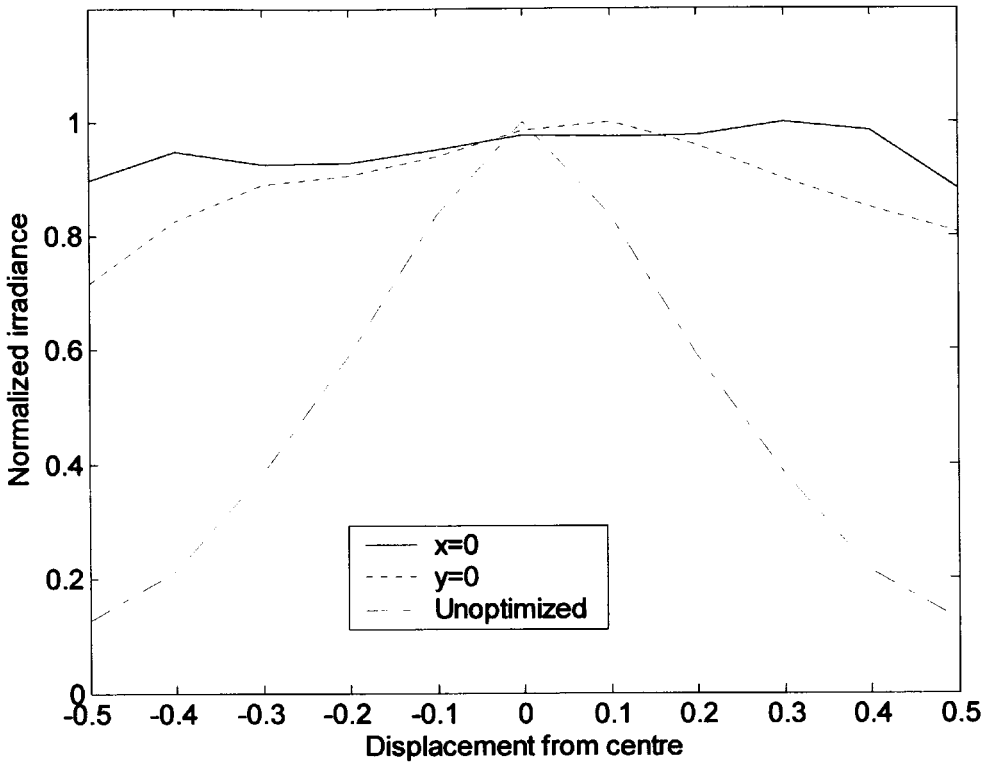


Figure 5.8 Comparison of the irradiance profiles for the optimized system and a system with the WLEDs pointing vertically towards the receiving surface.

Figure 5.8 compares the one-dimensional plot of the normalized irradiance profiles for the optimized angles and another system with the WLEDs pointed vertically downwards as in Figure 5.4. The $x = 0$ and $y = 0$ plots represent the irradiance along these lines in the measurement grid for the optimized system. As can be seen from the plots in Figure 5.8, the measured results for the optimized system gives a much higher level of uniformity for the irradiance as compared to the unoptimized system.

ATTENTION: The Singapore Copyright Act applies to the use of this document. Nanyang Technological University Library

5.7 Circuit design

To determine the effectiveness of the optical design presented earlier and to demonstrate the use of WLEDs in wireless communications, work was then undertaken to produce the WLED lamps. Using the data obtained from the optimization process, each lamp was assembled using 120 WLEDs, and would irradiate a $1m^2$ area. As the room environment to be demonstrated is a $2m^2$ area, four lamps were assembled. A photograph of one of the lamps is shown in Figure 5.9. A circuit was designed to enable the 480 WLEDs to be driven for illumination and communication, with the communications aspects being demonstrated using audio signals from a function generator, a digital music player and a microphone. The optical wireless system is configured as an Intensity Modulation / Direct Detection system, with the audio data signal directly modulating the intensity of the WLED lamps via analog intensity modulation. The signals are then received using a photodetector placed at the receiving plane 2m below the lamps.



Figure 5.9 Photograph of the lamp consisting of 120 WLEDs.

ATTENTION: The Singapore Copyright Act applies to the use of this document. Nanyang Technological University Library

For a WLED operating within the active region, the transmitted power is linearly proportional to the forward current passing through it, and thus the output can be modulated by controlling the forward current. To bias the WLED for illumination, the current passing through each WLED is chosen at 24mA to remain within the active region and avoid over-driving that would lead to the WLED burning out. Arranging the WLEDs in parallel, the required current for each lamp is 2.88A, and a bipolar junction transistor (BJT, 2SD913) was chosen to drive each lamp. Although the current rating of the BJT is specified at 3A, to provide an additional safety margin, two BJTs were used, each allowing 1.44A to pass through it. For the purposes of the demonstration analog modulation was used with the amplitude V_{BE} of the BJT controlling the WLED output. However, it was found that the signals from the MP3 player were too weak to drive the WLEDs, and a pre-amplifier (RC5534N) was added into the system to improve the strength of the input signal. The complete system model is presented in Figure 5.10

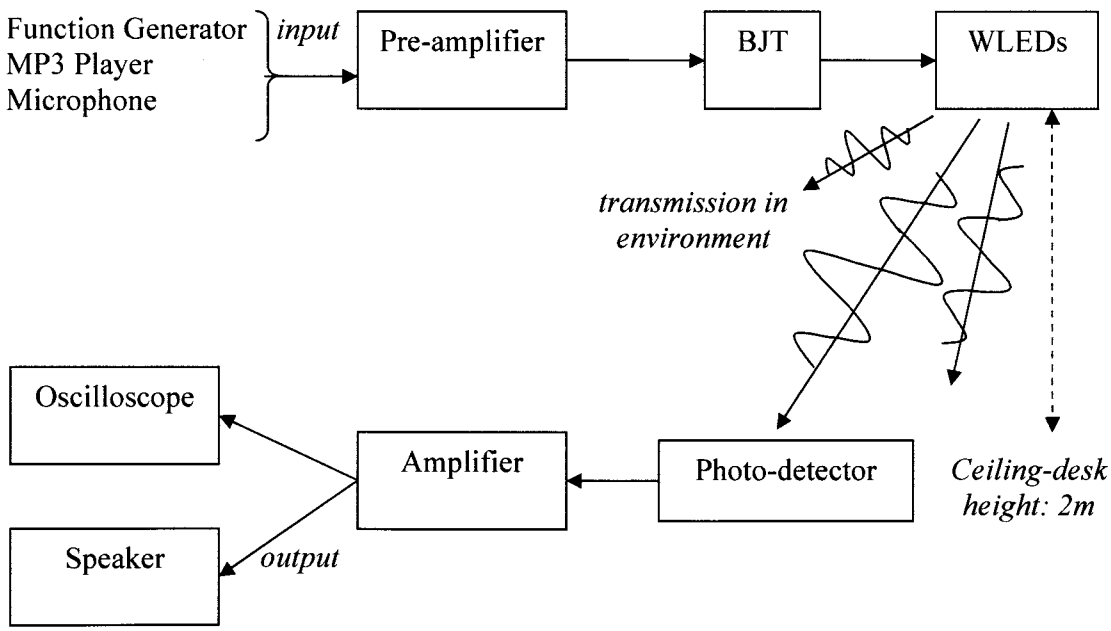


Figure 5.10 Setup of WLED communications system.

ATTENTION: The Singapore Copyright Act applies to the use of this document. Nanyang Technological University Library

5.8 Transmission measurements and discussion

The system shown in Figure 5.10 was set up in a custom 2m x 2m demonstration room environment, with the four lamps arranged in a 2x2 configuration centred on the room, as shown in Figure 5.11. To avoid ambient illumination from external sources, the walls were draped with canvas, and the measurements were taken at night. Each lamp was located 1m away from the two nearest lamps. The irradiance within the demonstration room was measured and it was found that the lowest reading was 28.83μW/cm^2 at the corners and the highest value was 55.35μW/cm^2 at the centre of the room. As the readings were found to be higher than the minimum level of 25μW/cm^2, the illumination level can be considered to be acceptable for reading. From Figure 5.6, it can be seen that the regions beyond the target region do not drop off sharply, and hence the higher levels measured at the centre of the room can be attributed to be due to the cumulative effect of all the four lamps and the contribution from light reflected off the walls, which was not considered during the design process.

To compare with typical lighting environments, the range of variation of the irradiance across the measured receiving floor was calculated. 11 points uniformly distributed across one quadrant of the environment was used, and it was found that the average and range were determined to be 37.07μW/cm^2 and [28.83μW/cm^2 – 55.35μW/cm^2] respectively. In comparison with a typical tutorial room illuminated with conventional fluorescent illumination, the average and range of irradiance was found to be 61.64μW/cm^2 and [19.93μW/cm^2 - 80.33μW/cm^2] respectively. Normalizing the minimum and maximum values to the average irradiance value, the corresponding values for the WLED illumination were found to be [0.78 – 1.49], and that for fluorescent illumination were found to be [0.33 – 1.3]. It can be seen from

ATTENTION: The Singapore Copyright Act applies to the use of this document. Nanyang Technological University Library

these values that the illumination levels in the WLED environment has a lower variation than that of the fluorescent illumination. In addition, despite the irradiance difference of about 26μW/cm^2 between the highest and lowest level for the WLED illumination, the difference is barely noticeable to the human eye.

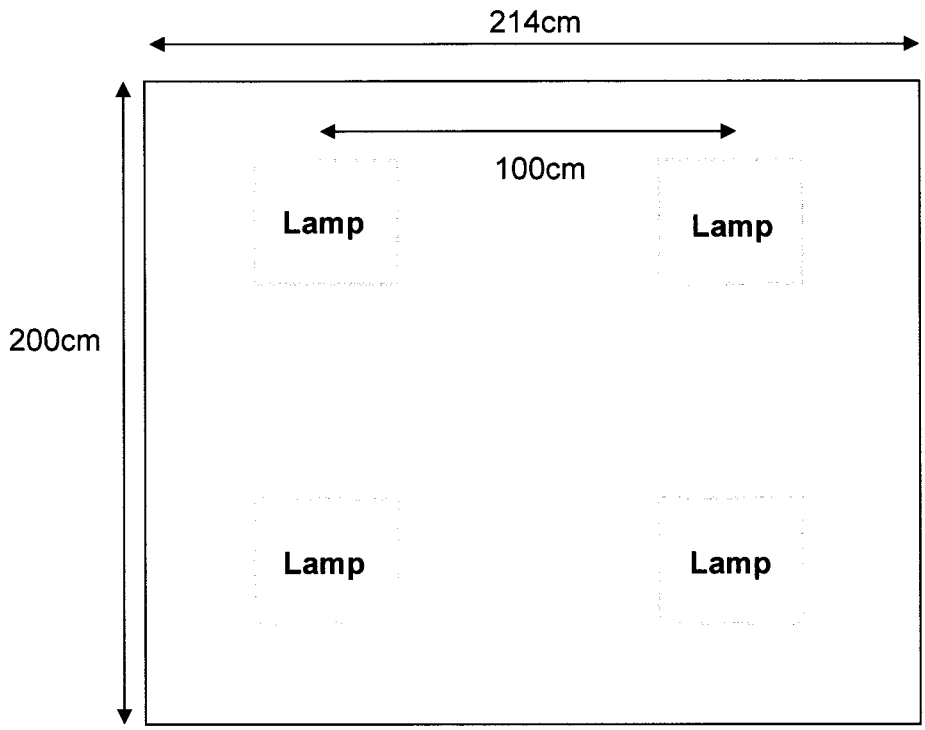


Figure 5.11 Setup of demonstration room.

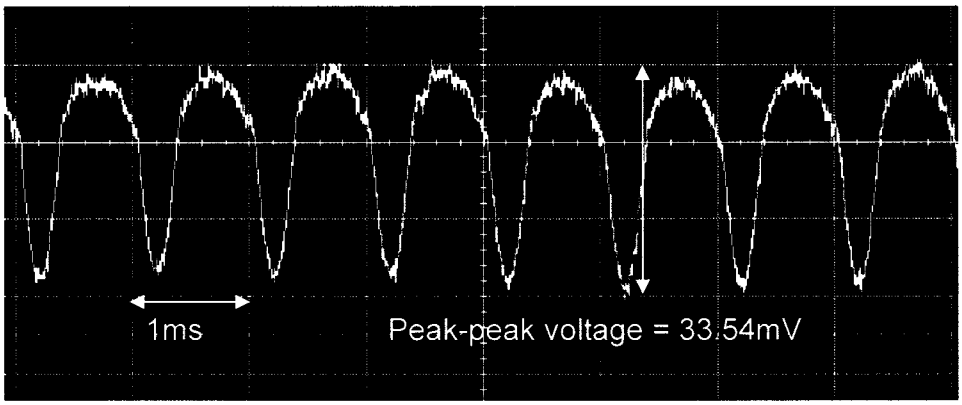


Figure 5.12 Signal waveform after being transmitted from the WLED lamps and picked up on the photodetector. Input signal is a 1kHz, 20mV sine wave.

ATTENTION: The Singapore Copyright Act applies to the use of this document. Nanyang Technological University Library

When a single tone frequency was transmitted through the system, the speaker output sounded clear. Figure 5.12 shows the signal waveform when the output of the detector is displayed up to an oscilloscope. The oscilloscope was used to measure the instantaneous signal amplitude a and noise variance σ^2 and it was found that the instantaneous signal power to noise variance ratios (a^2/σ^2) ranged from 60.56 to 21.10. Although a digital transmission setup was not used in the prototype system, the obtained results can be used to estimate the digital performance of the demonstrator system. An ideal matched filter receiver model for unipolar baseband signaling was used with a '1' bit having signal power a and a '0' bit represented by no received power at the detector, i.e. $I_1 = a$, and $I_0 = 0$. The noise variance is taken to be equal for both cases i.e. $\sigma_0 = \sigma_1$. Using Equation (3.21) from Chapter 3, the corresponding bit error rate was found to vary from 10^{-2} to 10^{-4}. The bit error performance could be further raised from the current results by making use of signal processing techniques such coding and forward error correction to improve the signal quality.

However, when the MP3 player and the microphone were used as an input source, the system was also able to output audible transmission with some distortion and the presence of noise could be heard. The noise and distortion could be minimized by designing a filter to remove the detected noise and obtain a flatter frequency response in the passband at the expense of added complexity to the system. Also, despite the modulation of the WLEDs for communication, there was no observable flickering in the light sources, and the illumination was observed to be constant even as the audio signals were being transmitted through the optical system.

ATTENTION: The Singapore Copyright Act applies to the use of this document. Nanyang Technological University Library

The demonstrator system was shown to be capable of transmitting audio signals. However, a major limitation of the current demonstrator system is the high current gain needed to drive the WLEDs from a relatively small signal from the input sources. The high current swing results in a tradeoff of bandwidth for current gain in the BJT from gain-bandwidth product considerations. By increasing the WLED to transistor ratio such that the current gain for each BJT is reduced, the effect of the bandwidth limits due to the electronic components could be alleviated. Furthermore, reducing the active area of the WLEDS used would result in a reduction in the capacitance due to the active area of the diode. This should allow higher transmission speeds closer to the 100MHz range of LED transmission systems, although more WLEDs would have to be used so that the illumination requirements are not compromised. However, such high transmission bitrates would also increase the effect of multipath dispersion in the receiver, reducing in the received signal quality and equalization techniques would have to be considered to account for this effect.

5.9 Comparison with other work

In the previously described work in this Chapter, a relatively uniform illumination of the room environment was first obtained via optimization of the WLEDs in a simulation and was then implemented in a demonstration system. To obtain a measure of the obtained simulated results, the ratio between the maximum values and minimum values within the specified target area is calculated in decibels and is tabulated in Table 5.3. This metric provides a convenient and simple means of comparing the dynamic range of the achieved illumination, and is easily applicable to published work. Hence, this metric was also applied to relevant results from the

ATTENTION: The Singapore Copyright Act applies to the use of this document. Nanyang Technological University Library

published work done by other researchers in WLED-based visible light optical wireless and are also represented in Table 5.3.

Table 5.3 Comparison of the ratio of the minimum and maximum intensity from the obtained results and in comparison with the results from related work

Research	Ratio of minimum power to maximum power in simulation	Ratio obtained from experimental results
Tanaka et al [130]	>10dB	-
Komine et al [131]	9.03dB	Demonstration using a lamp, no full room illumination, video transmission
Tanaka et al [132]	6.52dB	-
Komine et al [133]	6.37dB	-
Sugiyama et al [135]	4.5dB	-
Optimized results	0.2dB	Full room illumination with transmission of audio signals

As can be seen from Table 5.3, based on the simulation model results, the ratio for the optimized system results achieved the lowest compared to other work, which is to be expected as the position of the WLEDs was specifically optimized to minimize fluctuations in the received power. This is important to ensure that the lighting in the room environment is adequate and also uniform enough to avoid discomfort for the users and capacity outages for the transmission system.

ATTENTION: The Singapore Copyright Act applies to the use of this document. Nanyang Technological University Library

Further, among the research surveyed in Section 5.3 for [130-133], in most of the work there was no experimental system setup for the described systems. Although [131] reported on a demonstration system, this was based on a single lamp and was used for proof of concept of concept for the integrated powerline and visible wireless system, rather than a full room illumination with actual transmission of data, which was demonstrated in the described work in this Chapter of the Thesis.

In addition, all of the described previous published work have utilized an ideal Lambertian profile for the emitters in their simulation model. However, in the work presented here, the radiation profile of actual WLEDs was measured and used in the simulation and optimization work, providing a more realistic configuration for the visible light optical wireless system.

5.10 Conclusion

The illumination design process has been presented which optimizes the angular arrangement of the WLEDs so that the irradiation levels within the target area are able to meet the minimum required level. To enable the WLEDs to be capable of transmitting information, a driving circuit was designed and implemented into the fabricated WLED lamps. A wireless transmission system enabled using WLEDs has been demonstrated, in which audio signals are transmitted by modulating the WLEDs mounted on the ceiling, and detected by photodetectors located on the receiving plane. The system has been shown capable of providing both illumination and communication at the same time. With the bandwidth offered by the WLEDs being potentially greater than current RF networks, the system can also be configured for digital transmission of multimedia signals, including video, and the decreasing cost of

ATTENTION: The Singapore Copyright Act applies to the use of this document. Nanyang Technological University Library

WLEDs would aid the feasibility and widespread adoption of their use in such transmission systems.

ATTENTION: The Singapore Copyright Act applies to the use of this document. Nanyang Technological University Library

6

Optical design for broadband optical wireless in an aircraft passenger cabin application

6.1 Introduction to the Chapter

In this Chapter, the design of an optical wireless system for an aircraft cabin will be presented. Optical wireless is ideal for such applications as there is no potential for inference with avionics, which is a major concern regarding the use of radio frequency devices on board aircraft. The choice of wavelength with regards to eye safety and ambient lighting levels will be considered. A typical aircraft cabin geometry will also be modeled, and ray-tracing simulations using this model will be

ATTENTION: The Singapore Copyright Act applies to the use of this document. Nanyang Technological University Library

performed. By using the ray-trace information together with an optimization process the method to design the optical sources to allow for uniformity of signal distribution within the cabin will be presented. Also, using the ray-trace information to obtain the multipath information, a communications model will be used to determine the performance of the optical wireless system under ambient noise and multipath interference. For a bit error rate of 10^{-3} with equalization a bit rate of more than 400 Mbit/s will be shown.

6.2 Motivations

In the previous sections, the use of optical wireless in indoor applications based in domestic or commercial building applications was presented. As was previously mentioned, the chief advantage of optical wireless in these applications is the potentially large bandwidth due to the unregulated spectrum, and the property of the optical wireless network to be limited to the physical confines of the environment. These two properties are also extremely advantageous to the application of optical wireless for use in optical wireless in a commercial aircraft cabin as the medium for the transfer of information for in-flight entertainment (IFE).

In past years, copper wires were used to transmit information throughout a passenger aircraft, such as from the audio visual centre of the aircraft to each passenger's IFE terminal. However, with copper wires comes the increased possibility of fires due to shorts in the electrical wiring[138]. In fact, the investigation into the crash of flight Swissair 111 found that the melted and re-solidified copper near an IFE power supply unit was associated with the fire that caused the crash [139]. A short circuit in the wiring was also attributed to the loss of flight TWA 800 in 1996[140]. This has in part motivated the aviation industry's shift towards the use of fiber optics

ATTENTION: The Singapore Copyright Act applies to the use of this document. Nanyang Technological University Library

cables instead of copper cables. Another more practical reason for the shift is the weight savings from the use of fiber optics over cable, which in terms of the commercial bottom line can be used to extend operational range by carrying more fuel, or to increase the number of passengers that can be in the aircraft. The trend towards fiber optic cabling can be seen in new commercial airliners such as the Airbus A380 which make heavy use of fiber optics, such as between the IFE terminals and the central entertainment server. Although the shift towards fiber optics has been largely advantageous, the medium is still wired and it has been reported that there are approximately 500km of cabling in the Airbus 380 which has been attributed as the cause of the numerous delay in the deployment of the aircraft[141]. In particular, the delays have been reported as being due to the difficulties in wiring for the entertainment portals, rather than any issues with the flight performance of the aircraft itself [142].

An alternative to using a wired medium for the IFE network is to make use of wireless technologies in the passenger aircraft to create an onboard wireless local area network. However, radio frequency devices can potentially affect aircraft safety [36, 143]. In particular, a study by NASA has showed that spurious transmissions from wireless LANs have measured to exceed the emission limits for certain avionics systems [144]. Furthermore, with modern passenger capacities capable to carrying up to hundreds of passengers (the Airbus 380 can carry over 800 passengers[145]), and the close proximities between each wireless transceiver, radio frequencies emissions can become a valid cause for concern. As a result wireless devices are currently not allowed during flights and must be turned off or set to an 'aircraft' mode which disables the wireless transceiver.

ATTENTION: The Singapore Copyright Act applies to the use of this document. Nanyang Technological University Library

Given these limitations, optical wireless can be potentially used as an alternative for radio frequency wireless within the aircraft cabin. The high bandwidth would allow broadband communications, and this is aided by the short distances within the cabin which limits the multipath dispersion. Even more advantageous is the confinement of the optical wireless network to the physical boundaries of the optical network. Each section of the cabin can have its own optical wireless network which would not affect the networks in neighbouring cells. Furthermore, use of such a network would result in no interference with aircraft avionics, facilitating the employment of a broadband wireless network with no concerns over aircraft instrumentation safety issues.

6.3 Related work by other researchers

The work by other researchers in the use of optical wireless within the aircraft cabin has been a relatively unexplored area. The envisioning of the use of diffuse infrared wireless in an aircraft cabin was proposed as early as 1998 by Portega[146], who extolled the virtues of wireless networking, particularly optical-based infrared wireless networking, within in the aircraft cabin. However, in the largely descriptive paper, there were no technical developments or research developments presented. More recently, in [147], Schmitt et al presented the work done in the investigation of a diffuse optical wireless link within the aircraft cabin, including a possible system architecture for network traffic, and estimated power requirements based on link distances. An experimental system was setup in a mock cabin layout as part of the feasibility study with the transmitters arbitrarily placed, and it was reported that video transmission of up to 8 Mb/s was achievable.

ATTENTION: The Singapore Copyright Act applies to the use of this document. Nanyang Technological University Library

6.4 Wavelength selection

An important parameter in designing an optical wireless network is the choice of wavelength for the optical system. Particularly for optical wireless, the selection of an appropriate wavelength affects the maximum amount of power that can be transmitted through environment due to eye safety considerations. In addition the choice of an appropriate detector for the optical wireless can limit the ambient noise or background noise of the optical wireless system, due to the non-uniform distribution of the spectral intensity of light. Although discussed in the context of cabin-based optical wireless communications, the following discussion should also be applicable to most other types of optical wireless communications.

6.4.1 Eye safety considerations

The maximum permissible exposure (MPE) is a value determines the amount of laser radiation that a person can be exposed to without any adverse effects, whether for a short duration or an extended period of time. The value of the MPE is defined by IEC 80825 Safety of Laser Products [127] which is the international standard for the protection of persons from laser radiation by setting emission requirements for light emitting devices which includes lasers and light emitting diodes (LEDs). For an infrared optical wireless network, the wavelengths studied will be limited from 700nm to 1600nm.

The MPE calculations are determined by a number of variables besides the emitting wavelength. The timebase to be used is dependent on the time factor T_2. For laser sources which have a small diverging angle, T_2 = 10s. In an optical wireless environment, the source will always be emitting and thus the exposure time T is taken to be more than T_2, i.e. $T > T_2$. Using this timebase, the appropriate equations are

ATTENTION: The Singapore Copyright Act applies to the use of this document. Nanyang Technological University Library

shown in Table 6.1 and are used to plot the MPE limits from 700nm to 1600nm in Figure 6.1.

Table 6.1 Relevant equations used to calculate the MPE for $T > T_2$

λ (nm)	MPE (W/m^2)	C_4	C_7
700 to 1050	$10C_4C_7$	$10^{0.002(\lambda-700)}$	1
1050 to 1150	$10C_4C_7$	5	1
1150 to 1200	$10C_4C_7$	5	$10^{0.018(\lambda-1150)}$
1200 to 1400	$10C_4C_7$	5	8
1400 to 1500	1000	-	-
1500 to 1600	1000	-	-

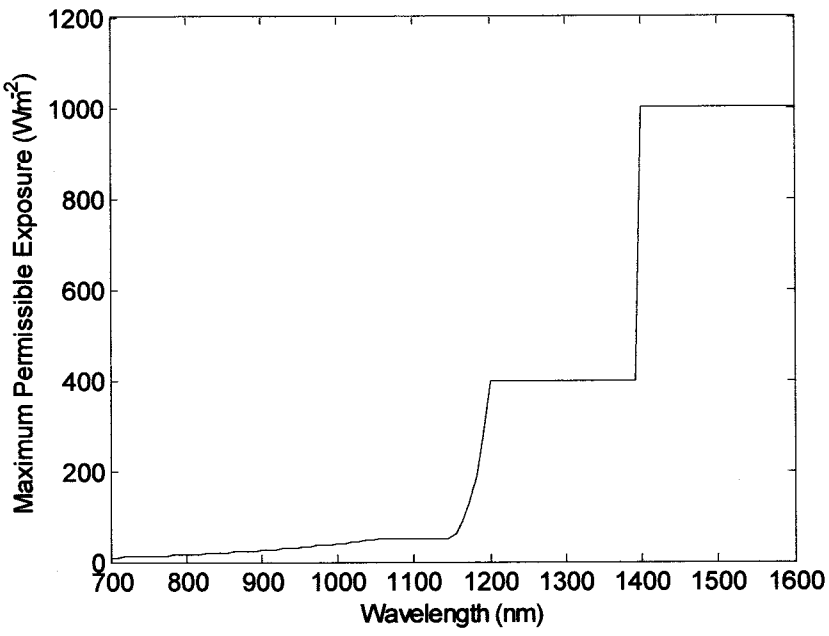


Figure 6.1 Maximum Permissible Exposure (MPE) limits for the wavelength range from 700nm to 1600nm.

ATTENTION: The Singapore Copyright Act applies to the use of this document. Nanyang Technological University Library

From Figure 6.1, it can be observed that the MPE for the range from 1400nm onwards is the highest. This is due to water absorption by the tissues and fluids within the eye such as the lens, the aqueous humour and the vitreous humour which attenuate the laser beam intensity before it reaches the photo-sensitive retina at the back of the eye. In contrast, wavelengths below 1000nm are not affected by water absorption and hence the lower permissible exposure levels. This clearly indicates that a good selection of wavelength should be from 1400nm onwards for the maximum emission level as well as lowest risk to human eye safety.

The classification of laser devices into the appropriate safety levels is determined by the allowable emission level (AEL) for that specific device. For an optical wireless system which will be in operation and continuously emitting, it is important to ensure that the device operates at the highest safety level, which is Class 1. This is the same as laser devices found in CD players and other household laser devices. Unlike the MPE, which defines the maximum exposure that can be experienced by the eye, the AEL defines the maximum emission for the device. For the purpose of comparison the Class 1 AELs of two commercially available optical wavelengths 850nm and 1550nm are shown in Figure 6.2.The Class 1 AEL for 1550nm is more than 10dB higher than that of 850nm. From a purely eye safety perspective it is obvious that 1550nm is preferable over 850nm, as 10dB more power can be emitted which translates as a 10dB increase in the signal level to improve the signal quality while still remaining in eye safety limits, as compared to using 850nm.

ATTENTION: The Singapore Copyright Act applies to the use of this document. Nanyang Technological University Library

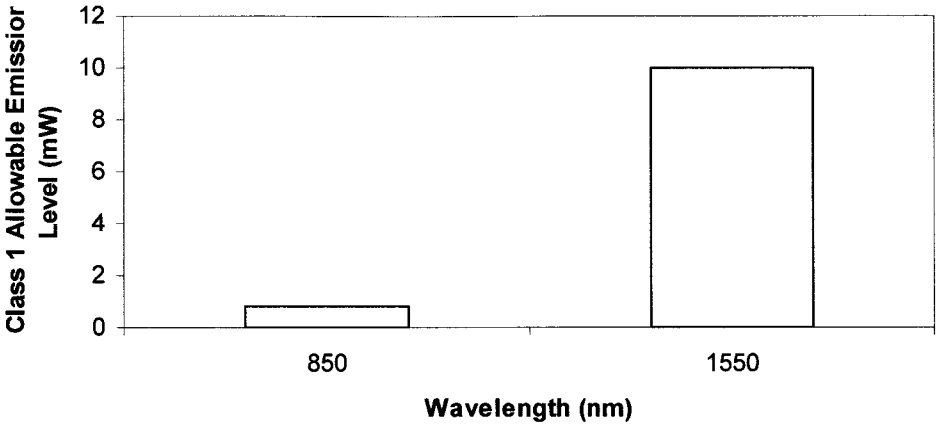
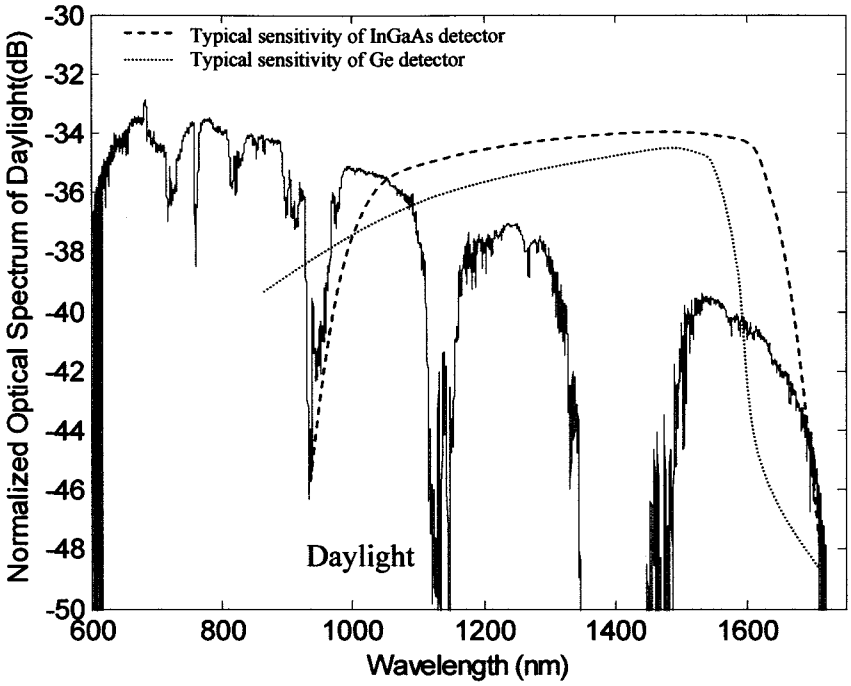


Figure 6.2 Class 1 Allowable Emission Limits (AEL) for 850nm and 1550nm.

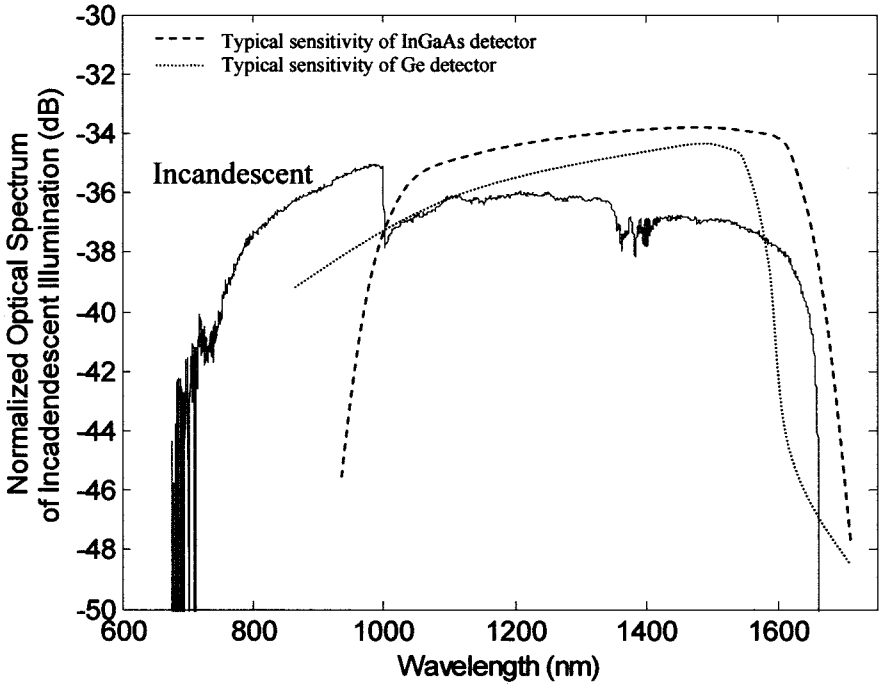
6.4.2 Ambient Noise Spectral Characteristics

Another factor that should be considered in selecting an appropriate wavelength is the amount of ambient background light which can interfere with the detected signal. This is primarily determined by the spectral characteristics of the ambient light, as well as the spectral sensitivity of the detector. An optical spectral analyzer was used to observe the spectral distribution of various types of background ambient light and the results are shown in Figure 6.3. Figure 6.3(a) shows the spectral distribution of daylight, Figure 6.3(b) shows the spectral distribution of incandescent lighting, Figure 6.3(c) shows the spectral distribution of fluorescent lighting employing an electronic ballast, and Figure 6.3(d) shows the spectral distribution of a white light emitting diode. The range of wavelengths considered range from 700nm to 1700nm, with a wavelength sensitivity of 0.2nm. The intensity levels were normalized against the total intensity detected by the optical spectral analyzer.

ATTENTION: The Singapore Copyright Act applies to the use of this document. Nanyang Technological University Library

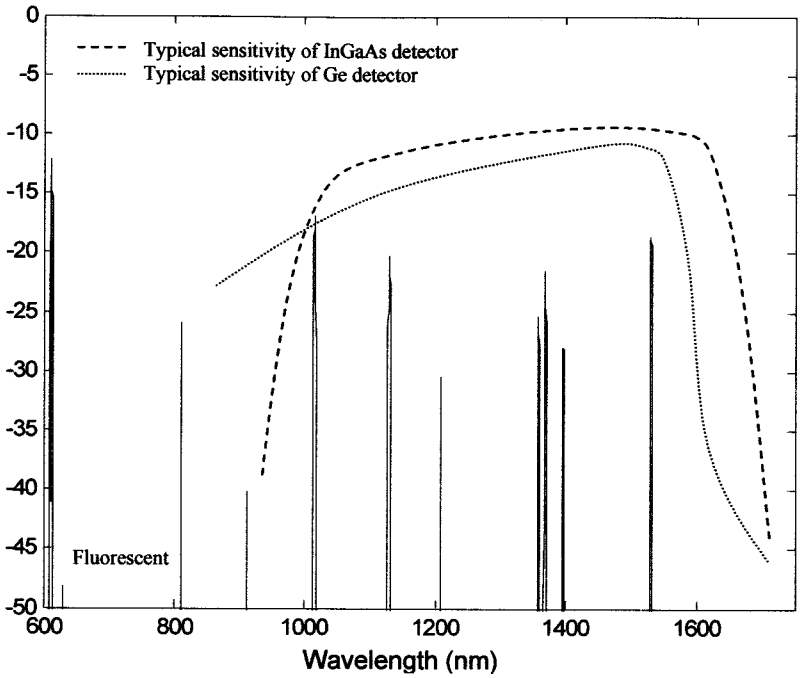


(a)

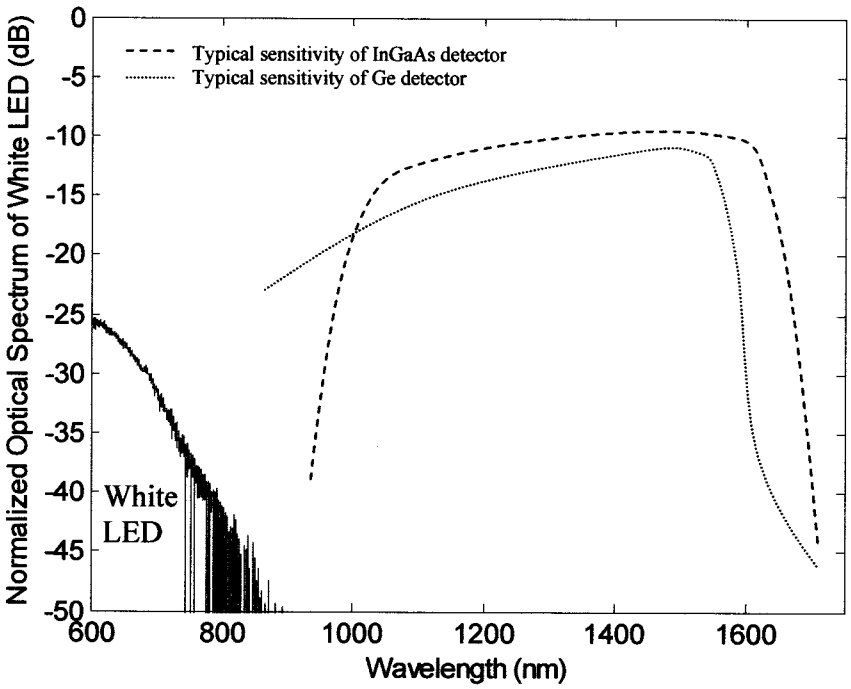


(b)

ATTENTION: The Singapore Copyright Act applies to the use of this document. Nanyang Technological University Library



(c)



(d)

Figure 6.3 Normalized spectral characteristics of (a) sunlight, (b) incandescent light, (c) fluorescent light and (d) white light emitting diode.

ATTENTION: The Singapore Copyright Act applies to the use of this document. Nanyang Technological University Library

To provide a comparison, the typical spectral sensitivity of an InGaAs detector and a Ge detector has also been included in the plots shown in Figure 6.3. As can be seen from the plots in Figures 6.3(a) and 6.3(b), for sunlight and incandescent lighting, longer wavelengths in general contain less energy as compared to shorter wavelengths such as 850nm. For a 1550nm wavelength, the difference compared to 850nm can range up to a few dB. When fluorescent lighting is considered in Figure 6.3(c), the energy distribution from 700nm to 1700nm is sporadic. In particular, when considering the use of a 1550nm device, there is an intensity peak from 1528nm to 1531nm. To avoid this peak and to limit the ambient noise from incandescent and sunlight, use of wavelength filter centred at the transmission wavelength of 1550nm with a 30nm linewidth from 1535 to 1565 would be preferable as this would filter out the fluorescent peak and most of the ambient noise. In addition, with the greater emphasis towards use of energy-saving fluorescent lighting in place of incandescent, the noise level could be further reduced. Furthermore, in indoor applications, such as in aircraft cabins, the amount of direct sunlight that falls onto a detector can be limited. From the analysis of the spectral contributions of sunlight and fluorescent lighting, which are the main contributors of ambient light in the aircraft cabin, it can be seen that there is reduced noise for longer wavelengths, and is particularly well-suited to 1550nm.

To determine the level of ambient light, measurements were carried out using a Melles Griot 20mm^2 active area Ge detector for the various lighting conditions mentioned. For sunlight, two different scenarios were used. Direct sunlight was used to indicate that the receiver was able to receive the sunlight directly, i.e. a 'line of sight' between the detector and the sun. Indirect sunlight refers to the intensity of the sunlight when the detector is placed in a shade with no 'line of sight' between the

ATTENTION: The Singapore Copyright Act applies to the use of this document. Nanyang Technological University Library

detector and the sun. A wavelength filter centered at 1550nm with a 40nm bandwidth was also used in a separate measurement to determine the level of reduction of ambient light when such a filter is used. The results are presented in Table 6.2. From the results it can be observed that when direct sunlight is allowed to fall onto the receiver, the measured intensity is much higher than any other condition at about 1.6mW. However, use of a wavelength filter in this case is extremely advantageous, as the measured intensity after filtering is reduced to 36μW, a reduction by 50 times. A similar reduction can also be seen for fluorescent light. To determine the irradiance falling onto the detector, the received intensity was divided by the area of the detector. These values will later be used to determine the system performance of the optical wireless communications system.

Table 6.2 Background illumination measurements

	Measured Power (μW)		Irradiance (μW/cm^2)	
Ambient lighting condition	No Filter	With filter (λ=1550nm, Δλ=40nm)	No filter	With filter (λ=1550nm, Δλ=40nm)
Fluorescent	0.53	0.01	2.65	0.05
Incandescent	80	3.32	400	16.6
Direct sunlight	1600	36	8000	180
Indirect sunlight	46.8	0.58	234	2.9

From the measurements of ambient lighting conditions and from the eye safety limitations considered in Section 6.3.1, it can be seen that use of 1550nm device offers significant advantages over shorter wavelengths such as 850nm due to the

ATTENTION: The Singapore Copyright Act applies to the use of this document. Nanyang Technological University Library

higher allowable emission levels and the decreased level of ambient noise. Together with proper filter design this could ensure a virtually noise free operating environment for the indoor optical wireless system.

6.4.3 White Light Emitting diodes

White light emitting diodes (WLEDs) are rapidly becoming popular due to their robustness and their higher efficiency as compared to other types of illumination sources. An advantage of using WLEDs as illumination sources when an optical wireless system is also used is that the spectral distribution of WLEDs are mainly contained within the visible range, as can be seem from Figure 5.1 in Chapter 5. To determine the spectral distribution of WLEDs beyond 700nm the light produced by a WLED was also measured by the same optical spectral analyzer was used in the other measurements and the results are plotted in Figure 6.3(d). As can be seen, the optical spectrum of a WLED is well-confined to within less than 900nm. This complements optical wireless at 1550nm as WLEDs used as illumination sources would not contribute much to the noise level at the detector. Furthermore, as proposed and demonstrated in Chapter 5, WLEDs themselves are also capable of being modulated, and another alternative to enabling optical wireless in the aircraft cabin as well as other environments is to use WLEDs in a dual role as both illumination sources and transmitters. While WLEDs are very attractive, one potential limitation is that the nature of the WLED device limits the bandwidth transmission to about 100MHz. In contrast, the infrared system could operate at much higher bandwidths due to the narrower linewidths offered by the infrared sources. A WLED-based optical wireless transmission system be used in tandem with an infrared-based system, by augmenting the infrared system during 'daytime' when most of the passengers are awake and a

ATTENTION: The Singapore Copyright Act applies to the use of this document. Nanyang Technological University Library

greater demand for bandwidth is required. During 'night' flights the lighting system could be turned off with passengers mainly using the infrared network.

As such the main focus of the work in the following sections in the Chapter is on the design of an infrared optical wireless system in the cabin, which, from the work done in characterizing noise contributions in the infrared, as shown in Figs 6.3(a) and (c), and in Table 6.2, as well as eye safety considerations, favour the use of 1550nm. Although the design was focused on the infrared, the methodology described could also very easily be applied to WLEDs with some adjustments.

6.5 Cabin optical network design

In this section, the optical design approach and process used to design the placement and tilt of the optical transmitters will be presented. The modeling of a realistic cabin environment is first shown, followed by the use of an optimization approach to obtain the best arrangement of sources for the mobile user along the aisles to obtain a uniform coverage. This will be followed by another optimization step where the optical coverage throughout the passenger cabin will be optimized for uniform coverage via the introduction of additional banks of sources along the windows and the central dorsal area of the passenger cabin.

ATTENTION: The Singapore Copyright Act applies to the use of this document. Nanyang Technological University Library

6.5.1 Modeling a typical aircraft cabin environment.

In the previous optical design work presented in the thesis, the optical wireless operating environment was based on a conventional indoor environment with regular dimensions which could be modeled using a simple square or rectangular environment. However, the passenger cabin of an aircraft is more complicated due to the more complex geometry involved. In this application a commercial ray-tracing software ASAP2005 by Breault Research Organization was utilized. ASAP is an optical analysis software which is mainly used to analyze the illumination produced by sources in various environments by making use of ray-tracing algorithms. The environments are first modeled in the accompanying 3D computer-aided design software package called RHINO3D, where the geometry of the environment is drawn. For the purpose of this design, an aircraft cabin based on the Boeing 777 was used. However, this could be carried for any other aircraft cabin by modeling it in RHINO3D. Using information obtained from Boeing's commercial website [148], the aircraft cabin was modeled and the layout from the top, front, side and angled perspectives are shown in Figure 6.4. Using RHINO3D the cabin geometry can also be rendered to produce the images shown in Figure 6.5. The seats are arranged in a conventional economy class manner as shown in Figure 6.4(b) with 3 seats at the sides and a central row of 4 seats. The seats are identified from A to J, with M representing the aisle location between seats C and D. A total of 9 rows of seats from Row # 1 to 9 were also modeled for the segment of the cabin that is considered. Using RHINO3D, the geometry can also be rendered to produce the images in Figure 6.5.

ATTENTION: The Singapore Copyright Act applies to the use of this document. Nanyang Technological University Library

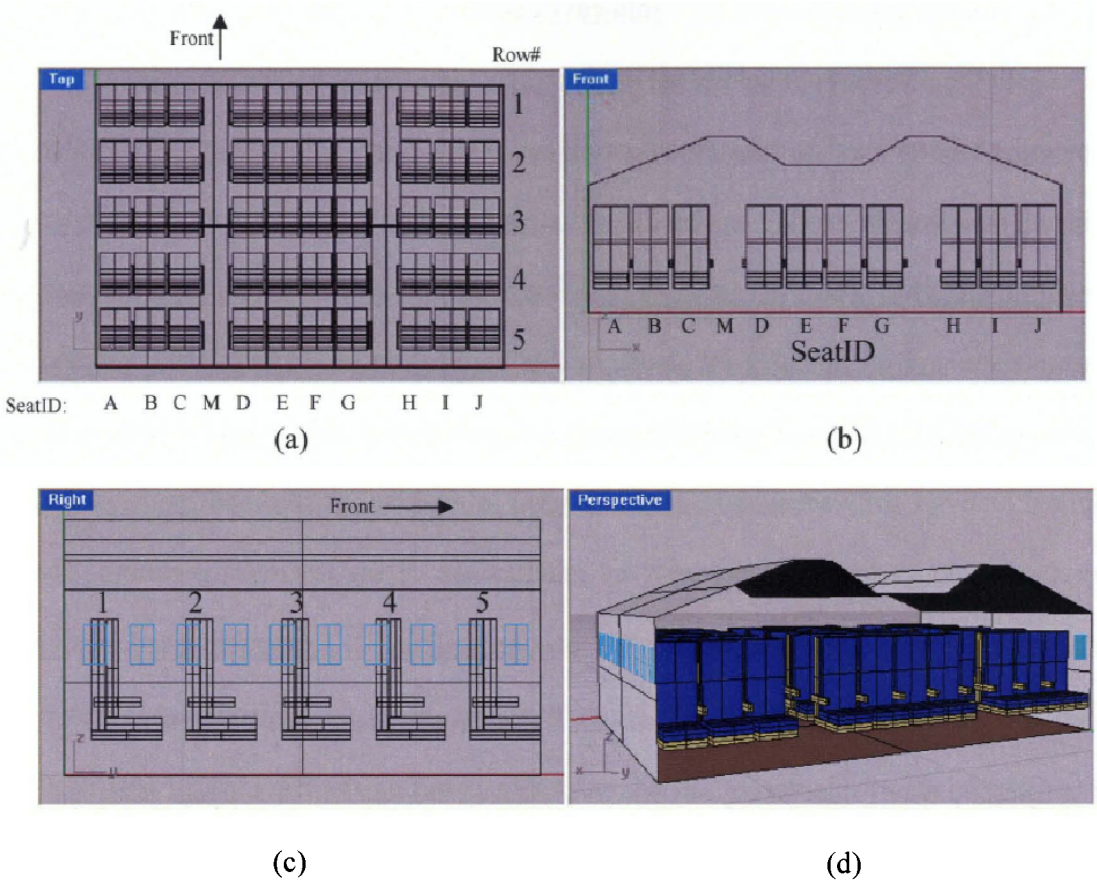


Figure 6.4 Layout of the aircraft cabin geometry based on a Boeing 777 commercial airliner. (a) Top view, (b) front view, (c) side view and (d) perspective view.



Figure 6.5 Rendered images obtained from the geometry shown in Figure 6.4.

ATTENTION: The Singapore Copyright Act applies to the use of this document. Nanyang Technological University Library

The CAD geometry file created using RHINO3D is then imported in ASAP where the information is converted into the native ASAP format. Initially it was observed that during the conversion process some of the geometry became missing or distorted. It was later found out that this was caused by a resolution mismatch between the two programs. For example, if the resolution of the CAD file was set at 0.1mm but the ASAP file was set at the minimum of 1mm, during the conversion process some parts of the geometry could end up occupying the same location in space which leads to errors in the file. To avoid this, some precautions had to be made during the import process which was to ensure that the resolution of the CAD file matched the geometry size defined in ASAP. The reflection coefficient for the reflecting surfaces in particular the ceiling and the walls was set to 0.7 which is a typical value for a diffuse white reflecting surface.

6.5.2 Optimization Methodology

Although ASAP and RHINO3D can be used in conjunction to analyse the effect of sources on the detected intensity at various locations in the environment, ASAP is primarily an analysis software package which does not provide in-built tools for the designing the placement and orientation of sources. To achieve this, the intensity distribution obtained from ASAP is used in conjunction with MATLAB where optimization routines can be programmed for the optical design of the indoor optical wireless network where a uniform intensity is desired so that the area of interest is illuminated uniformly. Moreover, as an optical analysis package ASAP does not offer any means to analyse the multipath dispersion for the environment which can affect the transmission capacity of the system. However, by making use of the ray-path information from ASAP which traces the path of each ray as it

ATTENTION: The Singapore Copyright Act applies to the use of this document. Nanyang Technological University Library

propagates from the source to the detector, the ray-path information can be converted to the time required from the source to the detector. By inputting this information into a MATLAB script file, the multipath dispersion can thus be obtained. Figure 6.6 shows the information flow for the optimization methodology described earlier.

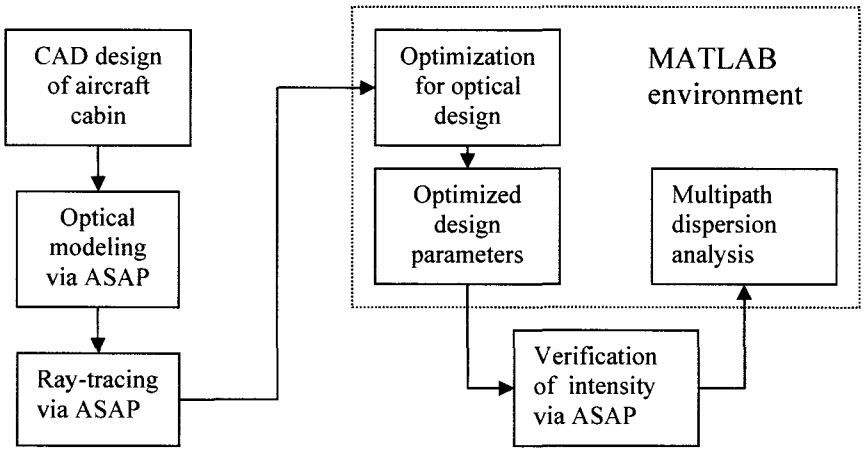


Figure 6.6 Optimization process flowchart.

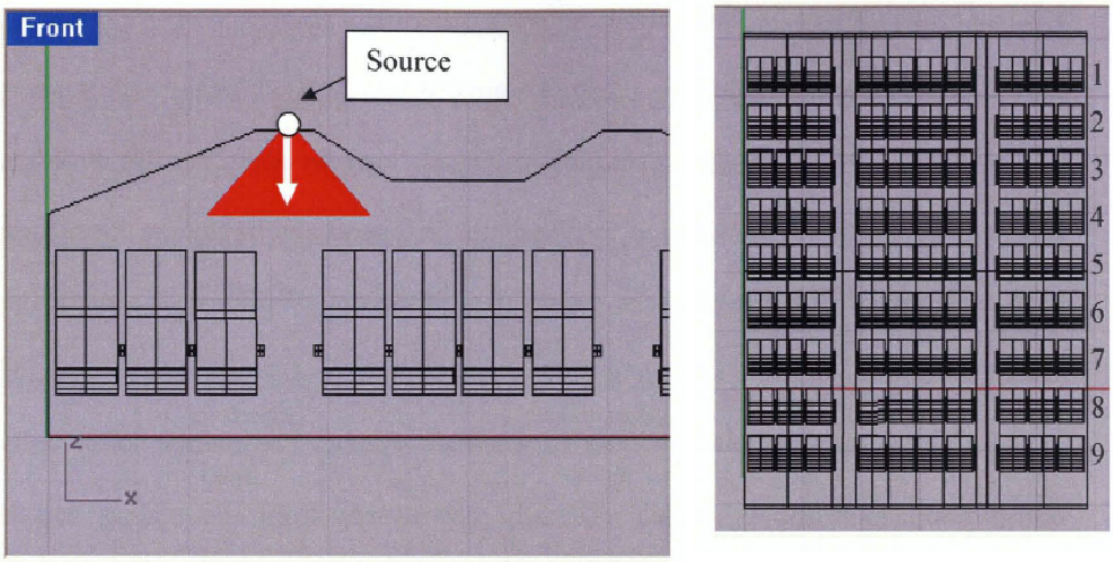
The optical design is carried out in two phases. For an optical wireless system in a cabin environment, users can be categorized into two categories: stationary and mobile. Unlike in most wireless applications where the users can be highly mobile, in an aircraft cabin due to the limited space available most of the time the users are in their seats. As such, the seated users are categorized as stationary users. However, there is another scenario where a user is moving along the aisle while still maintaining a wireless link. These users are considered as mobile users. The design of an optical wireless system for stationary users is generally simpler due to the stationary nature and can be met through use of various approaches. However, for the mobile user, the link coverage has to be detectable throughout the area of coverage, which in this case is focused along the aisle. Also, as the user is mobile, a diffuse source has to be used to ensure maximum coverage.

ATTENTION: The Singapore Copyright Act applies to the use of this document. Nanyang Technological University Library

6.5.3 Optical design for aisle mobile network coverage

As previously mentioned, a diffuse source would be used for the aisle sources for maximum coverage so as to avoid loss of signal along the aisle. For this design, a source with a Lambertian radiation profile which is a good approximation for diffuse sources, is modeled and used as the transmitters in the optical system. If a particular source profile relating to a specific source is desired, that profile can also be modeled in ASAP and used in place of the Lambertian source. The source, with unity transmission intensity, is angled vertically downwards from the ceiling and is positioned right above the centre of the aisle, as shown in Figure 6.7. The ray tracing step is then run for the single source with more than 80,000 rays traced. It was found that this gave a good balance between ray tracing computation time and accuracy, as increasing the number of rays traced resulted in a negligible change of less than 5% in the results while leading to increased computation time. The ray trace plot for a single source is shown in Figure 6.8. For the purpose of viewing the number rays in the figure has been reduced. The intensity distribution for the single source along the aisle, which is indicated as *M* in Figure 6.4(a), is plotted in Figure 6.9. Seat row #5 is taken as the 'origin' for the plot shown in Figure 6.9.

ATTENTION: The Singapore Copyright Act applies to the use of this document. Nanyang Technological University Library



(a) (b)

Figure 6.7 Position of the single source: (a) front view and (b) top view.

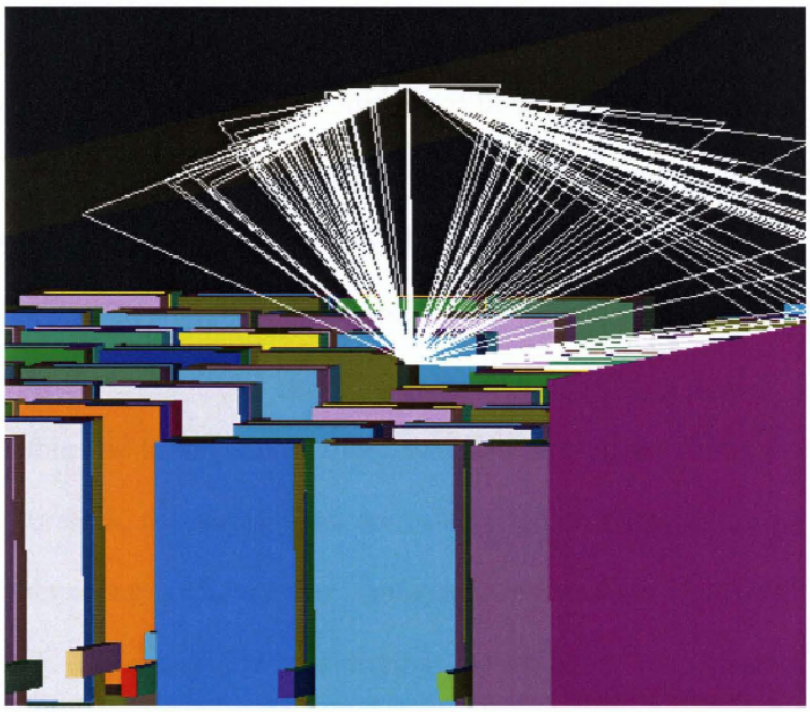


Figure 6.8 Ray trace plot for a single source.

ATTENTION: The Singapore Copyright Act applies to the use of this document. Nanyang Technological University Library

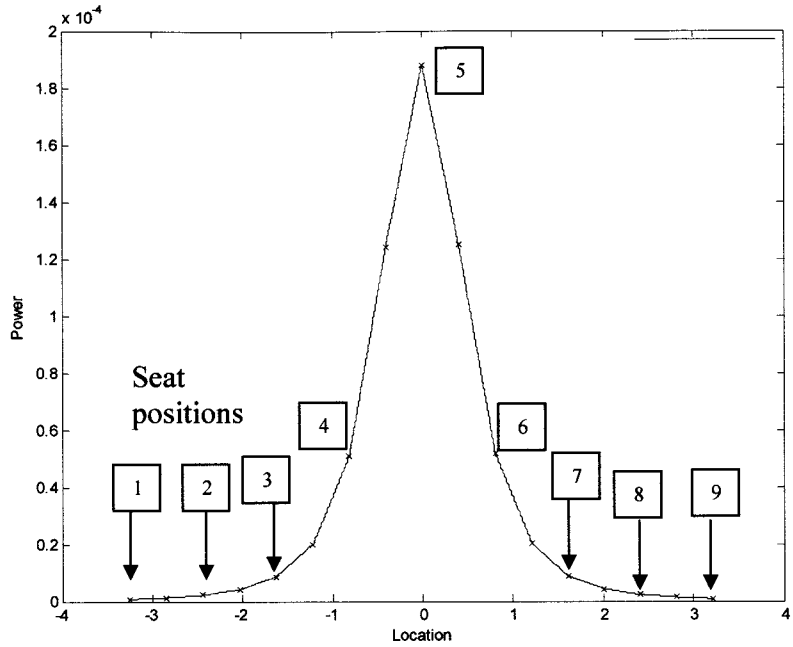


Figure 6.9 Intensity distribution along column M due to a single source.

From Figure 6.9 it can be seen that the intensity distribution drops off beyond the maximum. In order to achieve a uniform distribution more than one source would have to be used. The intensity information in Figure 6.9 was modeled in a MATLAB algorithm to do this, with the merit function defined to minimize the fluctuations in the area of interest, i.e. in the area between rows 1 and 9. An optimization routine was programmed into MATLAB, with the number of sources being a variable, and the source separation being the desired output from the optimization routine. As mentioned before, the target of the optimization process is to obtain as uniform a distribution of signal power as possible. Since the system can be considered a linear system, the resulting power detected P_M can be considered to be the linear sum of the contributions from the various sources. To simplify the optimization and reduce the number of variables that had to be optimized, the location of the sources was defined to be symmetrical about the centre source, such that the separation of pairs of sources about the central source is the same.

ATTENTION: The Singapore Copyright Act applies to the use of this document. Nanyang Technological University Library

The expression for the total power received from the three categories of sources is given in Equation (6.1)

$$P_R = I_M\left(A(0),R\right)+\sum_{l=1}^{Q}\left[I_M\left(A\left(d_Q\right),R\right)+I_M\left(A\left(-d_Q\right),R\right)\right] \tag{6.1}$$

$I_M\left(A\left(d_Q\right),\ R\right)$ refers to the sum of the power of the line of sight and multipath components from the $A(d_Q)$ aisle source to the receiver at position R where R refers to the row identifier, and d_Q is the distance of that source away from the source at the central position $A(0)$ position. d_Q is thus the desired output from the optimization routine. Q refers to the total number of pair of sources. For this section the area of interest is along the column M as the aisle is the focus of the optimization routine, which employed the Nelder-Mead algorithm from the MATLAB function `fminsearch`. Although the simulated annealing method described in Chapter 3 could also be used, the computationally less expensive Nelder-Mead method was used instead as the optimization problem is not as complicated as that in Chapter 3. In this problem, only a few sources are needed, compared to the 1600 possible sources in Chapter 3. Further, as the sources are constrained to be along the aisle, each source has only 1 degree of freedom. Hence, the optimization scenario did not justify the use of the more complicated algorithm and the simpler general optimization algorithm was used instead.

Optimization results

The optimized parameters were run for nine sources initially and a sample ray tracing plot due to the nine sources is shown in Figure 6.10. The obtained optimized intensity plot is shown in Figure 6.11. The red line shows the sum contribution from the 9 sources, while the blue line shows the individual contribution from each source.

ATTENTION: The Singapore Copyright Act applies to the use of this document. Nanyang Technological University Library

Although the optimized values was able to obtain a generally uniform region, it was limited to around-2m to 2m, corresponding to rows 2 to 8 only and thus it was concluded that nine sources, even optimized, were unable to achieve a uniform distribution for the range of points considered, i.e. from position 1-9, in particular for the locations at the extreme ends.

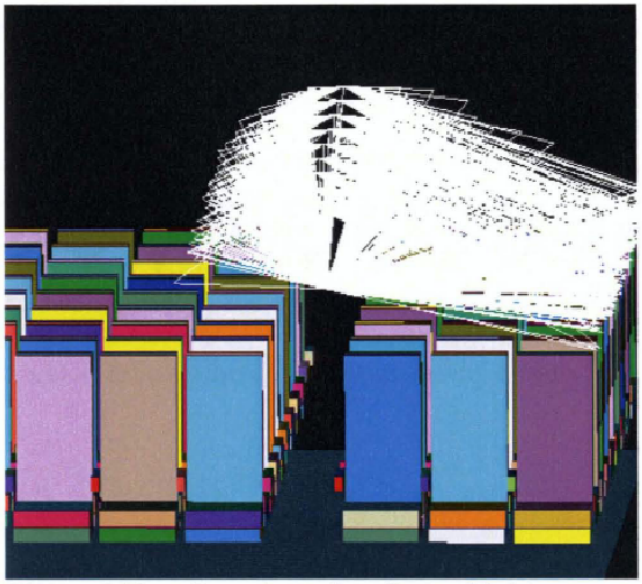


Figure 6.10 Ray trace plots for multiple sources.

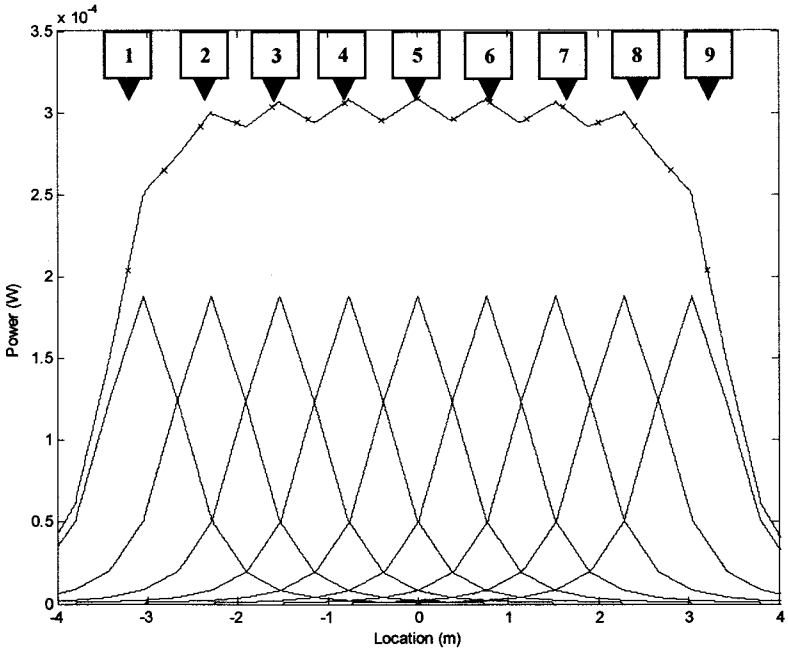


Figure 6.11 Intensity distribution due to nine sources.

The row locations are indicated by arrows and the numbers in the square boxes.

ATTENTION: The Singapore Copyright Act applies to the use of this document. Nanyang Technological University Library

To increase the intensity at the extreme ends eleven sources were used instead. The optimization routine was run again and the following intensity distribution in Figure 6.12 was obtained. It can be seen that there is a wider region where the intensity is uniform, as compared to the earlier results when only nine sources were utilized. There are some 'ripples' observed in the uniform area but the peak-peak variation is less than 5% of the average intensity within the area of interest and is acceptable. The optimized values for d_Q are presented in Table 6.3.

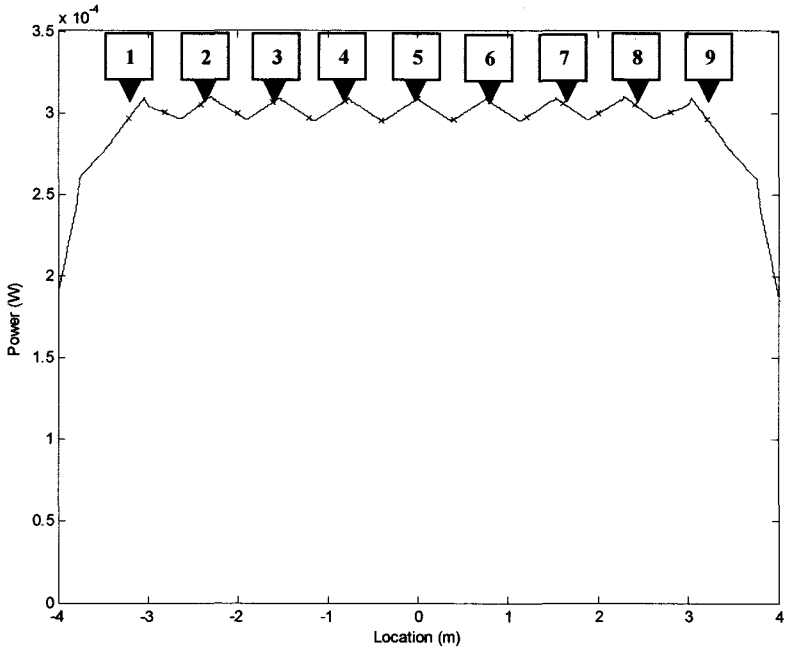


Figure 6.12 Optimized intensity distribution due to eleven sources. The row locations are indicated by arrows and the numbers in the square boxes.

Table 6.3 Optimized source separation with respect to the origin at Row 5

Q	1	2	3	4	5
d(mm)	1528.3	3060.1	4582.5	6086.4	7512.8

ATTENTION: The Singapore Copyright Act applies to the use of this document. Nanyang Technological University Library

The optimized source separation parameters were then used to arrange the sources in ASAP for the eleven sources, after which the ray-tracing step was run again to determine if the results for the uniformity of the sources within the area of interest could be observed. The results from ASAP ray tracing are shown in Figure 6.13. It can be observed from the Figure that the ray tracing simulation shows a higher intensity level than in the optimization model used in MATLAB, as well as smaller variations in the received intensity. This could be attributed to be due to the model used in the optimization, which is based on the sum of the contributions of shifted sources, whereas the ray tracing model is based on the actual path of rays from the sources to the detector. However, the difference is marginal and does not affect the shape of the curve which follows the optimization model closely.

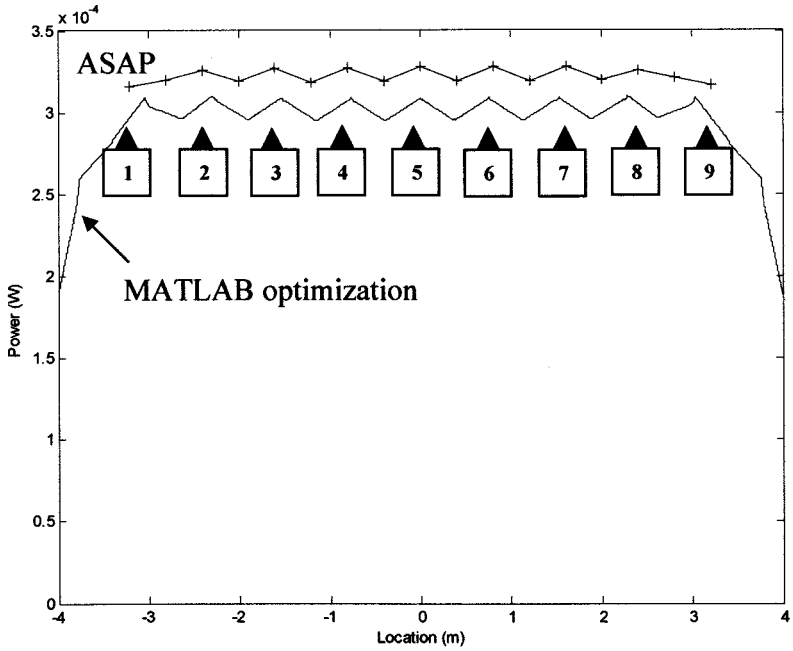


Figure 6.13 Intensity distribution from MATLAB optimization and ASAP ray tracing.

ATTENTION: The Singapore Copyright Act applies to the use of this document. Nanyang Technological University Library

The ray path information from ASAP for the rays from the sources to each receiver was obtained and was input into MATLAB to calculate the multipath dispersion, in a similar way as was performed in Chapter 3. Using the calculated multipath dispersion, the resulting transmission bit rate capacity at each section was calculated using the expression from Chapter 3 where the bitrate is approximately $1/(10\sigma_s)$, where σ_s represents the multipath dispersion. Instead of $1/(10\sigma_s)$, $4/(10\sigma_s)$ can also be used to estimate the bitrate [149] but for the current work, a more conservative estimate of $1/(10\sigma_s)$ is used. The transmission capacity is plotted in Figure 6.14. From the plot, an average transmission rate of about 90 Mbit/s can be observed, with a maximum of 95 Mbit/s and a minimum of 80 Mbit/s at the centre. This is due to the increased number of paths detected by receivers located at the centre of the aisle. It should be noted that this is an estimation of the transmission capacity. A more detailed analysis on the communication performance via bit error rate metrics will be performed in Section 6.5 later

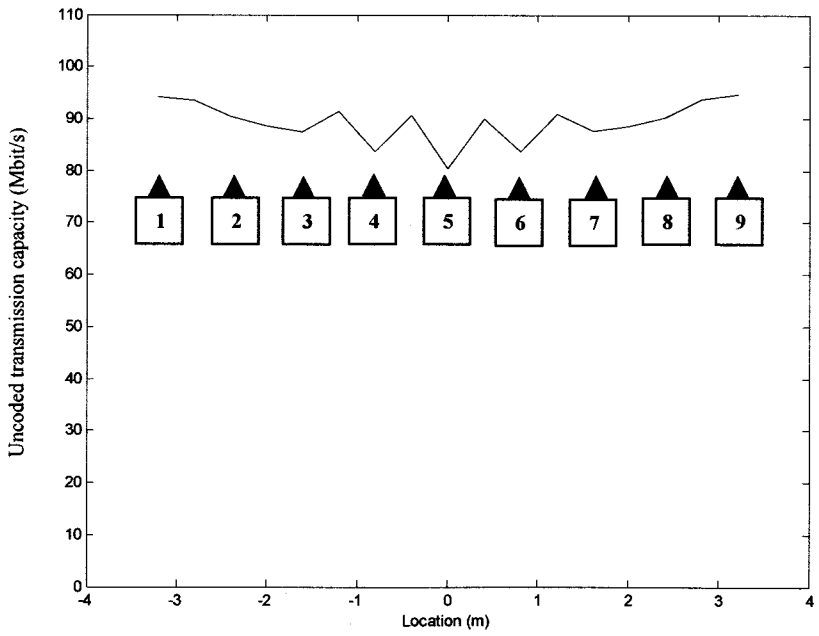


Figure 6.14 Uncoded transmission capacity along the aisle.

ATTENTION: The Singapore Copyright Act applies to the use of this document. Nanyang Technological University Library

6.5.4 Optical design for the stationary network coverage

In the previous section it was shown that a uniform optical network coverage for the mobile user along the aisle can be obtained by using ASAP to model the intensity distribution and then using MATLAB to optimize the placement of the sources. Using the optimized parameters in ASAP resulted in an intensity distribution which corresponded with the MATLAB optimization results.

The optimization optical wireless coverage for the stationary seated user can also be performed in a similar fashion. The optimized parameters for the aisle sources that were obtained earlier will remain in use during the optimization for the seated locations. Figure 6.15 shows the intensity distribution for row 5 for the seat IDs from 5A to 5E when only the aisle sources are active. This will be the region of focus for the subsequent optimization steps. The seat level is specified to be at the tops of the seats in the cabin

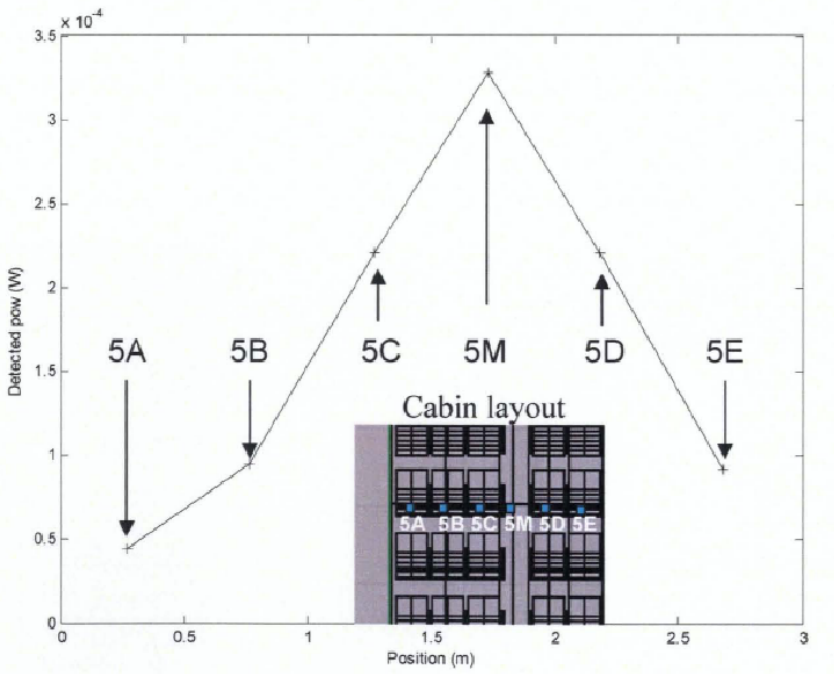


Figure 6.15 Intensity distribution for seat IDs from 5A to 5E using only the aisle sources. Inset shows the location of the seats.

ATTENTION: The Singapore Copyright Act applies to the use of this document. Nanyang Technological University Library

It can be observed from Figure 6.15 that there the power at the edges of the area under consideration is quite low. For example, the intensity at position 5A is less than 15% that of the maximum intensity along the aisle at location 5M. To increase the intensity for the seats from 5A to 5E, additional banks of sources would have to be used. From the observation of the intensity distribution in Figure 6.15, the minimum intensity locations are at 5A and 5E. To compensate for the minimum intensity and to use the least number of additional sources, a source was defined to be located directly above 5A and the angle, defined as the angle between the vertical and direction vector of the source, was allowed to be varied. This will be termed as the side source. For the central group of seats a source was also defined to be mounted along the dorsal line of symmetry on the ceiling, and this will be termed the dorsal source. The central source is angled vertically downwards. Each source is aligned to the location of the rows, such that each row has a side source and dorsal source. As there are nine rows considered in the geometry of the cabin, there would be a total of nine side sources and nine central sources. Figure 6.16 shows the positions of the sources discussed earlier.

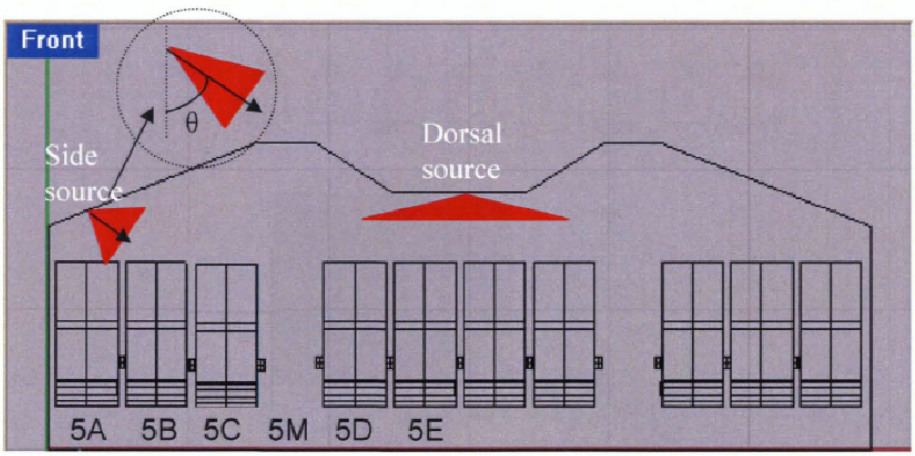


Figure 6.16 Location of the side and dorsal sources.

ATTENTION: The Singapore Copyright Act applies to the use of this document. Nanyang Technological University Library

To obtain the intensity contribution for the banks of side sources as the angles of the sources were varied, multiple ray trace simulations were run. Each side source was set to have the same tilt angle as the other sources, ranging from 30° to 85°. The ray trace simulation was repeated for each angle and the results are plotted below in Figure 6.17, showing the simulated intensity along a row as the tilt angle is varied. It can be observed that as the tilt angle is increased, there is an increase in the distribution of intensity towards the seats 5D and 5E. The contribution from the dorsal sources placed at the centre of the cabin was also obtained via ray trace simulations. The location is fixed to be aligned with the seats and the dorsal sources are pointed vertically downwards. The intensity distribution from the dorsal sources is also plotted in Figure 6.17

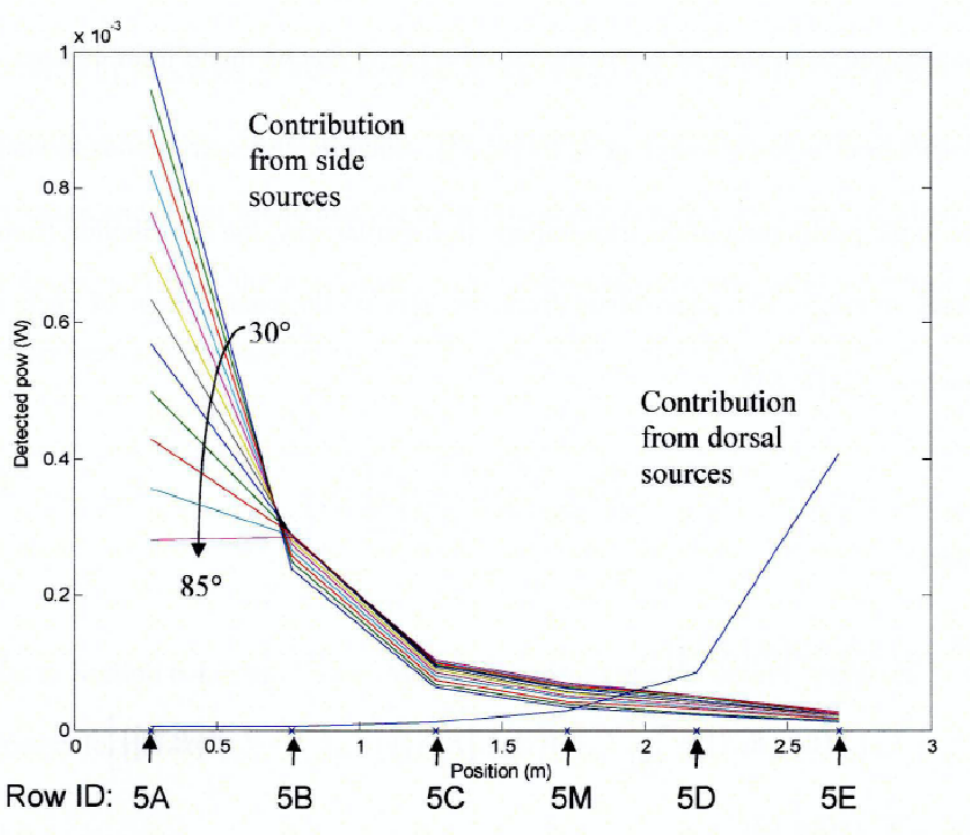


Figure 6.17 Received intensity as the tilt angle of the side sources is varied. Also shown is the contribution from the dorsal sources.

ATTENTION: The Singapore Copyright Act applies to the use of this document. Nanyang Technological University Library

6.5.5 Optimization for stationary and mobile users

In the ray trace simulations, angle intervals at 5° were ray traced. However, in order to obtain a finer angle adjustments the intensity contributions were modeled in MATLAB and interpolated for fine tuning the tilt angle. This is reasonable as it can be observed from Figure 6.17 that the change in the intensity distribution as the tilt angle is varied is continuous with no abrupt changes.

Also, the intensity distribution that was obtained earlier from the aisle distribution is unchanged. Due to the linear nature of the system, the total contribution $P_{[R,S]}$ from all the sources i.e. side $P^{W}_{[R,S]}$, aisle $P^{A}_{[R,S]}$ and dorsal $P^{D}_{[R,S]}$,at each location can be found by the summation of the contribution from each source, where $[R,S]$ describes the row and seat identifiers for each location. For the side sources, the contribution from each source to the location $[R,S]$ can be found from the sum of the contributions of each source m, $I^{m}_{W}(\theta,[R,S])$, where m also corresponds to each row due to the positioning of the transmitters. In a similar way, the contribution from each dorsal source is also determined from the sum of the contribution of each dorsal source n, $I^{n}_{d}([R,S])$.

$$P_{[R,S]} = P^{W}_{[R,S]} + P^{A}_{[R,S]} + P^{D}_{[R,S]} \tag{6.2}$$

where

$$P^{W}_{[R,S]}(\theta) = \sum_{m}^{9} I^{m}_{W}(\theta,[R,S]) \tag{6.3}$$

$$P^{A}_{[R,S]} = I_{M}(A(0),[R,S]) + \sum_{l=1}^{5}\left[I_{M}(A(d_{Q}),[R,S]) + I_{M}(A(-d_{Q}),[R,S])\right] \tag{6.4}$$

$$P^{D}_{[R,S]} = \sum_{n}^{9} I^{n}_{d}([R,S]) \tag{6.5}$$

ATTENTION: The Singapore Copyright Act applies to the use of this document. Nanyang Technological University Library

To optimize the distribution of the intensity distribution for Seat 5A to 5E, Equation (6.2) can be used, where the variables for the optimization step is set as α,β and γ, which can be used to represent the relative intensity emission settings for the banks of the side sources, the aisle sources and the dorsal sources respectively. Furthermore, although the positions of the sources have been fixed in this instance, the angle of the side sources is made a variable to be optimized. The modified form of Equation (6.2) including the optimization variables is presented in Equation (6.6) below.

$$P_{[R,S]} = \alpha P^{W}_{[R,S]}(\theta) + \beta P^{A}_{[R,S]} + \gamma P^{D}_{[R,S]} \tag{6.6}$$

Equation (6.6) was used in an optimization routine to obtain a uniform intensity for the locations 5A to 5E. Different merit function were attempted during the optimization and it was found that the most favourable results were obtained when the merit function Π used the peak intensity as a reference and attempted to reduce the difference between the peak intensity and the intensity at the other locations i.e.

$$\Pi = \sum \left| \left(P_{[R,S]} - \max P_{[R,S]} \right) \right| \tag{6.7}$$

Similar to Section 6.4.3, the Nelder-Mead method was used to obtain optimized parameters for α,β and γ.

ATTENTION: The Singapore Copyright Act applies to the use of this document. Nanyang Technological University Library

Optimization Results

After running the optimization routine using Equation (6.6) and Equation (6.7), the optimized parameters are as given in Table 6.4. Effectively besides the tilt angle of the side sources, the important optimization parameters are the ratio between the three banks of sources rather than the individual weights taken on their own. By normalizing the weighting values of α, β and γ, against β, the relative intensity of the side and dorsal sources can be determined against the aisle intensity which is taken as a reference. Thus by changing the aisle intensity level and keeping the ratios constant, the general intensity level can be changed. Figure 6.18 shows the intensity distribution when the optimization parameters are used, with the intensity weights normalized against the aisle intensity. This is also appropriate, as the aisle intensity is the highest, and this would be the major consideration for eye safety emission controls.

Table 6.4 Optimized parameters θ, α, β and γ

Optimization Variables	Optimized values	Optimized values normalized against β
θ	77.3312°	77.3312°
α	0.4392	0.6717
β	0.6538	1.0000
γ	0.2934	0.4487

ATTENTION: The Singapore Copyright Act applies to the use of this document. Nanyang Technological University Library

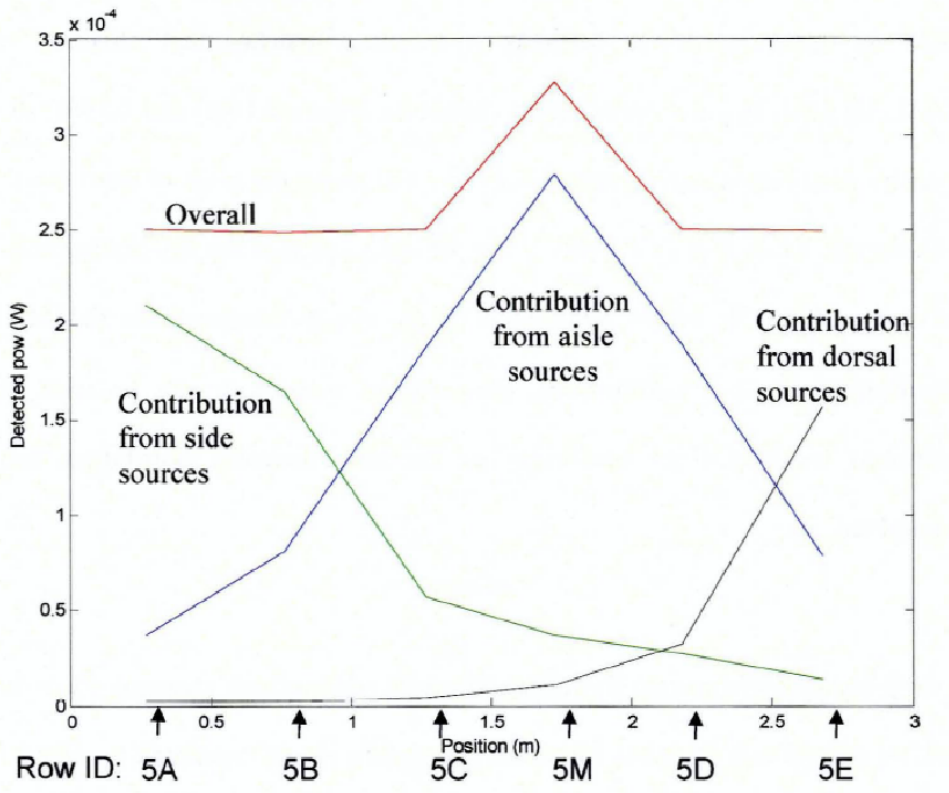
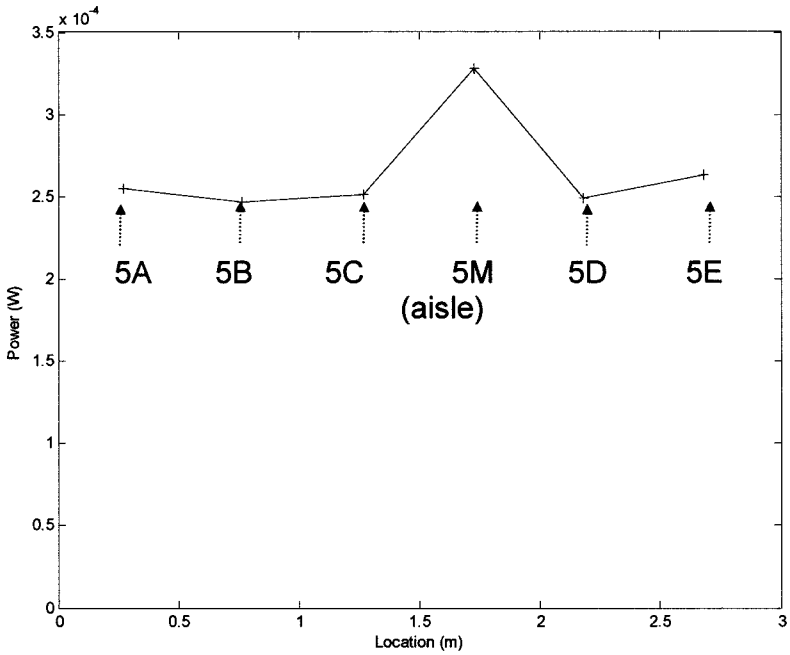


Figure 6.18 Intensity distribution using the optimized parameters in Table 6.3.

Figure 6.18 shows the total intensity in the row as well as the contributions from each bank of sources. From the figure, it can be observed that there in general the intensity distribution across the seat positions from 5A to 5E is uniform with minimal variation. At the aisle, there is a higher intensity which was unable to be reduced. This can actually be used to increase the link budget of users along the aisle As such users are more likely to be mobile users, the increased power budget would be useful improving signal quality through an increased signal to noise ratio, as opposed to stationary applications such as the seats where a lower can be acceptable.

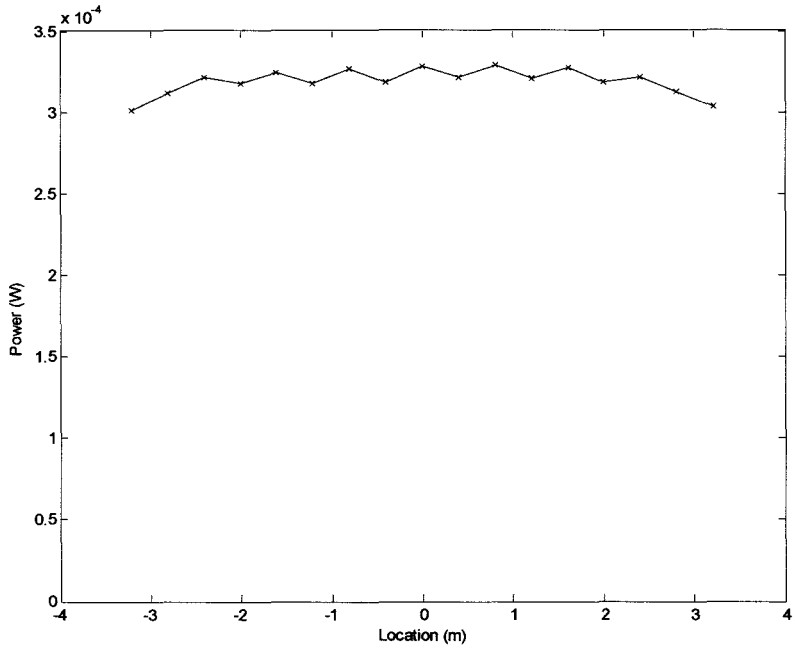
ATTENTION: The Singapore Copyright Act applies to the use of this document. Nanyang Technological University Library

Next, the optimized parameters were input into the ray tracing package in ASAP to determine if the intensity distribution matches that obtained via the MATLAB modeling and optimization processes. Figure 6.19(a) and 6.19(b) show the intensity distribution across seats 5A to 5E, and along the aisle *M* from rows 1 to 9 respectively. From Figure 6.19(a), it can be observed that the ray-tracing results for the seats 5A to 5E match up well with the results obtained via the MATLAB optimization process. Furthermore, from Figure 6.19(b), it can be seen that the optimized results for the uniformity of the aisle intensity distribution has been maintained.



(a)

ATTENTION: The Singapore Copyright Act applies to the use of this document. Nanyang Technological University Library



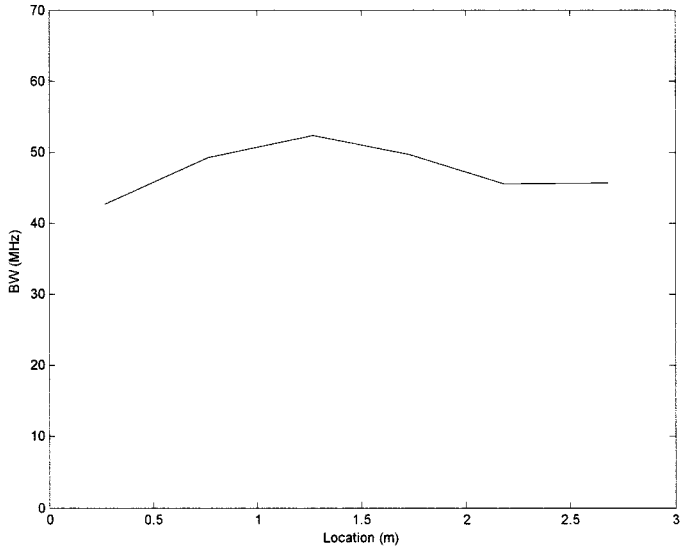
(b)

Figure 6.19. Intensity distributions using the optimized parameters obtained from MATLAB and simulated via ray tracing. (a) shows the intensity distribution for the seats 5A to 5E and (b) shows the intensity distribution along the aisle *M*.

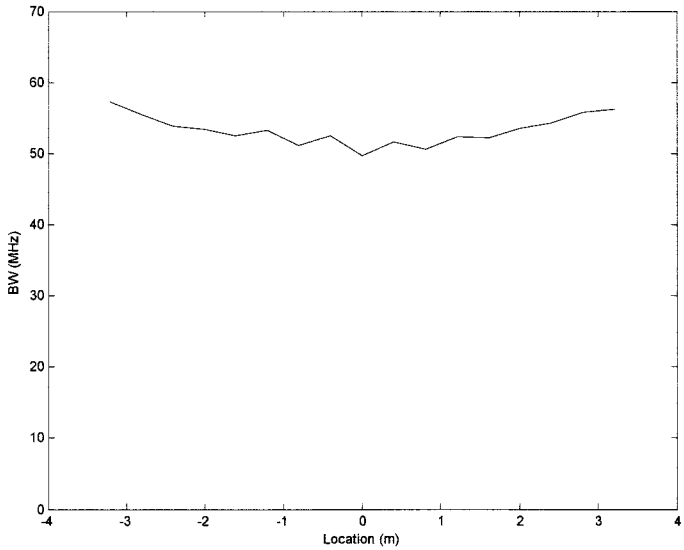
Next an estimation is made for the transmission capacity based on the multipath dispersion obtained from the ray tracing program, as was done earlier for the aisle optimization. The resulting transmission capacities for the seats from 5A to 5E, and that for the aisle are shown in Figures 6.20(a) and 6.20(b) respectively. From Figure 6.20(a), it can be seen that the transmission capacity ranges from 42 Mbit/s to 52 Mbit/s, with a calculated average transmission capacity of 48 Mbit/s. For the aisle transmission capacity in Figure 6.20(b), it can be seen that although the profile is similar to Figure 6.14, there has been an approximate 50% reduction in the transmission capacity. This is attributed to the increased number of multipaths and sources in the environment. In Figure 6.14, only 11 sources were considered but in Figure 6.20(b), 29 sources were used, which is more than twice that number. This is

ATTENTION: The Singapore Copyright Act applies to the use of this document. Nanyang Technological University Library

since there are 9 rows in the volume under consideration, and with each row having a 'side' cluster and a 'dorsal' cluster which consists of 1 source each aligned is aligned to each cluster in a row, the total number of sources used was 29. This increased the level of multipath dispersion, resulting in a limitation in the transmission capacity. It should be noted that this represents the capacity as defined only by the multipath dispersion limitations.



(a)

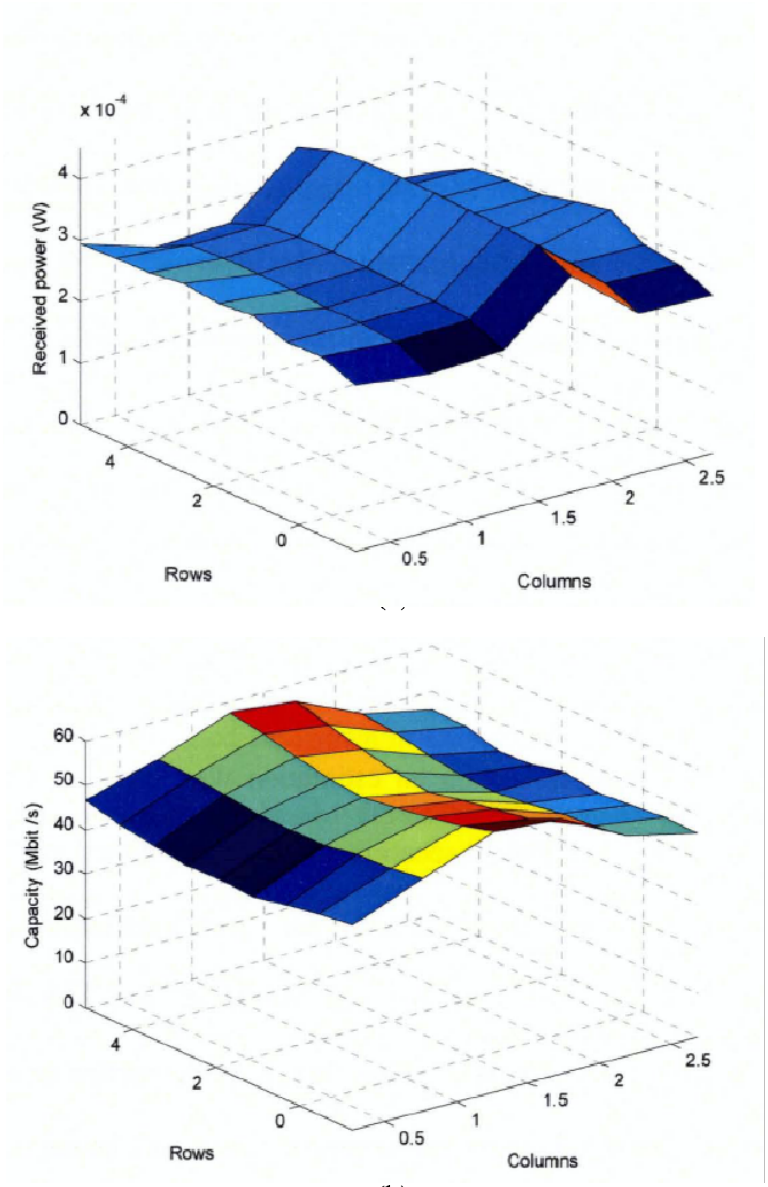


(b)

Figure 6.20 Transmission capacities estimated using multipath dispersion for (a) rows 5A to 5E and (b) along the aisle *M*.

ATTENTION: The Singapore Copyright Act applies to the use of this document. Nanyang Technological University Library

Figure 6.21 shows the received power and estimated transmission capacity for the locations considered in the optimization process. It can be seen from Figure 6.21(a) that it has resulted in a generally uniform distribution of power with a peak at the centre along the aisle. Figure 6.21(b) shows the transmission capacity across the locations considered. In the next section a study will be made on the bit error rate of the system, particularly the effect of multipath on a system model.



(b)

Figure 6.21 (a) Received power and (b) estimated transmission capacity across the cabin locations in the ray tracing simulations.

ATTENTION: The Singapore Copyright Act applies to the use of this document. Nanyang Technological University Library

6.5.6 Other possible approaches for source configuration

The work presented thus far was based on the use of a source with a diffuse Lambertian profile in within the simulation model. Other sources may well be used. For example, beam shaping could be used to shape the emitted beam from the source to exactly meet specified requirements. CGHs could also be used in a similar fashion with even tighter control over the shape of the illuminated area. Alternatively, a bank of sources could be used to track the users within the operating region of the source, similar to the tracked optical wireless approach in [65]. Even further, it may be possible to make use of mounted SLMs to dynamically generate a CGH pattern to fit a constantly changing user environment. However, most of the methods mentioned would cause an increase in the complexity of the system as well as cost, and are not further explored within the scope of this Thesis.

6.6 System bit error rate performance

In this section the results obtained previously will be used to determine the communications performance of the system as characterized by the bit error rate performance. In the previous section an estimation was made on the transmission capacity based on the multipath dispersion limitations outlined earlier, where the signal can be transmitted without interference from multipath effects and no equalization is required. From the previous results it can be observed that a transmission capacity of about 50Mbit/s is available. In this section an analysis will be made using the communications model presented earlier in Chapter 3. One scenario will be considered where the bit error performance is based solely on the signal quality from noise sources and the received power and it is assumed that the signals can be recovered without influence from multipath effects. In another scenario,

ATTENTION: The Singapore Copyright Act applies to the use of this document. Nanyang Technological University Library

multipath effects will be included without equalization, with the purpose to ascertain the magnitude of influence on the system performance when there is no equalization.

6.6.1 Bit Error Rate performance with no multipath effects

In this scenario it will be assumed that multipath effects have been negated through the use of equalization, and variation of the bit error rate as the transmission bitrate is increased will be determined. Also, it is assumed that an ideal equalizer is employed, such that multipath effects are completely suppressed, and all the dispersed energy of a transmitted bit can be recovered through the tapped delay lines in the equalizer, for example as described in Section 3.5.8. This represents the ideal case since multipath dispersion would be completely eliminated, leaving only background ambient light noise effects which causes an increase in the shot noise, and thermal noise. The effects of quantization and multipath will be discussed in Section 6.5.2. The model presented earlier for an On Off Keying (OOK) modulation scheme for the system in Section 3.5.4 is utilized. The bit error rate performance is determined by Equation (3.21), and the noise can be modeled using Equations (3.09) to (3.21). The receiver model parameters used are shown in Table 6.5. A 50Ω load resistance is used in this situation to maximize the bandwidth of the receiver. As the received signal I_S and background current I_{BG} are in the μW regime, and are much stronger than the dark current I_D, which is usually in nW, I_D can be considered to be negligible.

ATTENTION: The Singapore Copyright Act applies to the use of this document. Nanyang Technological University Library

Table 6.5 Receiver model parameters

Parameter	**Value**
Responsivity, R	0.9 A/W
Bandwidth, B	$0.8*R_b$ Hz
Boltzmann's Constant, k_B	1.38×10^{-23} J/K
Electron Charge, q	1.6×10^{-19} C
Temperature, T	293K
Load Resistance, R_L	50Ω

The received power at the detector is determined by multiplying the received power P_R with the sensitivity of the detector i.e. $I_R = R \times P_R$. From the earlier work done, the average received power was found to be about 300μW. However, this is based on setting each source to transmit 1W. Based on eye safety requirements defined earlier in Section 6.4.1, the AEL for a 1550nm source is 10mW. Scaling the emission power down and making use of the linearity of the system, the received power is thus 3μW.

ATTENTION: The Singapore Copyright Act applies to the use of this document. Nanyang Technological University Library

Background noise considerations

In Section 6.4.2, some measurements were made based on various ambient lighting conditions. To determine the effect on the bit error rate performance the measured results will be utilized. In an aircraft environment, the scenarios considered will be that of direct sunlight, indirect sunlight and fluorescent lighting and thus incandescent lighting conditions will not be considered. Also, to minimize out-of-band ambient spectral light, the filtered results from Table 6.2 will be utilized. To allow the modulated signal to be detected in the presence of strong ambient noise, a highpass frequency filter will also be used in the receiver model and is taken to preserve the integrity of the signal. However, due to the 'white' nature of noise, the noise variance must still be considered in the determination of the BER performance.

Bit error rate simulation results

Figure 6.22 shows the bit error rate variation as the transmission rate is varied. As the bitrate is increased, there is an increase in the error rate due to the larger bandwidth required in the receiver system which increases the amount of noise. The BER results for the indirect sunlight and the fluorescent lighting conditions are observed to be very close. This is due to the strong received signal relative to the magnitude of the noise variance σ^2, and that indicates a good signal quality. As can be seen, the system can allow transmission up to 700 Mbit/s for a BER of $1x10^{-5}$. When direct sunlight is the used as the background noise, it can be observed that it results in a power penalty that increases the bit error rate, due to increased level of noise at the receiver. For a BER of $1x10^{-3}$, the transmission rate is approximately 660 MBit/s. In the absence of multipath dispersion, the results presented in Figure 6.22

ATTENTION: The Singapore Copyright Act applies to the use of this document. Nanyang Technological University Library

represents the potential bit error rate performance that can be achieved, given that equalization can be ideally carried out.

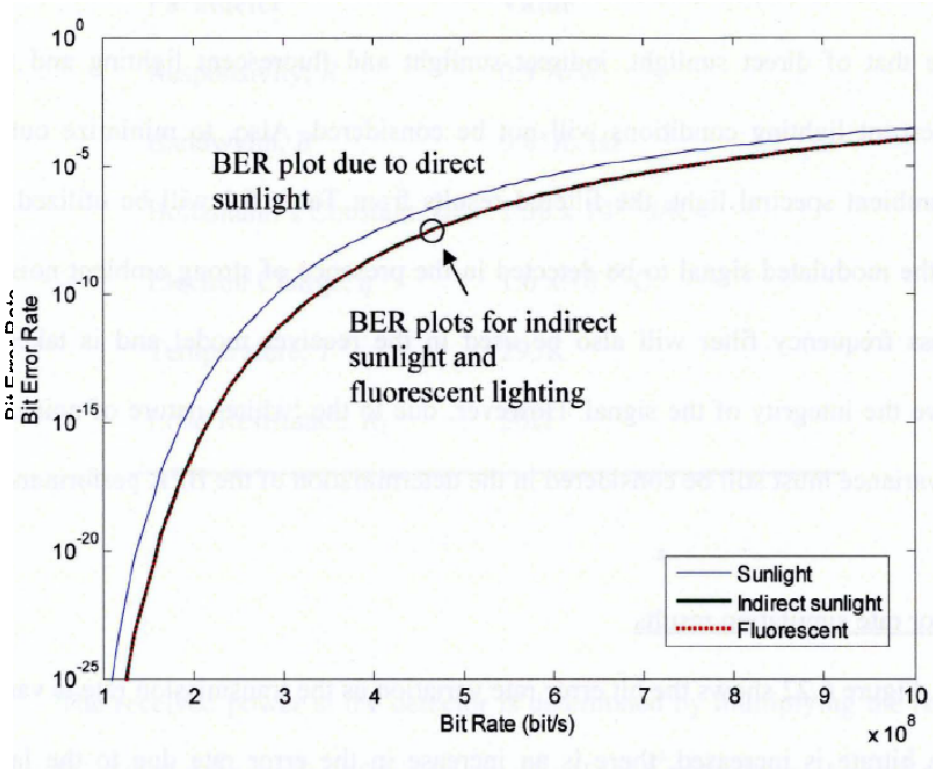


Figure 6.22 BER for direct sunlight, indirect sunlight and fluorescent lighting conditions.

6.6.2 System performance modelling considering multipath effects

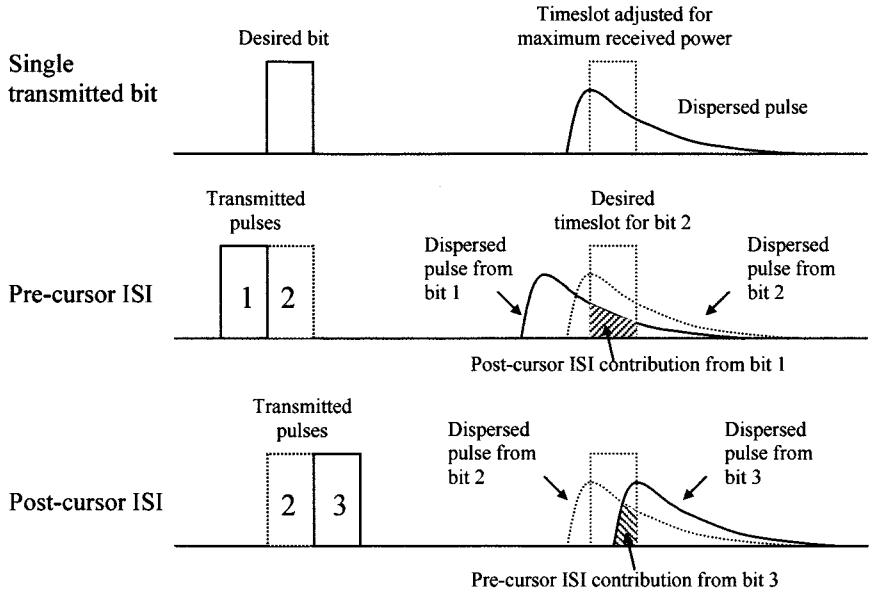
In this section the bit error rate performance is simulated while taking into account multipath dispersion effects with no equalization. The effect of multipath on a signal leads to a broadening of the signal pulse. The tail of the broadened pulse can extend into subsequent receiver timeslots, which affects the signal to noise ratio of the affected timeslots. This is known as pre-cursor intersymbol interference, due to the effect on the desired symbol by the preceding bit. For example, for an OOK system,

ATTENTION: The Singapore Copyright Act applies to the use of this document. Nanyang Technological University Library

the decision threshold of a receiver is usually taken to be half of the received pulse P_{on}, since there is no power transmitted during the OFF period. The decision threshold is thus 0.5 P_{on}. Then, consider that the next timeslot is affected by a portion of the power from the previous slot ΔP. The power entering the decision threshold is thus $P_R = P_{ON}+\Delta P_{on}$ *or* $P_R = \Delta P$, depending the whether the transmitted signal is an OFF or an ON signal. Given that the error probability depends on the difference between the decision threshold and the received power, the probability of error for the expected OFF is increased while the probability of error rate for the expected ON is decreased. In most cases the error rate increase is more significant that the reduction of the error rate, and as the overall bit error rate is determined by the average of the bit error rate for the ON signal and the OFF signal, given unbiased transmission probability, the effective result is a reduction in the bit error rate of the system.

The expected signal can also be affected by post-cursor intersymbol interference, where the expected signal is influenced by the bit transmitted after the desired bit. In general the timeslot for each received signal is usually adjusted to where the sum of the power in the timeslot is maximum. Thus the timeslot may not coincide with the instant the pulse is received, but instead the origin of the timeslot might be delayed to the time where the received power is maximum for the bit. This causes pre-cursor ISI where the timeslot is affected by signals sent after the expected signal. The two types of ISI are illustrated in Figure 6.23.

ATTENTION: The Singapore Copyright Act applies to the use of this document. Nanyang Technological University Library



6.23 Illustration showing pre-cursor and post-cursor ISI.

To determine the effect on the BER, first recall the expression for error when a '0' bit is expected, but a '1' bit is received, from Chapter 3, where the photocurrent for a '0' bit is a Gaussian random variable with mean I_0 and variance σ_0, as shown in Equation (6.8). A similar expression is shown in Equation (6.9) for the error corresponding to an error for an expected '1' bit. As before, γ_0 represents the threshold level as taken when no multipath is considered.

$$P(1/0) = \frac{1}{\sigma_0\sqrt{2\pi}} \int_{\gamma_0}^{\infty} \exp\left[-\frac{1}{2}\frac{(I-I_0)^2}{\sigma_0^2}\right] dI \tag{6.8}$$

$$P(0/1) = \frac{1}{\sigma_1\sqrt{2\pi}} \int_{-\infty}^{\gamma_0} \exp\left[-\frac{1}{2}\frac{(I-I_1)^2}{\sigma_1^2}\right] dI \tag{6.9}$$

ATTENTION: The Singapore Copyright Act applies to the use of this document. Nanyang Technological University Library

Multipath results in an additional amount of power being received by the photodetector, and the resulting photocurrent from the sum of the additional multipaths can be denoted as I_α. I_α can be considered to cause a shift in the received photocurrent, such that the average received power for an expected '0' and '1' bit becomes $I_0 + I_\alpha$ and $I_1 + I_\alpha$ respectively. Equations (6.8) and (6.9) thus become

$$P_m(1/0) = \frac{1}{\sigma_0\sqrt{2\pi}} \int_{\gamma_0}^{\infty} \exp\left[-\frac{1}{2}\frac{(I-(I_0+I_\alpha))^2}{\sigma_0^2}\right] dI \tag{6.10}$$

$$P_m(0/1) = \frac{1}{\sigma_1\sqrt{2\pi}} \int_{-\infty}^{\gamma_0} \exp\left[-\frac{1}{2}\frac{(I-(I_1+I_\alpha))^2}{\sigma_1^2}\right] dI \tag{6.11}$$

where P_m represents the probability in the presence of multipath. Rewriting the expressions into the Q-form shown in Equation (6.12)

$$Q(x) = \frac{1}{\sqrt{2\pi}} \int_x^{\infty} \exp\left[-\frac{y^2}{2}\right] dy \tag{6.12}$$

the following expression for the error rate can be obtained:

$$P(1/0) = Q\left(\frac{\gamma_0 - (I_0 + I_\alpha)}{\sigma_0}\right) \tag{6.13}$$

$$P(0/1) = Q\left(\frac{(I_1 + I_\alpha) - \gamma_0}{\sigma_1}\right) \tag{6.14}$$

ATTENTION: The Singapore Copyright Act applies to the use of this document. Nanyang Technological University Library

Using the expression for the optimum threshold condition $\gamma_0 = \frac{\sigma_0 I_1 + \sigma_1 I_0}{\sigma_0 + \sigma_1}$, Equations (6.13) and (6.14) can be re-written as Equations (6.15) and (6.16) respectively.

$$P_m(1/0) = Q\left(\frac{I_1 - I_0}{\sigma_1 + \sigma_0} - \frac{I_\alpha}{\sigma_0}\right) \tag{6.15}$$

$$P_m(0/1) = Q\left(\frac{I_1 - I_0}{\sigma_1 + \sigma_0} + \frac{I_\alpha}{\sigma_1}\right) \tag{6.16}$$

Given equal probability of a '0' bit and a'1' bit being transmitted, the average bit error probability thus becomes Equation (6.17). Unlike in the case where there is no multipath dispersion, the multipath error causes an increase in the error for $P_m(1/0)$ but a decrease in the error for $P_m(0/1)$. Due to the shape of the Gaussian probability function, $P_m(1/0) > P_m(0/1)$ resulting in an increase in the effective bit error rate P_{Bm}.

$$P_{Bm} = \frac{1}{2}\left[Q\left(\frac{I_1 - I_0}{\sigma_1 + \sigma_0} + \frac{I_\alpha}{\sigma_1}\right) + Q\left(\frac{I_1 - I_0}{\sigma_1 + \sigma_0} - \frac{I_\alpha}{\sigma_0}\right)\right] \tag{6.17}$$

Determination of the contribution of multipath signals towards I_α

As was shown earlier, the bit error rate as a result of multipath cannot be generalized. Instead, the effective bit error rate depends on the contribution by the multipath signals towards the desired timeslot, which can consist of pre-cursor and post-cursor ISI. Let the number of pre-cursor bits which affect the desired timeslot be P, and the number of post-cursor bits be S. Given the binary nature of the bits, the

ATTENTION: The Singapore Copyright Act applies to the use of this document. Nanyang Technological University Library

total number of bit sequences that can affect the desired timeslot is $B = 2^P$ x 2^S, or 2^{P+S} bit sequences, with the length of each bit sequence, including the desired timeslot, equal to $P+S+1$. Using $I_\alpha(B)$ to represent the contribution from each bit sequence, and letting each bit sequence have an equal probability of transmission, the effective system bit error rate P_{SBm} can be calculated by averaging the bit error rate from each bit sequence

$$P_{EBm} = \frac{1}{2^{P+Q}} \sum_{B=1}^{P+Q} \frac{1}{2} \left[Q\left(\frac{I_1 - I_0}{\sigma_1 + \sigma_0} + \frac{I_\alpha(B)}{\sigma_1} \right) + Q\left(\frac{I_1 - I_0}{\sigma_1 + \sigma_0} - \frac{I_\alpha(B)}{\sigma_0} \right) \right] \tag{6.18}$$

To determine $I_\alpha(B)$, the impulse response for the optical wireless system is first obtained from the previous multipath dispersion calculation in the earlier sections, and is defined as $h(t)$. Letting the bit sequence be $b(t)$ consisting of $P+S+1$ bits inclusive of the desired timeslot, at a transmission bitrate of $1/T$, the pulse at the receiver can thus be found by the convolution of the impulse response with the signal pulse , i.e. $y(t) = b(t) \otimes h(t)$. Discretizing the received pulse every T seconds, the power of each received bit is given by $y_k = b(t) \otimes h(t)|_T$, where it is assumed that the time origin is shifted to maximize the power in each timeslot. At the desired timeslot, the received signal consists of the desired signal as well as multipath components. The multipath components can be obtained by determining the difference between the multipath-contributing bitstream, and a single bit being transmitted at the desired timeslot. It should also be noted that the received power per bit in the absence of multipath is less than that in Section 6.6.1, due to the limitation to the received power of each bit to the timeslot where the received power is maximum. In cases where the multipath dispersion is severe, the dispersed pulse of each bit can extend to multiple

ATTENTION: The Singapore Copyright Act applies to the use of this document. Nanyang Technological University Library

timeslots, leading to a reduction of power in the desired timeslot. In Section 6.6.1, it was taken that the dispersed power could be fully recovered, however in this Section only the power in the desired timeslot is considered.

This approach requires multiple convolutions to determine the multipath components. With a multipath-contributing bit-sequence length of P pre-cursor bits and S post-cursor bits, a total of 2^{P+S} sequences would have to be considered. A modified approach involves making use of the linearity of the transmitted signal to obtain the multipath contribution from each bit in the bit sequence. Thus only $P+S$ convolutions would have to be performed. The multipath contribution from each bit sequence only depends on whether or not the actual bit in the sequence is being transmitted.

For example, let P1 be the 1st pre-cursor bit P1, P2 to be the 2nd pre-cursor bit, and S1 be the 1st post-cursor bit. The bit stream sequence is thus (P2) (P1) (K) (S1) where K is the desired bit. To find the multipath contribution where P_2, P_1 and S_1 are ON, (1101) is set as the bit-sequence and is convolved with *h(t)*. By setting K as 0, since no power is transmitted when a '0' bit is transmitted, the multipath contributions from P2, P1 and S1 can be found. For another bit sequence say (1100), the convolution would have to be performed again.

In contrast, the individual multipath contributions can first be obtained for each contributing bit. Let P_{1m} be the multipath contribution from the 1st pre-cursor bit P1, P_{2m} to be the multipath contribution from the 2nd pre-cursor bit P2, and S_{1m} to be the multipath contribution from the 1st post-cursor bit S1. For a sequence (1101), the multipath contribution from the bit-sequence is thus the sum of the 'ON' bits i.e. $P_{1m} + P_{2m} + S_{1m}$. For another bit sequence (1100) the multipath contribution is thus $P_{1m} + P_{2m}$. The multipath contribution is then used to determine the effect on the BER.

ATTENTION: The Singapore Copyright Act applies to the use of this document. Nanyang Technological University Library

Although the number of different sequences considered remains the same i.e. 2^{P+S}, the number of convolutions required is much less. Particularly when the multipath bit stream is long for example more than 10 bits, such an approach can help to reduce the computation time.

6.6.3 BER performance considering multipath effects

Using the approaches outlined in the previous discussion, the BER was determined as the bit rate is increased from 100 Mbit/s to 500 Mbit/s, and is shown in Figure 6.24. To determine the effect of ambient noise on the system, direct sunlight and fluorescent lighting conditions have also been included. It can be observed from the Figure that multipath dispersion has a greater impact on the system BER performance than ambient noise, causing approximately a 4 to 5 order increase in the BER at transmission rates from 100 Mbit/s to 200 Mbit/s.

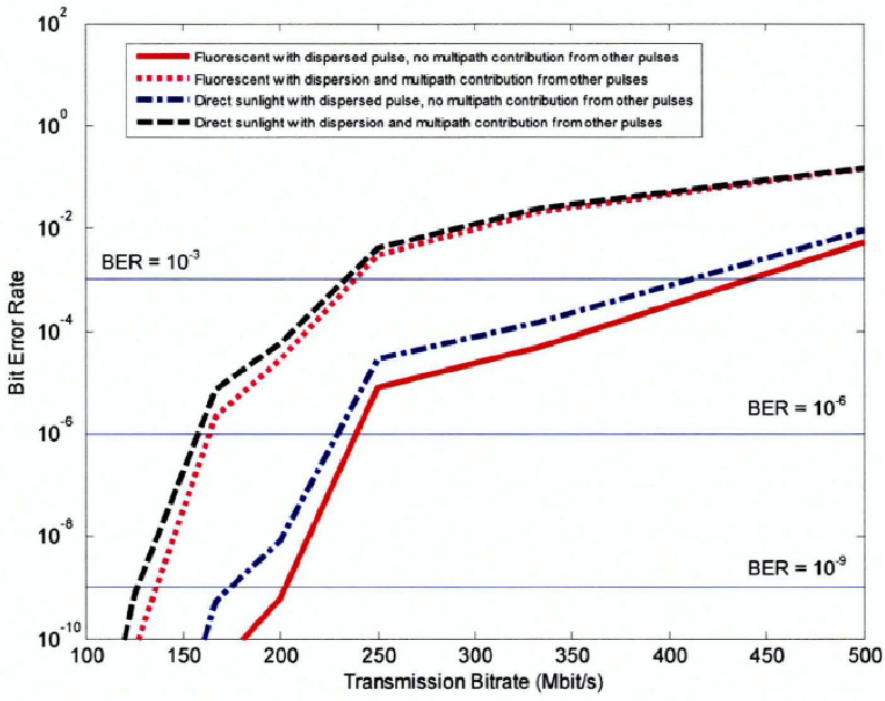


Figure 6.24 Bit error rate performance in the presence of multipath and ambient noise.

ATTENTION: The Singapore Copyright Act applies to the use of this document. Nanyang Technological University Library

Using the obtained results, the transmission bitrates corresponding to BER rates of 10^{-3}, 10^{-6} and 10^{-9} were estimated and are shown in Table 6.6. When the system performance requires a low bit error rate such as 10^{-9}, the maximum transmission under fluorescent lighting conditions with no multipath is approximately 203 MBit/s. However, when multipath is considered, the transmission bitrate is limited to 136 Mbit/s. When a higher BER of 10^{-3} is acceptable for the system performance, the scenario with fluorescent lighting and no multipath dispersion allows a transmission of 412 Mbit/s. Inclusion of multipath effects reduces the transmission bitrate to only 233 Mbit/s.

Table 6.6 Transmission bitrate for selected bit error rates

	Transmission bitrate (Mbit/s)			
	Ambient lighting conditions			
Bit Error Rate	Fluorescent with no multipath dispersion	Fluorescent with multipath dispersion	Direct sunlight with no multipath dispersion	Direct sunlight with multipath dispersion
10^{-9}	203	136	175	125
10^{-6}	239	164	229	158
10^{-3}	440	238	412	233

The effect of multipath is more pronounced at higher bitrates, leading to a greater reduction in the relative bitrates at the same signal quality level. In contrast, when considering the effect of ambient lighting on the system BER, it can be

ATTENTION: The Singapore Copyright Act applies to the use of this document. Nanyang Technological University Library

observed that the difference between the transmission rates between fluorescent lighting and direct sunlight is not as drastic as that of multipath. For example, at a BER of 10^{-3}, the bitrates corresponding to direct sunlight and fluorescent lighting are 412 Mbit/s and 440 Mbit/s respectively. The performance of a system exposed to both direct sunlight and fluorescent lighting was not simulated due to the strength of direct sunlight being more than two orders higher as compared to fluorescent lighting. In such a scenario, the effects of fluorescent ambient lighting would be drowned out by the effect of direct sunlight, and it would be reasonable to expect a performance similar to that of direct sunlight only. From the results it can be concluded that multipath has a greater effect on the signal quality and the transmission capacity of the optical wireless system than ambient noise.

For an aircraft cabin optical wireless network application, various system configurations have been simulated. Using fluorescent lighting as the ambient lighting condition, when no equalizers are used, the maximum transmission possible for a BER of 10^{-3} is 233 Mbit/s. In contrast, when equalization is used but only the power within a timeslot is considered the transmission bitrate increases to 440 Mbit/s. Furthermore, if sufficient taps are used in the equalization such that multipath effects are removed and the power of each pulse can be preserved, even greater performance can be achieved, as the system performance is only limited by noise which may not be of a considerable magnitude in an aircraft cabin environment.

ATTENTION: The Singapore Copyright Act applies to the use of this document. Nanyang Technological University Library

6.6.4 Discussion on the applicability of the design concepts to other aircraft cabins

The design proposed in this Chapter of the Thesis was optimized based on a typical medium-sized Boeing 777 aircraft cabin and the same identical placement may not be suitable to other sized cabins. While not optimized for other-sized cabins, the design methodologies proposed in the work presented here can be adopted to obtain the optimized source placement configurations for these other configurations, such as the smaller passenger cabins of private jets such as the Learjet 35, or larger-sized craft such as the new Airbus A380.

The over-arching objective in the work described was to design an optical system that is capable of achieving a relatively signal uniform distribution while using a minimal number of sources, based on balancing the needs between uniformity of the received signal and multipath effects. In general, multipath is affected by the number of copies of the same signal arriving at the receiver at different times. With an increased number of sources, there is an increased range of copies of the transmitted signal pulse being received by the detector, leading to a dispersed pulse and increased intersymbol interference.

Hence, an optimal solution would be to have a design approach that utilizes the minimum number of sources required, as more sources than necessary would lead to increased multipath effects. The approaches described in this Chapter embraced this approach by first considering the operating environments as comprising of stationary devices i.e. the seats, and mobile devices i.e. along the aisle. In terms of design, the configuration of the sources for the mobile devices took priority due to the greater challenge in designing a uniform signal distribution for the mobile user. The minimum number of sources required was found to be 11 to achieve this target.

ATTENTION: The Singapore Copyright Act applies to the use of this document. Nanyang Technological University Library

Next, the same minimalist approach was adopted in the placement of the sources for the stationary users. From Figure 6.15 in the Chapter, it can be observed that after placement of the optimized aisle sources in along the aisle, there is a drop-off of signal distribution for the seated positions as the displacement from the aisle is increased. To increase the signal power at these locations, sources were place accordingly at the sides, i.e. the "window" sources, and at the centre i.e. the "dorsal" sources, to boost up the signal intensity where it is needed the most, as shown in Figure 6.16, afterwhich the angular placement of the window sources and the power levels of all the sources were optimized. Although not described explicitly previously in the Chapter, another practical reason for the placement of the sources at these locations are the existing outlets for reading lamps and other passenger-centric devices that are usually clustered in these locations in the aircraft cabin ceiling. Optical wireless sources could thus be unobtrusively installed in these outlets to utilize existing wiring fixtures. Certainly other designs could be proposed in which the sources are arbitrarily located on the aircraft ceiling rather than being located near existing fixtures. However, new wiring arrangements may need to be planned, which can be a challenge in view of existing structures, such as overhead hand-luggage compartments.

By making use of the methods described in the Chapter and adopting it for specific cabin designs while taking into account the physical features of cabins, such as the location of lighting fixtures in the cabin, a practical optical wireless design configuration can be obtained which is particular to that specific cabin layout.

ATTENTION: The Singapore Copyright Act applies to the use of this document. Nanyang Technological University Library

6.7 Comparison with other work

As this section of the Thesis presents work on a relatively unexplored field of study, there is little common ground for a direct comparison with other research efforts. Of the research work described in Section 6.3, [146] is mainly a descriptive exploration of infrared wireless in an aircraft cabin, while [147] is primarily a feasibility study with a simple system with up to 8Mb/s for demonstration purposes.

In contrast, the work presented in this Chapter of the Thesis is an in-depth analysis of the wavelength selection for optical wireless, as well as a method to optimize the placement of optical transmitters within the aircraft cabin environment to obtain a generally uniform signal distribution strength. In addition, a communications model was used to determine the maximum transmission capacities in the presence of ambient noise as well as multipath. A simplified method of calculating the multipath contribution was also proposed in the Chapter. From the results, it was found that a transmission capacity of up to 440 Mb/s is achievable, which is comparable with the maximum capacity of next generation wireless links such as UWB, but without the radio frequency interference and potential hazard to avionics that such radio-frequency-based technologies possess.

6.8 Conclusion

In this Chapter the optical design for an optical wireless system for application in a passenger aircraft cabin was presented. Optical wireless is promising to enable a wireless network in passenger aircraft, due to there being potentially no interference with avionics, which is the prime concern when considering the use of radio frequency networks and devices in passenger aircraft cabin. An analysis was made on the most suitable wavelength, based on eye safety considerations and ambient light. It

ATTENTION: The Singapore Copyright Act applies to the use of this document. Nanyang Technological University Library

was found that from the AEL and MPE of the eye safety standard IEC 60825-1, a 1550nm wavelength device allows 10dB more power than a 850nm wavelength device. Furthermore, the lower ambient spectral noise in the 1550nm regions favours the use of the 1550nm wavelength.

Using a CAD program, a realistic cabin environment was designed. When used in conjunction with ray tracing simulations, the intensity distribution of sources placed within the environment could be determined. Using the data from ray tracing, optimization was performed to determine the positioning of sources within the aircraft environment. It was shown that this resulted in a uniform intensity distribution along the aisle as well as in the seated positions. Although this also resulted in a higher average power than the seated positions, the increased power could be used to increase the link margin of mobile users along the aisle.

The communications performance of the system was also characterized using the bit error rate performance. It was found that the multipath has a greater effect on the BER performance than the ambient noise. This is also due in part to the selection of the appropriate wavelength at 1550nm which minimizes ambient noise. It was found that, under fluorescent lighting conditions, the maximum transmission rate is almost halved from 440 Mbit/s to 233 Mbit/s for a BER requirement of 10^{-3} if multipath dispersion is not addressed. However, even at such levels the transmission capacity indicates a good potential for the use of broadband optical wireless in an aircraft passenger cabin environment. Use of white light emitting diodes to provide illumination would further limit ambient lighting effects to sunlight only.

ATTENTION: The Singapore Copyright Act applies to the use of this document. Nanyang Technological University Library

7

Conclusion and recommendations for future work

7.1 Conclusion

With the trend towards mobility and flexibility offered by wireless networks, there has been an increasing trend in the adoption of wireless networks over wired networks. Conventionally wireless networks make use of radio frequency carriers as the means of transmission of data. However, radio frequency use is limited by effects of interference, which has led to regulation and limitation of bandwidth, and security issues. In contrast, the virtually unlimited bandwidth of optical wireless, and the

ATTENTION: The Singapore Copyright Act applies to the use of this document. Nanyang Technological University Library

added wireless security from the confinement of the network to within the physical boundaries of the operating environment, make optical wireless attractive as an enabling technology for wireless networks, particularly in applications which are sensitive to radio frequency interference. The work presented in this thesis has investigated methods to improve the optical design elements of an optical wireless network, as well as explored the use of visible light optical wireless and the design of an optical wireless network in an aircraft passenger cabin.

A new design methodology was proposed for a multispot diffusing indoor optical wireless network. A survey of various conventional spot distribution patterns showed that a receiver field of view of 30° is optimal when the uniformity of signal distribution and the multipath delay spread are used as merit functions. Using this field of view, a global optimization simulated annealing approach was used to obtain a spot distribution pattern optimized based on the merit functions, and it was found that such an approach improved the performance over conventional grid patterns. Further, by adjusting the relative weights of the merit functions, the spot distribution pattern can be optimized for various requirements. The system is also capable of transmission at about 54 Mbit/s, and with diversity techniques the signal quality and hence transmission capacity can be further increased.

Computer generated holograms are often used as spot diffusers due to their robustness, flexibility and small form factor. However, such holograms are sensitive to the quality of fabrication, which can result in a strong zero order. Particularly for multispot diffused optical wireless which makes use of the reflections from multiple spots directed at the ceiling, the zero order intensity can distort the intensity distribution, biasing the intensity distribution towards the centre. In addition, a strong zero order can be hazardous to viewing by users. To reduce the zero order, an

ATTENTION: The Singapore Copyright Act applies to the use of this document. Nanyang Technological University Library

experimental setup was designed making use of polarization properties of the light that was able to reuse a portion of the zero order. Another technique was used which made use of a binary, phase-only optical element known as a phase checkerboard to redistribute the central zero order to higher orders. Theoretical expressions were derived from Fourier optics, and it was shown that use of a phase checkerboard together with a pre-shifted hologram resulted in the zero order being shifted away, leading to a reconstructed hologram pattern with no zero order interference. Various fabrication errors were simulated and it was also shown that the proposed technique was still effective in the presence of these errors, and this was also verified with experiments. The proposed technique shows promise in reducing the zero order error, particularly in complex surface relief structures of computer generated holograms where correcting the zero order by precise fabrication can be challenging.

With the advances in white light emitting diodes and the increased efficiency of white light emitting diode illumination over conventional lighting sources, solid state lighting has increasingly become popular. The optoelectronic nature of solid state lighting devices also raises the possibility of using these devices for transmission of data. However, unlike conventional lighting sources which are nearly omni-directional, white light emitting diodes are directional with an irradiance profile that sharply drops off. Using a commercial white light emitting diode, the irradiance profile was measured and modeled. With this model, an optimization process was used to obtain the angular position of multiple diodes in a lamp to create a uniform intensity distribution. Through the use of an amplification circuit, the lamps were modulated using audio signals, and it was demonstrated that the signals could be transmitted through the diodes and received using a photodetector and a speaker while no effect could be observed on the room illumination provided by the diodes. By

ATTENTION: The Singapore Copyright Act applies to the use of this document. Nanyang Technological University Library

making use of optimization to produce a uniform irradiance profile and modulation of the diodes for the transmission of data, the prototype system demonstrates the possibility of using such a system for the dual purpose of illumination and optical wireless transmission system.

The sensitivity of avionics on passenger airliners has limited the employment of radio frequency wireless networks in this environment, despite the potential weight savings from the reduced need for cabling. However, the immunity of avionics to optical wireless, and the confinement of the network to within the passenger cabin only, coupled with the wide bandwidth potential offered by optical wireless makes this technology a potential for employment in passenger aircraft. Based on eye safety requirements and ambient noise considerations it was found that the communications wavelength of 1550nm allowed a higher transmission power than other wavelengths. Using computer aided design, a realistic aircraft passenger cabin was modeled for ray tracing simulations. With the data from these simulations, the irradiance distributions of Lambertian diffuse sources from various positions were modeled and used in optimization routines to obtain a relatively uniform distribution. Furthermore, using the multipath data from the ray tracing simulations, the effect of ambient noise and multipath was investigated on the bit error rate performance of the system. A modification was made in the calculation of multipath to reduce the number of convolutions required. It was found that multipath effects were very significant at high data rates, nearly halving the data rate from 440 Mbit/s to 233 Mbit/s in the presence of fluorescent ambient noise for a bit error rate of 10^{-3} . Despite the effects of multipath, the optical wireless system is still capable of a large transmission capacity. Through the use of equalization to reduce multipath effects, the transmission capacity of the optical wireless system can be further improved.

ATTENTION: The Singapore Copyright Act applies to the use of this document. Nanyang Technological University Library

7.2 Recommendations for future work

- Improvements to the optimization of the spot pattern

Currently a simulated annealing process was used for the optimization algorithm. While simulated annealing has been shown to be effective in producing a global minimum, a much longer computation time is required compared to simpler techniques. Alternative optimization techniques that can be used are genetic algorithms, which make use evolutionary concepts in optimization. The performance of genetic algorithms and simulated annealing can be compared to determine the merits of each. Furthermore, other optimization methods can also be compared. In addition, the work on the reduction of zero order showed that the zero order could be redistributed to the higher orders. In optical wireless, this is advantageous as it boosts the intensity distribution at the corners, which can be used to improve the range of the system. This result could be integrated into the optimization process such that the spot distribution pattern is obtained and that takes into consideration of the shifted zero orders.

- Use of phase checkerboard function on the reverse side of the shifted hologram

Presently the phase checkerboard is taken to be on a separate optical element, and placed in contact with the shifted hologram. Instead of a separate optical element, the phase checkerboard could instead be fabricated on the reverse side of a hologram, with alignment taking place during fabrication. However, the propagation distance between the hologram and the phase checkerboard would have to be taken into consideration in such a scenario, and more research would

ATTENTION: The Singapore Copyright Act applies to the use of this document. Nanyang Technological University Library

have to be conducted to determine the effect on the produced intensity distribution.

- Encoding for visible light optical wireless

It was demonstrated that the visible light optical wireless system was able to transmit audio signals. For higher transmission capacity for transmission of broadband data, a digital transmission system would have to be designed. Another consideration would be the use of transmission encoding. Although the transmission rate is high such that instantaneous changes in the intensity of the white light emitting diodes are not detectable by human vision, a change in the time-average intensity due to a bias of transmission bits towards on or off bits could result in a noticeable momentary change in the output intensity. To counter this, balanced transmission codes should be used to ensure the average intensity is constant and there is no variation on the illumination from the white light emitting diode lamps

- Multiple in multiple out system for optical wireless

Recent research has shown the applicability of use of multiple in multiple out (MIMO) concepts for optical wireless. MIMO, also known as space time coding, essentially makes use of multiple transmitters to send correlated data to a receiver, and depending on the configuration, can be used to improve the reliability of transmission capacity of the system. Such a concept is particularly applicable in visible light wireless and the passenger aircraft optical wireless applications, where it would be possible to correlate the data sent through each transmitter by making use of MIMO concepts. However, this could result in a large increase in

ATTENTION: The Singapore Copyright Act applies to the use of this document. Nanyang Technological University Library

the complexity of the system, and the tradeoff between system performance and system complexity would have to be evaluated.

- Controlled intensity distribution using holograms in the aircraft environment

In the work done, it was taken that a Lambertian diffuse source was used as the sources in the aircraft environment. Besides using other intensity distribution modes for the sources, computer generated holograms can also be used to control the intensity distribution of the sources. Using holograms, the intensity distribution can be well-defined with a high contrast between illuminated and non-illuminated areas. The control of the intensity distribution makes full use of the transmission power by directing the signal power only to the desired areas. This can also be used to control the multipath interference on the system by reducing the influence from undesired neighbouring sources.

- Spatial light modulators for tracking mobile users

It was necessary to obtain a uniform illumination so as to avoid 'dark' spots with no signal at these locations. The need for a uniform illumination can be alleviated by making use of spatial light modulators as dynamic holograms for the tracking of passengers. By making use of a feedback system to update the locations of passengers, hologram patterns corresponding to these locations can be calculated and the spot distribution pattern continually adjusted to direct the signal intensity to exactly where the passengers are located.

ATTENTION: The Singapore Copyright Act applies to the use of this document. Nanyang Technological University Library

List of Author's Publications

1. W. K. Wong and G. Chen, "Indoor Diffuse Infrared Wireless LAN using a Spot-Weighted Hologram Pattern Approach", *Proceedings of the 3rd International Conference on Optical Communications and Networks,* Hong Kong, November 2004.

2. Damon W. K. Wong, George C. K. Chen, and Jianping Yao, "Optimization of spot pattern in indoor diffuse optical wireless local area networks", *Optics Express*, Vol. 13(8), p. 3000-3014, 2005.

3. T. C. Au Yeung, T. C. Chiam, C. K. Chen, C. Q. Sun, W. Z. Shangguan, W. K. Wong, and C. H. Kam, "Effect of surface bond-order loss on electrical resistivity of metallic polycrystalline thin films", *Physical Review B*, Vol. 72, p. 155417, 2005.

4. Mengtao Wen, Jianping Yao, Damon W. K. Wong and George C. K. Chen, "Holographic diffuser design using a modified genetic algorithm", *Optical Engineering*, 44(8), (2005), p. 085801

5. D. W. K. Wong and G. Chen, "Method of reduction of zeroth order intensity in computer generated holograms by use of phase addition technique", *Proceedings of the SPIE Conference on Integrated Optoelectronic Devices* 2007, Vol. 6488, p. 4880, San Jose CA, 2007.

6. D. W. K. Wong and G. Chen, "Illumination design of a white light emitting diode wireless transmission system', *Optical Engineering*, Vol. 46(8), p. 085002, 2007.

7. D. W. K. Wong and G. Chen, "Redistribution of the Zero Order by use of a Phase Checkerboard in Computer Generated Holograms", *Applied Optics*, Vol. 47(4), p 602-610, 2008.

8. D. W. K. Wong and G. Chen, "Optical design and multipath analysis for broadband optical wireless in an aircraft passenger cabin application", to appear in *IEEE Transactions on Vehicular Technology,* Nov 2008.

ATTENTION: The Singapore Copyright Act applies to the use of this document. Nanyang Technological University Library

Bibliography

[1] "IEEE 802.11 LAN/MAN Wireless LANS " IEEE ISO/IEC 8802-11:1999.

[2] D. J. T. Heatley, D. R. Wisely, I. Neild, and P. Cochrane, "Optical wireless: The story so far," *IEEE Communications Magazine*, vol. 36, pp. 72-+, 1998.

[3] A. M. Street, P. N. Stavrinou, D. C. Obrien, and D. J. Edwards, "Indoor optical wireless systems - A review," *Optical and Quantum Electronics*, vol. 29, pp.349-378, 1997.

[4] C. Singh, J. John, Y. N. Singh, and K. K. Tripathi, "Indoor optical wireless systems: Design challenges, mitigating techniques and future prospects," *IETE Technical Review*, vol. 21, pp. 101-117, 2004.

[5] D. O'Brien, G. Parry, and P. Stavrinou, "Optical hotspots speed up wireless communication," *Nature Photonics*, vol. 1, pp. 245-247, 2007.

[6] F. R. Gfeller and U. Bapst, "Wireless in-house data communication via diffuse infrared radiation," *Proceedings of the IEEE*, vol. 67, pp. 1474-1486, 1979.

[7] J. M. Kahn, W. J. Krause, and J. B. Carruthers, "Experimental Characterization of Non-Directed Indoor Infrared Channels," *IEEE Transactions on Communications*, vol. 43, pp. 1613-1623, 1995.

[8] G. W. Marsh and J. M. Khan, "50-Mb/S Diffuse Infrared Free-Space Link Using on-Off Keying with Decision-Feedback Equalization," *IEEE Photonics Technology Letters*, vol. 6, pp. 1268-1270, 1994.

[9] S. T. Jivkova and M. Kavehrad, "Multispot diffusing configuration for wireless infrared access," *IEEE Transactions on Communications*, vol. 48, pp. 970-978, 2000.

[10] M. Kavehrad and S. Jivkova, "Indoor broadband optical wireless communications: Optical subsystems designs and their-impact on channel characteristics," *IEEE Wireless Communications*, vol. 10, pp. 30-35, 2003.

[11] P. L. Eardley, D. R. Wisely, D. Wood, and P. McKee, "Holograms for optical wireless LANs," *IEE Proceedings-Optoelectronics*, vol. 143, pp. 365-369, 1996.

[12] A. D. Little, "Energy Savings Potential of Solid State Lighting in General Lighting Applications," US Department of Energy 2001.

[13] D. A. Steigerwald, J. C. Bhat, D. Collins, R. M. Fletcher, M. O. Holcomb, M. J. Ludowise, P. S. Martin, and S. L. Rudaz, "Illumination with solid state lighting technology," *IEEE Journal of Selected Topics in Quantum Electronics*, vol. 8, pp. 310-320, 2002.

[14] A. Bergh, G. Craford, A. Duggal, and R. Haitz, "The promise and challenge of solid-state lighting," *Physics Today*, vol. 54, pp. 42-47, 2001.

ATTENTION: The Singapore Copyright Act applies to the use of this document. Nanyang Technological University Library

[15] M. S. Shur and A. Zukauskas, "Solid-state lighting: Toward superior illumination," *Proceedings of the IEEE*, vol. 93, pp. 1691-1703, 2005.

[16] "Internet Usership and Penetration," *GMID - Global Market InformationDatabase*, 2006, accessed via NTU online database

[17] "Users' surging demand for bandwidth propels network growth: Tellabs annual report," *Tellabs Corporate Website*, 2007.
Available: http://www.tellabs.com/news/2007/nr022707.shtml

[18] W. Herman, "Internet video driving networks to unprecedented capabilities," *Nortel Corporate Website.*
Available: http://www.nortel.com/corporate/pressroom/feature_article/collateral/feature_metro_ethernet.pdf

[19] J. Hecht, *Understanding Fiber Optics*, 4th Edition ed: Prentice-Hall, 2002.

[20] "Telepresence Technology Overview: Being Here is Being There," *Cisco Systems, Inc.* Available:
http://www.cisco.com/en/US/products/ps7060/products_category_technologies_overview.html

[21] O. Kyas and G. Crawford, *ATM Networks*: Prentice-Hall, 2002.

[22] "Broadband growth speeds forward," *BBC News*, 2006.
Available: http://news.bbc.co.uk/1/hi/technology/4736526.stm

[23] L. B. Yang, "Talent, The Driver to Sustain Economic Success," *Information Development Authority of Singapore website*, 2007.
Available: http://www.ida.gov.sg/News%20and%20Events/20070323174318.aspx?getPagetype=21

[24] "IDC Press Release," *IDC*, 2003.
Available: http://www.idc.com/getdoc.jsp?containerId=pr2003_06_24_071500

[25] "IDC Press Release," *IDC*, 2004.
Available: http://www.idc.com/getdoc.jsp?containerId=pr2004_03_18_172424

[26] IDC, "Private communications with E. Tan," July 2007.

[27] M. Mallick, *Mobile and Wireless Design Essentials*: Wiley, 2003.

[28] X. Yang, "IEEE 802.11n: enhancements for higher throughput in wireless LANs," *IEEE Wireless Communications*, vol. 12, pp. 82-91, 2005.

[29] J. C. Haartsen, "The Bluetooth radio system," *IEEE PersonalCommunications*, vol. 7, pp. 28-36, 2000.

[30] D. P. Agrawal and Q. A. Zeng, *Introduction to Wireless and Mobile Systems*: Thomson-Engineering, 2005.

ATTENTION: The Singapore Copyright Act applies to the use of this document. Nanyang Technological University Library

[31] S. Roy, J. R. Foerster, V. S. Somayazulu, and D. G. Leeper, "Ultrawideband radio design, the promise of high-speed, short-range wireless connectivity," *Proceedings of the IEEE*, vol. 92, pp. 295-311, 2004.

[32] "New public safety applications and broadband internet access among uses envisioned by FCC authorization of ultra-wideband technology," United States Federal Communications Commission 14 Feb 2002.
Available: http://www.fcc.gov/Bureaus/Engineering_Technology/News_Releases /2000/nret0006.html

[33] "Revision of Part 15 of the Commission's Rules Regarding Ultra-Wideband Transmission Systems, First note and Order, Federal Communications Commission, ET-Docket 98-153," *US Federal Communications Commission website*, 2002.
Available :http://www.fcc.gov/Bureaus/Engineering_Technology/ Orders/2002/fcc02048.pdf.

[34] A. Molisch, *Wireless Communications*: Wiley-IEEE Press, 2005.

[35] K. Pahlavan and P. Krishnamurthy, *Principles of Wireless Networks: A Unified Approach*: Prentice Hall PTR, 2001.

[36] B. Strauss, M. G. Morgan, J. Apt, and D. D. Stancil, "Unsafe at Any Airspeed?", *IEEE Spectrum,* vol. 43, pp. 44-49, 2006.

[37] S. K. Miller, *Information Security Magazine*, "War Driving", November 2001,

[38] M. Ward, "Welcome to the era of drive-by hacking," *BBC News*, 2001.
Available: http://news.bbc.co.uk/1/hi/sci/tech/1639661.stm

[39] "Getting practical about wireless security," *IBM website*.
Available: http://www.ibm.com/developerworks/library/wi-rfsensor.html

[40] "Security in Cyberspace," *Congressional Hearings Intelligence and Security*, 1996. Available: http://www.fas.org/irp/congress/1996_hr/s960605a.htm

[41] "Denial of Service," *CERT Coordination Center* 2001.
Available: http://www.cert.org/tech_tips/denial_of_service.html

[42] J. Walker, "Unsafe at Any Key Size: An Analysis of the WEP Encapsulation," IEEE 802.11 Task Group E 2000.

[43] W. A. Arbaugh, N. Shankar, Y. C. J. Wan, and K. Zhang, "Your 802.11 wireless network has no clothes," *IEEE Wireless Communications*, vol. 9, pp.44-51, 2002.

[44] N. Borisov, I. Goldberg, and D. Wagner, "Intercepting Mobile Communications: The Insecurity of 802.11.," in *7th Annual Int'l. Conf. Mobile Comp. and Net.* Rome, Italy

[45] J. R. Barry, *Wireless Infrared Communications*: Kluwer Academic Publishers, 1994.

ATTENTION: The Singapore Copyright Act applies to the use of this document. Nanyang Technological University Library

[46] H. S. Hinton, T. J. Cloonan, F. B. McCormick, A. L. Lentine, and F. A. P. Tooley, "Free-Space Digital Optical-Systems," *Proceedings of the IEEE*, vol. 82, pp. 1632-1649, 1994.

[47] M. Forbes, J. Gourlay, and M. Desmulliez, "Optically interconnected electronic chips: a tutorial and review of the technology," *Electronics &Communication Engineering Journal*, vol. 13, pp. 221-232, 2001.

[48] D. A. B. Miller, "Rationale and challenges for optical interconnects to electronic chips," *Proceedings of the IEEE*, vol. 88, pp. 728-749, 2000.

[49] H. H. Refai, J. J. Sluss, H. H. Refai, and M. Atiquzzaman, "Comparative study of the performance of analog fiber optic links versus free-space optical links," *Optical Engineering*, vol. 45, 2006.

[50] C. C. Davis, I. I. Smolyaninov, and S. D. Milner, " Flexible optical wireless links and networks," *IEEE Communications Magazine*, vol. 41, pp. 51-57, 2003.

[51] M. C. Jeong, J. S. Lee, S. Y. Kim, S. W. Namgung, J. H. Lee, M. Y. Cho, S. W. Huh, Y. S. Ahn, J. W. Cho, and J. S. Lee, "8 x 10-Gb/s terrestrial optical free-space transmission over 3.4 km using an optical repeater," *IEEEPhotonics Technology Letters*, vol. 15, pp. 171-173, 2003.

[52] S. Williams, "IrDA: Past, present and future," *IEEE Personal Communications*, vol. 7, pp. 11-19, 2000.

[53] W. Hirt, M. Hassner, and N. Heise, "IrDA-VFIr (16 mb/s): Modulation code and system design," *IEEE Personal Communications*, vol. 8, pp. 58-71, 2001.

[54] J. J. G. Fernandes, P. A. Watson, and J. C. Neves, "Wireless Lans – Physical Properties of Infrared Systems Vs Mmw Systems," *IEEE Communications Magazine*, vol. 32, pp. 68-73, 1994.

[55] J. R. Barry, J. M. Kahn, W. J. Krause, E. A. Lee, and D. G. Messerschmitt, "Simulation of Multipath Impulse-Response for Indoor Wireless Optical Channels," *IEEE Journal on Selected Areas in Communications*, vol. 11, pp. 367-379, 1993.

[56] H. Hashemi, G. Yun, M. Kavehrad, F. Behbahani, and P. A. Galko, "Indoor Propagation Measurements at Infrared Frequencies for Wireless Local-Area Networks Applications," *IEEE Transactions on Vehicular Technology*, vol. 43, pp. 562-576, 1994.

[57] G. W. Marsh and J. M. Kahn, "Performance evaluation of experimental 50-Mb/s diffuse infrared wireless link using on-off keying with decision-feedback equalization," *IEEE Transactions on Communications*, vol. 44, pp. 1496-1504, 1996.

[58] J. M. Kahn and J. R. Barry, "Wireless infrared communications," *Proceedings of the IEEE*, vol. 85, pp. 265-298, 1997.

ATTENTION: The Singapore Copyright Act applies to the use of this document. Nanyang Technological University Library

[59] M. D. Audeh and J. M. Kahn, "Performance Evaluation of Baseband OOK for Wireless Indoor Infrared Lans Operating at 100 Mb/S," *IEEE Transactions on Communications*, vol. 43, pp. 2085-2094, 1995.

[60] J. R. Barry and J. M. Kahn, "Link Design for Nondirected Wireless Infrared Communications," *Applied Optics*, vol. 34, pp. 3764-3776, 1995.

[61] G. Yun and M. Kavehrad, "Spot-diffusing and fly-eye receivers for indoor infrared wireless communications," *Proceedings of the IEEE International Conference on Selected Topics in Wireless Communications*, 1992.

[62] J. M. Kahn, R. You, P. Djahani, A. G. Weisbin, B. K. Teik, and A. Tang, "Imaging diversity receivers for high-speed infrared wireless communication," *IEEE Communications Magazine*, vol. 36, pp. 88-94, 1998.

[63] P. Djahani and J. M. Kahn, "Analysis of infrared wireless links employing multibeam transmitters and imaging diversity receivers," *IEEE Transactions on Communications*, vol. 48, pp. 2077-2088, 2000.

[64] V. Jungnickel, T. Haustein, A. Forck, and C. von Helmolt, "155Mbit/s wireless transmission with imaging infrared receiver," *Electronics Letters*, vol.37, pp. 314-315, 2001.

[65] V. Jungnickel, A. Forck, T. Haustein, U. Kruger, V. Pohl, and C. von Helmolt, "Electronic tracking for wireless infrared communications," *IEEE Transactions on Wireless Communications*, vol. 2, pp. 989-999, 2003.

[66] J. B. Carruthers and J. M. Kahn, "Angle diversity for nondirected wireless infrared communication," *IEEE Transactions on Communications*, vol. 48, pp. 960-969, 2000.

[67] M. P. Dames, R. J. Dowling, P. McKee, and D. Wood, "Efficient Optical-Elements to Generate Intensity Weighted Spot Arrays - Design and Fabrication," *Applied Optics*, vol. 30, pp. 2685-2691, 1991.

[68] T. J. Svetla and K. Mohsen, "Multispot diffusing configuration for wireless infrared access: joint optimization of multibeam transmitter and angle diversity receiver," 1999.

[69] S. T. Jivkova and M. Kavehrad, "Wireless infrared indoor communications: how to combat the multipath distortion," 2001.

[70] K. Akhavan, M. Kavehrad, and S. Jivkova, "High-speed power-efficient indoor wireless infrared communication using code combining - Part I," *IEEE Transactions on Communications*, vol. 50, pp. 1098-1109, 2002.

[71] K. Akhavan, M. Kavehrad, and S. Jivkova, "High-speed power-efficient indoor wireless infrared communication using code combining - Part II," *IEEETransactions on Communications*, vol. 50, pp. 1495-1502, 2002.

ATTENTION: The Singapore Copyright Act applies to the use of this document. Nanyang Technological University Library

[72] A. G. Al-Ghamdi and J. M. H. Elmirghani, "Multiple spot diffusing geometries for indoor optical wireless communication systems," *International Journal of Communication Systems*, vol. 16, pp. 909-922, 2003.

[73] A. G. Al-Ghamdi and J. M. H. Elmirghani, "Optical wireless multibeam transmitter with line strip, diamond, and uniform geometries," *Optical Engineering*, vol. 42, pp. 3295-3301, 2003.

[74] A. G. Al-Ghamdi and J. M. H. Elmirghani, "Analysis of diffuse optical wireless channels employing spot-diffusing techniques, diversity receivers, and combining schemes," *IEEE Transactions on Communications*, vol. 52, pp. 1622-1631, 2004.

[75] A. G. Al-Ghamdi and J. M. H. Elmirghani, "Spot diffusing technique and angle diversity performance for high speed indoor diffuse infra-red wireless transmission," *IEE Proceedings-Optoelectronics*, vol. 151, pp. 46-52, 2004.

[76] D. Gesbert, M. Shafi, D. S. Shiu, P. J. Smith, and A. Naguib, "From theory to practice: An overview of MIMO space-time coded wireless systems," *IEEE Journal on Selected Areas in Communications*, vol. 21, pp. 281-302, 2003.

[77] Y. A. Alqudah and M. Kavehrad, "MIMO characterization of indoor wireless optical link using a diffuse-transmission configuration," *IEEE Transactions on Communications*, vol. 51, pp. 1554-1560, 2003.

[78] M. K. Simon and V. A. Vilnrotter, "Alamouti-type space-time coding for freespace optical communication with direct detection," *IEEE Transactions on Wireless Communications*, vol. 4, pp. 35-39, 2005.

[79] M. Garfield, C. Liang, T. P. Kurzweg, and K. R. Dandekar, "MIMO spacetime coding for diffuse optical communication," *Microwave and Optical Technology Letters*, vol. 48, pp. 1108-1110, 2006.

[80] D. Takase and T. Ohtsuki, "Spatial multiplexing in optical wireless MIMO communications over indoor environment," *IEICE Transactions on Communications*, vol. E89B, pp. 1364-1371, 2006.

[81] Z. Ghassemlooy, A. R. Hayes, and B. Wilson, "Reducing the effects of intersymbol interference in diffuse DPIM optical wireless communications," *IEE Proceedings-Optoelectronics,* vol. 150, pp. 445-452, 2003.

[82] H. G. Kim, "Performance enhancement of wireless LAN based on infrared communications using multiple-subcarrier modulation," *Computational Science and Its Applications - ICCSA 2005, Pt 2,* vol. 3481, pp. 295-303, 2005.

[83] M. R. Pakravan, E. Simova, and M. Kavehrad, "Holographic diffusers for indoor infrared communication systems," in *Global Telecommunications Conference, 1996. GLOBECOM '96. 'Communications: The Key to Global Prosperity*, 1996, pp. 1608-1612 vol.3.

ATTENTION: The Singapore Copyright Act applies to the use of this document. Nanyang Technological University Library

[84] S. Jivkova and M. Kavehrad, "Indoor wireless infrared local access, multi-spot diffusing with computer generated holographic beam-splitters," in *IEEE International Conference on Communications,1999. (ICC '99)*, pp. 604-608 vol.1.

[85] S. Jivkova and M. Kavehrad, "Receiver designs and channel characterization for multi-spot high-bit-rate wireless infrared communications," *IEEE Transactions on Communications,* vol. 49, pp. 2145-2153, 2001.

[86] H. Yang and C. Lu, "Infrared wireless LAN using multiple optical sources," *IEE Proceedings - Optoelectronics,*vol. 147, pp. 301-307, 2000.

[87] S. Arumugam and J. John, "Effect of transmitter positions on received power and bandwidth in diffuse indoor optical wireless systems," *Optical and Quantum Electronics,* vol. 39, pp. 1-14, 2007.

[88] J. W. Smith, *Modern Optical Engineering*, 3rd Edition ed.: McGraw-Hill Professional, 2000.

[89] T. S. Rappaport, *Wireless Communications, Principles and Practices*, 2nd ed.: Prentice-Hall, 2002.

[90] S. Kirkpatrick, C. D. Gelatt, and M. P. Vecchi, "Optimization by Simulated Annealing," *Science,* vol. 220, pp. 671-680, 1983.

[91] S. Kirkpatrick, "Optimization by Simulated Annealing - Quantitative Studies," *Journal of Statistical Physics,* vol. 34, pp. 975-986, 1984.

[92] R. E. Randelman and G. S. Grest, "N-City Traveling Salesman Problem - Optimization by Simulated Annealings," *J. Stat. Phys,* vol. 45, pp. 885-890, 1986.

[93] J. P. Yao, G. C. K. Chen, and T. K. Lim, "Holographic diffuser for diffuse infrared wireless home networking," *Optical Engineering,* vol. 42, pp. 317-324, Feb 2003.

[94] D. C. O'Shea, T. J. Suleski, A. D. Kathman, and D. W. Pratner, *Diffractive Optics: Design, Fabrication and Test.* Washington: SPIE Press, 2004.

[95] M. T. Wen, J. P. Yao, D. W. K. Wong, and G. C. K. Chen, "Holographic diffuser design using a modified genetic algorithm," *Optical Engineering,* vol. 44, Aug 2005.

[96] A. Yariv, *Optical Electronics in Modern Communications*, 5th Edition ed.

[97] G. P. Agrawal, *Fiber Optic Communication Systems*, 3rd Edition ed.

[98] A. Yariv, *Optical Electronics in Modern Communications*, 5th Edition ed.: Oxford University Press, 1997.

ATTENTION: The Singapore Copyright Act applies to the use of this document. Nanyang Technological University Library

[99] R. Ramaswami and K. Sivarajan, *Optical Networks: A Practical Perspective*, 2nd edition ed.: Morgan Kaufmann, 2001.

[100] G. Keiser, *Optical Fiber Communications*, 3rd Edition ed.: McGraw-Hill, 1999.

[101] "HFAN-09.0.1: NRZ Bandwidth - HF Cutoff vs. SNR," *Maxim IC website*, 2004. Available: http://www.maximic.com/appnotes.cfm/appnote_number/870

[102] J. M. H. Elmirghani, H. H. Chan, and R. A. Cryan, "Sensitivity evaluation of optical wireless PPM systems utilising PIN-BJT receivers," *IEE Proceedings-Optoelectronics,* vol. 143, pp. 355-359, Dec 1996.

[103] J. G. Proakis, *Wireless Communications* 4th Edition ed.: McGraw-Hill, 2001.

[104] M. D. Audeh, J. M. Kahn, and J. R. Barry, "Decision-feedback equalization of pulse-position modulation on measured nondirected indoor infrared channels," *IEEE Transactions on Communications,* vol. 47, pp. 500-503, Apr 1999.

[105] B. Sergio and B. Ezio, *Principles of Digital Transmission: With Wireless Applications*: Kluwer Academic Publishers, 1999.

[106] R. T. John, C. Richard Johnson, Jr., and J. L. Michael, *Theory and design of adaptive filters*: Wiley-Interscience, 1987.

[107] W. Bernard and D. S. Samuel, *Adaptive signal processing*: Prentice-Hall, Inc., 1985.

[108] P. S. R. Diniz, *Adaptive Filtering: Algorithms and Practical Implementation*, 2nd Edition ed.: Springer, 2002.

[109] J. R. Treichler, M. G. Larimore, and J. C. Harp, "Practical blind demodulators for high-order QAM signals," *Proceedings of the IEEE,* vol. 86, pp. 1907-1926, 1998.

[110] A. W. Lohmann and D. P. Paris, "Binary Fraunhofer holograms, generated by computer," *Applied Optics,* vol. 6, pp. 1739-, 1967.

[111] G. Tricoles, "Computer Generated Holograms - an Historical Review," *Applied Optics,* vol. 26, pp. 4351-4360, Oct 1987.

[112] D. C. O'Shea, "Reduction of the zero-order intensity in binary Dammann gratings," *Applied Optics,* vol. 34, p. 6533, 1995.

[113] E. Cuche, P. Marquet, and C. Depeursinge, "Spatial filtering for zero-order and twin-image elimination in digital off-axis holography," *Applied Optics,* vol. 39, pp. 4070-4075, Aug 2000.

[114] C. Liu, Y. Z. Li, X. T. Cheng, Z. G. Liu, F. Bo, and J. Q. Zhu, "Elimination of zero-order diffraction in digital holography," *Optical Engineering,* vol. 41, pp. 2434-2437, Oct 2002.

ATTENTION: The Singapore Copyright Act applies to the use of this document. Nanyang Technological University Library

[115] Y. M. Zhang, Q. N. Lu, and B. Z. Ge, "Elimination of zero-order diffraction in digital off-axis holography," *Optics Communications,* vol. 240, pp. 261-267, Oct 2004.

[116] G. L. Chen, C. Y. Lin, M. K. Kuo, and C. C. Chang, "Numerical suppression of zero-order image in digital holography," *Optics Express,* vol. 15, pp. 8851-8856, Jul 2007.

[117] G. Lu, Z. Zhang, S. Wu, and F. T. S. Yu, "Implementation of a non-zero-order joint-transform correlator by use of phase-shifting techniques," *Appl. Opt.,* vol. 36, pp. 470-483, 1997.

[118] S. Jutamulia and D. A. Gregory, "Soft blocking of the dc term in Fourier optical systems," *Optical Engineering,* vol. 37, pp. 49-51, Jan 1998.

[119] P. E. Keller and A. F. Gmitro, "Computer-Generated Holograms For Optical Neural Networks - On-Axis Versus Off-Axis Geometry," *Applied Optics,* vol. 32, pp. 1304-1310, Mar 1993.

[120] R. L. Morrison, "Symmetries That Simplify The Design Of Spot Array Phase Gratings," *Journal of the Optical Society of America a-Optics Image Science and Vision,* vol. 9, pp. 464-471, Mar 1992.

[121] Y. X. Liu, B. Wang, R. Y. Guo, and F. T. S. Yu, "Intelligent reduction of zero-order diffraction in Fourier optical systems," *Optical Engineering,* vol. 44, Oct 2005.

[122] D. Palima and V. R. Daria, "Holographic projection of arbitrary light patterns with a suppressed zero-order beam," *Applied Optics,* vol. 46, pp. 4197-4201, Jul 2007.

[123] J. Goodman, *Introduction to Fourier Optics*, 2nd Edition ed. New York: McGraw-Hill, 1996.

[124] V. R. Daria, P. J. Rodrigo, and J. Gluckstad, "Programmable complex field coupling to high-order guided modes of micro-structured fibres," *Optics Communications,* vol. 232, pp. 229-237, Mar 2004.

[125] E. H. Anderson, D. Ha, and J. A. Liddle, "Sub-pixel alignment for direct-write electron beam lithography," *Microelectronic Engineering,* vol. 73-74, pp. 74-79, Jun 2004.

[126] "User Manual, 512x512 SLM System," Boulder Nonlinear Systems July 2002.

[127] "Safety of Laser Products Part 1, incorporating amendments A2:2001 and A1:2002," IEC 60825-1:1994, 1994.

[128] S. Nakamura, T. Mukai, and M. Senoh, "Candela-Class High-Brightness Ingan/Algan Double-Heterostructure Blue-Light-Emitting Diodes," *Applied Physics Letters,* vol. 64, pp. 1687-1689, Mar 1994.

ATTENTION: The Singapore Copyright Act applies to the use of this document. Nanyang Technological University Library

[129] M. Yamada, T. Naitou, K. Izuno, H. Tamaki, Y. Murazaki, M. Kameshima, and T. Mukai, "Red-enhanced white-light-emitting diode using a new red phosphor," *Japanese Journal of Applied Physics Part 2-Letters,* vol. 42, pp. L20-L23, Jan 2003.

[130] Y. Tanaka, S. Haruyama, and M. Nakagawa, "Wireless optical transmissions with white colored LED for wireless home links," in *Personal, Indoor and Mobile Radio Communications, 2000. PIMRC 2000. The 11th IEEE International Symposium on*, 2000, pp. 1325-1329 vol.2.

[131] T. Komine and M. Nakagawa, "Integrated system of white LED visible-light communication and power-line communication," *Consumer Electronics, IEEE Transactions on,* vol. 49, pp. 71-79, 2003.

[132] Y. Tanaka, T. Komine, S. Haruyama, and M. Nakagawa, "Indoor visible light data transmission system utilizing white LED lights," *IEICE Transactions on Communications,* vol. E86B, pp. 2440-2454, Aug 2003.

[133] T. Komine and M. Nakagawa, "Fundamental analysis for visible-light communication system using LED lights," *Consumer Electronics, IEEE Transactions on,* vol. 50, pp. 100-107, 2004.

[134] T. Komine and M. Nakagawa, "A study of shadowing on indoor visible-light wireless communication utilizing plural white LED lightings," in *Wireless Communication Systems, 2004. 1st International Symposium on*, 2004, pp. 36-40.

[135] H. Sugiyama, S. Haruyama, and M. Nakagawa, "Experimental investigation of modulation method for visible-light communications," *IEICE Transactions on Communications,* vol. E89B, pp. 3393-3400, 2006.

[136] P. Amirshahi and M. Kavehrad, "Broadband access over medium and low voltage power-lines and use of white light emitting diodes for indoor communications," in *Consumer Communications and Networking Conference, 2006. CCNC 2006. 3rd IEEE*, 2006, pp. 897-901.

[137] W. K. E. Osterhaus, "Office lighting: a review of 80 years of standards and recommendations," 1993, pp. 2365-2374 vol.3.

[138] "Wiring Matters: An Overview of the Aircraft Wiring Issue," *Air Safety Week*, 2000. Available: http://findarticles.com/p/articles/mi_m0UBT/is_25_14/ai_62833854/pg_1

[139] "Aviation Investigation Report: In-Flight Fire Leading to Collision with Water," Transportation Safety Board of Canada A98H0003, 1998.

[140] "NTSB marks 10th anniversary of crash of TWA 800," *National Transportation and Safety Board website*, 2006. Available: http://www.ntsb.gov/pressrel/2006/060629.htm

ATTENTION: The Singapore Copyright Act applies to the use of this document. Nanyang Technological University Library

[141] P. Gumbel, *TIME.com*, "Trying to Untangle Wires", 8 Oct 2006. Available: http://www.time.com/time/magazine/article/0,9171,1543879-2,00.html

[142] "Airbus super-jumbo in new delay," *BBC News*, 2006. Available: http://news.bbc.co.uk/2/hi/business/5402922.stm

[143] B. Strauss and M. G. Morgan, "Everyday threats to aircraft safety," *Issues in Science and Technology,* vol. 19, pp. 82-86, Win 2002.

[144] T. N. Nguyen, S. V. Koppen, J. J. Ely, R. A. Williams, L. J. Smith, and M. T. P. Sahg, "Portable Wireless LAN DEvices and Two-way Radio Threat Assessement for Aircraft Navigation Radios " NASA/TP-2003-212438, 2003.

[145] "Airbus A380 specifications," in *Airbus Corporate Website.* Available: http://www.airbus.com.

[146] P. H. Potega, "Advanced infrared (AIR): intra-cabin wireless data network," in *Digital Avionics Systems Conference, 1998. Proceedings., 17th DASC. The AIAA/IEEE/SAE*, 1998, pp. G15/1-G15/8 vol.2.

[147] N. P. Schmitt, T. Pistner, C. Vassilopoulos, D. Marinos, A. C. Boucouvalas, M. Nikolitsa, C. Aidinis, and G. Metaxas, "Diffuse wireless optical link for aircraft intra-cabin passenger communication" in *Proc. Communication Systems Networks and Digital Signal Processing*, Univ. of Patras, Patras, Greece, 2006.

[148] "Boeing 777 specifications," in *Boeing Corporate Website.* Available : http://www.airbus.com.

[149] G. C. Giakos, N. Patnekar, S. Sumrain, L. Fraiwan, and V. Kumar, "A novel multipath light signal dispersion reduction technique based on controlled-polarization optical wireless link setup," *Instrumentation and Measurement, IEEE Transactions on,* vol. 54, pp. 1950-1956, 2005.